Nanostructured Semiconductor Electrodes for Solar Energy Conversion and Innovations in Undergraduate Chemical Lab Curriculum

by

Sudarat Lee

A dissertation submitted in partial fulfillment
of the requirements for the degree of
Doctor of Philosophy
(Chemistry)
in The University of Michigan
2017

Doctoral Committee:

Associate Professor Stephen Maldonado, Chair
Professor Mark M. Banaszak Holl
Associate Professor Bart M. Bartlett
Associate Professor Pei-Cheng Ku

Sudarat Lee
sudlee@umich.edu
OECID iD: 0000-0002-0851-4626

DEDICATION

To my grandma, parents, sister, and Alex

ACKNOWLEDGEMENTS

There are many, many people that I am fortunate enough to encounter in life who helped shape me into who I am today. I would like to thank my research advisor, Prof. Stephen Maldonado, for his support, encouragement, and countless career advancement opportunities he had given to me throughout my time here in the University of Michigan. I would also like to thank my dissertation committee members and collaborators for providing insightful discussion to help me advancing my research projects. During my time here in the U of M, I have made lasting friendships with people in the Maldonado lab a.k.a. my second home, FEMMES Executive Board, and MMSS Summer School etc., and I cannot thank you enough for the joy and laughter we have shared.

This page will not be complete without mentioning my closest friends and family on the other side of the globe, on a tropical paradise island called Penang in the northern peninsular of Malaysia. The 12-hour time difference seems to not have prevented us from updating each other with the latest news in our lives. I would really like to thank them for their support and for being "within reach" by phones all the time. Lastly, I would like to express my greatest gratitude and appreciation to Alex, for always being there for me for an entire decade. Thank you for being so understanding and patient with me. I cannot thank you enough for your company in all those nights in the research lab till the break of dawn. My graduate school would be colorless without these important people in my life.

TABLE OF CONTENTS

DEDICATION..... ii
ACKNOWLEDGEMENTS..... iii
LIST OF FIGURES..... vii
LIST OF TABLES..... xv
LIST OF EQUATIONS..... xvi
ABSTRACT..... xvii

CHAPTER
I. Introduction..... 1
A. Context and Importance..... 1
B. Gallium Phosphide as PEC Light Absorber..... 3
C. Preparation of High-Aspect Ratio Nanostructures: Theory..... 5
i. "Top-down" Anodic Etching..... 8
ii. "Bottom-up" Nanowire Growth..... 9
D. Content Description..... 11
E. References..... 16
II. Macroporous p-GaP Photocathodes Prepared by Anodic Etching and Atomic Layer Deposition Doping..... 20
A. Introduction..... 20
B. Materials and Methods..... 22
i. Materials..... 22
ii. GaP Anodization..... 22
iii. Atomic Layer Deposition of ZnO..... 23
iv. Photoelectrode Preparation..... 23

v. Photoelectrochemical Measurements..... 23
vi. Material Characterization..... 24
C. Results..... 24
D. Discussion..... 32
i. Synthesis of p-Type Macroporous III-V Semiconductors..... 34
ii. High-Aspect Ratio Photocathodes..... 42
E. Conclusion..... 42
F. References..... 44
III. Comparison of GaP Nanowires Grown from Au and Sn Vapor-Liquid-Solid Catalysts as Photoelectrode Materials..... 47
A. Introduction..... 47
B. Experimental Section..... 48
i. Nanowire Preparation..... 48
ii. Wet Etching..... 52
iii. Electrode Preparation..... 52
iv. Photoelectrochemical Measurements..... 52
C. Results..... 53
D. Discussion..... 63
E. Conclusion..... 65
F. References..... 67
IV. Synthesis of Photoactive $ZnSnP_2$ Semiconductor Nanowires..... 70
A. Introduction..... 70
B. Experimental Section..... 71
i. Nanowire Growth Setup..... 73
ii. Materials Characterization..... 73
iii. Photoelectrochemical Measurements..... 75
C. Results..... 76
D. Discussion..... 88
E. Conclusion..... 91
F. References..... 92

V. Preliminary Data for Realizing p-Type Nanowire Array for Photoelectrochemical Water Splitting and Dye-Sensitized Photocathodes 95
A. Introduction 95
B. GaP Nanowire Array 95
i. Experimental Section 95
ii. Results 100
iii. Discussion 110
iv. Summary 110
C. Dye-Sensitized GaP Photocathode 111
i. Experimental Section 111
ii. Results 113
iii. Discussion 120
iv. Summary 121
D. References 122
VI. Education Research Contributions in Entry Level Chemistry Laboratory Course 124
A. Overview 124
B. On-Chip Mixing for Colorimetric Quantitation of Salicylic Acid in Agar Microfluidics Channels: An Undergraduate Laboratory Experiment 125
i. Introduction 125
ii. Experimental Overview 126
iii. Results and Discussion 130
iv. Conclusion 140
C. Organic-Inorganic Hybrid Perovskite Materials Photovoltaic Cells 140
i. Introduction 140
ii. Experimental Overview 141
iii. Results and Discussion 145
iv. Conclusion 151
D. References 152
Appendix 153

LIST OF FIGURES

FIGURE

I.1 Schematic depiction of photoelectrochemical (PEC) cells. (a) Regenerative PEC cell using a n-type semiconductor as the light absorber or photoanode and (b) the same cell configuration with a p-type semiconductor as the photocathode. (c) A photosynthetic cell with a p-type semiconductor for water splitting reactions. The gray block represents a metal counter electrode..... 2

I.2 Solar energy spectrum at AM1.5. The area under the spectrum is the incidence of solar irradiance, I_r. The I_r available for conversion is determined by the band gap of the light absorber, which is indicated by the black lines. Data obtained from NREL..... 4

I.3 Band positions of several relevant semiconductors in contact with aqueous electrolyte at pH 1 in comparison to several redox couples shown on the right. Green and gray blocks represent the conduction band edge and valance band edge of the semiconductors, respectively. Figure modeled after Reference 23..... 6

I.4 (a) Schematic depiction of high-aspect ratio nanostructures functioning as a photoelectrode in a water splitting cell. (b, c) Comparison of photogenerated minority carrier collection pathway at (b) planar and (c) high-aspect ratio photoelectrodes. Figure originally published in Reference 37..... 7

I.5 (a) Schematic depiction of a typical vapor-liquid-solid (VLS) nanowire growth mechanism. There are three stages in a VLS process: (1) alloying, (2) nucleation, and (3) axial growth. (b) Au-Ge binary phase diagram to show the compositional and phase evolution as the VLS growth progresses. Adapted from Reference 57..... 10

I.6 Pseudobinary phase diagram for (a) Au and GaAs and (b) Sn and GaP. The liquid Au-Ga-As (or Sn-Ga-P for (b)) component is represented as L. Adapted from References 59 and 60..... 12

II.1 Schematic of p-type doping of anodically-etched macroporous GaP wafer using atomic layer deposition (ALD) ZnO as the Zn dopant source..... 21

II.2 Scanning electron micrographs of (a) top-down and (b, c, e, f) cross sections of intrinsic GaP wafers after being etched for various predetermined times. (d) Measured pore depth as a function of anodic etching duration at a constant current density of 100 mA cm^{-2}. The pore depth tracks with the linear relationship shown in (d). Scale bars: 2 μm..... 25

II.3 Scanning electron micrographs of (a) 40 μm-deep macroporous GaP after 150 27

cycles ZnO deposition at growth rate of 1.92 Å/s and (b) conformal ZnO films produced by ALD (indicated by red arrows) on the macroporous structures. Scale bars: 20 μm and 200 nm, respectively. (c) HAADF image and (d) corresponding elemental mapping of ZnO-coated GaP collected in STEM mode showing clear interfaces between Zn-containing layer and GaP. Scale bar: 50 nm. Average ZnO thickness is 28.9 nm.....

II.4 HAADF images of macroporous GaP surfaces annealed for (a) 2 h at 650 ºC in Ar and its corresponding elemental maps collected in STEM mode showing incorporation of Zn into GaP along with detectable amount of O mostly at the GaP surface. (b) HAADF image of the same sample after annealing for another 4 h further diffusion at 650 ºC. The elemental maps reveals migration of Zn towards the bulk of GaP, while O remained on the surface. Scale bar: 50 nm..... 28

II.5 Transmission electron micrographs of the surfaces of ZnO-coated macroporous GaP (a) before and (d) after annealing to affect Zn diffusion. (b, c, e f) Selected area electron diffraction (SAED) patterns from areas indicated showing the bulk of GaP remains single crystal after Zn diffusion, while the Zn-rich surface contains crystallites of GaP as measured from the d-spacings in the polycrystalline ring patterns in (e)..... 30

II.6 (a) Cross-section view of Hg/GaP heterojunction setup for current-voltage response measurements. (b) Current-voltage response of intrinsic GaP wafer (blue) and ZnO-coated GaP after annealing for 20 h (red). (c) Photoresponse of a representative ZnO-coated GaP annealed for 20 h measured in an aqueous solution containing 1 M KCl and 0.01 M methylviologen dichloride in a 3-electrode photoelectrochemical cell..... 31

II.7 a) Current density-potential response of a representative macroporous p-GaP photoelectrode before and after a brief etch in a commercial GaP etchant. b) Steady-state photocurrent density-potential responses of doped planar p-GaP (black) and macroporous p-GaP (red) immersed in 1 M KCl containing 10 mM MV^{2+} under 100 mW cm^{-2} illumination. c) Wavelength-dependent quantum yield profiles of the same macroporous p-GaP photoelectrodes in (b) in 1 M KCl with 10 mM MV^{2+} at E = -1.0 V vs E(Ag/AgCl). The corresponding profile for a planar p-GaP photoelectrode after the same Zn doping and etch steps (black dotted line) is also shown..... 33

II.8 Schematic depiction of an idealized ZnO-coated macropore wall viewed from the plane orthogonal to the anodic etching direction. Orange: GaP; Gray: ALD ZnO coating. (Not drawn to scale)..... 36

II.9 (a) Representative energy dispersive X-ray spectrum obtained at approximately 50 nm from the surface of a Zn-doped macroporous GaP. (b) Elemental line profile collected in the direction indicating in the corresponding HAADF image in (c). The intensity was corrected with respective sensitivity factors and conveyed in terms of atomic percent. Scale bar: 50 nm..... 37

II.10 (a) A representative capacitance-potential (C^{-2}-E) response for a Zn-doped planar p-GaP collected from a Hg/GaP Schottky barrier contact in the dark. (b) 38

Corresponding log f vs. log Z Bode plot at a reverse bias of -0.1 V. (c) Plot of hole concentration available at certain distances from the surface of Zn-doped planar GaP wafer.....

II.11 XPS depth profile of Zn in a Zn-doped planar p-GaP diffused at T = 650 ºC fro 6 h. The Zn concentration measured using impedance spectroscopy was plotted as black dotted line for comparison..... 40

II.12 (a) Survey and (b) Zn 2p spectra obtained from a Zn-doped planar GaP wafer after 6 h of diffusion at T = 650 ºC..... 41

III.1 Schematic depiction of the multi-zone tube furnace setup used for solid source sublimation GaP nanowires nanowire growth..... 50

III.2 Cross-section scanning electron micrographs of GaP nanowires grown via solid sublimation. a) Au-seeded GaP nanowires on GaP(111)B grown at T = 620 °C. b) Sn-seeded GaP nanowires on GaP(111)B at T = 500 °C. Scale bars: a) 5 μm; b) 2 μm..... 54

III.3 a) Low-magnification transmission electron micrographs of a representative Au-seeded GaP nanowire. b) High-magnification transmission electron micrograph of the edge of a Au-seeded GaP nanowire. c) Selected area electron diffraction (SAED) pattern collected along the [110] zone axis of the Au-seeded GaP nanowire. d) Low-magnification transmission electron micrographs of a representative Sn-seeded GaP nanowire. e) High-magnification transmission electron micrograph of the edge of a Sn-seeded GaP nanowire. f) SAED pattern collected along the [211] zone axis. Scale bars: a) 100 nm; b) 5 nm; d) 50 nm; e) 2 nm..... 55

III.4 a) Unpolarized Raman spectra of Au- and Sn-seeded GaP grown on Si(111) substrates. b) Comparison of the Raman spectra for Sn-seeded GaP nanowires before and after etching in 1 M HCl for 10 min. Excitation wavelength: 785 nm... 57

III.5 Energy dispersive X-ray spectra collected from Sn-seeded GaP nanowire films (a) before and (b) after etching in 1 M HCl for 10 min and also from Au-seeded GaP nanowire films (c) before and (d) after etching in KI/I_2 solution for 30 s..... 59

III.6 Steady-state current-potential responses in both the presence and absence of 100 mW cm^{-2} ELH illumination for (a) a representative Au-GaP nanowire film photoelectrodes on n-GaP(111)B collected in dry acetonitrile containing 0.5 mM ferrocenium, 49.5 mM ferrocene, and 1 M $LiClO_4$. b) Wavelength-dependent short-circuit photocurrent quantum yields for five separate Au-seeded GaP nanowire film phototelectrodes in the same electrolyte as (a). A representative response from an uncoated substrate is also shown. c) Steady-state current-potential for a representative Sn-seeded GaP nanowire film electrode on n-GaP(111)B immersed in the same electrolyte as in (a) in both the presence and absence of 100 mW cm^{-2} ELH illumination. d) Representative steady-state current-potential responses in both the presence and absence of 100 mW cm^{-2} ELH illumination for Sn-seeded GaP nanowire film electrodes on n-GaP(111)B and p-GaP(111)B substrates in aqueous electrolyte containing 10 mM methyl viologen dichloride (MV^{2+}) and 1 M KCl..... 60

IV.1 $ZnSnP_2$ unit cell with either (a) cation-ordered chalcopyrite crystal structure or (b) cation-disordered sphalerite crystal structure. Note for (b), the Zn and Sn atoms have 0.5 probability of occupying the cation sites, and the resulting unit cell is cubic $Zn_{0.5}Sn_{0.5}P$, i.e. two unit cells are shown in (b)..... 72

IV.2 Schematic depiction (not to scale) of the single-zone tube furnace setup used for $ZnSnP_2$ nanowire growth..... 74

IV.3 a) Cross-sectional scanning electron micrograph of a $ZnSnP_2$ nanowire film grown on 20 nm Sn islands for 1 h. b) The corresponding Raman spectrum collected with 785 nm excitation source. (c) The powder X-ray diffractogram collected for the same nanowire film..... 77

IV.4 (Left) $ZnSnP_2$ nanowire films on Si substrates after 1 h growth. (Right) Appearance of growth substrates synthesized under conditions that produced predominantly Zn_3P_2 nanowires..... 78

IV.5 Figure IV.5. Bright-field diffraction-contrast transmission electron micrograph and (b) the selected-area electron diffraction pattern collected from the highlighted area of an isolated $ZnSnP_2$ nanowire. (c) Phase-contrast image showing lattice fringes..... 80

IV.6 (a) Raman spectra of nanowire films grown on 20 nm Sn islands for various duration. The presented data were collected after 1 h (black), 1.5 h (maroon), and > 2 h (red) of growth, respectively. (b) Raman spectra of nanowire films grown on 5 nm (black) and 30 nm (red and blue) Sn islands for 1 h to 1.5 h. Excitation source: 785 nm..... 81

IV.7 Elemental distribution of a representative $ZnSnP_2$ nanowire. a) HAADF image of the nanowire taken in STEM mode. b) Radial and c) axial EDS line scans depicting the relative amounts of Zn, Sn, and P..... 84

IV.8 Differentiated Auger spectrum collected from representative $ZnSnP_2$ nanowires sample prepared from 20 nm Sn islands for 30 min..... 85

IV.9 The distribution of Zn, Sn and P in these $ZnSnP_2$ nanowires (different nanowire within the sample) is homogenous throughout the length of the nanowire as shown in EDS mapping..... 86

IV.10 Optical properties of $ZnSnP_2$ nanowires films plotted using Tauc equation. The direct bandgap energy was determined to be 1.51 eV..... 87

IV.11 a) Current density vs. potential response of as-prepared $ZnSnP_2$ nanowire films in the dark (black) as well as under white light illumination (red). b) Chopped photoresponse of nanowire films when a bias of -0.4 V vs. Ag/AgCl was applied. The nanowires showed cathodic behavior when tested in 20 mM methylviologen and 1 M KCl..... 89

V.1 Schematic depiction of the photolithography process employed to create metal particle array for “bottom-up” nanowire growth..... 97

V.2 Schematic illustration of the multi-zone tube furnace setup used for nanowire growth experiments. The temperature profile of Zone T_2 was measured with a thermocouple and T_2 was set to 500 ºC during the measurement..... 98

V.3 Scanning electron micrographs of patterned SiO_x well array (a) with as-deposited ~140 nm Au film, (b) after annealing at 900 ºC in Ar (g) for 1 h. (c) Cross-sectional scanning electron micrograph of annealed Au film in patterned SiO_x well array..... 101

V.4 (a-c) Cross-section scanning electron micrographs of nanowire array prepared from Au-patterned Si substrate using conditions in Table VI.1. (d) Unpolarized Raman spectrum collected from as-prepared nanowire array in (a)..... 102

V.5 (a) Top-down scanning electron micrograph of as-deposited Au films in patterned GaP wafer. (b) Au-patterned GaP wafer after annealing at T = 650 ºC for 1 h. (c, d) Cross-sectional scanning electron micrograph of Au-patterned GaP wafer after annealing at T = 800 ºC for 30 min imaged at two different locations within a substrate..... 104

V.6 Cross-sectional scanning electron micrographs of GaP nanowires grown from Au-patterned GaP (111)B substrates under conditions summarized in Table VI.2.. 105

V.7 Cross-sectional scanning electron micrographs of GaP nanowires grown from Sn-patterned GaP (111)B substrates under conditions summarized in Table VI.3..... 107

V.8 Transmission electron micrographs of an individual nanowire coated with 10 cycles ALD ZnO (a) before and (c) after annealing at T = 650 ºC in the presence of P vapors. (b) EDS spectrum collected from (c). (d) Spectral responses of Sn-seeded GaP nanowire films measured at -0.5 V vs. Ag/AgCl in 1 M KCl with 2 mM $EuCl_3$ as-prepared (blue) and after annealing (red)..... 109

V.9 The measured reflectivity of a GaP(111)B substrate coated with 25 cycles of ALD ZnO vs. incident X-ray angles. Fast-Fourier transform (FFT) of the periods indicated the ZnO film thickness was 3.4 nm..... 114

V.10 High-resolution transmission electron micrographs of the ZnO/GaP wafer interface. (a) High-magnification image taken from the region indicated in (b) showing nanoparticles with lattice d-spacing that matched the d(002) and d(011) planes of wurzite ZnO [Inset: FFT of the polycrystalline ZnO nanoparticles] (c) High-resolution image taken from the region indicated in (b) showing atomic columns of GaP single-crystalline wafer. The lattice d-spacing was measured to be 0.32 nm, consistent with d(111) of zinc blende GaP. [Inset: FFT of the wafer confirms the plane orthogonal to the incident electron beam was [110]]..... 115

V.11 (a) Schematic of an ALD ZnO-coated GaP wafer and the molecular structure of Rose Bengal without the cations. (b, c) High-resolution Zn 2p and I 3d XP spectra of a p-GaP(111)B/ZnO substrate adsorbed with Rose Bengal dyes before (black) and after (red) being in aqueous electrolyte for 30 min..... 116

V.12 Measured external quantum yield at sub-band gap wavelengths for a p-GaP(100)/ZnO photoelectrode in clear 1 M KCl at pH 7.8. The electrode had been soaked in aqueous solutions containing concentrations of dissolved rose bengal ranging from 0.05 mM to 8 mM for 30 min prior to measurements. (b) Plot of measured external quantum yield at 580 nm as a function of the concentration of rose Bengal in the adsorption step. The data were collected at - 118

0.6 V vs. Ag/AgCl.....

V.13 Measured external quantum yield at sub-band gap wavelengths for (a) ZnO-coated p-GaP(100), (b) (111)A, and (c) (111)B photoelectrode in clear 1 M KCl at pH 7.8. (b, d, f) Current-potential photoresponses of said electrodes in dark and under 580 nm light illumination. The EQY data collected at -0.6 vs. Ag/AgCl..... 119

VI.1 The outline of the channel geometries students will construct in the experiment. (a) A "Y" channel, (b) "90°" channel, and (c) "Zigzag" channel. Figures are not drawn to scale..... 127

VI.2 Experimental setup..... 129

VI.3 Representative digital photographs taken from student-built "90°" channel: (a) 100% DI water; the flow remains laminar. (b) 50/50 water/methanol; some degrees of mixing is observed. (c) 100% methanol; mixing is observed. The photos were taken from the same region of the channel. Scale bars: 5 mm..... 133

VI.4 Figure VI.4: Digital photographs of student-built microfluidic devices. Channels shown in (a-c) has 100% water flowing through the channels. Despite the channel geometry, the flow remains laminar. Channels shown in (d-f) has 50% methanol added in the solvent. In this case, mixing is observed with the "Zigzag" and "90°" channels. Despite the fluid composition, very little to no mixing was observed in the "Y" channels..... 134

VI.5 Kinematic viscosity as a function of methanol composition at room temperature... 135

VI.6 Close-up digital photographs of colored iron (III) – salicylate complex at increasing concentrations of salicylate ions. Scale bars: 5 mm..... 137

VI.7 Representative calibration curve from student-built microfluidic device (a) and calibration curve generated via UV-vis spectroscopy (b). Very good correlation is observed between the RGB analysis and salicylate concentration as per the R^2 value of 0.96, comparable with the correlation observed in the absorbance vs. salicylate curve. 138

VI.8 Results of student surveys: We surveys students across two sections (N = 25) before and after they completed the microfluidics experiment. Students replied to a series of statements with values that ranged from 1 (strongly disagree) to 5 (strongly agree)..... 139

VI.9 Schematic depiction of the electrodeposition experiment. The working electrode is the TiO_2-coated FTO glass, and the counter electrode is a platinized Cu strip. The dimensions and measurements of the electrochemical cell are listed in mm..... 143

VI.10 Current-potential curves of several counter electrode materials..... 144

VI.11 Schematic depiction at cross-section of the $MAPbI_3$ photovoltaic cell: (a) electrodeposition of PbO_2 on TiO_2-coated FTO glass, (b) conversion of PbO_2 to PbI_2, (c) conversion of PbI_2 to $MAPbI_3$, and (d) final assembly of photovoltaic cell completed with CuSCN layer, Kapton tape mask, and carbon ink as the ohmic contact. (e) Top-down view of the complete cell making electrical contact to a custom-built photovoltaic cell testing device for J-E measurement. (f) The J-E plot of a representative $MAPbI_3$ photovoltaic cell prepared as described in the 146

text. Under 100 mW cm^{-2} illumination, η = 0.02 %.....

VI.12 Transmittance spectra collected from the (a) yellow PbI_2 film and (b) the same film after converted to an orange Et-NH_2-PbI_2. (c) The measurements of the thin film UV-vis holder made from a 6 mm thick acrylic sheet in a CO_2 laser cutter; shaded area denotes "rastering mode" instead of cutting. (d) The digital photograph of the finished holders. The single-substrate holder is done by rastering the shaded area in (c) at 50% laser power while 80% is used to make the double-substrate holder..... 149

A.1 Measured potential dependence of p-GaP(100) sensitized with 5 μM Rh-B in deaerated 1 M KCl electrolyte containing 2, 5 or 10 mM $1e^-$ reductive redox couples. (a) $EuCl_3$ and (c) methyl viologen dichloride ($MVCl_2$), and the electrodes were illuminated with 580 nm light at 0.27 mW cm^{-2}; pH = 4.2. (b, d) Current-potential responses collected from Au electrode in 1 M KCl with 2 mM (b) $EuCl_3$ and (d) $MVCl_2$; pH = 4.2..... 156

A.2 High-resolution (a) S 2p, (b) N 1s, and (c) I 3d XP spectra of planar GaP(100) samples as-etched (black), after treating in 10 v/v% $(NH_4)_2S$ for 6 h (red), and after immersing in 6 mM rose Bengal solution for 30 min (blue). The black vertical lines indicate the expected binding energies for each element..... 157

A.3 Measured wavelength dependence net photocurrent generation from p-GaP(100) electrode in clear 1 M KCl. The electrode had been soaked in 10 v/v% $(NH_4)_2S$ (black dotted-line) and followed by 6 mM rose Bengal (anionic dye; blue line) or 6 mM rhodamine-6G (cationic dye; red line). The structure of each dye is shown. The electrode was poised at -0.65 V vs. Ag/AgCl..... 158

A.4 (a) Measured external quantum yield at sub-band gap wavelengths of p-GaP(100) electrode that was previously treated with 10 v/v% $(NH_4)_2S$ and adsorbed with rose Bengal dyes in deaerated clear 1 M KCl at various pH. (b) External quantum yield measured at 580 nm and 640 nm light as a function of the pH of the electrolyte. The EQY were collected at -0.65 V vs. Ag/AgCl..... 159

A.5 Technique reproducibility: Measured external quantum yield in deaerated 1 M KCl (pH 4.2) at sub-band gap wavelengths of the same p-GaP(100) electrode that was previously treated with 10 v/v% $(NH_4)_2S$. The electrode was immersed in 6 mM RB for 30 min before each measurement, and subsequently cleaned in acetone and acid to remove adsorbed dye before the next data collection. The same electrode was soaked in RB solution to re-adsorb the dye molecule before next experiment. The EQY were collected at -0.65 V vs. Ag/AgCl..... 160

A.6 (a) Measured external quantum yield at sub-band gap wavelengths of p-GaP(100) electrode that was previously treated with 10 v/v% $(NH_4)_2S$ and adsorbed with rose Bengal dyes in deaerated 1 M KCl containing 0 – 2 mM $EuCl_3$ at pH 4.2. The data were collected at -0.65 V vs. Ag/AgCl. (b) External quantum yield measured at 580 nm as a function of the concentration of Eu^{3+} species in the electrolyte..... 162

A.7 (a, c) Measured external quantum yield at sub-band gap wavelengths of RB-adsorbed p-GaP(100) electrode in deaerated 1 M KCl containing 0 – 20 mM 163

MV^{2+}. (b, d) External quantum yield measured at 580 nm as a function of the concentration of MV^{2+} species in the electrolyte. (e, g) External quantum yield collected from two separate RB-adsorbed GaP(100) electrodes in 1 M KCl with 0 – 2 mM MV^{2+}. The electrolyte was stirred rigorously throughout the data acquisition. (f, h) The corresponding plots of quantum yield measured at 580 nm against the concentration of MV^{2+} species. Note that (g) and (h) were collected in decreasing order, i.e. from electrolyte containing 2 mM MV^{2+} to 0 mM MV^{2+}. ($E_{applied}$: 0.65 V vs. Ag/AgCl).....

A.8 (a, c, e) Measured external quantum yield at sub-band gap wavelengths of three separate RB-adsorbed p-GaP(100) electrodes in deaerated 1 M KCl containing 0 – 2 mM MV^{2+}. The data were collected in decreasing order, i.e. from electrolyte containing 2 mM MV^{2+} to 0 mM MV^{2+}. (b, d, f) Plots of external quantum yield measured at 580 nm from three separate electrodes as a function of the concentration of MV^{2+} species in the electrolyte. The data were collected at -0.65 V vs. Ag/AgCl..... 164

LIST OF TABLES

TABLE

III.1 Comparison of Sn and Au properties..... 49

III.2 Summary of Photoresponses from 5 Separate Au-seeded GaP Nanowire Film Electrodes in Dry Acetonitrile[a]..... 62

IV.1 Observed active Raman scattering of as-grown nanowire films..... 82

V.1 Summary of growth conditions used to prepare GaP NW on Au-patterned Si wafer..... 102

V.2 Summary of growth conditions used to prepare GaP nanowires on Au-patterned GaP(111)B wafer..... 106

V.3 Summary of growth conditions used to prepare GaP nanowires on Sn-patterned GaP(111)B wafer..... 108

VI.1 R_e as a function of methanol composition and channel geometry..... 132

A.1 Summary of sample names and the corresponding treatments..... 157

LIST OF EQUATIONS

EQUATION

I.1 Equation for depletion width..... 9

II.1 Mott-Schottky relationship..... 39

IV.1 Kubelka-Munk relationship..... 83

IV.2 Tauc Equation..... 83

IV.3 Chemical reaction for in-situ generation of P_2..... 88

IV.4 Chemical reaction for formation of $ZnSnP_2$..... 90

VI.1 Equation for calculating Reynolds' number..... 130

VI.2 Half reaction at anode..... 147

VI.3 Half reaction at cathode..... 147

VI.4 Chemical reaction for conversion of PbO_2 to PbI_2..... 147

VI.5 Chemical reaction for conversion of PbI_2 to $MAPbI_3$..... 147

VI.6 Equation for calculating conversion efficiency..... 148

VI.7 Equation for calculating fill factor..... 148

ABSTRACT

This dissertation presents the methodology and discussion of preparing nanostructured, high aspect ratio p-type phosphide-based binary and ternary semiconductors *via* "top-down" anodic etching, a process which creates nanostructures from a large parent entity, and "bottom-up" vapor-liquid-solid growth, a mechanism which builds up small clusters of molecules block-by-block. Such architecture is particularly useful for semiconducting materials with incompatible optical absorption depth and charge carrier diffusion length, as it not only relaxes the requirement for high-grade crystalline materials, but also increases the carrier collection efficiencies for photons with energy greater than or equal to the band gap.

The main focus of this dissertation is to obtain nanostructured p-type phosphide semiconductors for photoelectrochemical (PEC) cell applications. Chapter II in the thesis describes a methodology for creating high-aspect ratio p-GaP that function as a photocathode under white light illumination. Gallium phosphide (GaP, $\mathbf{E}_g$ = 2.26 eV) is a suitable candidate for solar conversion and energy storage due to its ability to generate large photocurrent and photovoltage to drive fuel-forming reactions. Furthermore, the band edge positions of GaP can provide sufficient kinetics for the reduction of protons and CO_2. The structure is prepared by anodic etching, and the resulting macroporous structures are subsequently doped with Zn by thermally driving in Zn from conformal ZnO films prepared by atomic layer deposition (ALD). The key finding of this work is a viable doping strategy involving ALD ZnO films for making functioning p-type GaP nanostructures.

Chapter III compares the GaP nanowires grown from gold (Au) and tin (Sn) VLS catalysts in a benign solid sublimation growth scheme in terms of crystal structure and photoactivity. Sn is less noble than Au, allowing complete removal of Sn metal catalysts from the nanowires through wet chemical etching which found to be useful for subsequent thermal diffusion p-type doping without fear of contaminations like Au. The main finding of this work is Sn-seeded GaP nanowires although Sn was removed without any residues and the nanowires had less twin defects than Au-seeded GaP, the nanowires were degenerately n-doped. On the

contrary, Au-seeded GaP nanowires exhibited n-type characteristics with orthogonalized light absorption and charge separation.

Chapter IV describes the synthesis of $ZnSnP_2$, a ternary analog of GaP comprised of low-cost, earth-abundant elements in the nanowire form using Sn nanoparticles as the VLS growth seed. The as-prepared $ZnSnP_2$ nanowire film is capable of sustaining stable cathodic photoresponse in aqueous electrolyte under white light illumination. The nanowires were crystalized in the stoichiometric sphalerite form and possessed a direct optical band gap of ~ 1.5 eV instead of the chalcopyrite structure that has comparable band gap energy to GaP. The Sn nanoparticles acted as the VLS seed as well as Sn source for the $ZnSnP_2$ nanowires growth.

Chapter V summarizes the progress and findings of p-GaP nanowire array films as well as a phase non-specific, persistent ALD dye attachment scheme that facilitates hole injection into p-GaP photocathodes, extending the photon absorption range beyond its band gap. Lastly, a separate work about undergraduate chemical education development is documented in Chapter VI of this thesis. Chapter VI details the efforts made in two distinct undergraduate laboratory coursework with the intention to introduce modern microfluidics and photovoltaic technologies including multidisciplinary research experience to the undergraduate students.

CHAPTER I
Introduction

A. Context and Importance

The world population is estimated to reach 10 billion by year 2050.[1-2] Existing technologies and energy infrastructure are expected to supply 20 to 40 terawatts of power to meet the estimated global energy demand.[1, 3] If our rate of consumption of fossil fuels remains the same as today, the equivalent CO_2 emission rate would be at least 40 billion metric tons per year by 2050.[4] CO_2 is a greenhouse gas, and such unregulated emission greatly accelerates global warming.[5] There is a pressing need for us to reduce our reliance on fossil fuels and we can achieve so without trading our standard of living, by converting to renewable energy resources like sunlight, which emits more energy in an hour than the global energy consumption per year.[3] However, one disadvantage of utilizing solar energy is insolation intermittency.[6] Factors such as seasons (angle of the sun and hour of insolation) and weather (cloudy vs. sunny day) determine the available power that can be delivered to households.

For more than four decades, photoelectrochemical (PEC) water splitting system has often been presented as an elegant approach to store converted solar energy in the form of chemical bonds for rainy days.[7-9] The first demonstration of a PEC water splitting cell was in 1972 by Fujishima and Honda,[8] who used TiO_2 as the light absorber in aqueous electrolyte to split water into H_2 and O_2 under irradiation of 500 W Xe lamp. Owing to its wide band gap, TiO_2 has very low solar energy conversion efficiency and since then numerous researches had been conducted to find suitable materials to realize the PEC cell technology. Comprehensive reviews can be found in Walter et al. for water splitting cell,[10] Ager III et al. for device efficiency compilation,[11] and Lewis N. for perspectives on integrated PEC system.[12]

In general, there are two types of PEC cells, namely regenerative cell and photosynthetic cell. Components and band structures of both PEC cells are presented in Figure I.1. Figure I.1a illustrates the operation of an n-type semiconductor or photoanode under illumination in a regenerative cell with the presence of an oxidative redox couple. Band-bending formed as a

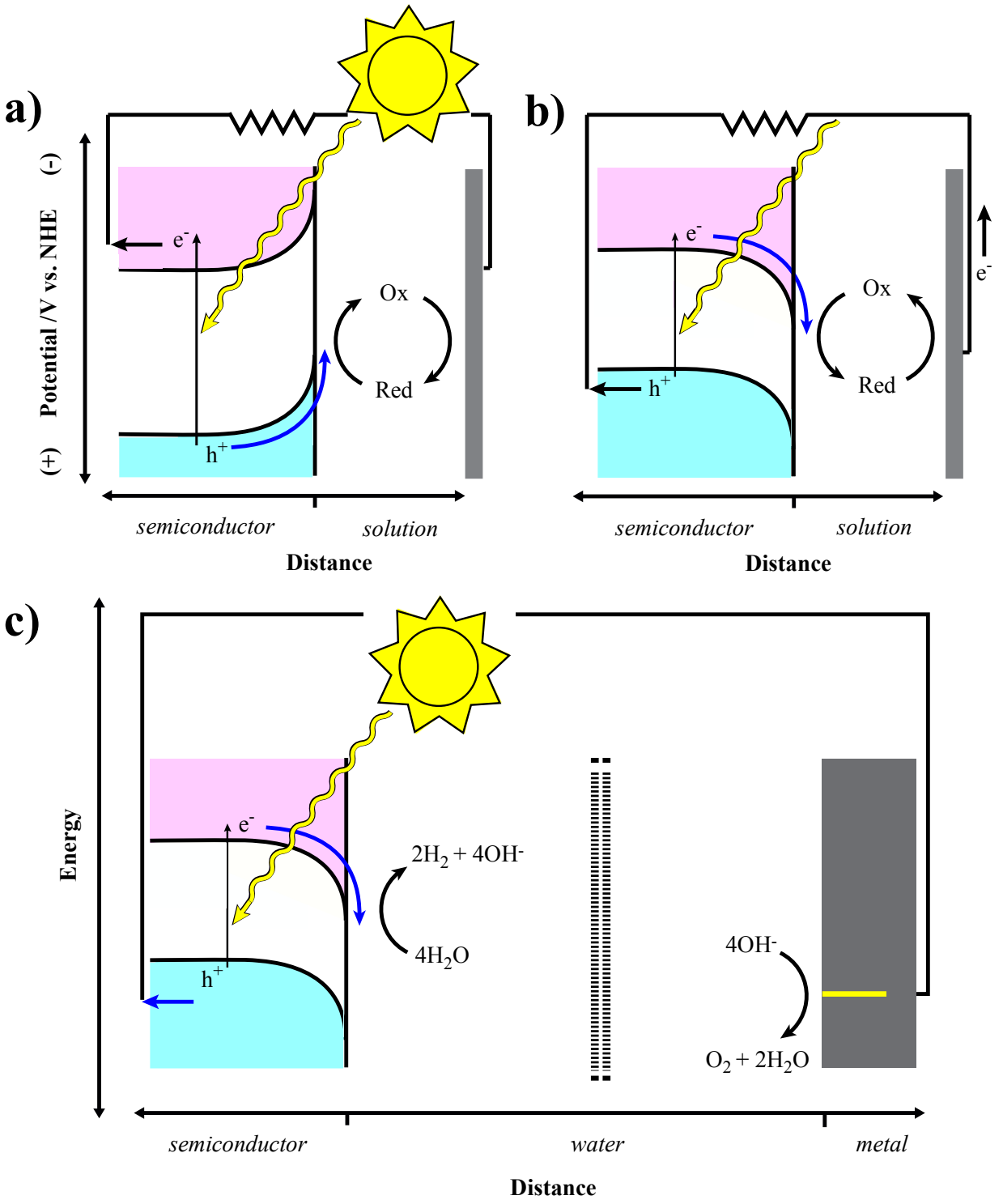

Figure I.1 Schematic depiction of photoelectrochemical (PEC) cells. (a) Regenerative PEC cell using a n-type semiconductor as the light absorber or photoanode and (b) the same cell configuration with a p-type semiconductor as the photocathode. (c) A photosynthetic cell with a p-type semiconductor for water splitting reactions. The gray block represents a metal counter electrode.

result of charge equilibration between the photoanode and the solution in contact. When a photon with energy greater than the band gap is absorbed by the photoanode to generate free charge carriers (e^- and h^+), the minority carrier, h^+, is separated by existing electric field to the surface to be captured by the redox species while the majority carrier, e^-, is drawn towards the back contact and traveled through an external load to recombine with the h^+ (shuttled by the redox species) at the counter electrode. An analogous process is seen with p-type semiconductor or photocathode with a reductive redox couple (Figure I.1b). In the case of photosynthetic cell (Figure I.1c) two redox couples are involved at the respective electrodes: proton reduction and water oxidation reactions for water splitting system. Under illumination, H_2 and O_2 are produced at respective electrodes in which H_2 can be stored as feedstock for fuel cells.

In order to make PEC water splitting technology viable, high solar-to-fuel conversion efficiency is necessary. However, the required input energy depends on the thermodynamic potential needed to drive the chemical reactions. For water splitting reaction, the energy requirement is $\Delta E = 1.23$ V.[2, 13-14] However, due to losses caused by polarization within the PEC system, recombination of the photogenerated e^--h^+ pairs, resistance of electrodes and electrical connections, and voltage losses at the contacts, the optimal energy of a photon has to be 1.7-2.0 eV for unassisted water splitting.[13-14] This poses limitations on using single band gap materials for PEC water splitting as TiO_2 ($\mathbf{E_g}$ = 3.2 eV) contains large free Gibbs energy (high photovoltage) but does not absorb enough photons to be efficient (relatively low photocurrent) while Si ($\mathbf{E_g}$ = 1.12 eV) has high photon-to-electricity conversion efficiency but not enough free Gibbs energy to do the reaction (Figure I.2). Although Gibbs energy per photon decreases as wavelength increases, fortunately, the tradeoffs can be remediated with mid-sized band gap light absorbers ($\mathbf{E_g} \sim 2.0$ eV) and sensitizer ≤ 610 nm.[13]

B. Gallium Phosphide as PEC Light Absorber

Gallium phosphide (GaP) is a suitable candidate material for PEC cells. First, it is already a technologically relevant semiconductor material with a preexisting infrastructure for production at large scales.[15] Secondly, GaP has a favorable mid-sized band gap ($\mathbf{E_g}$ = 2.26 eV) that offers the possibility of a large photovoltage and an appreciable photocurrent (i.e. ~10 mA cm^{-2}) under illumination with sunlight at an intensity of 100 mW cm^{-2}.[16-18] Furthermore, its conduction band edge situated ~ 1 V more energetic for proton reduction and CO_2 reduction,

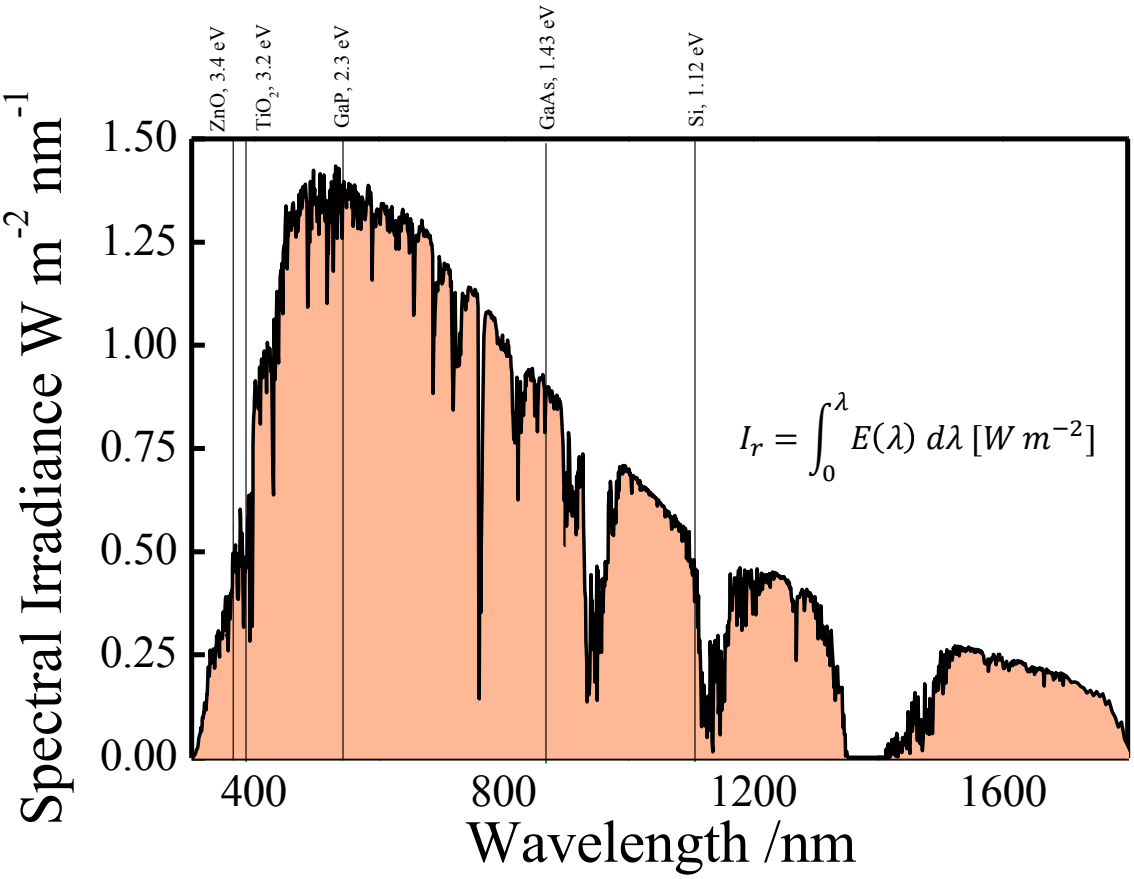

Figure I.2. Solar energy spectrum at AM1.5. The area under the spectrum is the incidence of solar irradiance, I_r. The I_r available for conversion is determined by the band gap of the light absorber, which is indicated by the black lines. Data obtained from NREL.

perfect for solar energy conversion and storage.[19-22] The band edge position of GaP relative to aforementioned chemical reactions as well as other wide-band gap semiconductors are tabulated in Figure I.3.[23] Thirdly, crystalline GaP can possess much larger charge carrier mobilities than known metal oxide semiconductors with comparable mid-size band gap such as α-Fe_2O_3, Cu_2O, and $BiVO_4$.[24-27]

Nevertheless, the use of GaP also has two tangible and formidable drawbacks. The intrinsic deficiencies of the native surface chemistry of GaP are well documented,[28-29] as are recent advancements in surface passivation strategies.[30-35] The other drawback with GaP involves the indirect optical band gap, which means the photogeneration process at band gap requires not only a photon and an electron to proceed, but also a phonon, which can significantly slow down the rate of e^--h^+ pairs generation in the material. GaP has a small absorption coefficient near its band gap ($\alpha = 3.6 \times 10^2$ cm^{-1}), in return a large penetration depth ($\alpha^{-1} = \sim 28$ μm),[36] resulting in photogenerated charge carriers that can be far (i.e. microns) from collection interfaces in the conventional planar photoelectrode architecture. These long distances place a high demand on the duration of photoexcited lifetimes needed to realize large photocurrents with GaP using light near the bandgap wavelength.

A solution to the optical/transport mismatch in GaP is to employ photoelectrodes with high-aspect ratio form factors as illustrated in Figure I.4. High-aspect ratio designs that preserve the ability to sustain large internal electric fields can decouple the optical absorption constraints from the carrier-collection path lengths in GaP.[2, 18, 37-39] Specifically, strong internal electric fields sweep photogenerated minority carriers to the semiconductor surface while simultaneously directing majority carriers to the back contact with high efficiency. Our group and others have separately realized the high-aspect ratio advantage quantitatively through anodically etched macroporous n-GaP.[18, 40]

C. Preparation of High-Aspect Ratio Nanostructures: Theory

There are two distinct ways to prepare high-aspect ratio nanostructures, namely "top-down" and "bottom-up" syntheses. A "top-down" synthetic method involves etching a single crystalline semiconductor wafer straight down to affect tall and skinny macroporous films that resemble a forest of standing nanowires when viewed at cross-section. This can be achieved either chemically or electrochemically. Chemical etching to construct such feature is also known

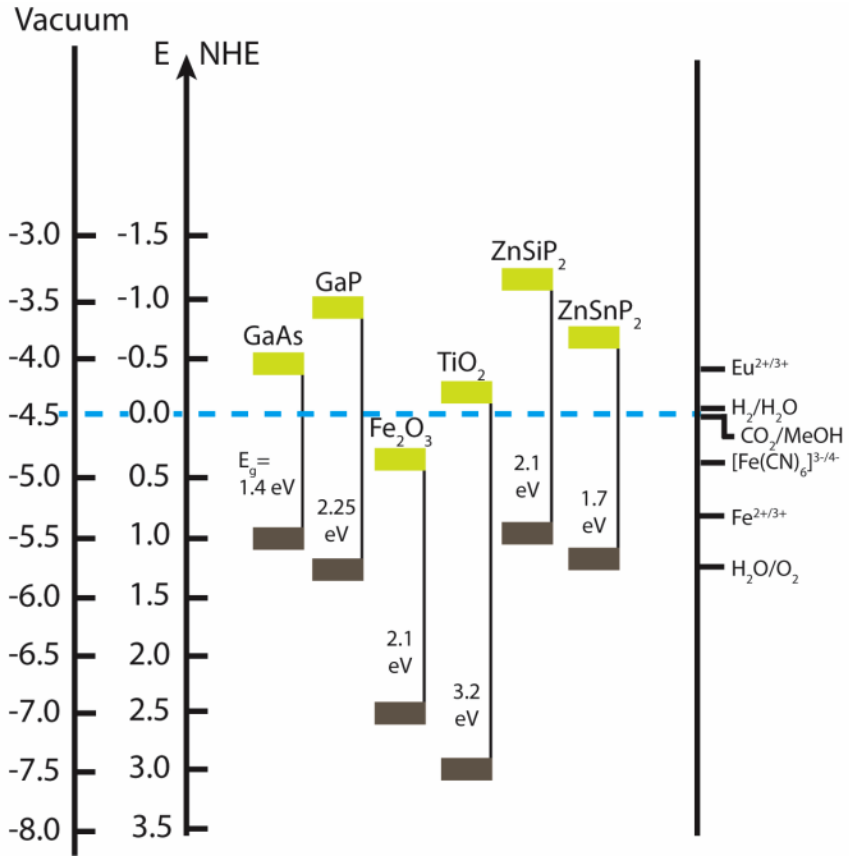

Figure I.3. Band positions of several relevant semiconductors in contact with aqueous electrolyte at pH 1 in comparison to several redox couples shown on the right. Green and gray blocks represent the conduction band edge and valance band edge of the semiconductors, respectively. Figure modeled after Reference 23.

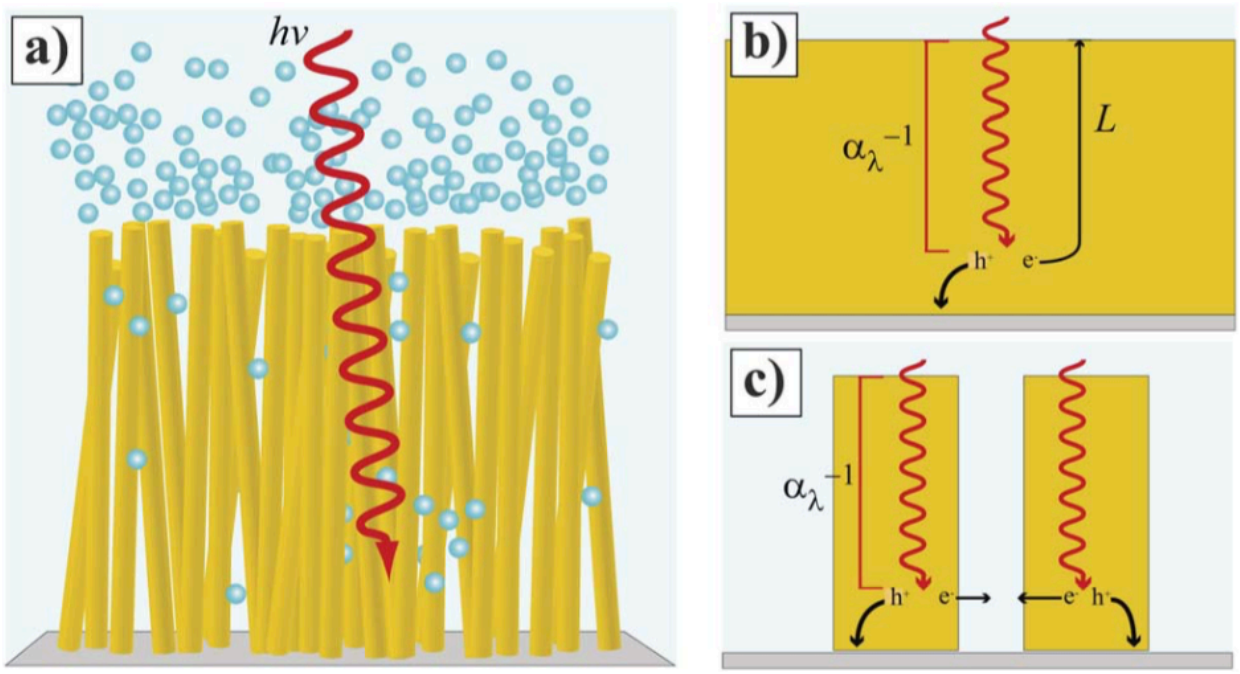

Figure I.4. (a) Schematic depiction of high-aspect ratio nanostructures functioning as a photoelectrode in a water splitting cell. (b, c) Comparison of photogenerated minority carrier collection pathway at (b) planar and (c) high-aspect ratio photoelectrodes. Figure originally published in Reference 37.

as metal-assisted etching, which uses a noble metal particles and caustic/oxidative solution, e.g. HF, H_2O_2 and H_2SO_4 to enhance the dissolution rates at the semiconductor/metal interface. Metal-assisted etching of Si, InP, GaAs, and GaP are reported in the literature.[41-44] Another equally interesting "top-down" method is electrochemical etching or more specifically, anodic etching. The theory and details are outlined in the next section. However, etching down a semiconductor wafer that is already very energy-intensive to produce to form macroporous film is not economical. Therefore, a "bottom-up" synthetic method involves the presence of a metal catalyst/seed is often used to prepare one-dimensional crystalline nanowires. The details are in the next section as well.

i. Top-down Anodic Etching

Anodic etching is an ideal method to generate such macroporous constructs as the electrochemical etching mechanism occurs right at the semiconductor/liquid junction and is governed by the local concentration of holes (h^+) at the surface, which is dictated by the depletion condition of the semiconductor. The thickness of the resulting macropore walls tracks with the dopant concentration of the semiconductor parent wafer. In this section we focus our discussion on n-GaP(100). When an n-GaP is in contact with oxidative aqueous electrolyte like H_2SO_4 or HF, band-bending forms in GaP as shown in Figure I.1a after charge equilibration. Under forward bias in dark, the Fermi level of GaP rises. Outflow of electron from the conduction band causes cathodic current and proton reduction on the surface of GaP. Under reserve bias in dark, however, the current is too low due to low amount of h^+ present in the valence band of n-GaP to perform any appreciable oxidative reactions while under illumination too much photogenerated h^+ are accumulated on the surface and cause uncontrollable, undesirable oxidation and dissolution of the semiconductor with no macroporous features (i.e. electropolishing).[29]

In order to create macroprous film *via* anodic dissolution, some holes must be localized in the surface bonds in dark. Erné et al. and Chase et al. reported the use of very high reverse or anodic bias in dark (i.e. +10 - +120 V).[40, 45] Such extreme applied bias causes large depletion junction on the semiconductor surface, concentrating h^+ to the defect sites and initiating pits formation at those sites. Since no other new pits form as the anodic dissolution progress, it is widely believed that the defect sites under large anodic bias provide surface states for hole generation and tunneling.[40] Once anodic etching is initiated and pits are formed, the curvature of

the pore provides consistently enhanced electric field for more generated h^+ to be swept to the region to continue the dissolution process. The GaP dissolution product is readily dissolved in aqueous electrolyte such as H_2SO_4, HF and KOH. The degree of applied anodic bias is crucial at this point as crystallographically oriented features "crysto pores" grow at low, and current line oriented features "curro pores" at high voltages (or constant current densities) applied to the semiconductor.[46] "Curro pores" is the etching mechanism that created the high aspect ratio macroporous film utilized in Chapter 2 of this thesis.

The duration of anodic etching dictates the depth of the macropore structure, but the fate is not the same for the pore wall thickness. The wall thickness is an intrinsic property of the semiconductor dictated by the depletion width of the semiconductor wafer.[18, 40, 47] The lateral etching halts when the surface of the macropore feature are fully depleted, and the wider the depletion region the sooner the charges are being depleted and thicker the wall of pores would be. The depletion width is related to the dopant concentration in Eq. I.1:

$$W = \sqrt{\frac{2\varepsilon\varepsilon_0\phi_b}{qN_D}} \qquad \text{Eq. I.1}$$

where ε is the effective dielectric constant of the semiconductor, ε_0 is the permittivity of free space, ϕ_b is the equilibrium junction barrier height, q is the change of eletron, N_D is the dopant concentration of the semiconductor.

In the literature, both high-aspect ratio macroporous n-Si and p-Si can be prepared by anodic etching,[48-49] but unfortunately, it does not yield equivalently structured macroporous p-type GaP since the concentration of h^+ at the surface is uniformly large everywhere in dark.[46, 50]

ii. "Bottom up" Nanowire Growth

Alternatively, 'bottom up' synthetic methods readily exist for GaP nanowires, most commonly by either the solution-liquid-solid (SLS)[51-52] or the vapor-liquid-solid (VLS) processes.[53] In this thesis, VLS is explored and discussed throughout so it will be appropriate to focus this section on VLS mechanism to grow III-V nanowires. VLS growth was first reported in 1964 by Wagner et al to prepare single crystalline Si whiskers using Au.[54] Since then the growth technique has been expanded to crystalline binary III-V using Au and Ga.[55-56] As the name suggested, the crystal growth mechanism involves three well-identified stages during the growth process as illustrated in Figure I.5a: (1) Incorporation/dissolution of gaseous percursors "vapor" into the metal particle above the eutectic point to form liquid alloy "liquid", (2) crystal

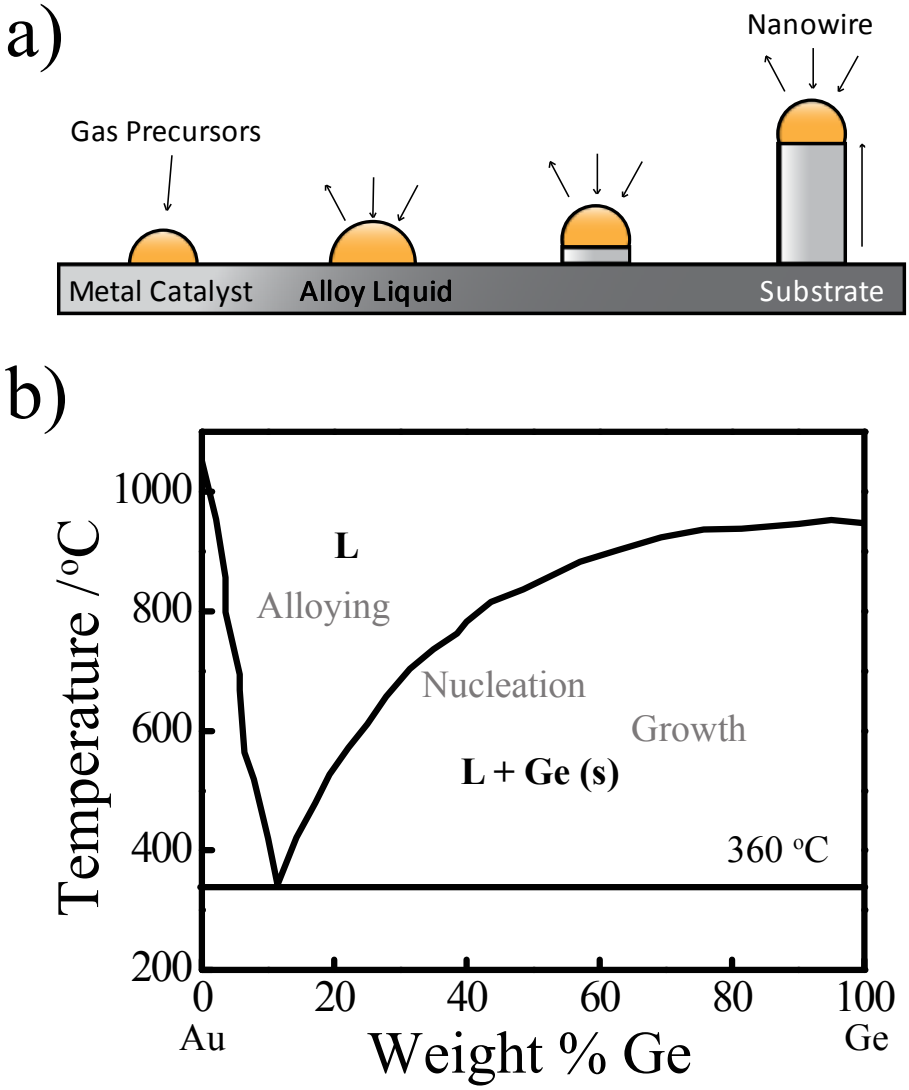

Figure I.5. (a) Schematic depiction of a typical vapor-liquid-solid (VLS) nanowire growth mechanism. There are three stages in a VLS process: (1) alloying, (2) nucleation, and (3) axial growth. (b) Au-Ge binary phase diagram to show the compositional and phase evolution as the VLS growth progresses. Adapted from Reference 57.

nucleation from the liquid alloy "solid", and (3) axial 1-dimensional growth at the liquid/solid interface. The VLS nanowire growth mechanism has been validated by Wu et al with in-situ transmission electron microscopy (TEM) using the Au-Ge nanowire system.[57] The three well-identified stages mentioned earlier correspond well with the binary phase diagram of Au-Ge in Figure I.5b.

The binary and compound nanowires growth such as III-V and II-IV-V are significantly more complicated than the Au-Ge system due to the complexity of ternary and higher order phase diagram, but one can effectively utilize the pseudobinary phase diagram of more complex system to predict the growth conditions for growing binary and ternary nanowires *via* VLS.[58] Figure I.6 shows the pseudobinary diagrams of Au-GaAs[59] and Sn-GaP[60]. The pseudobinary phase diagram of metal-III-V closely resembles the Au-Ge system. Once the temperature in the reactor is above the pseudo-eutectic point of the system and that the phase present in the reactor is liquid metal-III-V liquid and solid III-V as labeled in Figure I.6 as "**L + III-V(s)**", nanowire nucleation begins. As the dissolution of III-V precursors into the liquid alloy increases, more III-V solid precipitate at the liquid/solid interface and proceeds until termination or depletion of III-V feedstock.

D. Content Description

In this thesis, the methodology and details of preparing nanostructured, high-aspect ratio p-type phosphide-based binary and ternary semiconductors via "top-down" anodic etching as well as "bottom-up" VLS growth using non-noble metal particles as the catalyst are discussed for solar energy conversion technology whether to electricity or fuels directly. The p-type characteristics of the prepared nanomaterials are made by thermal diffusion of Zn-containing thin films reservoir from the surface prepared by atomic layer deposition (ALD). P-type mid-sized nanomaterials, particularly GaP, is an extremely important photocathode material for unassisted light-induced water-splitting reactions and dye-sensitized solar cell system. The technological viability of p-GaP photocathode in dye-sensitized solar cell is evaluated for extension of light absorption beyond the $\mathbf{E}_g$ of GaP to sustain larger photocurrent density. Last but not least, this thesis also recorded some of the contributions I have done for chemical education research here at the University of Michigan to introduce modern technology and multidisciplinary research experience to undergraduate students.

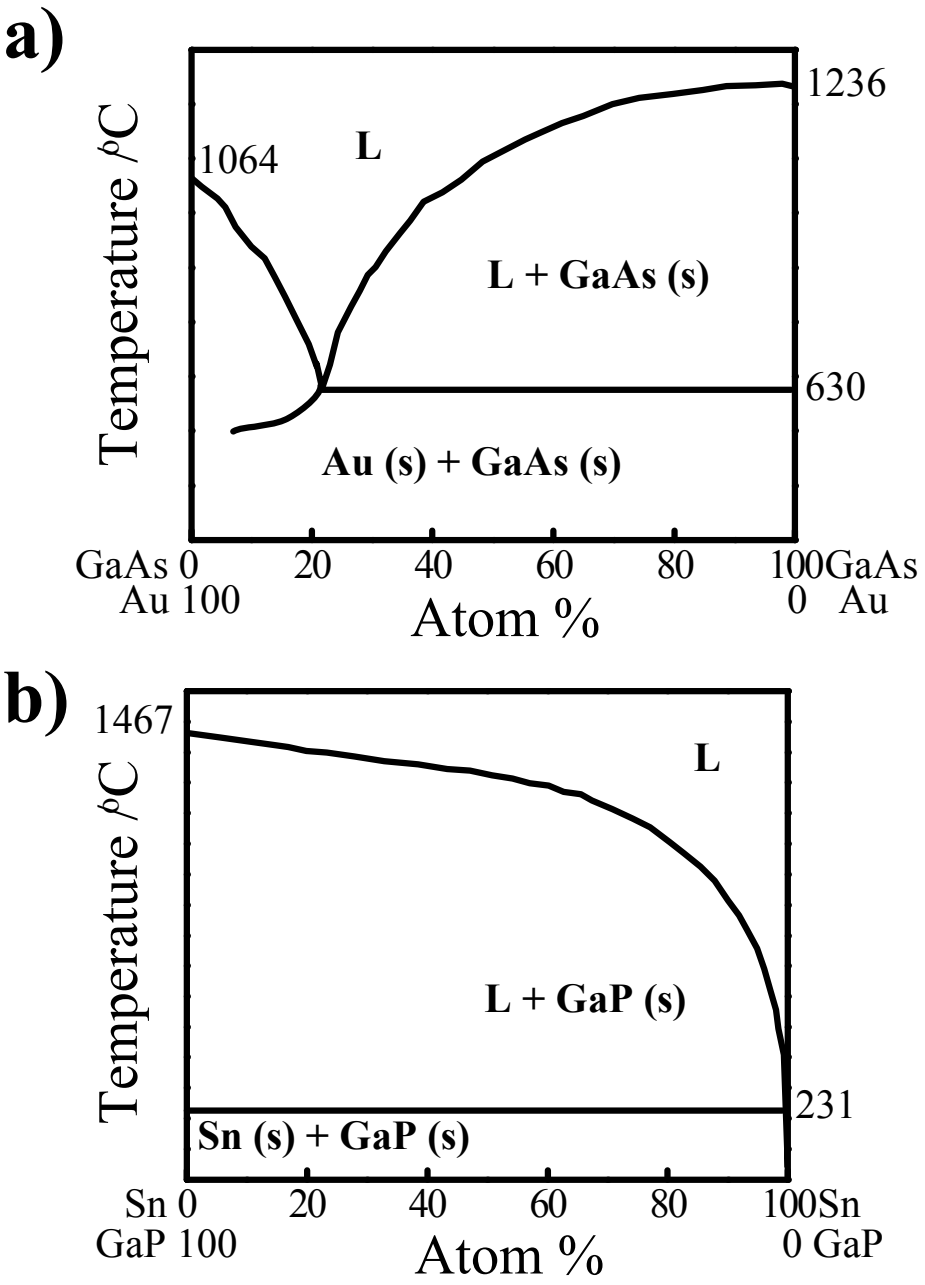

Figure I.6. Pseudobinary phase diagram for (a) Au and GaAs and (b) Sn and GaP. The liquid Au-Ga-As (or Sn-Ga-P for (b)) component is represented as L. Adapted from References 59 and 60.

Chapter II describes a methodology for creating high-aspect ratio p-GaP that function as a photocathode under white light illumination. The "top-down" porous architecture is prepared by anodic etching of an undoped, intrinsically n-type GaP(100). The resulting macroporous structures are subsequently doped with Zn, a common shallow p-type dopant for III-V semiconductors, done by thermally driving in Zn from conformal ZnO films prepared by ALD. The photoresponse properties of the p-type macroporous GaP photoelectrodes in aqueous electrolyte containing methyl viologen are investigated and discussed. This chapter presents advancement towards a doping strategy with a potentially high degree of controllability for high-aspect ratio III-V materials, where the ZnO ALD film is a practical dopant source for Zn.

Chapter III compares and contrasts the GaP nanowires grown using gold (Au) and tin (Sn) nanoparticles as the VLS catalysts on Si(111) and GaP(111)B substrates in terms of structures and photoactivity in photoelectrochemical half-cells. This chapter also describes a simple solid sublimation growth scheme that circumvents the need for toxic and pyrophoric precursors such as phosphine and trimethyl gallium. Sn-seeded GaP nanowires showed fewer twinning defects than Au-seeded GaP nanowires in general. Sn is less noble than Au, facilitating complete wet etching removal of metallic VLS catalysts from as-prepared GaP nanowires, which is not possible with Au catalysts. The photoresponses of both Sn- and Au-seeded GaP nanowire films were collected and examined under 100 mW cm^{-2} white light illumination. Au-seeded nanowire films exhibited strong n-type characteristics when measured in nonaqueous electrolyte with ferrocene/ferricenium as the redox species while Sn-seeded nanowires showed behavior consistent with degenerate n-type doping.

Chapter IV introduces a ternary analog of GaP comprised of earth-abundant elements in the nanostructure form. Ternary II-IV-V_2 chalcopyrite semiconductors are one class of semiconductors that are potentially ideal for photoelectrochemical technologies. Specifically, zinc-based phosphides (Zn-*IV*-P_2; *IV*= Ge, Sn or Si) have been identified as analogues and low-cost alternatives to the aforementioned class of III-V semiconductors.[61-63] This chapter details the preparation of single-phase crystalline $ZnSnP_2$ nanowires *via* simple chemical-vapor-deposition (CVD) method using powdered Zn and SnP_3 as the precursors and Sn nanoparticles as growth seeds in a custom-built tube furnace reactor that is different than that in Chapter III. The cumulative observations suggest that the Sn nanoparticles served both as the growth seed and main contributor of Sn, and the crystallographic data indicated that the as-prepared $ZnSnP_2$

nanowires possessed a sphalerite crystal structure, as opposed to the antisite defect-free chalcopyrite structure. Photoelectrochemical measurements in aqueous electrolyte showed the as-prepared $ZnSnP_2$ nanowires capable of sustaining stable cathodic photoresponse under white light illumination. Overall, this chapter presents a benign and straightforward approach to prepare single-phase Zn-based phosphide nanowires suitable for energy conversion applications.

Chapter V discusses the prospects of high-aspect ratio p-GaP photocathodes prepared entirely *via* solid sublimation process with highly tunable Zn dopant concentration, and their application as a p-type dye-sensitized photocathode material. Conditions that yield nanowires with large diameter ($d > 300$ nm) are described. Using the doping methodology developed in Chapter 2, the as-prepared GaP nanowire films are thermally diffused with Zn from conformal ZnO coating deposited by ALD process. The crystallinity of the resulting nanowires is probed in high-resolution TEM for any structural damages. The second part of the chapter contains data set for a non-surface specific dye/sensitizer attachment scheme on p-GaP photocathode. The persistent dye attachment is done through metal-carboxylate chelation on an ultrathin (3-5 nm) ZnO coating prepared by ALD. Spectral response confirmed sensitization or "hole injection" from the dyes to p-GaP photoelectrode. The mechanism of the injection will be discussed in this chapter.

Chapter VI documents my contributions to the designs and improvements of two introductory chemistry laboratory courses in the Department of Chemistry at the University of Michigan as a Graduate Student Instructor (GSI). The first course is *CHEM 242: Introduction to Chemical Analysis and Laboratory* to which we developed a specific microfluidic laboratory experiment that spans 2 weeks (8 hours total) to introduce the students to the concepts of soft lithography as they design and characterize their own agar-based microfluidic chips. A RGB colorimetric analysis is added to help students to quantify the degree of fluid mixing and the concentrations of salicylic acid in iron(III)-salicylate complex samples. The second course is *CHEM 125 (Research-based): Organic-Inorganic Hybrid Perovskite Photovoltaic Cells*, which spans 14 weeks (a 3-hour laboratory session and a 50-min lecture per week) oriented to introduce Freshmen to multidisciplinary research experience. The organic-inorganic hybrid perovskite photovoltaic cell is chosen as the basis of the course due to its simplicity of construction and relevancy to the scope of general chemistry. This chapter also accounts for my thoughts as well

as suggestions for the concept of multidisciplinary research laboratory course after being a GSI for this course for two semesters.

E. References

1. Faunce, T. A.; Lubitz, W.; Rutherford, A. W.; MacFarlane, D.; Moore, G. F.; Yang, P.; Nocera, D. G.; Moore, T. A.; Gregory, D. H.; Fukuzumi, S.; Yoon, K. B.; Armstrong, F. A.; Wasielewski, M. R.; Styring, S., Energy and Environment Policy Case for a Global Project on Artificial Photosynthesis. *Energy Environ. Sci.* **2013,** *6*, 695.
2. Liu, C.; Dasgupta, N. P.; Yang, P., Semiconductor Nanowires for Artificial Photosynthesis. *Chem. Mater.* **2014,** *26*, 415-422.
3. Lewis, N. S.; Nocera, D. G., Powering the Planet: Chemical Challenges in Solar Energy Utilization. *Proc. Natl. Acad. Sci. U. S. A.* **2006,** *103*, 15729-15735.
4. Boden, T. A.; Marland, G.; Andres, R. J., Global, Regional, and National Fossil-Fuel Co_2 Emissions. *Carbon Dioxide Information Analysis Center, Oak Ridge National Laboratory, U.S. Department of Energy, Oak Ridge, Tenn., U.S.A.* **2017**.
5. Inventory of U.S. Greenhouse Gas Emissions and Sinks: 1990–2014. **2016**.
6. Data Obtained from Bonneville Power Administration (BPA).
7. Boettcher, S. W.; Warren, E. L.; Putnam, M. C.; Santori, E. A.; Turner-Evans, D.; Kelzenberg, M. D.; Walter, M. G.; McKone, J. R.; Brunschwig, B. S.; Atwater, H. A.; Lewis, N. S., Photoelectrochemical Hydrogen Evolution Using Si Microwire Arrays. *J. Am. Chem. Soc.* **2011,** *133*, 1216-1219.
8. Fujishima, A.; Honda, K., Electrochemical Photolysis of Water at a Semiconductor Electrode. *Nature.* **1972**, 37-38.
9. Khaselev, O.; Turner, J. A., A Monolithic Photovoltaic-Photoelectrochemical Device for Hydrogen Production Via Water Splitting. *Science.* **1998,** *280*, 425-427.
10. Walter, M. G.; Warren, E. L.; McKone, J. R.; Boettcher, S. W.; Mi, Q.; Santori, E. A.; Lewis, N. S., Solar Water Splitting Cells. *Chem. Rev.* **2010,** *110*, 6446-6473.
11. Ager, J. W.; Shaner, M. R.; Walczak, K. A.; Sharp, I. D.; Ardo, S., Experimental Demonstrations of Spontaneous, Solar-Driven Photoelectrochemical Water Splitting. *Energy Environ. Sci.* **2015,** *8*, 2811-2824.
12. Lewis, N. S., Developing a Scalable Artificial Photosynthesis Technology through Nanomaterials by Design. *Nat. Nanotechnol.* **2016,** *11*, 1010-1019.
13. Bolton, J. R.; Stricker, S. J.; Connolly, J. S., Limiting and Realizable Efficiencies of Solar Photolysis of Water. *Nature.* **1985,** *316*.
14. Bak, T.; Nowotny, J.; Rekas, M.; Sorrell, C. C., Photo-Electrochemical Hydrogen Generation from Water Using Solar Energy. Materials-Related Aspects. *Int. J. Hydrog. Energy.* **2002,** *27*, 991-1022.
15. Carter, M. A.; Mottram, A.; Peaker, A. R.; Sudlow, P. D.; White, T., Monolithic Light Emitting Diode Arrays Using Gallium Phosphide. *Nature.* **1971,** *232*, 469-470.
16. Kohl, P. A.; Bard, A. J., Semiconductor Electrodes. 13. Characterization and Behavior of n-Type ZnO, CdS, and GaP Electrodes in Acetonitrile Solutions. *J. Am. Chem. Soc.* **1977,** *99*, 7531–7539.
17. Gronet, C. M.; Lewis, N. S., Design of a 13% Efficient N-$GaAs_{1-X}P_x$ Semiconductor-Liquid Junction Solar Cell. *Nature.* **1982,** *300*, 733-735.
18. Price, M. J.; Maldonado, S., Macroporous n-GaP in Nonaqueous Regenerative Photoelectrochemical Cells. *J. Phys. Chem. C.* **2009,** *113*, 11988-11994.
19. Dasgupta, N. P.; Yang, P., Semiconductor Nanowires for Photovoltaic and Photoelectrochemical Energy Conversion. *Front. Phys.-Beijing.* **2014,** *9*, 289-302.

20. Tomkiewicz, M.; Woodall, J. M., Photoassited Electrolysis of Water by Visible Irradiation of a p-Type Gallium Phosphide Electrode. *Science.* **1977,** *196*, 990-991.
21. Parkinson, B. A., On the Efficiency and Stability of Photoelectrochemical Devices. *Acc. Chem. Res.* **1984,** *17*, 431-437.
22. Ohashi, K.; McCann, J.; Bockris, J. O. M., Stable Photoelectrochemical Cells for the Splitting of Water. *Nature.* **1977,** *266*, 610-611.
23. Grätzel, M., Photoelectrochemical Cells. *Nature.* **2001,** *414*, 338-344.
24. Rettie, A. J. E.; Lee, H. C.; Marshall, L. G.; Lin, J.-F.; Capan, C.; Lindermuth, J.; McCloy, J. S.; Zhou, J.; Bard, A. J.; Buddie Mullins, C., Combined Charge Carrier Transport and Photoelectrochemical Characterization of $BiVO_4$ Single Crystals: Intrinsic Behavior of a Complex Metal Oxide. *J. Am. Chem. Soc.* **2013,** *135*, 11389-11396.
25. Kennedy, J. H.; Frese Jr., K. W., Photooxidation of Water at a-Fe_2O_3 Electrodes. *J. Electrochem. Soc.* **1978,** *125*, 709-714.
26. Brillet, J.; Grätzel, M.; Sivula, K., Decoupling Feature Size and Functionality in Solution-Processed, Porous Hematite Electrodes for Solar Water Splitting. *Nano Lett.* **2010,** *10*, 4155-4160.
27. Sivula, K.; Zboril, R.; Le Formal, F.; Robert, R.; Weidenkaff, A.; Tucek, J.; Frydrych, J.; Grätzel, M., Photoelectrochemical Water Splitting with Mesoporous Hematite Prepared by a Solution-Based Colloidal Approach. *J. Am. Chem. Soc.* **2010,** *132*, 7436-7444.
28. Stringfellow, G. B., Effect of Surface Treatment on Surface Recombination Velocity and Diode Leakage Current in GaP. *J. Vac. Sci. Technol. A.* **1976,** *13*, 908.
29. Gerischer, H., Electrolytic Decomposition and Photodecomposition of Compound Semiconductors in Contact with Electrolytes. *J. Vac. Sci. Technol. A.* **1978,** *15*, 1422.
30. Peczonczyk, S. L.; Brown, E. S.; Maldonado, S., Secondary Functionalization of Allyl-Terminated GaP(111)A Surfaces via Heck Cross-Coupling Metathesis, Hydrosilylation, and Electrophilic Addition of Bromine. *Langmuir.* **2014,** *30*, 156-164.
31. Brown, E. S.; Peczonczyk, S. L.; Maldonado, S., Wet Chemical Functionalization of GaP(111)B through a Williamson Ether-Type Reaction. *J. Phys. Chem. C.* **2015,** *119*, 1338-1345.
32. Brown, E. S.; Peczonczyk, S. L.; Wang, Z.; Maldonado, S., Photoelectrochemical Properties of Ch_3-Terminated P-Type GaP(111)A. *J. Phys. Chem. C.* **2014,** *118*, 11593-11600.
33. Mukherjee, J.; Peczonczyk, S. L.; Maldonado, S., Wet Chemical Functionalization of III-V Semiconductor Surfaces: Alkylation of Gallium Phosphide Using a Grignard Reaction Sequence. *Langmuir.* **2010,** *26*, 10890-10896.
34. Richards, D.; Zemlyanov, D.; Ivanisevic, A., Assessment of the Passivation Capabilities of Two Different Covalent Chemical Modifications on GaP(100). *Langmuir.* **2010,** *26*, 8141-8146.
35. Hu, S.; Shaner, M. R.; Beardslee, J. A.; Lichterman, M.; Brunschwig, B. S.; Lewis, N. S., Amorphous TiO_2 Coatings Stabilize Si, GaAs, and GaP Photoanodes for Efficient Water Oxidation. *Science.* **2014,** *344*, 1005-1009.
36. Aspnes, D.; Studna, A., Dielectric Functions and Optical Parameters of Si, Ge, GaP, GaAs, GaSb, InP, InAs, and InSb from 1.5 to 6.0 eV. *Phys. Rev. B.* **1983,** *27*, 985-1009.
37. Foley, J. M.; Price, M. J.; Feldblyum, J. I.; Maldonado, S., Analysis of the Operation of Thin Nanowire Photoelectrodes for Solar Energy Conversion. *Energy Environ. Sci.* **2012,** *5*, 5203-5220.

38. Maiolo III, J. R.; Atwater, H. A.; Lewis, N. S., Macroporous Silicon as a Model for Silicon Wire Array Solar Cells. *J. Phys. Chem. C.* **2008,** *112*, 6194-6201.
39. Spurgeon, J. M.; Atwater, H. A.; Lewis, N. S., A Comparison Between the Behavior of Nanorod Array and Planar Cd(Se, Te) Photoelectrodes. *J. Phys. Chem. C.* **2008,** *112*, 6186-6193.
40. Erné, B. H.; Vanmarkelbergh, D.; Kelly, J. J., Morphology and Strongly Enhanced Photoresponse of GaP Electrodes Made Porous by Anodic Etching. *J. Electrochem. Soc.* **1996,** *143*, 305-314.
41. Asoh, H.; Suzuki, Y.; Ono, S., Metal-Assisted Chemical Etching of Gaas Using Au Catalyst Deposited on the Backside of a Substrate. *Electrochim. Acta.* **2015,** *183*, 8-14.
42. Kim, J.; Oh, J., Formation of GaP Nanocones and Micro-Mesas by Metal-Assisted Chemical Etching. *Phys. Chem. Chem. Phys.* **2016,** *18*, 3402-3408.
43. Kim, S. H.; Mohseni, P. K.; Song, Y.; Ishihara, T.; Li, X., Inverse Metal-Assisted Chemical Etching Produces Smooth High Aspect Ratio InP Nanostructures. *Nano Lett.* **2015,** *15*, 641-648.
44. Li, X., Metal Assisted Chemical Etching for High Aspect Ratio Nanostructures: A Review of Characteristics and Applications in Photovoltaics. *Curr. Opin. Solid St. M.* **2012,** *16*, 71-81.
45. Chase, B. D.; Holt, D. B., Jet Polishing of Semiconductors. *J. Electrochem. Soc.* **1972,** *119*, 314-317.
46. Langa, S.; Carstensen, J.; Christophersen, M.; Steen, K.; Frey, S.; Tiginyanu, I. M.; Föll, H., Uniform and Nonuniform Nucleation of Pores During the Anodization of Si, Ge, and III-V Semiconductors. *J. Electrochem. Soc.* **2005,** *152*, C525.
47. Lee, S.; Bielinski, A. R.; Fahrenkrug, E.; Dasgupta, N. P.; Maldonado, S., Macroporous p-GaP Photocathodes Prepared by Anodic Etching and Atomic Layer Deposition Doping. *ACS Appl Mater Interfaces.* **2016,** *8*, 16178-16185.
48. Rönnebeck, S.; Carstensen, J.; Ottow, S.; Föll, H., Crystal Orientation Dependence of Macropore Growth in n-Type Silicon. *Electrochem. Solid-State Lett.* **1999,** *2*, 126-128.
49. Astrova, E. V.; Borovinskaya, T. N.; Tkachenko, A. V.; Balakrishnan, S.; Perova, T. S.; Rafferty, A.; Gun'ko, Y. K., Morphology of Macro-Pores Formed by Electrochemical Etching of p-Type Si. *J. Micromech. Microeng.* **2004,** *14*, 1022-1028.
50. Föll, H.; Langa, S.; Cartensen, J.; Christophersen, M.; Tiginyanu, I. M., Pores in III-V Semiconductors. *Adv. Mater.* **2003,** *15*, 183-198.
51. Liu, C.; Sun, J.; Tang, J.; Yang, P., Zn-Doped p-Type Gallium Phosphide Nanowire Photocathodes from a Surfactant-Free Solution Synthesis. *Nano Lett.* **2012,** *12*, 5407-5411.
52. Sun, J.; Liu, C.; Yang, P., Surfactant-Free, Large-Scale, Solution-Liquid-Solid Growth of Gallium Phosphide Nanowires and Their Use for Visible-Light-Driven Hydrogen Production from Water Reduction. *J. Am. Chem. Soc.* **2011,** *133*, 19306-19309.
53. Aparna, A. R.; Brahmajirao, V.; Karthikeyan, T. V., Review on Synthesis and Characterization of Gallium Phosphide. *Proc. Mat. Sci.* **2014,** *6*, 1650-1657.
54. Wagner, R. S.; Ellis, W. C., Vapor‐Liquid‐Solid Mechanism of Single Crystal Growth. *Appl. Phys. Lett.* **1964,** *4*, 89-90.
55. Barns, R. L.; Ellis, W. C., Whisker Crystals of Gallium Arsenide and Gallium Phosphide Grown by the Vapor—Liquid—Solid Mechanism. *J. Appl. Phys.* **1965,** *36*, 2296-2301.
56. Ellis, W. C.; Frosch, C.; Zetterstrom, R. B., Morphology of Gallium Phosphide Crystals Grown by VLS Mechanism with Ga as Liquid-Forming Agent. *J. Cryst. Growth.* **1968,** *2*, 61-68.

57. Wu, Y.; Yang, P., Direct Observation of Vapor-Liquid-Solid Nanowire Growth. *J. Am. Chem. Soc.* **2001,** *123*, 3165-3166.
58. Duan, X.; Lieber, C. M., General Synthesis of Compound Semiconductor Nanowires. *Adv. Mater.* **2000,** *12*, 298-302.
59. Panish, M. B., Ternary Condensed Phase Systems of Gallium and Arsenic with Group IB Elements. *J. Electrochem. Soc.* **1967,** *114*, 516-521.
60. Kuznetsov, G. M.; Tsurgan, L. S.; Krainyuchenko, I. A., Alloys of the Cross Sections GaP-Cd, GaP-Sn, and GaP-Pb. *Inorg. Mater.* **1976,** *12*, 976-979.
61. Collins, S. M.; Hankett, J. M.; Carim, A. I.; Maldonado, S., Preparation of Photoactive $ZnGeP_2$ Nanowire Films. *J. Mater. Chem.* **2012,** *22*, 6613-6622.
62. van Schilfgaarde, M.; Coutts, T. J.; Newman, N.; Peshek, T., Thin Film Tandem Photovoltaic Cell from II-IV-V Chalcopyrites. *Appl. Phys. Lett.* **2010,** *96*, 143503.
63. Yokoyama, T.; Oba, F.; Seko, A.; Hayashi, H.; Nose, Y.; Tanaka, I., Theoretical Photovoltaic Conversion Efficiencies of $ZnSnP_2$, $CdSnP_2$, and $Zn_{1-X}Cd_xSnP_2$ Alloys. *Appl. Phys. Express*. **2013,** *6*, 061201-061204.

CHAPTER II

Macroporous p-GaP Photocathodes Prepared by Anodic Etching and Atomic Layer Deposition Doping

A. Introduction

This chapter describes a methodology for doping high-aspect ratio GaP with Zn, a common shallow p-type dopant for III-V semiconductors. Macroporous GaP prepared by anodic etching of an undoped, intrinsically n-type GaP(100) is used as the model for the high-aspect ratio structures, and the doping step is done by thermally driving in Zn from conformal ZnO films prepared by atomic layer deposition (ALD). The photoresponse properties of the p-type macroporous GaP photoelectrodes in aqueous electrolyte containing methyl viologen are investigated and discussed. Collectively, this work presents a doping strategy with a potentially high degree of controllability for high-aspect ratio III-V materials, where the ZnO ALD film is a practical dopant source for Zn.

P-type GaP is a potential photocathode material for photoelectrochemical applications.[1-7] The optical/transport mismatch in GaP can be overcome by employing photoelectrodes with high-aspect ratio architectures, as mentioned in Chapter I. Films of p-GaP nanowires have been previously explored in this context.[3, 8] However, to accurately and precisely control the dopant level is challenging in vapor-phase based nanowire growth, making it difficult to realize an appreciable internal electric field within the nanostructure.[9-11] Anodic etching is an ideal method to generate such constructs as the electrochemical etching mechanism is necessarily governed by the local concentration of holes (h^+) at the surface, which is dictated by the depletion condition of the semiconductor, as discussed in Chapter I. Unfortunately, anodic etching does not yield equivalently structured macroporous p-type GaP since the concentration of h^+ at the surface is uniformly large everywhere.[12]

In this chapter, ALD is explored as a method to conformally coat the surface of GaP with a layer of ZnO that can serve as a p-type dopant source by thermally driving in Zn. In this capacity, ALD is well suited since precise control over thickness and composition of the surface

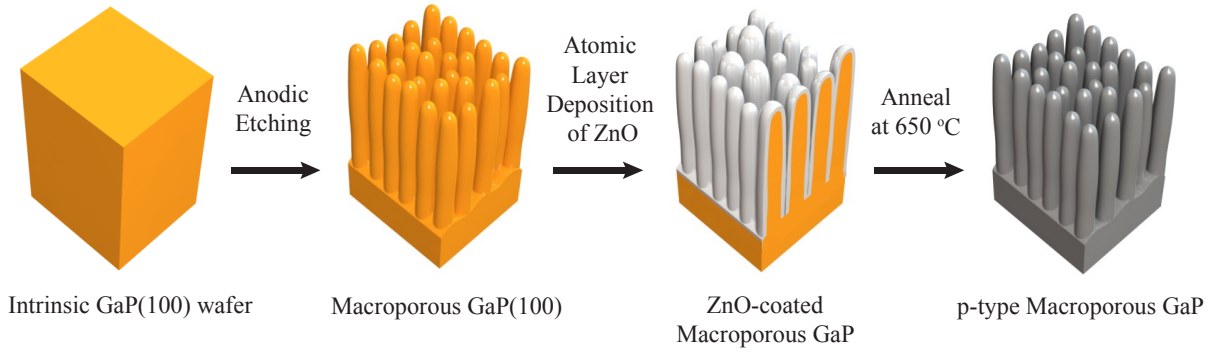

Figure II.1. Schematic of p-type doping of anodically-etched macroporous GaP wafer using atomic layer deposition (ALD) ZnO as the Zn dopant source.

layer is possible.[13] To date, there have been relatively few reports exploiting ALD as a means to facilitate doping of nanostructured semiconductors[14-16] and no reports have been disclosed regarding any III-V semiconductor material, including GaP. Herein, we report on the step-wise preparation of high-aspect ratio p-GaP photoelectrodes through a combined anodic etching and ALD sequence for the purpose of use as photocathode in a photoelectrochemical system. We describe a strategy where lightly n-type GaP is first anodically etched and then separately coated with ZnO by ALD. This composite is then annealed to selectively introduce Zn into the GaP lattice, rendering the entire macroporous material p-type (Figure II.1). The resulting materials are characterized with scanning and transmission electron microscopy, and energy dispersive x-ray spectroscopy (EDS) in scanning transmission electron microscopy (STEM) mode. The steady-state photoresponse of the p-type macroporous GaP samples under 100 mW cm^{-2} white light illumination are reported and discussed.

B. Materials and Methods

i. Materials

Undoped, double-side polished, and 275 μm thick single crystal GaP(100) wafers (12.6 Ω cm and N_D = 3.3 x 10^{15} cm^{-3}) were obtained from El-CAT Inc. The wafers were diced into 0.5 x 0.5 cm squares, degreased with sequential immersion/sonication in distilled water (> 18 MΩ cm, Barnstead Nanopure III purifier), methanol (> 99.8 % ACS Reagent, Sigma-Aldrich), acetone (Fisher Scientific), methanol, distilled water, and finally dried with N_2.

ii. GaP Anodization

All GaP samples were etched in 18 M H_2SO_4 (conc. 98 %, Fisher Scientific) for 30 s to remove native oxides before use. Anodic etching of GaP wafers was performed in a custom-built Teflon cell with a 0.12 cm^2 opening as described elsewhere.[17] 1 M H_2SO_4(aq) was used as the etching solution and a mixture of In-Ga (25:75 wt.) was used to create a low resistance ohmic contact to the GaP working electrode. The GaP samples were etched at a constant current of 100 mA cm^{-2} for 1 to 15 min to achieve the desired pore depth using a custom-built high voltage constant-current circuit. The In-Ga was removed from the backside immediately after anodic etching through acid etching.

iii. Atomic Layer Deposition of ZnO

Diethylzinc (≥ 52 wt. % Zn basis, Sigma-Aldrich) and deionized water were used as the precursors for ZnO deposition in a custom-built ALD tool.[18] No pretreatments were performed on the GaP samples prior to commencing ALD. During the deposition, the reaction chamber was kept at 150 ºC and a base pressure of 69.3 Pa. The diethylzinc precursor was pulsed for 0.05 s followed by 10 sccm Ar purge for 30 s. The cycle was repeated with 0.1 s pulse of DI water. The growth rate of ZnO films was 2.0 Å/cycle as measured by ellipsometry (Woollam M-2000DI Ellipsometer).

Planar GaP or macroporous GaP substrates were first coated with 150 ALD cycles of ZnO and then annealed at T = 650 ºC in 100 sccm Ar flow at 101325 Pa in a quartz tube. Excess or unreacted Zn on the substrates after annealing was removed by 5% v/v HF for 30 s, rinsed with DI water and dried in N_2.

iv. Photoelectrode Preparation

The back of all GaP samples was coated with nominally 1-2 μm Zn^0 (99.99 %, Kurt J. Lesker) in a thermal evaporator. Immediately after the evaporation, the substrates were transferred into a 1 in quartz tube to anneal at 800 ºC for 2 - 4 h in 100 sccm Ar flow at 101325 Pa. Excess or unreacted Zn on the substrates were removed with 1 M HCl(aq), rinsed with water and dried in N_2. This set of process steps resulted in conversion of the electrode behavior of the wafer from slight n-type to predominantly p-type character.

Ohmic contacts to GaP were prepared by first scratching the back of the substrate with a diamond scribe to mechanically remove oxide(s) and increase the surface roughness for better contact with the soldered metal, then etching with conc. H_2SO_4 for 30 s, followed by soldering a thin film of In-Zn (99:1 wt.), and then annealing in forming gas (5 % H_2 in N_2, Metro Welding) for 10 min at 400 ºC.

v. Photoelectrochemical Measurements

GaP electrodes were fabricated by attaching a tinned-copper wire to the back of substrate that already had an In-Zn ohmic contact with silver print (GC Electronics). The wire was then threaded through a glass tube, and the electrode was finally sealed with inert epoxy (Hysolc C, Loctite) to expose approximately 0.09 cm^2 active area. The epoxy was cured for at least 24 h at room temperature before the electrodes were used. A custom-built, 3-electrode quartz cell with an optically flat bottom was used for photoelectrochemical measurements. The reference and counter electrodes were an Ag wire coated with AgCl immersed in sat. KCl and a section of Pt

mesh, respectively. An aqueous solution of 0.01 M methyl viologen (98 %, Sigma-Aldrich) and 1 M KCl was used as the active redox species (Mallinckrodt, Analytical Reagent). The steady-state *J-E* photoresponses were collected with a CH Instruments 420A potentiostat. A tungsten halogen lamp (ELH, Osram) was used as the white light source. The solution was stirred during the measurement. Spectral response measurements were collected with a lab-built system detailed previously.[17] The light was chopped at 15 Hz during measurements.

vi. Material Characterization

Scanning electron micrographs were collected with an FEI Nova Nanolab Dualbeam Workstation equipped with Schottky field-emitter and a through-the-lens detector (TLD). Transmission electron microscopy (TEM) images, selected-area electron diffraction patterns (SAED), and elemental analyses were acquired with a JEOL 2010F AEM equipped with a zirconated tungsten field-emitter operated at 200 kV. The elemental analysis was performed in scanning-TEM (STEM) mode with probe size of 1.0 nm and an EDAX energy dispersive spectroscopy. The samples for TEM were prepared in an FEI Helios Nanolab 650 Dualbeam Focused ion beam (FIB) workstation via conventional in-situ lift-out methods. The XPS data were acquired using a Kratos Ultra Axis XPS with a monochromatic Al Ka source and 20 eV pass energy with a DLD detector. An Ar^+ ion gun operating at 4 keV was used to sputter the Zn-doped sample to obtain the depth profile. The sputtering rate was roughly 1 nm/min. The spectra were calibrated to the C 1s at 284.8 eV.

C. Results

Figure II.2 shows top-down and cross sectional views of representative macroporous GaP films prepared at several different etch times. At an applied current density of 100 mA cm^{-2}, the resultant macroporous film displayed a morphology that was slightly different than what was observed previously for galvanostatic etching of more heavily doped ($N_D \sim 10^{17}$ cm^{-3}) n-GaP.[17] Specifically, the macroporous films produced here still consisted of 'curro pores' (i.e. pores formed perpendicular to surface plane in the direction of the current flow)[19] but the pore walls were tapered with the thinnest portions at the top. For the purposes of this study, an etch time of 12.5 min yielded a 40 μm thick film. Since this depth roughly corresponds to the optical penetration depth of light with wavelengths near the band gap of GaP,[20] these films were used for subsequent photoelectrochemical studies.

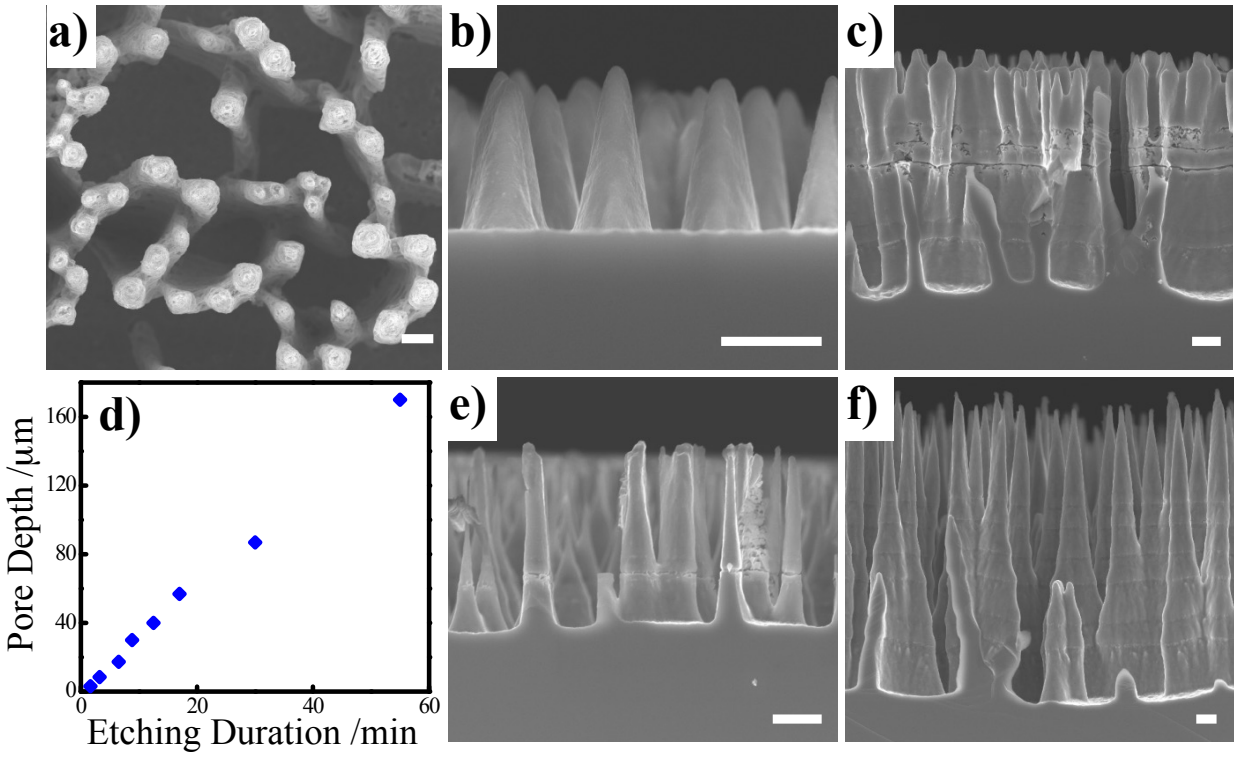

Figure II.2. Scanning electron micrographs of (a) top-down and (b, c, e, f) cross sections of intrinsic GaP wafers after being etched for various predetermined times. (d) Measured pore depth as a function of anodic etching duration at a constant current density of 100 mA cm^{-2}. The pore depth tracks with the linear relationship shown in (d). Scale bars: 2 µm.

These macroporous films were then treated by drive-in doping of Zn to convert the lightly n-type character into p-type character. Based on the established precedent of ZnO as a Zn-dopant source for GaP,[21-22] a thin layer of ZnO was deposited by ALD on these materials. Figure II.3a illustrates that this process did not cause any perceptible change to the film porosity or pore morphology, i.e. the aspect ratio of the pores was preserved due to the highly conformal nature of ALD. Figure II.3b shows a high magnification SEM image of a sample after 150 ALD cycles. The ZnO layer can be clearly distinguished as a consistent and conformal film on the macroporous walls, including uniform coating of the internal surface of both convex and concave features on the etched GaP surface. Elemental mapping by energy dispersive spectroscopy was performed on selected samples that had first been prepared by FIB. Figure II.3c illustrates the elemental composition of the 29 nm films on the surface of the GaP after ALD treatment.

Figure II.4 shows the results of the STEM analyses performed to determine the effect of thermal annealing on these films. Data are shown for films annealed at T = 650 °C for 2 h and 6 h, in conjunction with a series of EDS maps. Figure II.4a shows a STEM high-angle annular dark-field image (HAADF) for a macroporous GaP sample annealed for 2 h. In this image, the light and dark contrast regions are within and outside, respectively of the GaP macroporous wall. After annealing, discrete films along the edge of the GaP were not observed, implying diffusion of the film into GaP. As seen in the corresponding elemental maps for Ga, P, Zn, O, the elemental distribution was non-uniform and distinct from the elemental maps shown in Figure II.3d prior to annealing. Unlike after ALD deposition but before annealing (Figure II.3d), the elemental maps in Figure II.4a show that Zn was detected throughout the probed volume of GaP. The signal levels were low and Zn still seemed predominantly concentrated at the GaP surface. Oxygen was also detected within 50 nm into the GaP structure, consistent with the presence of a surface oxide. Figure II.4b presents a corresponding HAADF image of a separate GaP macroporous film after annealing for a total of 6 h. This extended annealing time further altered the distribution of Zn and O within GaP. Zn was detected more extensively throughout the probed volume of GaP. Conversely, O signals were more localized at the surface. Three separate factors may support the empirical observation of selective enrichment of Zn into GaP. First, the diffusivity of Zn in GaP is significantly greater than the diffusivity of O in GaP at temperatures up to 1300 ºC.[22-26] Second, the solubility of Zn in GaP is much greater than O in GaP (2 x 10^{20}

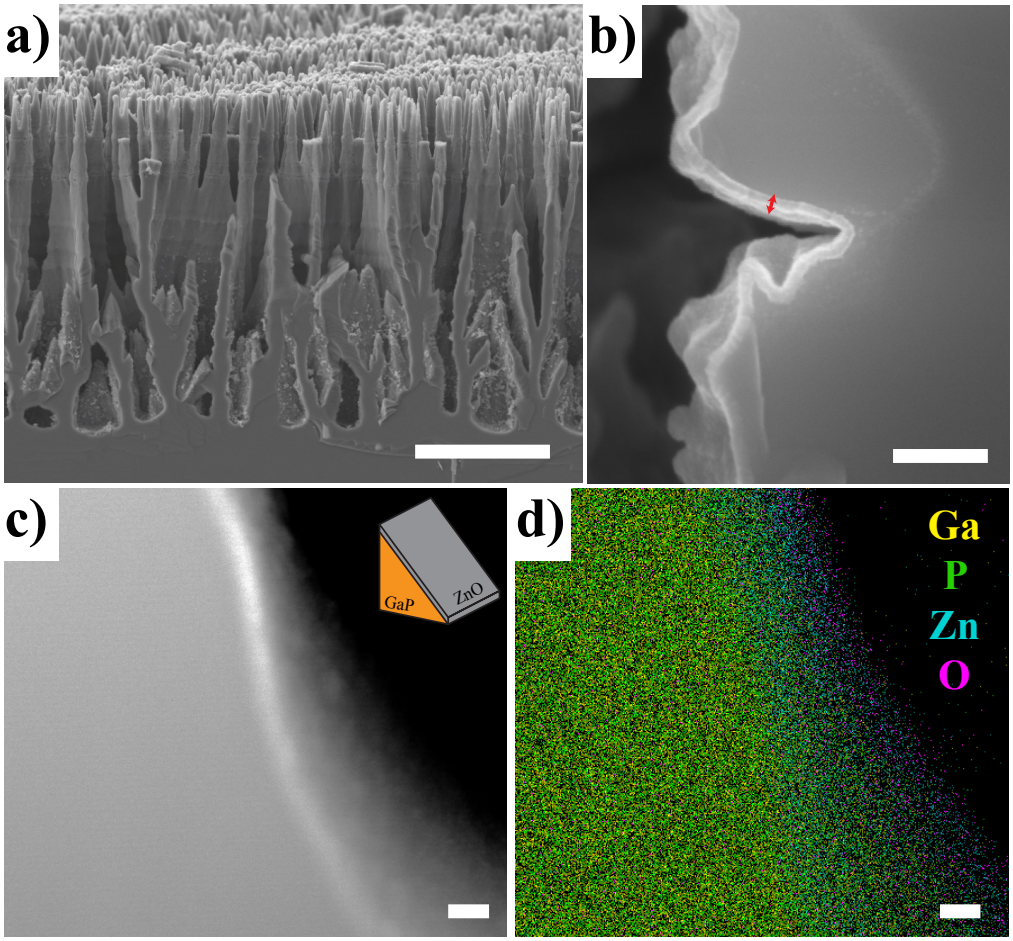

Figure II.3. Scanning electron micrographs of (a) 40 µm-deep macroporous GaP after 150 cycles ZnO deposition at growth rate of 1.92 Å/s and (b) conformal ZnO films produced by ALD (indicated by red arrows) on the macroporous structures. Scale bars: 20 µm and 200 nm, respectively. (c) HAADF image and (d) corresponding elemental mapping of ZnO-coated GaP collected in STEM mode showing clear interfaces between Zn-containing layer and GaP. Scale bar: 50 nm. Average ZnO thickness is 28.9 nm.

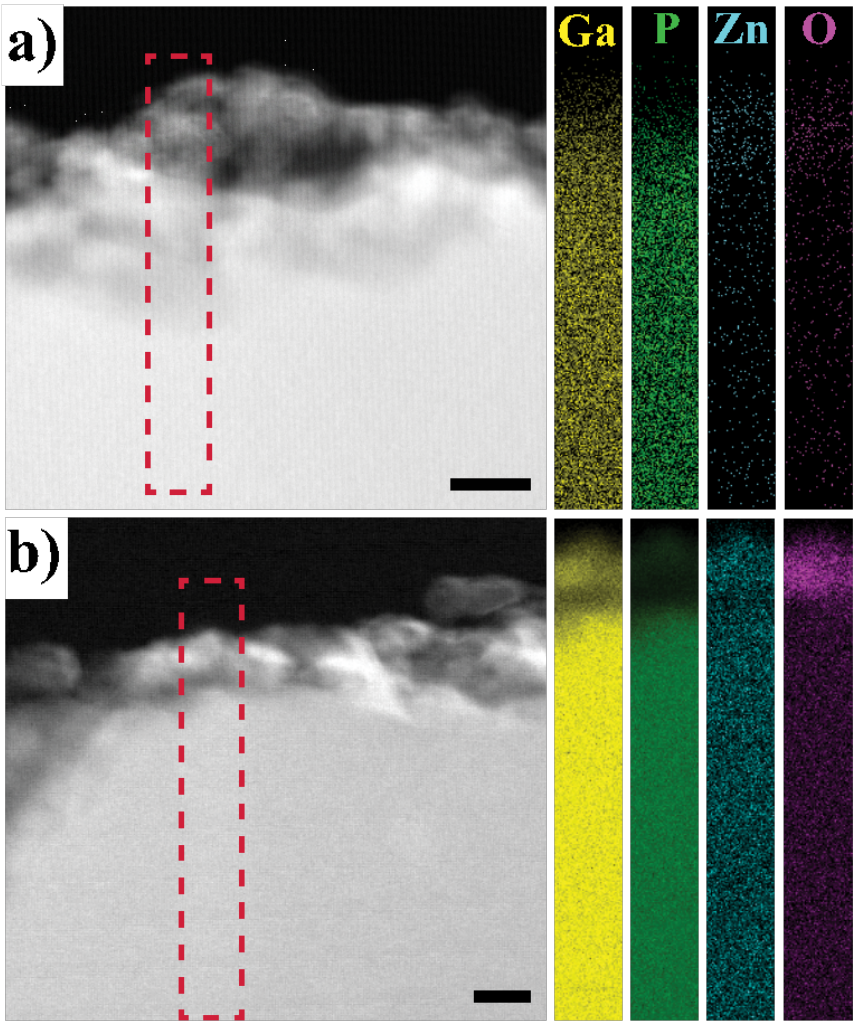

Figure II.4. HAADF images of macroporous GaP surfaces annealed for (a) 2 h at 650 ºC in Ar and its corresponding elemental maps collected in STEM mode showing incorporation of Zn into GaP along with detectable amount of O mostly at the GaP surface. (b) HAADF image of the same sample after annealing for another 4 h further diffusion at 650 ºC. The elemental maps reveals migration of Zn towards the bulk of GaP, while O remained on the surface. Scale bar: 50 nm.

cm^{-3} at 1100 ºC vs. $<5 \times 10^{16}$ cm^{-3} at 1040 ºC).[24, 27-28] Third, ZnO films prepared by ALD with an unintended slight excess in Zn are known.[29]

The structure of these annealed materials was further probed through TEM analysis. Figure II.5a shows an image of a ZnO-coated macroporous GaP sample before annealing. The selective area electron diffraction (SAED) patterns collected at the outer edge of the oxide film and 50 nm within the interior of GaP are shown in Figures II.5b and II.5c, respectively. The SAED pattern presented in Figure II.5b is fully consistent with polycrystalline ZnO.[18] The data in Figure II.5c is separately diagnostic of a single crystallite of zinc blende GaP, as viewed along the [100] zone axis. These data cumulatively indicate that there was no intermixing of ZnO and GaP during the ALD coating step. Figure II.5d shows a transmission electron micrograph of a sample after 6 h of annealing at $T = 650$ °C. As compared to Figure II.5a, the interface was much rougher and discontinuous, with distinct crystal grains visible at the surface of the macropore. The SAED pattern collected at the outer edge of this surface (Figure II.5e) differed significantly from the data without annealing. Figure II.5e shows the existence of two types of crystals within the probed volume. First, the diffuse rings could be indexed to polycrystalline GaP, indicating the presence of small GaP grains with random orientation. Second, the bright spots could be indexed to larger grains of crystalline GaP viewed along the [211] zone axis. None of the diffraction features could be matched to either ZnO or Zn_3P_2 crystallites. Figure II.5f shows a SAED pattern collected 50 nm into the interior of the GaP. These diffraction data were consistent with the interior of the sample constituting a single GaP crystal viewed along the [211] zone axis, similar to what was observed in Figure II.5c.

Following annealing of the ALD coating layer, macroporous GaP samples were then used as photoelectrodes. For clarity, in these photoelectrochemical studies, the underlying wafer was rendered p-type through drive-in doping of a Zn film on the backside, as described in the Materials and Methods section. This substrate conversion to p-type character was confirmed through control photoelectrochemical and Schottky contact measurements performed on planar GaP samples (i.e. without a macroporous film) (Figure II.6). Accordingly, all the photoelectrochemical measurements were performed with p-type macroporous GaP films on a p-type substrate. Figure II.7 shows a representative photoresponse for p-GaP samples produced in this work immersed in 1 M KCl(aq) with 0.01 M methyl viologen (MV^{2+}). Figure II.7a shows voltammetric responses for macroporous p-GaP samples after the annealing step and after an

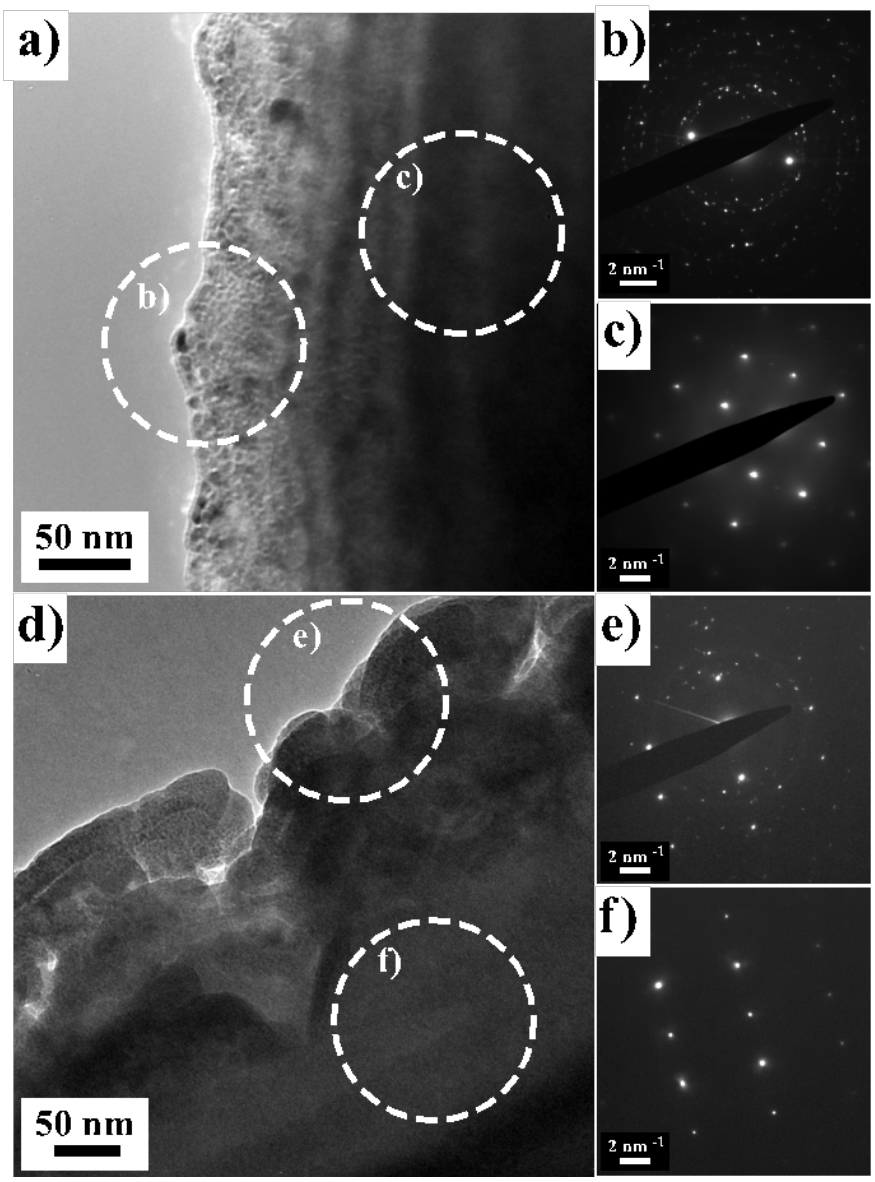

Figure II.5. Transmission electron micrographs of the surfaces of ZnO-coated macroporous GaP (a) before and (d) after annealing to affect Zn diffusion. (b, c, e f) Selected area electron diffraction (SAED) patterns from areas indicated showing the bulk of GaP remains single crystal after Zn diffusion, while the Zn-rich surface contains crystallites of GaP as measured from the d-spacings in the polycrystalline ring patterns in (e).

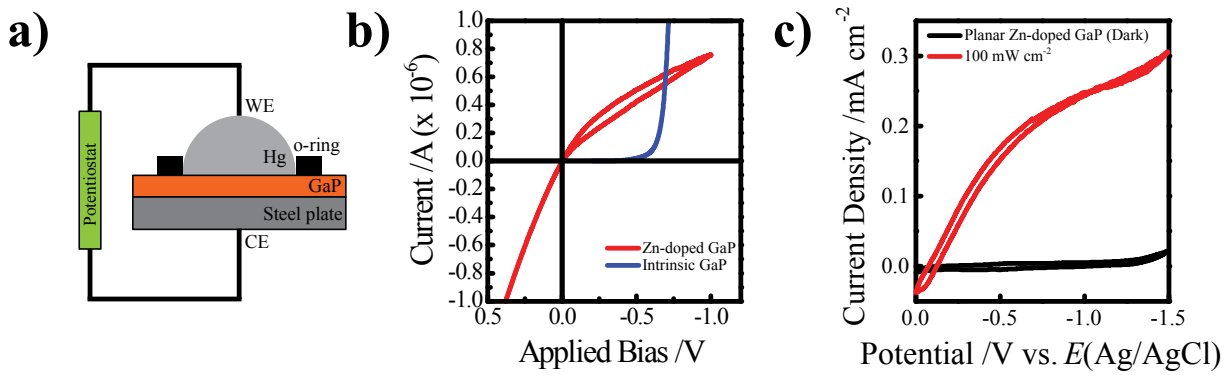

Figure II.6. (a) Cross-section view of Hg/GaP heterojunction setup for current-voltage response measurements. (b) Current-voltage response of intrinsic GaP wafer (blue) and ZnO-coated GaP after annealing for 20 h (red). (c) Photoresponse of a representative ZnO-coated GaP annealed for 20 h measured in an aqueous solution containing 1 M KCl and 0.01 M methylviologen dichloride in a 3-electrode photoelectrochemical cell.

additional 10 s etch in concentrated aqueous HF (48% v/v) performed to remove surface damage affected during the processing steps (as in Figure II.5d). After doping, the macroporous p-GaP samples consistently showed p-type photoelectrode behavior, i.e. the rest potential shifted positive and the net photocurrent was cathodic. However, these samples exhibited a large dark current at negative potentials that increased with more negative applied bias. Under illumination, the total cathodic current was a superposition of the dark current and the photocurrent, with the total current never reaching a steady-state value. Upon etching, the dark current was substantially suppressed. For these electrodes, the steady-state photocurrent-potential response more closely matched the expected response of a photocathode under depletion conditions. Figure II.7b compares the photoresponse characteristics of another etched macroporous p-GaP photoelectrode and a representative planar p-GaP photoelectrode. In these data, the planar p-GaP sample represents a control, i.e. it came from the same nearly intrinsic GaP wafer with slight n-type character that was then coated with ZnO by ALD and then subjected to the same annealing and etching treatment as-received by the macroporous GaP samples. The photoresponses between these two types of p-GaP were clearly different, with macroporous p-GaP samples consistently exhibiting higher cathodic photocurrents under the same illumination intensity. The origin for the enhanced photocurrents of the macroporous p-GaP samples is shown in Figure II.7c. As typically observed for planar p-GaP photoelectrodes with short minority carrier lifetimes,[30-31] [32] the external quantum yields were only appreciable at short wavelengths, where the minority carrier collection path length is comparable to or shorter than the optical penetration depth defined by the absorptivity at each wavelength. In contrast, all the doped macroporous p-GaP photoelectrodes supported non-zero external quantum yields out to the band gap wavelength of λ = 548 nm, despite having the same bulk optoelectronic properties as the control planar sample.

D. Discussion

This chapter represents the first demonstration of a rational and controllable synthesis of macroporous p-type III-V photoelectrodes. The data demonstrate the power of ALD for well-controlled doping of highly non-planar III-V substrates. The suitability of high aspect ratio p-type III-V semiconductors for the study and design of advanced photoelectrochemical systems are discussed below.

i. Synthesis of p-type Macroporous III-V Semiconductors

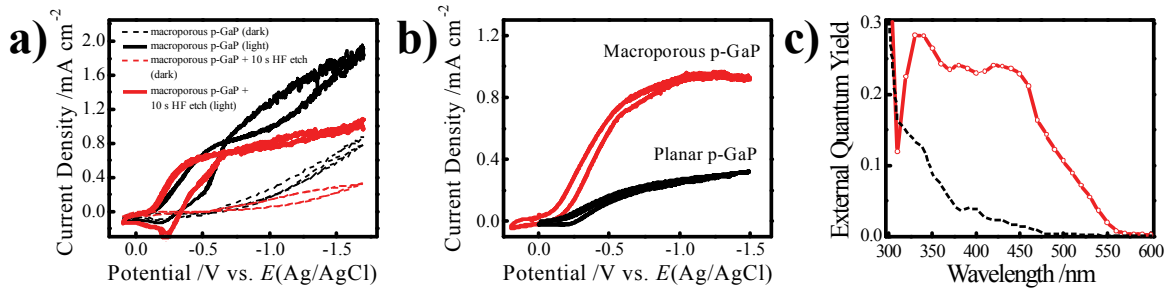

Figure II.7. a) Current density-potential response of a representative macroporous p-GaP photoelectrode before and after a brief etch in a commercial GaP etchant. b) Steady-state photocurrent density-potential responses of doped planar p-GaP (black) and macroporous p-GaP (red) immersed in 1 M KCl containing 10 mM MV^{2+} under 100 mW cm^{-2} illumination. c) Wavelength-dependent quantum yield profiles of the same macroporous p-GaP photoelectrodes in (b) in 1 M KCl with 10 mM MV^{2+} at E = -1.0 V vs E(Ag/AgCl). The corresponding profile for a planar p-GaP photoelectrode after the same Zn doping and etch steps (black dotted line) is also shown.

Our group previously investigated the use of pulsed anodic etching to form p-type macroporous GaP films.[33] However, that work, similar to what was observed with p-GaAs,[34-35] illustrated the primary issue that arises when anodic etching is performed with p- instead of n-type III-V semiconductor wafers, i.e. isotropic etching that does not form curro pores. Although electrolytes with halide acids and pulsed waveforms do impart some anisotropy in anodic etching of p-type III-V electrodes,[33-34] the resultant macropore wall thicknesses have no relation to the semiconductor's ability to support an internal electric field. As photoelectrodes, these materials showed almost no photoactivity [33] and failed to increase the capture and conversion efficiency of deeply penetrating photons. Thus, despite the fact that preparation of high efficiency macroporous n-GaP photoanodes by one-step anodic etching has been known for more than 20 years,[36] efficient p-type macroporous III-V photocathode films simply by anodic etching alone has yet to be demonstrated.

Figures II.2, II.3, II.4, and II.5 cumulatively illustrate that an alternative, multi-step route to achieve high efficiency macroporous *p-type* GaP films is by first anodic etching intrinsic n-type macroporous films and then doping with Zn. In this way, anodic etching of undoped GaP (which always exhibits slight n-type character)[37] still produces tall, thin macropores with macropore walls sufficiently thick to maintain a depletion region, but subsequent thermal doping converts the entire structure p-type. The drawback of the necessity of an additional process step is outweighed by the fact that the methodology is effective at producing consistently p-type materials.

Thin ALD-derived coatings of ZnO are well suited for doping of macroporous GaP. Following previous demonstration of this concept using MnO_x (and ZrO_2) films on rutile TiO_2 nanostructures,[14] Figures II.4 and II.5 further illustrates ALD coatings are suitable for doping of III-V nanostructures in three ways. First, the amount of dopant atom (i.e. Zn) can be controlled by the thickness of the film. Since the number of ALD cycles determines the thickness, the precision for doping exists. Second, the conformality of ALD coatings (as shown in Figure II.3) is an absolute necessity for doping high-aspect-ratio structures such as these macroporous films. As exhibited here, ALD films coated uniformly the ridged topology of the macropore walls. Third, annealing thin oxide coatings rather than annealing in an ambient containing dopant vapor minimized damage to the crystalline structure of GaP. In separate experiments, we consistently observed that annealing GaP above 600 °C in the presence of sublimed Zn resulted in the loss of

P and degradation of the remaining GaP.[8] In contrast, annealing of the ZnO films limited the disruption of the crystallinity of GaP to just the near surface region (< 50 nm). Further, the crystallinity and stoichiometry in the interior of the GaP macropore walls was not compromised. We posit that the Zn-deficient oxide surface film serves as a barrier that prevents out-diffusion of Zn, Ga, and P during the doping process.

We did not extensively or rigorously measure the amount of dopant present in the thermally diffused p-type macroporous GaP. Based on the geometry of the macropore walls, if all of the 30 nm ZnO film ended up diffusing into the macroporous structures, the highest possible Zn content would be 12 at. % as calculated following the treatment introduced previously by Yang et. al[14] with adaptation for conical shapes as described in Figure II.8. Given the annealing conditions chosen for this study, the amount of Zn detected from initial diffusion of ZnO film into GaP was estimated to be 6-8 at. % from the EDS analyses using Cliff-Lorimer method assuming $C_{Ga} + C_P + C_{Zn} = 100\%$ (Figure II.9). However, this measurement does not imply the dopant concentration is 10^{-1} at. % nor is this much Zn desirable in GaP. Rather, only a fraction of the detected Zn can function as electrically active dopant (the highest possible concentration of Zn substitutions that are p-type dopants in GaP is 10^{20} cm^{-3}).[38] Impedance data collected for control wafer samples coated with the same type of ZnO layer and annealed under the same conditions showed the maximum electrically active dopant concentration of 7.5×10^{20} cm^{-3} (Figure II.10) The carrier concentration of the control sample was estimated from the capacitance of a Hg/GaP Schottky junction (in Figure II.6a) under reverse bias. The Randles equivalent circuit was used as the model for the junction for simplicity, and the capacitance values were obtained from the intercept of the equation $\log Z = -\log f - \log C$. The Bode slopes were in between -0.8 and -0.93 (Figure II.10b). Using the Mott-Schottky relationship, the plot of C^{-2} vs. V was generated in Figure II.10a. Note that the plot is not linear, which is a characteristic of a semiconductor with non-uniform carrier concentration distribution. The slope of the plot at any particular bias voltage is inversely proportional to the carrier concentration at the edge of the depletion region as shown in Eq. II.1.[39-40] Hence, the information of carrier concentration with respect to the distance from the semiconductor surface could be obtained from Eq. II.1 and the total hole density was plotted against the distance from GaP surface in Figure II.10c.

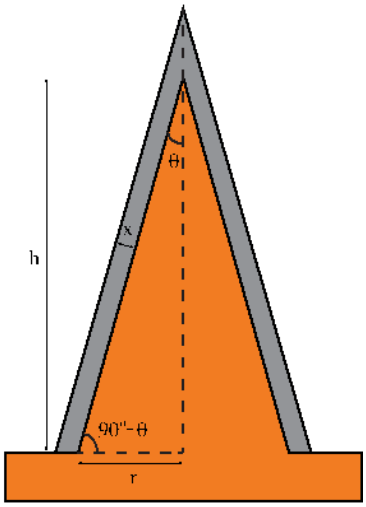

$$N_{GaP} = \frac{V_{GaP}\rho_{GaP}}{MW_{GaP}} = \frac{\left[\frac{1}{3}\pi hr^2\right]\rho_{GaP}}{MW_{GaP}} \quad (1)$$

$$N_{Zn} = \frac{V_{ZnO}\rho_{ZnO}}{MW_{ZnO}} = \frac{\frac{1}{3}\pi\left[(h+\frac{x}{sin\theta})(r+\frac{x}{\sin(90-\theta)})^2 - hr^2\right]\rho_{ZnO}}{MW_{ZnO}} \quad (2)$$

$$at.\%\ Zn = \frac{N_{Zn}}{N_{Zn}+N_{GaP}} \quad (3)$$

Where *N, V, MW*, represent the number of units, volume, and molecular weight, respectively.

Figure II.8. Schematic depiction of an idealized ZnO-coated macropore wall viewed from the plane orthogonal to the anodic etching direction. Orange: GaP; Gray: ALD ZnO coating. (Not drawn to scale)

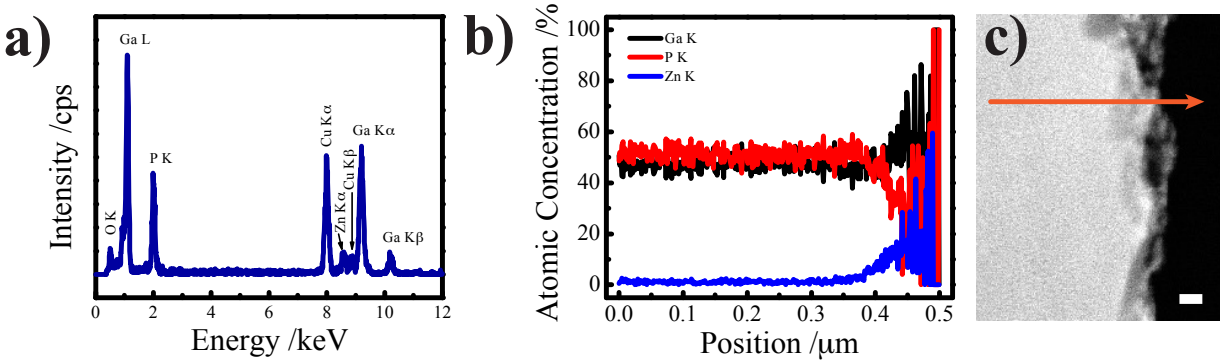

Figure II.9. (a) Representative energy dispersive X-ray spectrum obtained at approximately 50 nm from the surface of a Zn-doped macroporous GaP. (b) Elemental line profile collected in the direction indicating in the corresponding HAADF image in (c). The intensity was corrected with respective sensitivity factors and conveyed in terms of atomic percent. Scale bar: 50 nm.

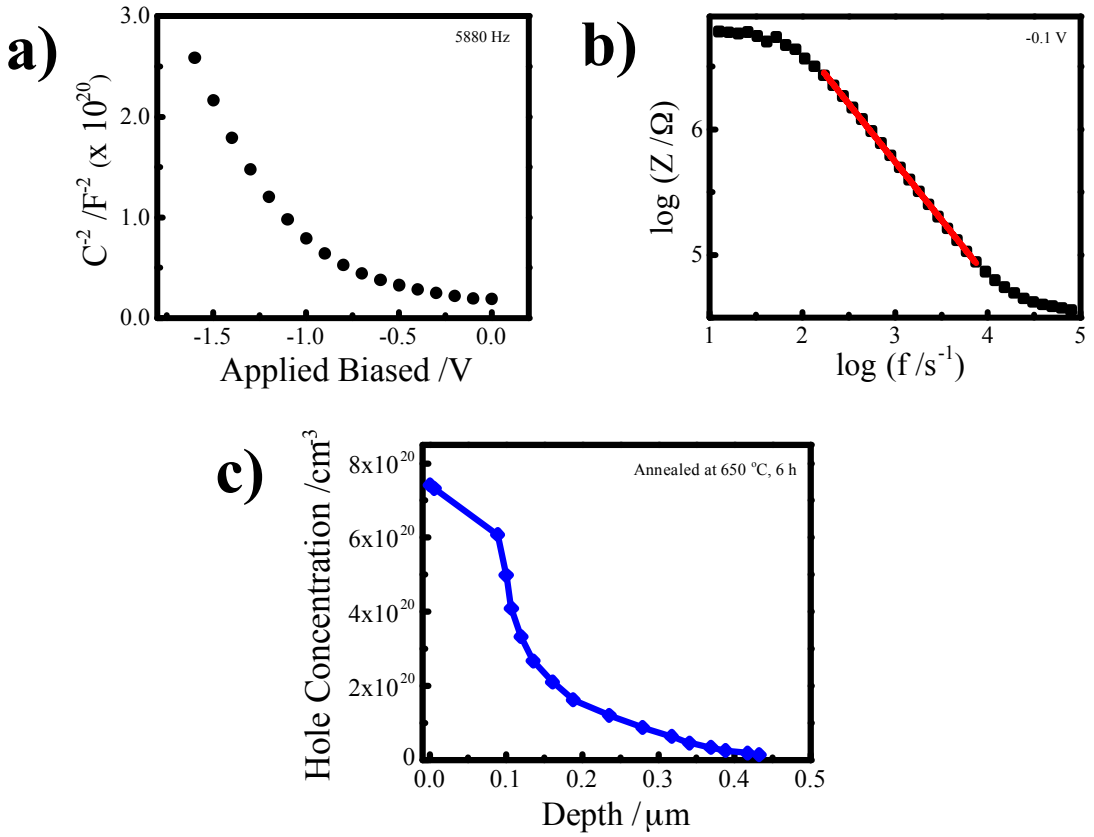

Figure II.10. (a) A representative capacitance-potential (C^{-2}-E) response for a Zn-doped planar p-GaP collected from a Hg/GaP Schottky barrier contact in the dark. (b) Corresponding log f vs. log Z Bode plot at a reverse bias of -0.1 V. (c) Plot of hole concentration available at certain distances from the surface of Zn-doped planar GaP wafer.

$$\frac{\partial C^{-2}}{\partial V} = \frac{2w}{\varepsilon\varepsilon_0^2}\left(\frac{\partial w}{\partial V}\right) = \frac{2}{\varepsilon\varepsilon_0 q N_d(w)}, \qquad and \qquad C = \frac{\varepsilon\varepsilon_0}{w} \qquad \text{Eq. II.1}$$

where C is the capacitance, V is the voltage bias, w is the depletion width, ε is the dielectric constant of semiconductor, ε_0 is the permittivity of free space, q is the elementary charge, and N_d is the carrier concentration.

To further describe the distribution of Zn in the planar GaP wafer, the profile of Zn concentration as a function of depth was collected using X-ray photoelectron spectroscopy (XPS) and presented in Figure II.11. The Zn concentration fell below the detection limit of the instrument (~ 0.1 at. %) after approximately 105 nm from the surface. There were some discrepancies between the amount of Zn measured in XPS and in impedance spectroscopy. This is because the diffused Zn dopants need to compensate the existing n-type dopants in the wafer, which reduces the amount of the overall electrically active dopants in GaP wafer. Figure II.12a shows the XPS survey of a Zn-doped planar p-GaP wafer, and the peak area for Zn 2p was used for quantification after correcting with the sensitivity factors. Figure II.12b shows the core scan of the Zn 2p region. The binding energy of the Zn $2p_{3/2}$ signal was found to be 1022.6 eV, which is consistent with a Zn^{2+} oxidation state and no metallic Zn signals were observed in the XP spectra. The peak fittings were performed in CASAXPS software as described in Kimball et al. and Brown et al.[41-42]

Irrespective of the specific value, the key point is the annealing conditions chosen here were sufficient to compensate completely the existing n-type carriers to render a p-type character without using excessive temperatures that sublime GaP.

The data do suggest that the excess Zn could negatively impact the electronic properties of the material. For example, photoanode measurements were separately performed with electrodes made from macroporous n-GaP immediately after anodic etching. These n-type macroporous GaP photoanodes yielded steady-state photocurrent densities approaching 1.0 mA cm^{-2} under 100 mW cm^{-2} white light illumination. As seen in Figure II.7, after doping and conversion to p-type macroporous p-GaP films (pore depth = 40 μm), analogous GaP electrodes sustained slightly lower photocurrent densities (0.9 mA cm^{-2}). In addition, the approximate photovoltage in Figure II.7 is less than the maximum photovoltage attainable with crystalline

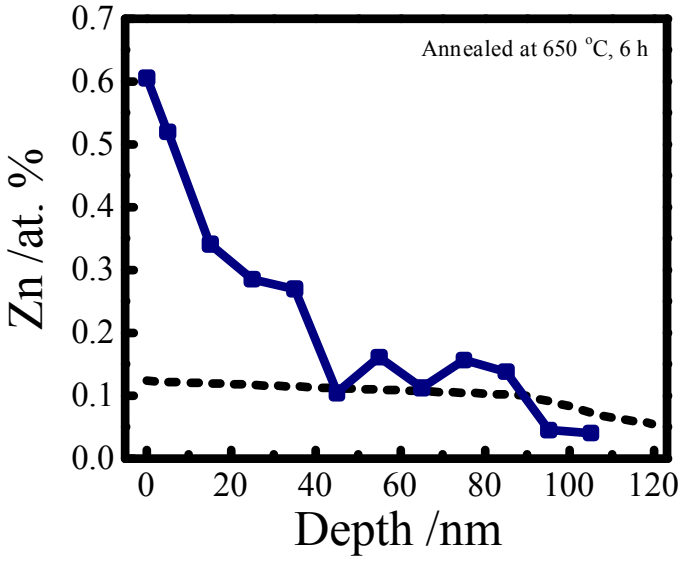

Figure II.11. XPS depth profile of Zn in a Zn-doped planar p-GaP diffused at T = 650 ºC fro 6 h. The Zn concentration measured using impedance spectroscopy was plotted as black dotted line for comparison.

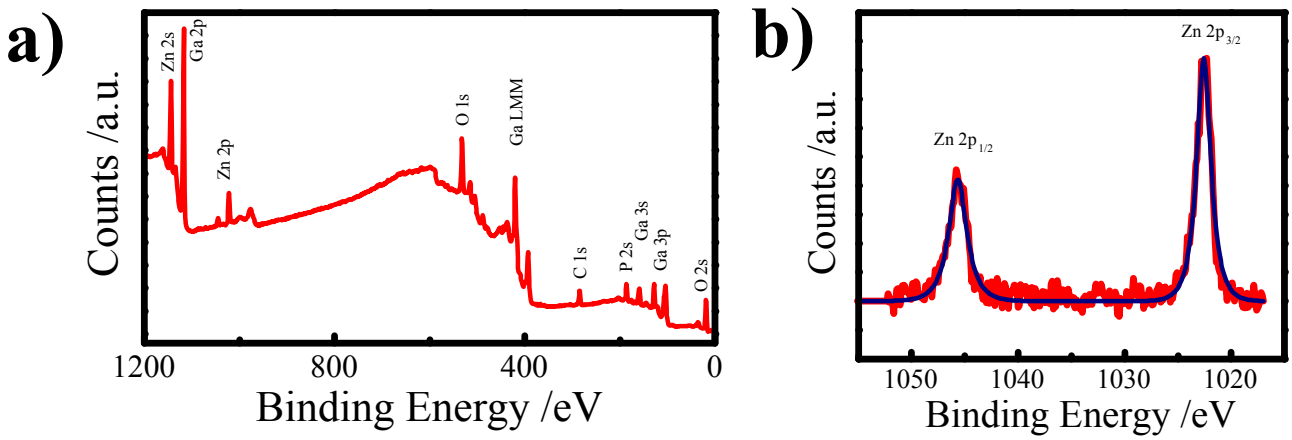

Figure II.12. (a) Survey and (b) Zn 2p spectra obtained from a Zn-doped planar GaP wafer after 6 h of diffusion at $T = 650$ ºC.

GaP, even though the valence band edge is approximately 1.5 V more positive than the standard potential for $MV^{2+/+}$.[30, 43] Finally, the apparent shapes (i.e. 'fill factors') of the photoresponses in Figure II.7 were not purely rectangular. These cumulative observations are consistent with material electronic properties (e.g. mobility of the minority carrier) that could stand further improvement. Further work is needed to refine the doping method to minimize excess Zn.

ii. High Aspect Ratio Photocathodes

Macroporous p-type GaP films have utility in the design of photoelectrochemical systems in three respects. The data here are the first realization of p-type macroporous III-V semiconductor films that exhibit enhanced photocurrents relative to the corresponding planar analog. Simply, this report shows unambiguously that if tall, thin p-type GaP is adequately doped, then increased photocurrents are attainable. This observation further validates the concept that a sufficiently doped, high-aspect-ratio form factor is more germane to the capacity to capture and convert long wavelength light than the defect density of the bulk material. This work also illustrates that 'optimal' doping is not synonymous with constant doping when the material size is not uniform throughout. Anodic etching of the undoped GaP resulted here in macropores that are thinner at the top than at the bottom. At a constant doping level, we have previously shown that tapered photoelectrodes will necessarily exhibit external quantum yield values less than 1 if any portion of the material is too small to support the depletion condition dictated by the energetics of the semiconductor/liquid heterojunction.[17] Since we did not prepare any ZnO films with thicknesses that changed as a function of macroporous film depth, we did not attempt to generate an optimal doping profile within the macroporous GaP. Accordingly, the wavelength-dependent external quantum yields with macroporous p-GaP in Figure II.7 were lower than what was previously observed for macroporous n-GaP photoanodes.[17]

E. Conclusion

The presented data show both specifically a new route to prepare macroporous p-type GaP photoelectrodes and more generally an ALD method to render nanostructured III-V semiconductor materials p-type. These aspects have two immediate consequences on the development of advanced photoelectrochemical architectures involving high-aspect ratio photocathodes with the capacity for large photovoltages and photocurrent densities under illumination. First, studying processes that dope macroporous III-V films is useful for the

development of protocols to dope high-aspect ratio semiconductor nanostructures. Macroporous semiconductor films are useful because the relevant bulk electronic properties are defined by the parent wafer and are easily and quickly measured beforehand using standard methods. Accordingly, determining whether the doping process imparts the intended type of conductivity and concentration of dopants is unambiguous. This aspect is particularly advantageous if more complex variations in doping strategies (e.g. ZnO film thicknesses that are a function of vertical depth) are pursued. Second, many organic chromophores can inject a h^+ into GaP upon photoexcitation.[30, 41, 44] This principle has been tested numerous times on planar p-GaP photocathodes but has never been assessed on high surface area p-GaP platforms. The p-type macroporous GaP films developed here should be amenable for high dye loading, offering a pathway for sensitized photocathodes with both high external quantum yields and the possibility for large photovoltages. If realized, such constructs would represent a substantial advancement over the state-of-the-art sensitized p-NiO photocathodes.[45-48] Such work is ongoing in our laboratory.

F. References

1. Barton, E. E.; Rampulla, D. M.; Bocarsly, A. B., Selective Solar-Driven Reduction of CO_2 to Methanol Using a Catalyzed p-GaP Based Photoelectrochemical Cell. *J. Am. Chem. Soc.* **2008,** *130*, 6342-6344.
2. Halmann, M., Photoelectrochemical Reduction of Aqueous Carbon Dioxide on p-Type Gallium Phosphide in Liquid Junction Solar Cells. *Nature* **1978,** *275*, 115-116.
3. Liu, C.; Sun, J.; Tang, J.; Yang, P., Zn-Doped p-Type Gallium Phosphide Nanowire Photocathodes from a Surfactant-Free Solution Synthesis. *Nano Lett* **2012,** *12* (10), 5407-11.
4. Malizia, M.; Seger, B.; Chorkendorff, I.; Vesborg, P. C. K., Formation of a P–N Heterojunction on GaP Photocathodes for H_2 production Providing an Open-Circuit Voltage of 710 mV. *J. Mater. Chem. A* **2014,** *2* (19), 6847-6853.
5. McCann, J. F.; Handley, L. J., The Photoelectrochemical Effect at p-GaP Electrode. *Nature.* **1980,** *283*, 843-845.
6. Ohashi, K.; McCann, J.; Bockris, J. O. M., Stable Photoelectrochemical Cells for the Splitting of Water. *Nature.* **1977,** *266*, 610-611.
7. Standing, A.; Assali, S.; Gao, L.; Verheijen, M. A.; van Dam, D.; Cui, Y.; Notten, P. H.; Haverkort, J. E.; Bakkers, E. P., Efficient Water Reduction with Gallium Phosphide Nanowires. *Nat. Comm.* **2015,** *6*, 7824.
8. Wen, W. Synthesis and Nanoengineering of Gallium Phosphide Nanostructures for Photoelectrochemical Solar Energy Conversion. Ph.D. Thesis, University of Michigan, 2014.
9. Hasenöhrl, S.; Eliáš, P.; Šoltýs, J.; Stoklas, R.; Dujavová-Laurenčíková, A.; Novák, J., Zinc-Doped Gallium Phosphide Nanowires for Photovoltaic Structures. *Appl. Surf. Sci.* **2013,** *269*, 72-76.
10. Moselund, K. E.; Ghoneim, H.; Schmid, H.; Bjork, M. T.; Lortscher, E.; Karg, S.; Signorello, G.; Webb, D.; Tschudy, M.; Beyeler, R.; Riel, H., Solid-State Diffusion as an Efficient Doping Method for Silicon Nanowires and Nanowire Field Effect Transistors. *Nanotechnology.* **2010,** *21* (43), 435202.
11. Wallentin, J.; Borgström, M. T., Doping of Semiconductor Nanowires. *J. Mater. Res.* **2011,** *26* (17), 2142-2156.
12. Föll, H.; Langa, S.; Cartensen, J.; Christophersen, M.; Tiginyanu, I. M., Pores in III-V Semiconductors. *Adv. Mater.* **2003,** *15* (3), 183-198.
13. Leskela, M.; Ritala, M., Atomic Layer Deposition Chemistry: Recent Developments and Future Challenges. *Angew Chem Int Ed Engl.* **2003,** *42* (45), 5548-54.
14. Resasco, J.; Dasgupta, N. P.; Rosell, J. R.; Guo, J.; Yang, P., Uniform Doping of Metal Oxide Nanowires Using Solid State Diffusion. *J. Am. Chem. Soc.* **2014,** *136* (29), 10521-6.
15. Wang, D.; Chen, H.; Chang, G.; Lin, X.; Zhang, Y.; Aldalbahi, A.; Peng, C.; Wang, J.; Fan, C., Uniform Doping of Titanium in Hematite Nanorods for Efficient Photoelectrochemical Water Splitting. *ACS Appl. Mater. Interfaces.* **2015,** *7* (25), 14072-8.
16. Kalkofen, B.; Amusan, A. A.; Bukhari, M. S. K.; Garke, B.; Lisker, M.; Gargouri, H.; Burte, E. P., Use of B_2O_3 Films Grown by Plasma-Assisted Atomic Layer Deposition for Shallow Boron Doping in Silicon. *J. Vac. Sci. Technol., A.* **2015,** *33* (3), 031512.
17. Price, M. J.; Maldonado, S., Macroporous n-GaP in Nonaqueous Regenerative Photoelectrochemical Cells. *J. Phys. Chem. C.* **2009,** *113* (28), 11988-11994.
18. Bielinski, A. R.; Kazyak, E.; Schlepütz, C. M.; Jung, H. J.; Wood, K. N.; Dasgupta, N. P., Hierarchical ZnO Nanowire Growth with Tunable Orientations on Versatile Substrates Using Atomic Layer Deposition Seeding. *Chem. Mater.* **2015,** *27* (13), 4799-4807.

19. Langa, S.; Carstensen, J.; Christophersen, M.; Steen, K.; Frey, S.; Tiginyanu, I. M.; Föll, H., Uniform and Nonuniform Nucleation of Pores During the Anodization of Si, Ge, and III-V Semiconductors. *J. Electrochem. Soc.* **2005,** *152* (8), C525.
20. Aspnes, D.; Studna, A., Dielectric Functions and Optical Parameters of Si, Ge, GaP, GaAs, GaSb, InP, InAs, and InSb from 1.5 to 6.0 eV. *Phys. Rev. B.* **1983,** *27* (2), 985-1009.
21. Starkiewicz, J.; Allen, J. W., Injection Electroluminescence at P-N Junction in Zn-Doped Gallium Phosphide. *J. Phys. Chem. Solids.* **1962,** *23*, 881-884.
22. Groves, W. O.; Epstein, A. S. Gallium Phosphide Light-Emitting Diodes. 3,931,631, January 6, 1976.
23. Moore, W. J.; Williams, E. L., Diffusion of Zinc and Oxygen in Zinc Oxide. *Discuss. Faraday Soc.* **1959,** *28*, 86-93.
24. Allison, H. W., Solubility and Diffusion of Zn in Gallium Phosphide. *J. Appl. Phys.* **1963,** *34*, 231-233.
25. Dean, P.; Ilegems, M., The Optical Properties of Be, Mg and Zn-Diffused Gallium Phosphide. *J. Lumin.* **1971,** *4*, 201-230.
26. Dosen, M. Fabricating a Gallium Phosphide. 3,870,575, 1975.
27. Lightowlers, E. C.; North, J. C.; Jordan, A. S.; Derick, L.; Merz, J. L., Nuclear Microanalysis of Oxygen Concentration in Liquid-Phase Epitaxial Gallium Phosphide. *J. Appl. Phys.* **1973,** *44*, 4758.
28. Chang, L. L.; Pearson, G. L., Diffusion and Solubility of Zinc in Gallium Phosphide Single Crystals. *J. Appl. Phys.* **1964,** *35* (2), 374.
29. Miikkulainen, V.; Leskelä, M.; Ritala, M.; Puurunen, R. L., Crystallinity of Inorganic Films Grown by Atomic Layer Deposition: Overview and General Trends. *J. Appl. Phys.* **2013,** *113* (2), 021301.
30. Chitambar, M.; Wang, Z.; Liu, Y.; Rockett, A.; Maldonado, S., Dye-Sensitized Photocathodes: Efficient Light-Stimulated Hole Injection into p-GaP under Depletion Conditions. *J. Am. Chem. Soc.* **2012,** *134*, 10670-10681.
31. Foley, J. M.; Price, M. J.; Feldblyum, J. I.; Maldonado, S., Analysis of the Operation of Thin Nanowire Photoelectrodes for Solar Energy Conversion. *Energy Environ. Sci.* **2012,** *5* (1), 5203-5220.
32. Memming, R.; Tributsch, H., Electrochemical Investigations on the Spectral Sensitization of Gallium Phosphide Electrodes. *J. Phys. Chem.* **1971,** *75* (4), 562-570.
33. Hagedorn, K.; Collins, S. M.; Maldonado, S., Preparation and Photoelectrochemical Activity of Macroporous p-GaP(100). *J. Electrochem. Soc.* **2010,** *157* (11), D588-D592.
34. Schmuki, P.; Fraser, J.; Vitus, C. M.; Graham, M. J.; Isaacs, H. S., Initiation and Formation of Porous Gaas. *J. Electrochem. Soc.* **1996,** *143* (10), 3316-3322.
35. Beji, L.; Sfaxi, L.; Ismail, B.; Zghal, S.; Hassen, F.; Maaref, H., Morphology and Photoluminescence Studies of Electrochemically Etched Heavily Doped p-Type GaAs in Hf Solution. *Microelectr. J.* **2003,** *34* (10), 969-974.
36. Erné, B. H.; Vanmarkelbergh, D.; Kelly, J. J., Morphology and Strongly Enhanced Photoresponse of GaP Electrodes Made Porous by Anodic Etching. *J. Electrochem. Soc.* **1996,** *143* (1), 305-314.
37. Bass, S. J.; Oliver, P. E., Pulling of Gallium Phosphide Crystals by Liquid Encapsulation. *J. Cryst. Growth.* **1968,** *3* (4), 286-290.

38. Panish, M. B.; Casey, J., H. C., The 1040 C Solid Solubility Isotherm of Zinc in GaP: The Fermi Level as a Function of Hole Concentration. *J. Phys. Chem. Solids.* **1968,** *29*, 1719-1726.
39. Rhoderick, R. H., *Metal-Semiconductor Contacts*. 2nd ed.; Oxford University Press: New York, USA, 1988; p 252.
40. Knübel, A.; Polyakov, V. M.; Kirste, L.; Aidam, R., Nonuniformity of Electron Density in In-Rich InGaN Films Deduced from Electrolyte Capacitance-Voltage Profiling. *Appl. Phys. Lett.* **2010,** *96* (8), 082106.
41. Brown, E. S.; Peczonczyk, S. L.; Maldonado, S., Wet Chemical Functionalization of GaP(111)B through a Williamson Ether-Type Reaction. *J. Phys. Chem. C.* **2015,** *119* (3), 1338-1345.
42. Kimball, G. M.; Bosco, J. P.; Müller, A. M.; Tajdar, S. F.; Brunschwig, B. S.; Atwater, H. A.; Lewis, N. S., Passivation of Zn_3P_2 Substrates by Aqueous Chemical Etching and Air Oxidation. *J. Appl. Phys.* **2012,** *112* (10), 106101.
43. Schoenmakers, G. H.; Waagenaar, R.; Kelly, J. J., Methylviologen Redox Reactions at Semiconductor Single Crystal Electrodes. *Ber. Bunsen-Ges. Phys. Chem.* **1996,** *100* (7), 1169-1175.
44. Ilic, S.; Brown, E. S.; Xie, Y.; Maldonado, S.; Glusac, K. D., Sensitization of p-GaP with Monocationic Dyes: The Effect of Dye Excited-State Lifetime on Hole Injection Efficiencies. *J. Phys. Chem. C.* **2016,** *120* (6), 3145-3155.
45. Ji, Z.; He, M.; Huang, Z.; Ozkan, U.; Wu, Y., Photostable p-Type Dye-Sensitized Photoelectrochemical Cells for Water Reduction. *J. Am. Chem. Soc.* **2013,** *135* (32), 11696-9.
46. Li, L.; Duan, L.; Wen, F.; Li, C.; Wang, M.; Hagfeldt, A.; Sun, L., Visible Light Driven Hydrogen Production from a Photo-Active Cathode Based on a Molecular Catalyst and Organic Dye-Sensitized p-Type Nanostructured NiO. *Chem Commun (Camb).* **2012,** *48* (7), 988-90.
47. Nattestad, A.; Mozer, A. J.; Fischer, M. K.; Cheng, Y. B.; Mishra, A.; Bauerle, P.; Bach, U., Highly Efficient Photocathodes for Dye-Sensitized Tandem Solar Cells. *Nat. Mater.* **2010,** *9* (1), 31-5.
48. Tong, L.; Iwase, A.; Nattestad, A.; Bach, U.; Weidelener, M.; Götz, G.; Mishra, A.; Bäuerle, P.; Amal, R.; Wallace, G. G.; Mozer, A. J., Sustained Solar Hydrogen Generation Using a Dye-Sensitised NiO Photocathode/$BiVO_4$ Tandem Photo-Electrochemical Device. *Energy Environ. Sci.* **2012,** *5* (11), 9472.

CHAPTER III

Comparison of GaP Nanowires Grown from Au and Sn Vapor-Liquid-Solid Catalysts as Photoelectrode Materials

A. Introduction

This chapter compares and contrasts the GaP nanowire film electrodes prepared *via* solid sublimation of GaP powder using both gold (Au) and tin (Sn) nanoparticles as the vapor-liquid-solid (VLS) catalysts on Si(111) and GaP(111)B substrates in a custom-built multi-zone chemical-vapor-deposition (CVD) setup. The resultant GaP nanowires are evaluated in terms of structures and photoactivity in photoelectrochemical half-cells. Sn-seeded GaP nanowires showed fewer twinning defects than Au-seeded GaP nanowires. Raman spectra implicated a difference in the surface condition of the two types of nanowires. Complete wet etching removal of metallic VLS catalysts from the as-prepared GaP nanowires was possible with Sn catalysts but not with Au catalysts. The photoresponses of both Sn- and Au-seeded GaP nanowire films were collected and examined under 100 mW cm^{-2} white light illumination. Au-seeded nanowire films exhibited strong n-type characteristics when measured in nonaqueous electrolyte with ferrocene/ferricenium as the redox species while Sn-seeded nanowires showed behavior consistent with degenerate n-type doping.

As explained in Chapter I, GaP is an important and extensively studied photoelectrode material for photoelectrochemical energy conversion, particularly for water-splitting reactions.[1-3] Although GaP interfaces are reasonably stabilized by wet chemical surface modifications and/or physical passivation methods,[4-7] the weak light absorbing properties arising from the indirect bandgap, in conjunction with finite carrier diffusion lengths, place a premium on GaP materials with large aspect ratios like nanowires and porous films.[8]

We have previously described 'top-down' methods to etch crystalline GaP wafers to render macroporous p-GaP films in literature as well as in Chapter II of this thesis.[9-10] The merits and challenges of such efforts have been detailed elsewhere.[9-11] Alternatively, 'bottom up' synthetic methods readily exist for GaP nanowires, most commonly by either the solution-liquid-

solid (SLS)[1, 12] or the vapor-liquid-solid (VLS) processes.[13] Au nanoparticles are most often used as the preferred VLS catalysts,[14-15] but Au in semiconductors can be problematic. The incorporation of Au into semiconductor nanowires is known[16-17] and can affect the optoelectronic properties of the resultant crystals.[18-20] All known wet etchants for Au removal simultaneously attack crystalline GaP[21] with equal or greater reactivity making it difficult to remove Au from the as-prepared nanowires. The cumulative effects of these points on the potential photoelectrochemical properties of GaP are yet unclear. Nevertheless, given the propensity for Au to act as deleterious traps in crystalline GaP (Table III.1)[22-23], a search for an alternative VLS catalyst has utility.

One potential alternative VLS metal catalyst for GaP is tin (Sn). We have previously shown nanoparticulate Sn is a suitable VLS catalyst for structurally related phosphides ($ZnGeP_2$ and $ZnSnP_2$)[24-25], and Sn has been used as a melt solvent for the growth of crystalline GaP boules by liquid phase epitaxy.[26-30] In addition, Sn is less noble than Au, possibly facilitating metal removal from as-prepared GaP nanowires.

Accordingly, in this chapter, we demonstrate the VLS growth of Sn-seeded GaP nanowires by solid-source sublimation of powdered GaP and contrast their observable physicochemical and electrochemical properties with Au-seeded GaP nanowires prepared in a similar manner. Solid source sublimation is convenient since it obviates the need of caustic, toxic P-containing reagents (e.g. PH_3) and further eliminates any thermal cracking step that could serve as a bottleneck in nanowire growth. The crystallinities of the as-prepared GaP nanowires are described with electron microscopies and diffraction techniques. Results from X-ray dispersion spectroscopy, Raman spectroscopy, and photoelectrochemical measurements in a regenerative cell with 'high' and 'low' work function solutions further highlighted the differences between GaP nanowires prepared from these two metal types.

B. Experimental Section

i. Nanowire Preparation

Nanowire growths were conducted in a custom-built quartz tube reactor as depicted in Figure III.1. Briefly, 15 mg of finely ground GaP powder (99.99%, metal basis, Sigma-Aldrich) was placed on a quartz platform and subsequently inserted into a quartz tube (2.2 cm diameter

Table III.1. Comparison of Sn and Au properties.

Metal	T_m /°C	*Atomic Mass* / amu	ρ / g cm^{-3} [a]	*Solubility in GaP* / cm^{-3}	φ / eV [d]
Sn	232	118.71	7.31	1.58×10^{19} [b]	4.42
Au	1063	196.97	19.32	1×10^{16} [c]	5.31

a. $T = 25$ °C
b. $T = 1070$ °C, Reference 30.
c. $T = 1050$ -1250 °C, Reference 22.
d. Reference 23.

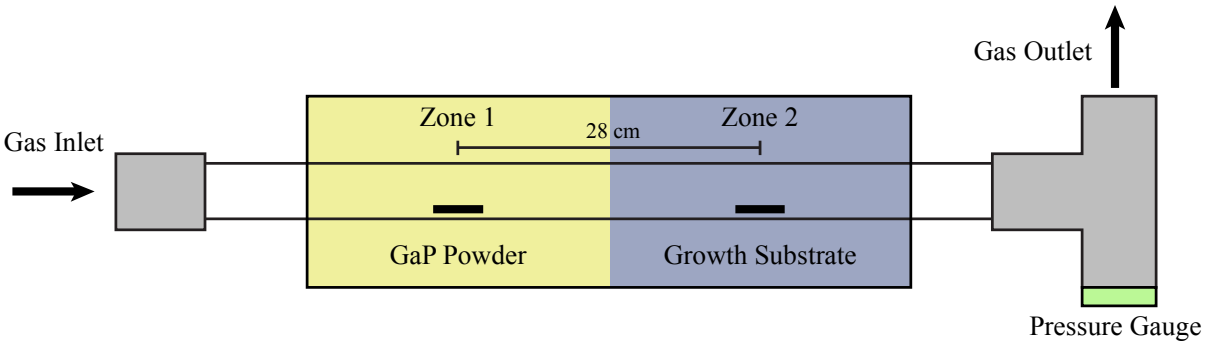

Figure III.1. Schematic depiction of the multi-zone tube furnace setup used for solid source sublimation GaP nanowires nanowire growth.

and 86 cm length). Growth substrates were separately and previously decorated with thin (5 - 25 nm) metal thin films by metal evaporation. To minimize oxidation of Sn nanoparticles, the reactor was carefully purged and annealed with forming gas to reduce the surface oxidation before the nanowire growth. Si(111) (As-doped, 0.006 Ω cm, thickness = 0.5 mm, Wafer Works Corp.), p-type GaP(111)B (Zn-doped, miscut ≤ 0.5º, 0.0536 Ω cm, thickness = 0.4 mm, ITME), n-type GaP(111)B (S-doped, miscut ≤ 0.5º, 0.083 Ω cm, thickness = 0.4 mm, ITME) or GaP(100) wafer (miscut ≤ 1º, thickness = 0.5 mm, MTI Corporation) were used as growth substrates. Prior to use, all substrates were etched in concentrated H_2SO_4 (doubly distilled, Sigma-Aldrich) for 30 s and rinsed well with H_2O (>18 ΩM cm, Barnstead Nanopure Purifier). Once the metal-coated substrate and the source powders were loaded into the quartz tube, the assembly was evacuated with a roughing pump to below 0.06 torr before flushing the tube with 12-50 sccm forming gas (95:5 N_2:H_2). For Au-based nanowire growth, the GaP source powder was heated to T = 800 ºC for 60 min under a static vacuum. The growth substrate was kept in a region where the temperature was approximately 620 °C. For Sn-based nanowire growth, the GaP source powder was sublimed at T = 830 ºC while the growth substrate was kept at a set temperature (T = 300-600 ºC, *vide infra*). The carrier gas flow rate and pressure were maintained at 12 sccm and 0.5 torr respectively throughout the growth duration. For both nanowire deposition types, the system was allowed to cool down to room temperature radiatively over the course of 4 h upon completion of the nanowire growth.

Materials Characterization. Scanning electron micrographs were collected with a FEI NOVA Nanolab Dualbeam Workstation equipped with Schottky field emitter, a through-the-lens detector (TLD), and an EDS detector. High-resolution transmission electron microscopy images and the selected-area electron diffraction patterns (SAED) were acquired with a JEOL 3011 TEM equipped with a LaB_6 source operated at 300 keV. The samples for TEM were prepared by sonicating the as-prepared GaP nanowires in ethanol (190 proof, ACS spectrophotometric grade, Sigma-Aldrich) for 15 s to create a homogenous suspension. The suspension was then drop-casted onto copper TEM grids supported by an ultra-thin carbon film (Ted Pella). Raman spectra of the nanowire films were acquired using Renishaw RM series spectrometer equipped with Leica microscope, a Nikon LU Plan 20x objective (numerical aperture = 0.4), edge filters to reject the excitation line, and a CCD detector (578 x 400) in a 180º backscatter geometry. The excitation source was a 785 nm diode laser.

ii. Wet etching

As-prepared GaP nanowires substrate were etched by immersion in wet etchant solutions, followed by a copious rinse with water (>18 ΩM cm, Barnstead Nanopure Purifier) and finally with methanol (ACS-grade, Sigma-Aldrich) before air-drying. For Sn-based GaP nanowire films, 1 M HCl for 10 min was used. For Au-seeded nanowires, the same etchant in addition to 0.6 M KI(aq) /0.1 M I_2(aq) was used.

iii. Electrode Preparation

Electrodes were only prepared from nanowire films grown on GaP substrates. Ohmic contact to the supports was made by etching the back of the substrates in concentrated H_2SO_4 for 30 s, rinsing with distilled water, soldering a thin layer of In (99.9+% metal basis, Sigma-Aldrich) on the back of the wafers, and then annealing at 400 ºC for 10 min in forming gas (5% H_2 95% N_2). The electrodes were then fabricated by attaching a copper wire to the back of each growth substrate with silver print (GC Electronics), threading the wire through a glass tube, and sealing it with inert epoxy (Hysolc C, Loctite).

iv. Photoelectrochemical Measurements

An optically flat bottom custom-built glass cell was used for all photoelectrochemical measurements. Dry acetonitrile (Sigma-Aldrich) was prepared with MBraun solvent purification system. Lithium perchlorate (99.99%, battery grade, Sigma-Aldrich) was opened in an inert atmosphere glovebox and used as received. The redox couple was prepared by subliming and drying ferrocene (Fc, Sigma-Aldrich) in Schlenk line, and ferricenium (Fc^+) was generated by electrolysis in a second compartment separated by a Vycor frit. The cell, including a platinum gauze counter electrode and a Luggin capillary reference electrode, was assembled in an inert atmosphere glovebox. The ensemble was then removed from the glovebox, connected to an Ar(g) line, and kept under a positive pressure of Ar(g) during use. Aqueous electrolytes consisting of dissolved methyl viologen dichloride (MV^{2+}, Aldrich) and potassium chloride (Aldrich) were prepared in lab ambient but sparged with N_2(g) prior to use. The *J-E* photoresponse was collected with CH Instruments 420A under a white light tungsten halogen lamp source (ELH, Osram). Quantum efficiency measurements were conducted using monochromatic light obtained with a custom-built apparatus described previously.[31] The absolute photocurrents were measured with a PAR 273 potentiostat under a potentiostatic bias.

C. Results

Figure III.2a shows a representative cross-sectional scanning electron micrograph of GaP nanowire films prepared with Au VLS catalyst particles. Similar to previous reports,[14, 32] Au catalysts readily seeded GaP nanowire growth. The spread in the Au-based nanowire diameters reflects the variation in Au nanoparticle radii. On both Si and GaP substrates, the nanowires routinely exhibited epitaxial growth along the [111] direction. On the substrates used in these studies, this aspect was manifest in nanowire orientation normal to the surface plane. Figure III.2b shows a representative cross sectional image of a film of Sn-based GaP nanowires on the same substrate type. In general, Sn-based VLS nanowires were observed at temperature as low as T = 350 ºC, a condition which was not suitable for Au nanoparticles, and as high as T = 550 ºC. However, the Sn-seeded GaP nanowires did not grow in a preferred direction or orientation, indicating no epitaxial relationship with the growth substrate. The Sn-seeded nanowires also appeared to be more curled, with fewer straight nanowires, and often featured a metallic tip that extended slightly beyond the diameter of the nanowire. For both Sn and Au, GaP nanowire films prepared at T = 500 ºC were the most consistent in terms of quality and growth rate, therefore this temperature was chosen for further comparison studies.

Figure III.3 contrasts the differences in the two GaP nanowire types observable by transmission electron microscopy. In Figure III.3a, the Au-seeded GaP nanowire was untapered and straight with a sharp boundary between the GaP nanowire and the rounded Au nanoparticle. The nanowire showed substantial contrast that arose from the numerous twinning defects (Figure III.3b). On average, twin defects were observed at a linear density of 1 per 50 nm in length. The selected area electron diffraction pattern obtained from the nanowire similarly showed evidence of twinning, as two sets of cubic zinc blende diffraction patterns were seen and offset by a rotational angle of 60º (Figure III.3c). In comparison, the representative Sn-based GaP nanowire in Figure III.3d also featured the metal catalyst at the tip but the boundary with the GaP nanowire was not as distinct. This GaP nanowire appeared less straight. Higher magnification imaging (Figure III.3e) showed some dislocation defects but no heavy twinning, with less than 1 twinning defects per 100 nm in length. The selected area electron diffraction pattern collected over a large area of the nanowire in Figure III.3f separately showed a single cubic zinc blende crystal along the [211] zone axis, without any evidence of twinning.

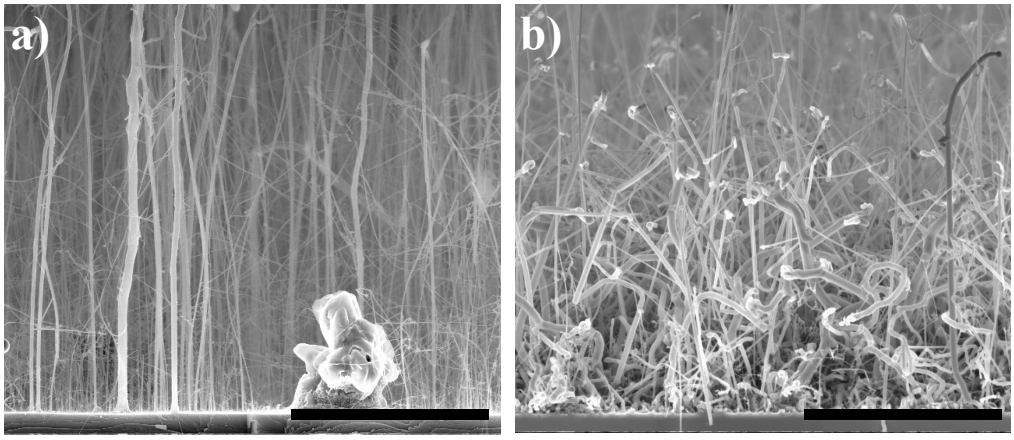

Figure III.2. Cross-section scanning electron micrographs of GaP nanowires grown via solid sublimation. a) Au-seeded GaP nanowires on GaP(111)B grown at T = 620 °C. b) Sn-seeded GaP nanowires on GaP(111)B at T = 500 °C. Scale bars: a) 5 μm; b) 2 μm.

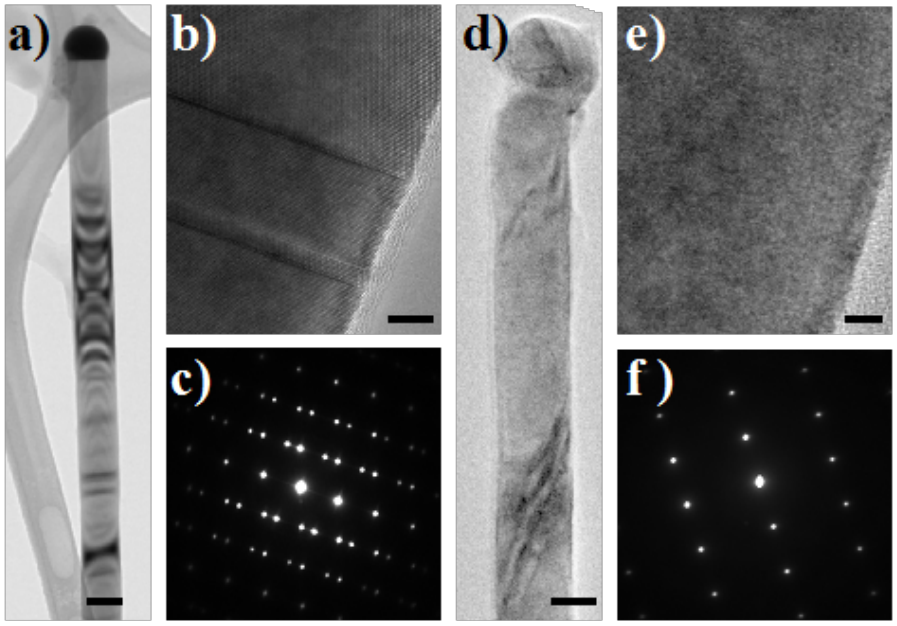

Figure III.3. a) Low-magnification transmission electron micrographs of a representative Au-seeded GaP nanowire. b) High-magnification transmission electron micrograph of the edge of a Au-seeded GaP nanowire. c) Selected area electron diffraction (SAED) pattern collected along the [110] zone axis of the Au-seeded GaP nanowire. d) Low-magnification transmission electron micrographs of a representative Sn-seeded GaP nanowire. e) High-magnification transmission electron micrograph of the edge of a Sn-seeded GaP nanowire. f) SAED pattern collected along the [211] zone axis. Scale bars: a) 100 nm; b) 5 nm; d) 50 nm; e) 2 nm.

To probe the GaP nanowires more globally, Raman spectra were obtained (Figure III.4). Figure III.4a shows the collected Raman scattering of both Au- and Sn-seeded GaP nanowires grown on a Si(111) substrate. For both nanowire types, the two characteristic phonons expected for crystalline GaP were observed. For the Au-seeded GaP nanowires, Raman peaks at 364.0 cm^{-1} and 396.3 cm^{-1} were observed, corresponding to the transverse (TO) and longitudinal optical (LO) modes of GaP, respectively.[33] For the Sn-seeded GaP nanowires, Raman peaks at 363.0 cm^{-1} and 398.4 cm^{-1} were noted. Both Raman spectra showed noticeably broader TO phonon modes (*fwhm* = 14.6 and 12.2 cm^{-1} for Au- and Sn-catalyzed GaP nanowires) than the corresponding phonon in Raman spectra from a single crystalline GaP(111)B wafer (*fwhm* = 8.9 cm^{-1}, data not shown). Nevertheless, the peak positions were nominally the same. However, for the LO phonon mode, the peak positions and intensities for the Au- and Sn-seeded GaP nanowire were different. The LO mode for the Sn-based GaP nanowires was markedly less intense. The LO modes for both GaP nanowire types were substantially red-shifted relative to the corresponding LO phonon position for bulk crystalline GaP (401.8 cm^{-1}).[33] Although the peak shape of the LO mode is reported to be more sensitive to phonon confinement effects in small GaP crystals,[34-36] the red-shift of the LO phonon modes in both nanowire types cannot be ascribed to just phonon confinement. Such effects as predicted by the Richter-Fauchet-Campbell model[37] are only substantial for very thin nanowires (radius less than 10 nm),[38] far below the diameters of the nanowires prepared here. Rather, the broadness of both the TO and LO modes and the notable red-shift of the LO mode in both spectra are consistent with the presence of either impurities[39] or considerable strain[40] in the GaP nanowires. The most likely impurity is the metal catalyst. The more substantial shift in the Au-seeded GaP nanowires could imply a higher metal loading. However, another aspect is notable in both Raman spectra in Figure III.4a. The broadness and asymmetry of the LO modes are suggestive of a large contribution from a surface phonon mode, as described previously for the Raman spectra of GaP nanowires.[34-35] Intense surface phonons, although not common in Raman spectra of macro-sized GaP crystals, are expected for high-aspect-ratio nanowires in polar semiconductors.[34, 38] These modes are a function of the semiconductor, the dielectric properties of the contacting medium, and the periodicities of features on the semiconductor surface that disrupt phonon mode propagation (e.g. crystallographic defects, impurities).

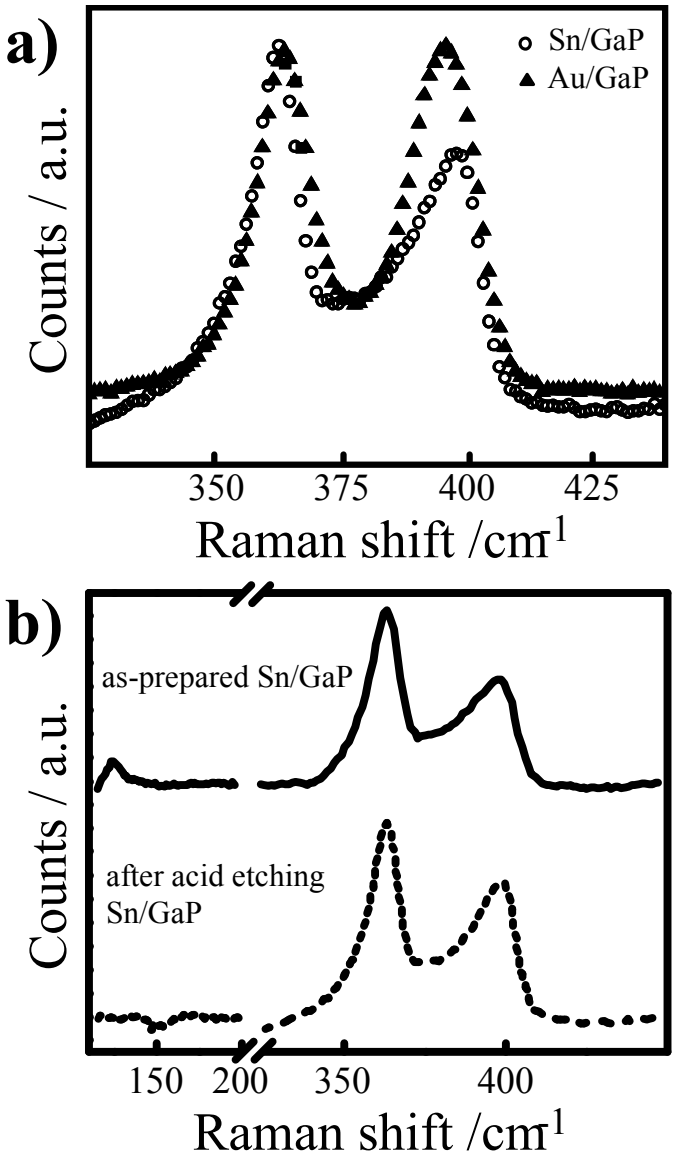

Figure III.4. a) Unpolarized Raman spectra of Au- and Sn-seeded GaP grown on Si(111) substrates. b) Comparison of the Raman spectra for Sn-seeded GaP nanowires before and after etching in 1 M HCl for 10 min. Excitation wavelength: 785 nm.

Another feature in the Raman spectra was notable for as-prepared Sn-based GaP nanowires. A peak at 126 cm^{-1} was noted, consistent with crystalline β-Sn (Figure III.4b).[24-25, 41] Wet etching these nanowires in 1 M HCl for 10 min did not perceptibly alter the shapes, intensities, or positions of the GaP TO and LO phonon modes but did eliminate the peak at 126 cm^{-1}. The loss of this peak indicated both that the wet etching removed metallic Sn from the as-prepared GaP nanowires and that the broadness of the LO mode could not be ascribed to the presence of metallic Sn on the surface of the nanowires.

The effectiveness of wet etchants on the removal of metallic impurities from as-prepared GaP nanowire samples was further investigated. Figure III.5 shows as-prepared Au-seeded GaP nanowires after being treated with a dilute aqueous KI/I_2 solution for 30 s. The presence of Au in the majority of the sample remained after prolonged etching was confirmed by energy dispersive X-ray spectroscopy (Figure III.5c and 5d), where significant levels of Au were seen after this treatment. Prolonged times and etching at higher temperatures removed both the Au and a considerable fraction of GaP. A tolerable etching condition that eliminated Au but did not dissolve a substantial fraction of the GaP nanowires was not found. Alternatively, the impact of the 1 M HCl etch used in the data in Figure III.4 on Sn-based GaP nanowires was also assessed. The corresponding energy dispersive X-ray spectra separately (Figure III.5a and 5b) showed no evidence of Sn above the detection limit in the GaP nanowires.

The photoelectrochemical responses of GaP nanowire film electrodes were recorded in a regenerative, three-electrode cell to ascertain their doping character. This type of cell was useful since liquid electrolytes readily and naturally formed conformal contacts to high aspect ratio photoelectrodes. Further, the use of a simple $1e^-$ outer-sphere redox couple (ferrocene/ferricenium) in a poised, non-aqueous electrolyte obviates any confounding aspects regarding electrocatalysis and corrosion, in strong contrast to studies employing fuel forming reactions like water-splitting. In this regenerative cell, the photoresponse characteristics directly elucidate the responsivity of the photoelectrode material.

Figure III.6a shows the performance of as-prepared Au-seeded GaP nanowire films in dry acetonitrile containing the ferrocene/ferricenium redox couple and 1 M $LiClO_4$. In the dark, the recorded current was minimal in the investigated potential range. Under 100 mW cm^{-2} white light illumination, these GaP nanowire films exhibited n-type behavior, i.e. an anodic current at short-circuit and an open-circuit photovoltage at potentials more negative than 0 V. The short-

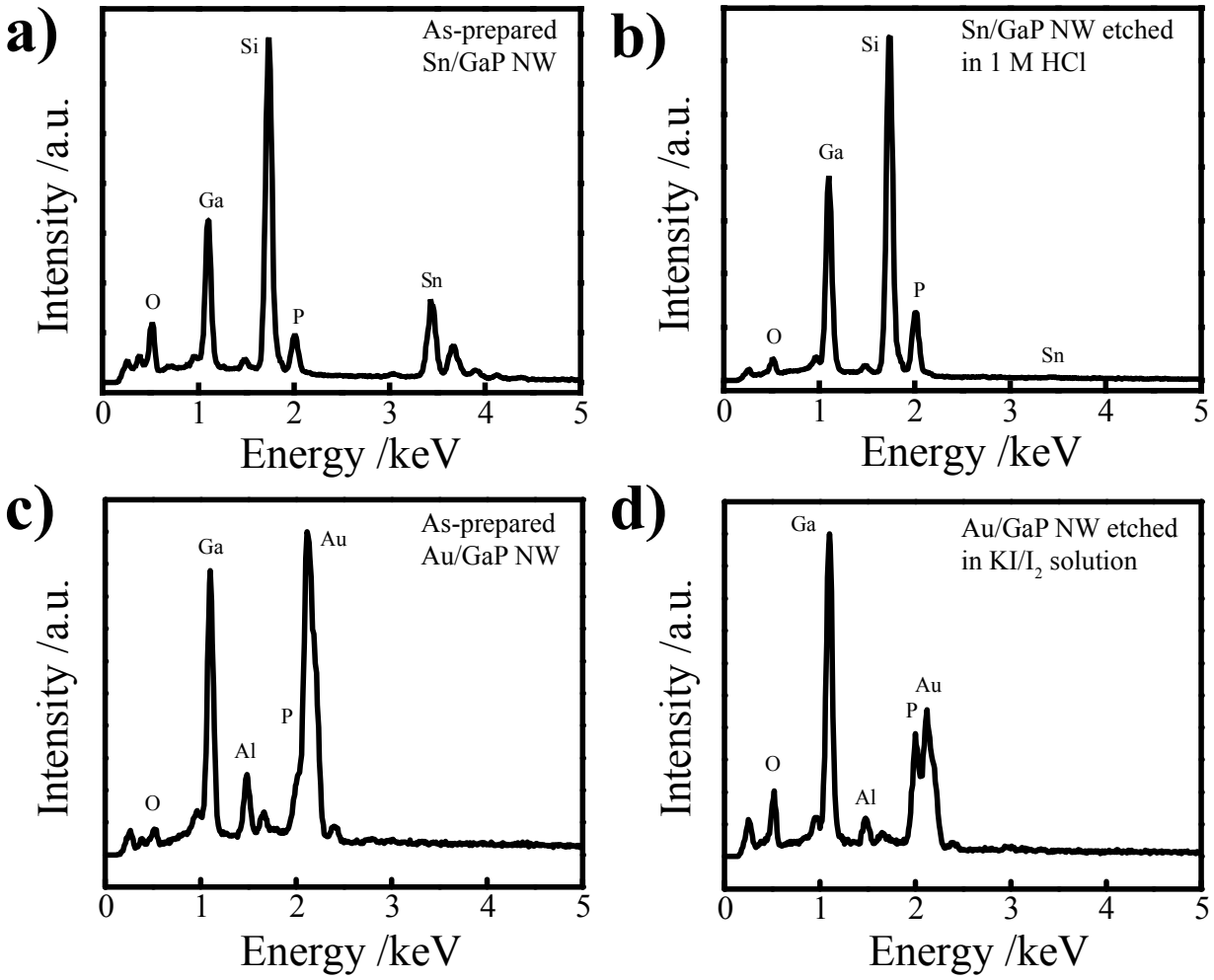

Figure III.5. Energy dispersive X-ray spectra collected from Sn-seeded GaP nanowire films (a) before and (b) after etching in 1 M HCl for 10 min and also from Au-seeded GaP nanowire films (c) before and (d) after etching in KI/I_2 solution for 30 s.

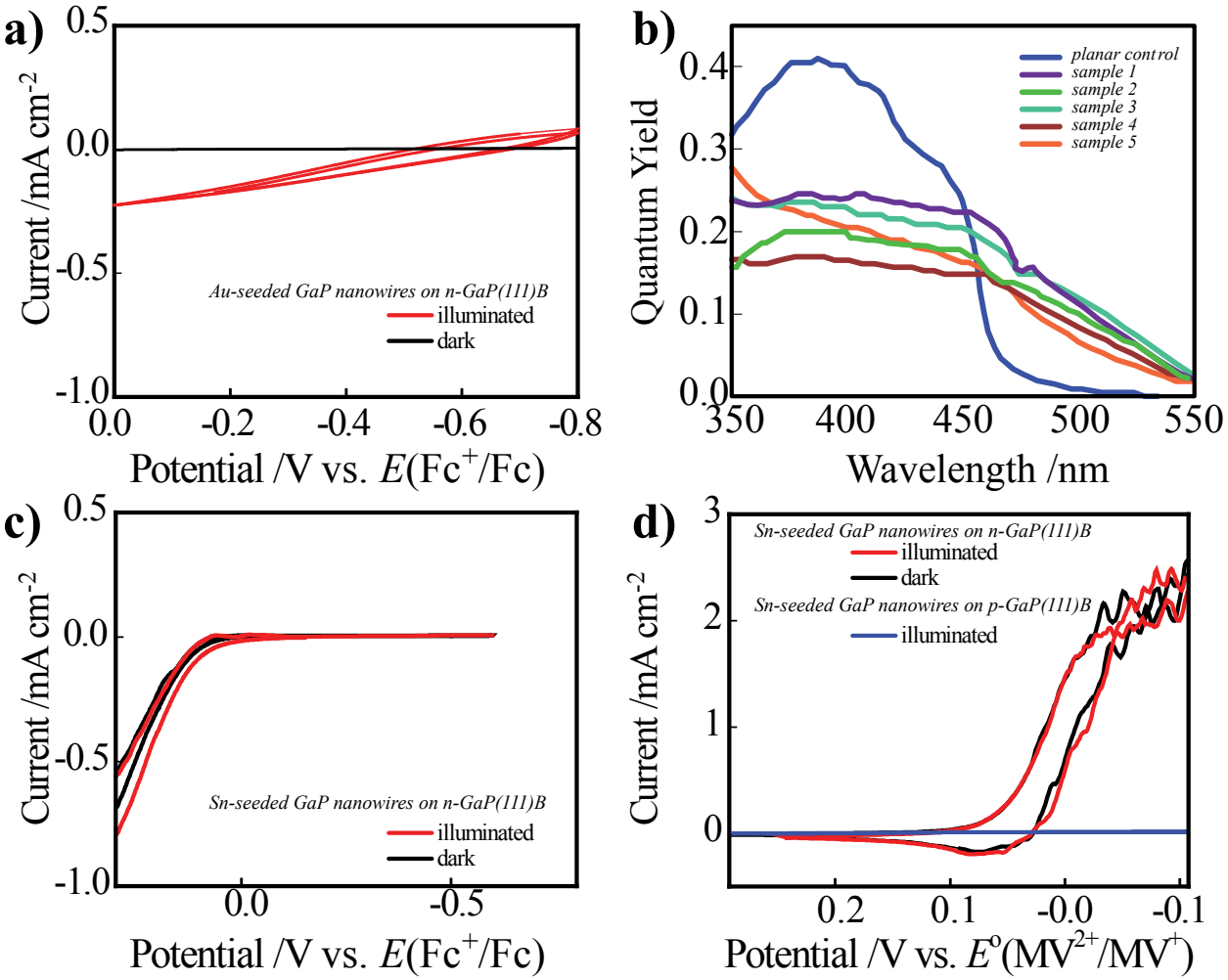

Figure III.6. Steady-state current-potential responses in both the presence and absence of 100 mW cm^{-2} ELH illumination for (a) a representative Au-GaP nanowire film photoelectrodes on n-GaP(111)B collected in dry acetonitrile containing 0.5 mM ferrocenium, 49.5 mM ferrocene, and 1 M $LiClO_4$. b) Wavelength-dependent short-circuit photocurrent quantum yields for five separate Au-seeded GaP nanowire film phototelectrodes in the same electrolyte as (a). A representative response from an uncoated substrate is also shown. c) Steady-state current-potential for a representative Sn-seeded GaP nanowire film electrode on n-GaP(111)B immersed in the same electrolyte as in (a) in both the presence and absence of 100 mW cm^{-2} ELH illumination. d) Representative steady-state current-potential responses in both the presence and absence of 100 mW cm^{-2} ELH illumination for Sn-seeded GaP nanowire film electrodes on n-GaP(111)B and p-GaP(111)B substrates in aqueous electrolyte containing 10 mM methyl viologen dichloride (MV^{2+}) and 1 M KCl.

circuit photocurrent was ~ 0.2 mA cm^{-2} and the photovoltage 0.8 V, consistent with strongly depleted semiconductor photoelectrodes. The photoresponses and fill factors of five separate GaP nanowire photoelectrodes in this same electrolyte were tabulated in Table III.2. All interrogated electrodes showed clear photoanodic behavior, indicating the as-prepared Au-seeded GaP nanowires were n-type as prepared. Although the calculated photoelectrode efficiencies were low, separate measurements of the quantum yield for photocurrent at 0 V with supra-bandgap light were performed (Figure III.6b). All five electrodes showed two noticeable features that differed from control measurements performed with the same n-type GaP(100) substrate without a nanowire film. First, all five nanowire electrodes showed lower quantum yields at wavelengths equal to or shorter than the direct bandgap wavelength of GaP (λ = 446 nm). This observation is consistent with higher carrier recombination at the surface/near surface of the photoelectrode material.[42] This aspect was corroborated by the observation that brief etching in the KI/I_2 solution did increase the quantum yields at short wavelengths. Second, all five nanowire samples showed higher quantum yields at wavelengths longer than 470 nm out to the bandgap energy. This feature is consistent with the premise that high-aspect ratio photoelectrode form factors orthogonalize light absorption and carrier collection, enabling the more efficient collection of photogenerated carriers that have absorption depths greater than the minority carrier diffusion length in the photoelectrode material.[8, 43-44]

Analogous experiments were performed with Sn-seeded GaP nanowire films (Figure III.6c). However, the current-potential responses collected with and without illumination were essentially the same, with no appreciable photovoltage. The responses in both the dark and under illumination showed oxidative currents for the oxidation of ferrocene that increased exponentially with increasing overpotential, indicating large surface hole concentrations in both the light and dark near E = 0 V. This feature is inconsistent with strong depletion in a semiconductor electrode. To distinguish whether degenerate doping or p-type doping was the reason why the Sn-seeded GaP nanowires were not strongly depleted, additional photoelectrochemical measurements were performed. Figure III.6d shows the current-potential responses of Sn-seeded GaP nanowire films grown on both n-type and p-type GaP(111)B in aqueous electrolyte containing methyl viologen (MV^{2+}) as an electron acceptor. In this electrolyte, the nanowire films on the p-type substrate again exhibited no discernable difference in the dark and under illumination, with the current rapidly increasing past the standard potential

Table III.2. Summary of Photoresponses from 5 Separate Au-seeded GaP Nanowire Film Electrodes in Dry Acetonitrile[a]

Sample	V_{oc} /V	J_{sc} /mA cm^{-2}	*FF*
1	0.70	0.39	29.40%
2	0.65	0.22	23.50%
3	0.70	0.17	22.20%
4	0.65	0.26	7.90%
5	0.65	0.15	19.40%

a. Contains 0.5 mM ferrocenium, 49.5 mM ferrocene, and 1 M $LiClO_4$

for reduction of MV^{2+} to MV^{+}. The additional experiments in this same electrolyte with GaP nanowires grown on p-type substrates also showed no photocurrent, indicating no photogenerated electrons were transferred across the GaP nanowire/electrolyte interface.

D. Discussion

The observations presented here demonstrated conclusively that the preparation of GaP nanowires by solid source sublimation using Sn nanoparticles as the VLS seeds is possible. The action of Sn as a VLS catalyst for GaP is noteworthy because Sn forms only a 'pseudo-eutectic' with dissolved GaP, i.e. the melting point of the eutectic is essentially the same as Sn.[45] Although the corresponding pseudo-binary Au-GaP phase diagram is not known, it most likely resembles the Au-GaAs diagram, where a true eutectic exists with a melting point substantially below that of pure Au.[46-47] A result of the difference between growth from a pseudo-eutectic and a eutectic should be that the concentration of GaP in Au is higher than in Sn at the same growth temperature. As a corollary, for the same temperature and GaP partial pressure, the supersaturation driving nucleation and crystal growth should be higher in the pseudo-eutectic melt as compared to the eutectic melt.

Precisely how the differences in the solvent properties of Sn and Au affect the crystal growth cannot be determined exhaustively from these results alone. However, the data are persuasive in that these two metal VLS catalysts lead to GaP nanowires with perceptible differences in crystallinity. The extent of twinning defects in the Au nanowires is consistent with previous reports of GaP nanowires from Au seeds.[48] Twinning in zinc blende binary semiconductor nanowires is common when the growth follows the <111> direction since the 60 ° rotation at the crystal growth that causes inversion has very low activation energy.[14, 49] Curiously, the electron microscopy data imply that twinning is less extensive when Sn is used. Some possible rationales for this observation are that the presence of Au at the growth front perturbs the crystal growth front more because Au has a larger atomic diameter. The Raman spectra are supportive of these points, where the possible effects from strain and metal inclusion appeared more substantial with Au-based, rather than Sn-based, GaP nanowires. An interesting future test of this premise would be to perform GaP nanowire growth with Pb, another metal that has previously been used for melt growth of macroscale GaP crystals.[27-28] Like Sn, Pb forms

only a 'pseudo-eutectic' with GaP but has a much larger atomic radius (1.54 Å),[50] making it possible to determine whether size alone impacts the tendency to form twinning defects.

A more tacit advantage with Sn VLS catalysts is the simpler removal of the metal from the as-prepared GaP nanowires. Brief immersion in strong acidic solutions readily eliminates Sn from the surface of GaP without perturbing the nanowire structure, while removal of Au could not be performed without etchants that simultaneously degraded GaP. This aspect of Sn VLS seeds has obvious benefits if the removal of metal from the nanowire surface is necessary for a given application, e.g. photoelectrochemistry. Correspondingly, the greater reactivity of Sn towards etchants is a result of its propensity to oxidize. Sn nanoparticles that possessed a substantial native oxide were less reliable for uniform GaP nanowire film deposition, requiring that Sn particles were used immediately after preparation.

With regards to the photoactivity of as-prepared GaP nanowires, the photoelectrochemical measurements highlighted some unexpected findings. However, to be clear, the overall photoelectrode efficiencies are not germane to the present analysis. There was no expectation that either (or any) type of as-prepared GaP nanowires would exhibit high photocurrents and support large photovoltages. Simply, realization of the benefits of high-aspect-ratio form factors in photoelectrode materials requires precise tuning of the dopant concentration in concert with the material size.[51-52] Such efforts were not performed here, so no substantive comment can be made on the optimal photoactivity of these GaP nanowires.

Still, the following points are evident from the photoelectrochemical measurements. First, Au-seeded GaP nanowires were nominally n-type as prepared. The signs of the photovoltage and photocurrent clearly indicated the nanowires acted as photoanodes. The activity of the nanowires specifically was confirmed by the long wavelength quantum yields, which were improved relative to planar GaP, in accord with expectations for tall, thin photoelectrode materials.[8] The specific dopant was not clear, as either substituted Au or O (from residual O_2 in the reactor) could act as a donor in GaP. Nevertheless, the level of residual n-type doping was low enough that a strong photoeffect was observable. Specifically, the large photovoltage is in line with n-type doping at the non-degenerate level. The magnitude of the photovoltage further implied that whatever impurities/traps/defects remained in the Au-seeded GaP nanowires, they did not negate the possibility of capturing photogenerated minority carriers. This aspect stands somewhat in contrast to recent reports of GaP nanowires used as photoelectrodes for fuel-forming systems,

where the materials failed to generate large photovoltages under comparable illumination.[1] Second, the Sn-based GaP nanowires were also doped but at a significantly higher level. The voltammetry response showed essentially no photoeffect. If the Sn-seeded GaP nanowires were undoped or all the available dopants were compensated to the point that there were minimal mobile charges, then the expectation would have been no photoeffect at underpotentials *and* no passage of current at any moderate overpotential. However, the data clearly showed diffusion-limited current for the oxidation of ferrocene at potentials just positive of 0 V, meaning the nanowires are in fact highly conductive. The current-potential responses measured in 1 M KCl containing MV^{2+} in Figure III.6d further implicate n^+-, rather than p-type doping, in the Sn-seeded GaP nanowires. The identical dark and light responses for the reduction of MV^{2+} on an n-type substrates are again in accord with a negligible depletion condition. The total suppression of photocurrent on a p-type substrate for the reduction of MV^{2+} in Figure III.6d, however, specifically implies the Sn-seeded GaP nanowires are n^+-doped. That is, a charge-blocking n^+-p junction forms at the base of the Sn-seeded GaP nanowires and the p-type substrate that prevents any photocurrent collection.

The reasons for higher levels of n-type doping in Sn-seeded GaP as compared to Au-seeded GaP nanowires are unclear. If the dominant dopant mechanism was from metal substitution (rather than from residual oxygen doping) into the GaP lattice, then two points follow. First, the residual doping of the nanowire is a function of the ability of the VLS catalyst metal to substitute into the GaP lattice. Since the atomic radii, r, of Sn and Ga are more comparable than either Au and Ga or Sn and P (r_{Au} = 1.74 Å, r_{Sn} = 1.40 Å, r_{Ga} = 1.25 Å, and r_P = 1.10 Å for P),[30] this premise is in accord with observations here. Second, the concentration of Sn dopants in GaP nanowires must be > 10^{20} cm^{-3} at the growth temperature to render degenerate doping. Such a high level of Sn incorporation is noticeably larger than estimates of Sn solubility in bulk GaP from melt-growth studies.[30] The reasons are not clear why but could arise from size-dependent doping (i.e. increased doping in small diameter nanowires) or the comparatively fast growth rate of the nanowires as compared to bulk crystal melt growths.

E. Conclusion

The cumulative data presented in this work supports the following three related points. First, Sn can readily act as a VLS growth catalyst for GaP nanowire deposition in the

temperature range of 350-550 °C. The data are clear that if an oxide-free interface is maintained, Sn particles facilitate the formation of GaP nanowires at elevated temperatures in the presence of sublimed GaP. Second, the physicochemical properties of GaP nanowires grown with Sn catalysts differed slightly from those grown with Au catalysts. The available electron microscopy, electron diffraction, and Raman spectroscopy all suggest that GaP crystals grow differently in Sn than Au. The net effects may be fewer twinning defects and simpler methods to removal the growth catalysts in Sn-seeded GaP nanowires. Third, the photoelectrochemical properties of as-prepared Au-seeded GaP nanowires were consistent with non-degenerate n-type doping while as-prepared Sn-seeded GaP nanowires showed evidence of degenerate n-type doping. If either type of GaP nanowire is to be utilized as a photocathode, subsequent p-type doping steps will be needed to first compensate the existing n-type donors.

F. References

1. Sun, J.; Liu, C.; Yang, P., Surfactant-Free, Large-Scale, Solution-Liquid-Solid Growth of Gallium Phosphide Nanowires and Their Use for Visible-Light-Driven Hydrogen Production from Water Reduction. *J. Am. Chem. Soc.* **2011,** *133*, 19306-19309.
2. Standing, A.; Assali, S.; Gao, L.; Verheijen, M. A.; van Dam, D.; Cui, Y.; Notten, P. H.; Haverkort, J. E.; Bakkers, E. P., Efficient Water Reduction with Gallium Phosphide Nanowires. *Nat. Comm.* **2015,** *6*, 7824.
3. Malizia, M.; Seger, B.; Chorkendorff, I.; Vesborg, P. C. K., Formation of a P–N Heterojunction on GaP Photocathodes for H_2 production Providing an Open-Circuit Voltage of 710 Mv. *J. Mater. Chem. A.* **2014,** *2* (19), 6847-6853.
4. Brown, E. S.; Peczonczyk, S. L.; Maldonado, S., Wet Chemical Functionalization of GaP(111)B through a Williamson Ether-Type Reaction. *J. Phys. Chem. C.* **2015,** *119* (3), 1338-1345.
5. Brown, E. S.; Peczonczyk, S. L.; Wang, Z.; Maldonado, S., Photoelectrochemical Properties of CH_3-Terminated P-Type GaP(111)A. *J. Phys. Chem. C.* **2014,** *118*, 11593-11600.
6. Mukherjee, J.; Peczonczyk, S. L.; Maldonado, S., Wet Chemical Functionalization of Iii-V Semiconductor Surfaces: Alkylation of Gallium Phosphide Using a Grignard Reaction Sequence. *Langmuir.* **2010,** *26* (13), 10890-10896.
7. Hu, S.; Shaner, M. R.; Beardslee, J. A.; Lichterman, M.; Brunschwig, B. S.; Lewis, N. S., Amorphous TiO_2 Coatings Stabilize Si, GaAs, and GaP Photoanodes for Efficient Water Oxidation. *Science.* **2014,** *344* (6187), 1005-1009.
8. Price, M. J.; Maldonado, S., Macroporous n-GaP in Nonaqueous Regenerative Photoelectrochemical Cells. *J. Phys. Chem. C.* **2009,** *113* (28), 11988-11994.
9. Hagedorn, K.; Collins, S. M.; Maldonado, S., Preparation and Photoelectrochemical Activity of Macroporous p-GaP(100). *J. Electrochem. Soc.* **2010,** *157* (11), D588-D592.
10. Lee, S.; Bielinski, A. R.; Fahrenkrug, E.; Dasgupta, N. P.; Maldonado, S., Macroporous p-GaP Photocathodes Prepared by Anodic Etching and Atomic Layer Deposition Doping. *ACS Appl Mater Interfaces.* **2016,** *8* (25), 16178-16185.
11. Wen, W. Synthesis and Nanoengineering of Gallium Phosphide Nanostructures for Photoelectrochemical Solar Energy Conversion. Ph.D. Thesis, University of Michigan, 2014.
12. Liu, C.; Sun, J.; Tang, J.; Yang, P., Zn-Doped p-Type Gallium Phosphide Nanowire Photocathodes from a Surfactant-Free Solution Synthesis. *Nano Lett.* **2012,** *12* (10), 5407-11.
13. Aparna, A. R.; Brahmajirao, V.; Karthikeyan, T. V., Review on Synthesis and Characterization of Gallium Phosphide. *Procedia Materials Science.* **2014,** *6*, 1650-1657.
14. Johansson, J.; Wacaser, B. A.; Dick, K. A.; Seifert, W., Growth Related Aspects of Epitaxial Nanowires. *Nanotechnology.* **2006,** *17* (11), S355-S361.
15. Messing, M. E.; Hillerich, K.; Johansson, J.; Deppert, K.; Dick, K. A., The Use of Gold for Fabrication of Nanowire Structures. *Gold Bull.* **2009,** *42* (3), 172-181.
16. Perea, D. E.; Allen, J. E.; May, S. J.; Wessels, B. W.; Seidman, D. N.; Lauhon, L. J., Three-Dimensional Nanoscale Composition Mapping of Semiconductor Nanowires. *Nano Lett.* **2006,** *6* (2), 181-185.
17. Bar-Sadan, M.; Barthel, J.; Shtrikman, H.; Houben, L., Direct Imaging of Single Au Atoms within GaAs Nanowires. *Nano Lett.* **2012,** *12* (5), 2352-2356.
18. Breuer, S.; Pfuller, C.; Flissikowski, T.; Brandt, O.; Grahn, H. T.; Geelhaar, L.; Riechert, H., Suitability of Au- and Self-Assisted GaAs Nanowires for Optoelectronic Applications. *Nano Lett.* **2011,** *11* (3), 1276-1279.

19. Tambe, M. J.; Ren, S.; Gradecak, S., Effects of Gold Diffusion on N-Type Doping of GaAs Nanowires. *Nano Lett.* **2010,** *10* (11), 4584-4589.
20. Whang, S. J.; Lee, S. J.; Yang, W. F.; Cho, B. J.; Liew, Y. F.; Kwong, D. L., Complementary Metal-Oxide-Semiconductor Compatible Al-Catalyzed Silicon Nanowires. *Electrochem. Solid-State Lett.* **2007,** *10* (6), E11-E13.
21. Oda, T.; Sugano, T., Studies on Chemically Etched Silicon, Gallium Arsenide, and Gallium Phosphide Surfaces by Auger Electron Spectroscopy. *Jpn. J. Appl. Phys.* **1976,** *15* (7), 1317-1327.
22. Dzhafarov, T. D.; Litvin, A. A.; Khudyakov, S. V., Diffusion, Solubility, and Electrotransport of Gold in Gallium Phosphide. *Sov. Phys. Solid State* **1978,** *20* (1), 152-153.
23. Holzl, J.; Schulte, F., *Work Functions of Metals, in Solid Surface Physics*. Springer-Verlag: Berlin, 1979.
24. Collins, S. M.; Hankett, J. M.; Carim, A. I.; Maldonado, S., Preparation of Photoactive $ZnGeP_2$ Nanowire Films. *J. Mater. Chem.* **2012,** *22* (14), 6613-6622.
25. Lee, S.; Fahrenkrug, E.; Maldonado, S., Synthesis of Photoactive $ZnSnP_2$ Semiconductor Nanowires. *J. Mater. Res.* **2015,** *30* (14), 2170-2178.
26. Faust, J. W.; John, H. F., The Growth of Semiconductor Crystals from Solution Using the Twin-Plane Reentrant-Edge Mechanism. *J. Phys. Chem. Solids.* **1964,** *25*, 1407-1415.
27. Luzhnaya, N. P., Growth from Metal Solutions. *J. Cryst. Growth.* **1968,** *3* (4), 97-107.
28. Rubenstein, M., *Electrochem. Soc. Abstracts.* **1962,** *11*, 129.
29. Trumbore, F. A.; Kowalchik, M.; White, H. G.; Logan, R. A.; Luke, C. L., Solid Solubility and Amphoteric Behavior of Tin in Solution Grown Gallium Phosphide. *J. Electrochem. Soc.* **1964,** *111* (6), 748-750.
30. Trumbore, F. A.; White, H. G.; Kowalchik, M.; Luke, C. L.; Nash, D. L., Solubility and Electrical Behavior of Group IV Impurities in Solution Grown Gallium Phosphide. *J. Electrochem. Soc.* **1965,** *112* (12), 1208-1211.
31. Wen, W.; Carim, A. I.; Collins, S. M.; Price, M. J.; Peczonczyk, S. L.; Maldonado, S., Structural and Photoelectrochemical Properties of GaP Nanowires Annealed in NH_3. *J. Phys. Chem. C.* **2011,** *115* (45), 22652-22661.
32. Zhang, G.; Tateno, K.; Sogawa, T.; Nakano, H., Growth and Characterization of GaP Nanowires on Si Substrate. *J. Appl. Phys.* **2008,** *103*, 014301.
33. Hobden, M. V.; Russell, J. P., The Raman Spectrum of Gallium Phosphide. *Phys. Lett. A.* **1964,** *13* (1), 39-41.
34. Gupta, R.; Xiong, Q.; Mahan, G. D.; Eklund, P. C., Surface Optical Phonons in Gallium Phosphide Nanowires. *Nano Lett.* **2003,** *3* (12), 1745-1750.
35. Hayashi, S.; Ruppin, R., Raman Scattering from GaP Microcrystals: Analysis of the Surface Phonon Peak. *J. Phys. C: Solid State Phys.* **1985,** *18*, 2583-2592.
36. Tiginyanu, I. M.; Ursaki, V. V.; Karavanskii, V. A.; Sokolov, V. N.; Raptis, Y. S.; Anastassakis, E., Surface-Related Phonon Mode in Porous GaP. *Solid State Commun.* **1996,** *97* (8), 675-678.
37. Campbell, I. H.; Fauchet, P. M., The Effects of Microcrystal Size and Shape on the One Phonon Raman Spectra of Crystalline Semiconductors. *Solid State Commun.* **1986,** *58* (10), 739-741.
38. Xiong, Q.; Gupta, R.; Adu, K. W.; Dickey, E. C.; Lian, G. D.; Tham, D.; Fischer, J. E.; Eklund, P. C., Raman Spectroscopy and Structure of Crystalline Gallium Phosphide Nanowires. *J. Nanosci. Nanotechno.* **2003,** *3* (4), 335-339.

39. Galtier, P.; Martinez, G., Bound Phonons in n-Type GaP. *Phys. Rev. B.* **1988,** *38* (15), 10542-10549.
40. Shi, W. S.; Zheng, Y. F.; Wang, N.; Lee, C. S.; Lee, S. T., Synthesis and Microstructure of Gallium Phosphide Nanowires. *J. Vac. Sci. Technol., B.* **2001,** *19*, 1115.
41. Roldan Cuenya, B.; Doi, M.; Keune, W., Epitaxial Growth and Interfacial Structure of Sn on Si(111)-(7 X 7). *Surf. Sci.* **2002,** *506*, 33-46.
42. Allen, J. E.; Hemesath, E. R.; Perea, D. E.; Lensch-Falk, J. L.; Li, Z. Y.; Yin, F.; Gass, M. H.; Wang, P.; Bleloch, A. L.; Palmer, R. E.; Lauhon, L. J., High-Resolution Detection of Au Catalyst Atoms in Si Nanowires. *Nat. Nanotechnol.* **2008,** *3* (3), 168-73.
43. Maiolo Iii, J. R.; Atwater, H. A.; Lewis, N. S., Macroporous Silicon as a Model for Silicon Wire Array Solar Cells. *J. Phys. Chem. C.* **2008,** *112*, 6194-6201.
44. Spurgeon, J. M.; Atwater, H. A.; Lewis, N. S., A Comparison between the Behavior of Nanorod Array and Planar Cd(Se, Te) Photoelectrodes. *J. Phys. Chem. C.* **2008,** *112*, 6186-6193.
45. Lee, S. H.; Green, M. A., Evaluation of Binary and Ternary Melts for the Low Temperature Liquid Phase Epitaxial Growth of Silicon. *J. Electron. Mater.* **1991,** *20* (8), 635-641.
46. Panish, M. B., Ternary Condensed Phase Systems of Gallium and Arsenic with Group Ib Elements. *J. Electrochem. Soc.* **1967,** *114* (5), 516-521.
47. Duan, X.; Lieber, C. M., General Synthesis of Compound Semiconductor Nanowires. *Adv. Mater.* **2000,** *12* (4), 298-302.
48. Johansson, J.; Karlsson, L. S.; Svensson, C. P.; Martensson, T.; Wacaser, B. A.; Deppert, K.; Samuelson, L.; Seifert, W., Structural Properties of <111>B -Oriented III-V Nanowires. *Nat. Mater.* **2006,** *5* (7), 574-80.
49. Caroff, P.; Dick, K. A.; Johansson, J.; Messing, M. E.; Deppert, K.; Samuelson, L., Controlled Polytypic and Twin-Plane Superlattices in III-V Nanowires. *Nat. Nanotechnol.* **2009,** *4* (1), 50-5.
50. Kuznetsov, G. M.; Tsurgan, L. S.; Krainyuchenko, I. A., Alloys of the Cross Sections GaP-Cd, GaP-Sn, and GaP-Pb. *Inorg. Mater.* **1976,** *12*, 976-979.
51. Foley, J. M.; Price, M. J.; Feldblyum, J. I.; Maldonado, S., Analysis of the Operation of Thin Nanowire Photoelectrodes for Solar Energy Conversion. *Energy Environ. Sci.* **2012,** *5* (1), 5203-5220.
52. Hagedorn, K.; Forgacs, C.; Collins, S. M.; Maldonado, S., Design Consideration for Nanowire Heterojunctions in Solar Energy Conversion/Storage Applications. *J. Phys. Chem. C.* **2010,** *114*, 12010-12017.

CHAPTER IV

Synthesis of Photoactive $ZnSnP_2$ Semiconductor Nanowires

A. Introduction

This chapter details the preparation of single-phase crystalline $ZnSnP_2$ nanowires *via* simple chemical-vapor-deposition (CVD) method using powdered Zn and SnP_3 as the precursors in a custom-built tube furnace reactor that is different than that of Chapter III. The sublimed precursors were allowed to react with thermally evaporated Sn nanoparticles to yield $ZnSnP_2$ nanowire films over areas of 40 mm^2. The cumulative observations suggest that the Sn nanoparticles served both as the growth seed and main contributor of Sn. For optimal growth conditions, surface and bulk elemental analyses showed homogenous elemental distribution of Zn, Sn, and P, with chemical composition close to 1:1:2 stoichiometry. Crystallographic data indicated that the as-prepared $ZnSnP_2$ nanowires possessed a sphalerite crystal structure, as opposed to the antisite defect-free chalcopyrite structure. Photoelectrochemical measurements in aqueous electrolyte showed the as-prepared $ZnSnP_2$ nanowires capable of sustaining stable cathodic photoresponse under white light illumination. Overall, this chapter presents a benign and straightforward approach to prepare single-phase Zn-based phosphide nanowires suitable for energy conversion applications.

Both the fields of photovoltaic and photoelectrochemistry have sought to exploit nanostructured, high aspect ratio forms of GaAs, GaP, and InP as efficient photoelectrode platforms.[1-4] These classic III-V materials can exhibit excellent optoelectronic properties (i.e. optimal bandgaps, high charge-carrier mobilities, ability to be doped precisely) that are critical for efficient charge generation and separation. However, the prospects for constructing photoelectrochemical technologies at a globally relevant scale based solely on these materials are complicated by the relative scarcity and high cost of Ga and In.[5] Accordingly, there is a pressing need and opportunity for materials with similarly favorable properties but which are composed of only earth abundant elements.[5-6]

Ternary II-IV-V_2 chalcopyrite semiconductors are one class of semiconductors that are

potentially ideal for photoelectrochemical technologies. Specifically, zinc-based phosphides (Zn-*IV*-P_2; *IV*= Ge, Sn or Si) have been identified as analogues and low-cost alternatives to the aforementioned class of III-V semiconductors.[7-9] These semiconductors both are comprised of naturally abundant elements and are isoelectronic with the III-V semiconductors. Moreover, the respective band structures are remarkably similar, resulting in nearly identical bandgap energies and the possibility of high charge carrier mobilities.[10-11]

In this chapter we focus on $ZnSnP_2$. $ZnSnP_2$ is isoelectronic with InP and can exhibit either chalcopyrite or sphalerite crystal structure (Figure IV.1). For $ZnSnP_2$, the optoelectronic bandgap energy is a function of the crystalline phase. The chalcopyrite phase of $ZnSnP_2$ has a bandgap of 1.68-1.75 eV and the sphalerite phase of $ZnSnP_2$ has a smaller bandgap energy between 1.22-1.38 eV.[14] In either phase, $ZnSnP_2$ natively exhibits p-type conductivity with the capacity for good majority carrier mobilities (10-70 $cm^2\ V^{-1}\ s^{-1}$),[11-12] thus rendering $ZnSnP_2$ amenable for solar energy capture/conversion.[13-15]

To date, the preparation of single-phase $ZnSnP_2$ crystals has proven challenging. Based on the pseudo-binary Sn-ZnP_2 phase diagram, $ZnSnP_2$ melts incongruently and forms peritectically.[11, 16] Thus far, $ZnSnP_2$ bulk crystals have been synthesized from melts,[12, 16-18] vapor phase deposition,[19-21] and organometallic synthesis.[22] The occurrence of impurity phases such as Sn_3P_2, Sn_4P_3 and Zn_3P_2 in as-prepared $ZnSnP_2$ has stymied practical interest.

$ZnSnP_2$ has never been prepared with high aspect ratio form factors, e.g. nanowires. The objective of this chapter is to demonstrate the possibility of preparing pure-phase $ZnSnP_2$ in *nanostructured* form. We demonstrate a benign, simple chemical-vapor-deposition (CVD) method that does not involve the use of metallorganic or toxic gaseous precursors (e.g. PH_3). Instead, we used powdered Zn and SnP_3 as the sublimation sources for the growth of $ZnSnP_2$ nanowires via a vapor-liquid-solid (VLS) mechanism through the action of Sn nanoparticle catalysts. Raman scattering, powder X-ray diffraction patterns (XRD) and high-resolution transmission electron microscopy (HR-TEM) are presented to illustrate the purity and crystallinity of the materials prepared by the employed approach. Preliminary photoelectrochemical measurements are also shown that speak to the conductivity type of the as-prepared materials.

B. Experimental Section

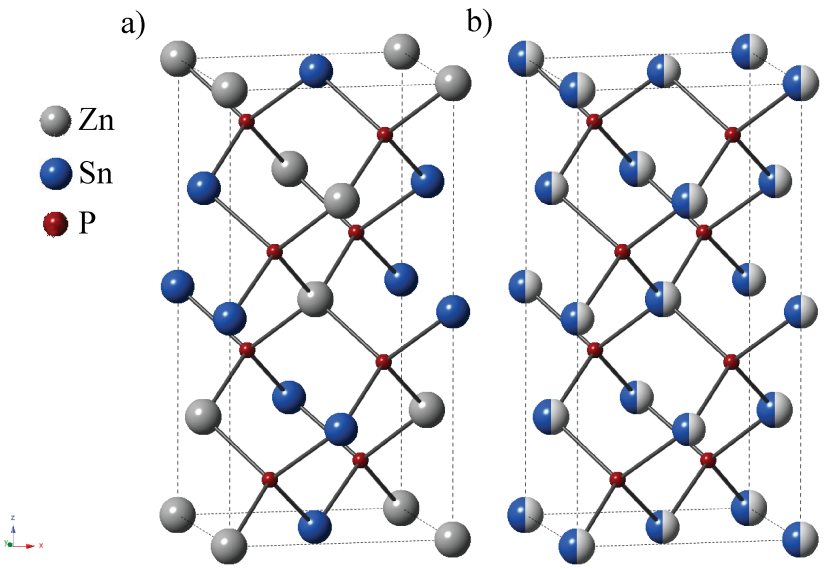

Figure IV.1. $ZnSnP_2$ unit cell with either (a) cation-ordered chalcopyrite crystal structure or (b) cation-disordered sphalerite crystal structure. Note for (b), the Zn and Sn atoms have 0.5 probability of occupying the cation sites, and the resulting unit cell is cubic $Zn_{0.5}Sn_{0.5}P$, i.e. two unit cells are shown in (b).

i. Nanowire Growth Setup

$ZnSnP_2$ nanowires were prepared in custom-built quartz tube in a single-zone furnace (MTI Corporation, GSL-1100X-S) as illustrated in Figure IV.2. Zn powder (J. T. Baker, 98.0%) and SnP_3 powder (prepared by high-energy ball milling Sn powder (Strem, 99.5%) and red P (Alfa Aesar, 99.999%) in inert environment in a Spex 8000 laboratory shaker mill for 4 h) were used as the precursors for Zn and P, respectively in the growth process. Zn and SnP_3 powders in stoichiometric ratio were loaded into a customized quartz precursor holder (21 mm diameter x 250 mm in length) with a piece of iron enclosed on the other end for a contactless introduction of precursor powders with a magnetic sliding mechanism. When the holder was loaded with the powders, it was placed in a long quartz tube (25 mm diameter x 825 mm in length) that had two growth substrates (total area: 40 mm^2) placed on the sealed end. Initially, the holder was left outside of the furnace to prevent premature sublimation of precursor powders. The assembly was then evacuated with a mechanical pump to <100 mTorr. Under static vacuum, the furnace was heated to 600 ºC and the temperature was maintained for 30 min to allow the substrate temperature to reach 400-440 ºC. While still heating at 600 ºC, the holder was introduced into the furnace and the powders were allowed to sublime in the center of the furnace. The temperature was maintained throughout the duration of the nanowire growth. At the end of the growth, the assembly was again actively pumped down to remove any unreacted precursor vapors prior to cooling the furnace radiatively to room temperature.

B-doped Si(111) wafers (MTI Corporation) decorated with Sn islands were used as the substrate for the nanowire growth. The Si wafers were etched in hydrofluoric acid (Transene, 49% by wt.) for 30 s, rinsed in distilled water (>18 MΩcm, Barnstead Nanopure III purifier) and dried under N_2 gas prior to transferring into a thermal evaporator chamber for Sn evaporation. The metal evaporation chamber was pumped to $6x10^{-6}$ Torr, and a layer of Sn islands (Kurt J. Lesker, 99.99%) was evaporated onto the substrate for thicknesses of approximately 5 nm, 20 nm, and 30 nm, as measured by atomic force microscopy. All Sn-coated substrates were used immediately. After nanowire growth, unreacted Sn was removed by placing the substrate in 0.1 M HCl for 10 min, rinsing with distilled water (>18 MΩcm, Barnstead Nanopure III purifier) and drying under N_2 gas.

ii. Materials Characterization

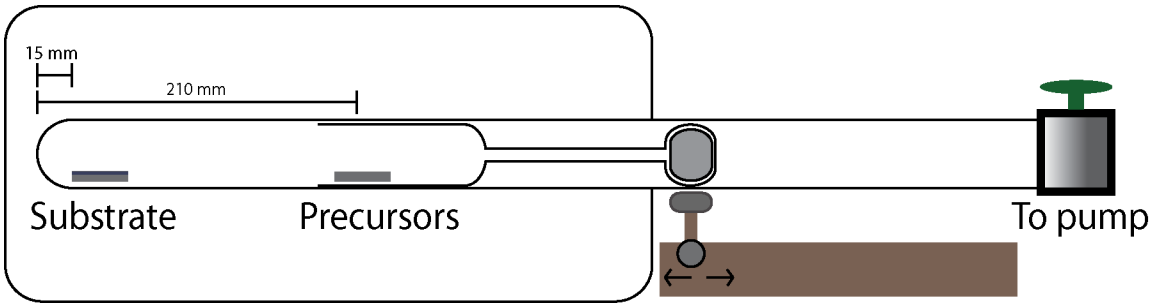

Figure IV.2. Schematic depiction (not to scale) of the single-zone tube furnace setup used for $ZnSnP_2$ nanowire growth.

Raman spectra of the nanowire films were acquired using Renishaw RM series spectrometer equipped with Leica microscope, a Nikon LU Plan 20x objective (numerical aperture = 0.4), edge filters to reject the excitation line, and a CCD detector (578 x 400) in a 180º backscatter geometry. The excitation source was a 785 nm diode laser. Powder X-ray diffraction patterns of the nanowire films were obtained with Bruker D8 Advance diffractometer equipped with Cu-Kα source. The lattice constant, a, of the nanowires was obtained using Pawley refinement conducted in Materials Studio, and the reflections were assigned with simulated diffraction data of ICSD #77804.[23]

Cross-sectional scanning electron micrographs of as-prepared nanowires were taken with Philips XL30 equipped with a zirconated tungsten Schottky-type field emitter operating at 10.0 kV. High-resolution transmission electron microscopy (HR-TEM) imaging and selected-area electron diffraction (SAED) were performed in JEOL 3011 TEM equipped with LaB_6 electron source operating at 300 kV. The samples for TEM investigation were prepared by scraping off the nanowires off the substrate with a sharp razor blade into 0.5 mL methanol (190 proof, ACS spectrophotometric grade, Aldrich) to create a homogenous suspension. The suspension was sonicated for 3 s to disperse the nanowires, then drop-casted onto a copper supported TEM grid with holey carbon film (Ted Pella). Elemental analysis of the nanowires was performed in a JEOL 2010F AEM, which was equipped with an EDAX energy dispersive spectroscopy (EDS). The data were obtained in scanning TEM mode (STEM) with a zirconated tungsten field emitter operated at 200 kV and probe size of 1.0 nm. The EDS signals were corrected with respective sensitivity factors for quantification according to Cliff-Lorimer method. Surface chemical composition of the nanowire was acquired with a Physical Electronics Scanning Auger Nanoprobe 680 equipped with a field emission source. The samples were sputtered with a PHI model 06-350E Ar^+ source to remove C and oxide layers on the surface of the nanowires prior to performing quantitative analyses.

The optical bandgap of the as-prepared materials were determined from reflectance data. Specifically, diffuse reflectance spectra were collected with a Varian Carey 5000 spectrophotometer equipped with an integrating sphere. Polytetrafluoroethylene (PTFE) was used as a reflectance standard in the visible portion of the spectrum.

iii. Photoelectrochemical Measurements

$ZnSnP_2$ nanowire film photoelectrodes were prepared on degenerately doped p-Si(111) substrates (0.001-0.005 Ωcm). Ohmic contact to the nanowire films was made by scratching the back of the Si substrate, etching in 5% hydrofluoric acid, and coating the exposed area with a thin layer of In-Ga eutectic. The substrate was then mounted onto a copper wire coil and secured with silver paint (GC Electronics). The photoelectrode was sealed with 1C Hysol epoxy (Loctite) and cured for 24 h at room temperature before using it for photoelectrochemical measurements. The measurements were conducted in an optically flat bottom quartz three-electrode electrochemical cell with a Pt mesh counter electrode (~0.1 cm^2) and a Ag/AgCl (in saturated KCl) reference electrode. The electrolyte consisted of 20 mM methyl viologen in 1.0 M KCl(aq). The illumination source was a tungsten halogen lamp (ELH, Osram) calibrated using a thermopile (S302A, Thorlabs) for an incident power density of 100 mW cm^{-2}. All measurements were performed with a CHI760 workstation (CH Instruments).

C. Results

Figure IV.3a presents a cross-sectional scanning electron micrograph of a $ZnSnP_2$ nanowire film grown using 20 nm Sn nanoparticles film over 1 h in the setup described above. The nanowire films appeared dull dark-gray with a uniform density over the substrate area (Figure IV.4). The optimal temperature for the growth substrate was determined to be between 400 ºC and 440 ºC, slightly higher than previously reported for vapor phase synthesis of bulk $ZnSnP_2$[19, 21] but still lower than the temperature reported for $ZnSnP_2$ by melt growth.[12, 16-18] For temperatures above 440 ºC, no nanowire was observed on the substrate. When the substrate temperature was below 400 ºC, nanowires were still deposited but these materials were not $ZnSnP_2$. Instead, the composition was exclusively Zn_3P_2.

Figure IV.3b shows the Raman spectrum of as-deposited nanowire films collected with a 785 nm laser. Raman signals spanning 275 cm^{-1} to 375 cm^{-1} were observed. The dominant band in the Raman spectra was at 354 cm^{-1}, assigned to the longitudinal optical (LO) phonon mode of $ZnSnP_2$.[24-27] The position of this band suggested a crystal structure with some cation disordering, i.e. argued against the chalcopyrite form of $ZnSnP_2$.[24] Two other bands could be discerned at 295 cm^{-1} and 329 cm^{-1}, both similarly consistent with phosphorus-based modes normally seen for sphalerite (but not chalcopyrite) $ZnSnP_2$.[24] Within the optimal temperature range for synthesis, no modes at 220 cm^{-1}, 289 cm^{-1}, and 347 cm^{-1} suggestive of Zn_3P_2,[28-29] were observed.

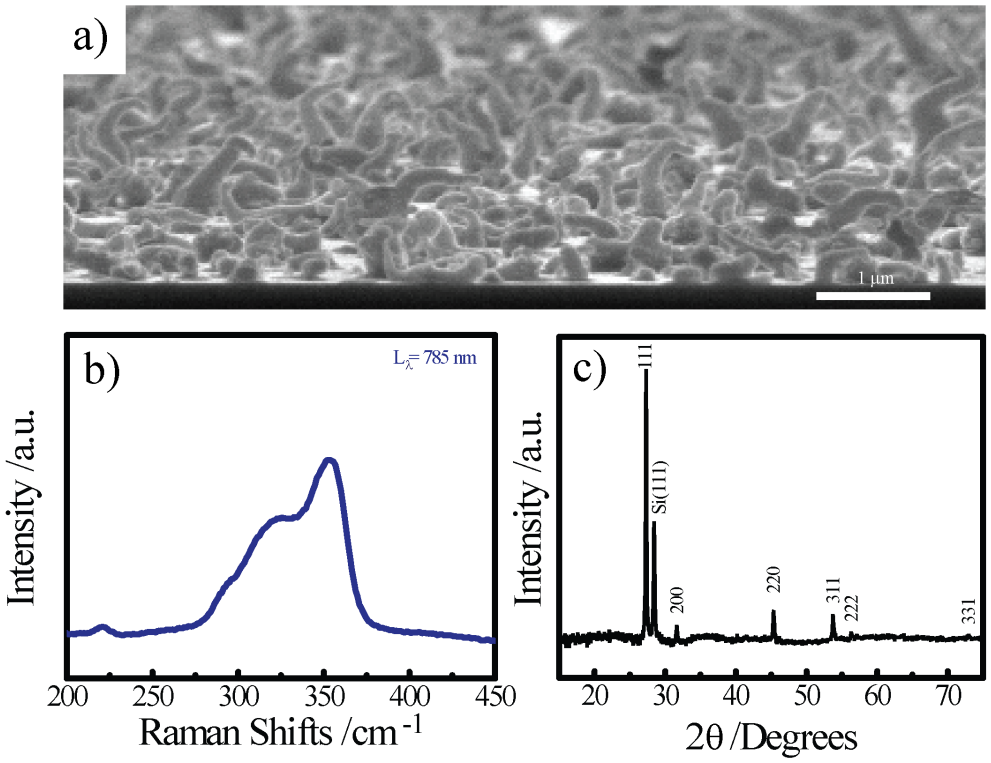

Figure IV.3. a) Cross-sectional scanning electron micrograph of a $ZnSnP_2$ nanowire film grown on 20 nm Sn islands for 1 h. b) The corresponding Raman spectrum collected with 785 nm excitation source. (c) The powder X-ray diffractogram collected for the same nanowire film.

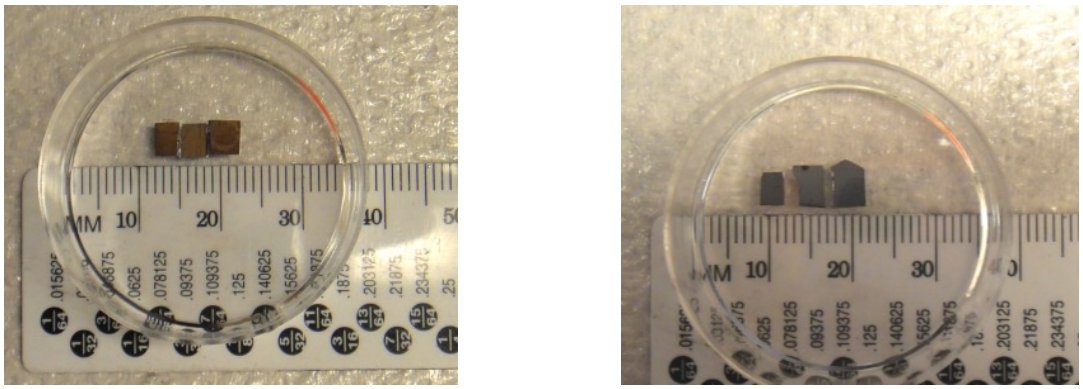

Figure IV.4. (Left) $ZnSnP_2$ nanowire films on Si substrates after 1 h growth. (Right) Appearance of growth substrates synthesized under conditions that produced predominantly Zn_3P_2 nanowires.

Raman analyses were not sufficient to detect all possible impurity species. Crystalline tin phosphides have no reported strong Raman active modes. Nevertheless, the XRD patterns for many crystalline tin phosphides are known.[30]Accordingly, XRD was used to examine both the crystallinity of the as-prepared $ZnSnP_2$ nanowires as well as the purity. Figure IV.3c presents a representative XRD pattern of the as-prepared $ZnSnP_2$ nanowire films. All reflections indexed to $ZnSnP_2$ but in the cubic sphalerite phase,[13, 21] consistent with the Raman data. A lattice constant of 5.649 ± 0.0019 Å was measured from the X-ray data, in agreement with the reported value for bulk $ZnSnP_2$.[11] No signatures for trigonal SnP_3, cubic SnP, or tetragonal Zn_3P_2 were observed.

The fundamental reflections of the ordered chalcopyrite and disordered sphalerite $ZnSnP_2$ are the same because such crystal does not exhibit tetragonal distortion, that is, c = 2a. [11] The level of ordering in $ZnSnP_2$ can be determined from natural atomic superlattice reflections due to formation of $(ZnP)_2(SnP)_2$ superlattice in the [201] direction.[21] If the $ZnSnP_2$ were chalcopyrite, a weak (101) reflection at $2\theta = 17.5^{\circ}$ would be observed in powder XRD. For the nanowire films prepared here we did not observe a signal consistent with the (101) reflection. Nevertheless, since it may be possible that a small level of chalcopyrite phases exists but does not generate a (101) reflection that rises above the detection level. The intensity of the superlattice reflections decreases when the chalcopyrite to sphalerite volume ratio decreases. [13, 21, 31] Hence, we cannot determine that there is absolutely no chalcopyrite phases present in our sample but are confident that our samples are (at least) overwhelmingly predominantly sphalerite.

Transmission electron microscopy (TEM) was performed to examine the local composition and crystallinity of as-prepared $ZnSnP_2$ nanowires. Figure IV.5a shows the bright-field TEM image of a representative nanowire grown from 20 nm Sn islands film for 30 min. The as-prepared $ZnSnP_2$ nanowires were tapered, with the base diameter consistently larger than the diameter of the nanowire tip. This morphology was consistent with the premise that the Sn nanoparticle facilitated the crystal growth of $ZnSnP_2$ but was incorporated into the nanowire during growth,[32] i.e. the Sn particles were both a crystal growing medium and a source for Sn^0. This notion was separately validated with growth experiments performed for longer times. Even within the optimal temperature range, the major product switched to Zn_3P_2 at sufficiently long times, implying the Sn supply was exhausted. The specific time necessary to deplete Sn and switch the major product to Zn_3P_2 was a function of Sn nanoparticle size (Figure IV.6, Raman phonon assignments in Table IV.1). The corresponding selected-area electron diffraction pattern

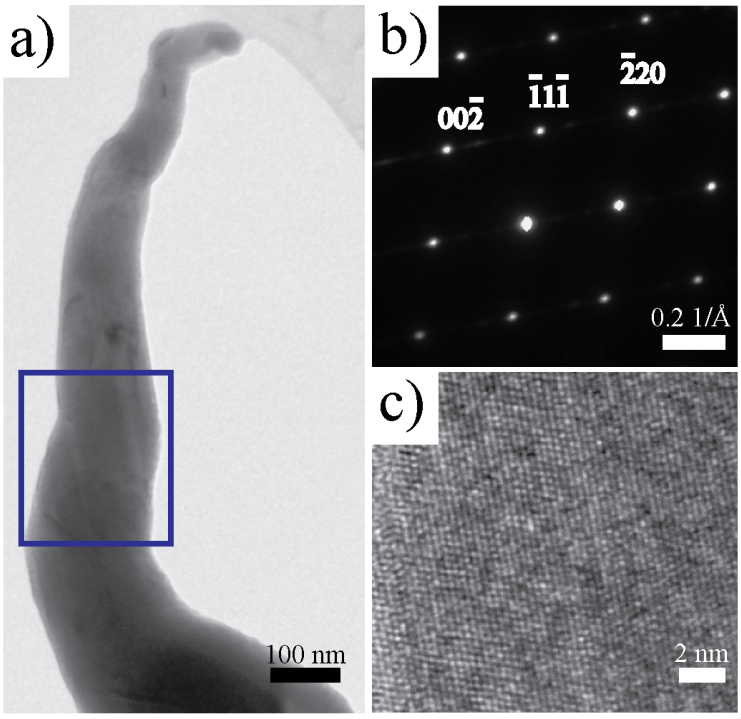

Figure IV.5. Bright-field diffraction-contrast transmission electron micrograph and (b) the selected-area electron diffraction pattern collected from the highlighted area of an isolated $ZnSnP_2$ nanowire. (c) Phase-contrast image showing lattice fringes.

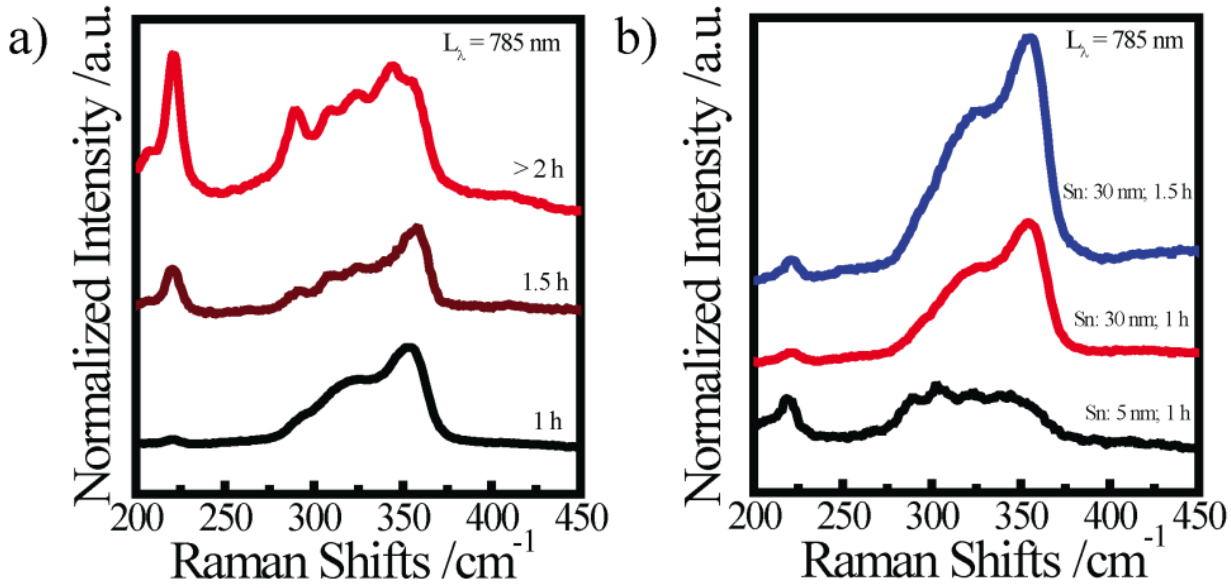

Figure IV.6. (a) Raman spectra of nanowire films grown on 20 nm Sn islands for various duration. The presented data were collected after 1 h (black), 1.5 h (maroon), and > 2 h (red) of growth, respectively. (b) Raman spectra of nanowire films grown on 5 nm (black) and 30 nm (red and blue) Sn islands for 1 h to 1.5 h. Excitation source: 785 nm.

Table IV.1. Observed active Raman scattering of as-grown nanowire films

	Peak Position /cm^{-1}	
Assignment	Nanowire Films	Bulk Single Crystal
Zn_3P_2 (A_1)	220	224
Zn_3P_2 (B_1)	289	290
Zn_3P_2 (B_1)	347	345-347
Assignment	Nanowire Films	Bulk Single Crystal
$ZnSnP_2$ (A_2)	295[a]	292-295
$ZnSnP_2$ (A_1)	313	304-309
$ZnSnP_2$ (A_2)	329[a]	330-333
$ZnSnP_2$ (B_1)	-	346-353
$ZnSnP_2$ (B_2 LO)	354	356-365

a indicates cation disorder-activated Raman scattering

in Figure IV.5b was indexed to $ZnSnP_2$ at [110] zone axis and suggested the nanowire was single-crystalline. The long axis of the nanowires was along the <111> direction. Figure IV.5c presents the phase-contrast image of the nanowire showing continuous well-defined lattice fringes, corresponding to $ZnSnP_2$ crystal. Since $ZnSnP_2$ does not exhibit tetragonal distortion, the d-spacing values in the selected-area electron diffraction patterns on [110] zone axis are the same for chalcopyrite and sphalerite structures. The only difference between the two is the intensity of the diffraction beam, but dynamical effects at the Bragg angle complicate the differentiation between the two phases along the nanowire axis. The absence of the (101) reflection in XRD as well as the broadening of the LO phonon mode in the Raman spectrum substantiated the fact that the as-prepared $ZnSnP_2$ nanowires were sphalerite.

The composition of $ZnSnP_2$ nanowires was assessed using EDS in STEM mode. As presented in Figure IV.7, the normalized intensities for Zn Kα, Sn Lα, and P Kα signals were 1:2 cation to anions ratio expected for crystalline $ZnSnP_2$ along both the long and short axes. Separate compositional analyses of the nanowires were performed with Auger Nanoprobe Spectroscopy (Figure IV.8). An average nanowire composition of 25.7 at% Zn, 27.5 at% Sn and 46.8 at% P was observed. The high angle annular dark field (HAADF) image of the nanowire showed no apparent contrast, implying Zn and Sn were dispersed uniformly throughout the length of the nanowire. Separate elemental mapping (Figure IV.9) was also performed to confirm directly the homogeneity of the metals.

To determine the band gap of as-prepared $ZnSnP_2$ nanowires, wavelength-dependent diffuse reflectance were collected and converted to absorption profiles using the Kubelka-Munk function (Eq. IV.1). In Figure IV.10, the onset of light absorption is plotted using the Tauc relation (Eq. IV.2) for direct allowed transition. The data in Figure IV.8 are consistent with an optoelectronic bandgap of approximately 1.51 eV. This value is less than 1.68 eV, the expected bandgap for $ZnSnP_2$ with no disorder in the cation distribution, i.e. the chalcopyrite, and is instead in line with the sphalerite form of $ZnSnP_2$.[11, 14-15]

$$F(R) = \frac{(1-R)^2}{2R} = \frac{\alpha}{s} \qquad \text{(IV.1)}$$

$$\left(h\nu F(R)\right)^2 = A(h\nu - E_g) \qquad \text{(IV.2)}$$

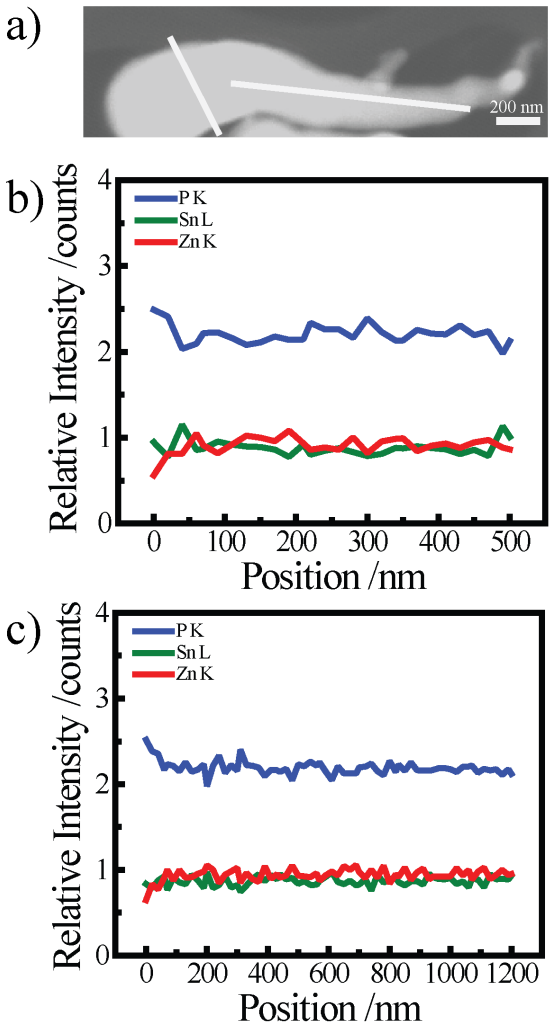

Figure IV.7. Elemental distribution of a representative $ZnSnP_2$ nanowire. a) HAADF image of the nanowire taken in STEM mode. b) Radial and c) axial EDS line scans depicting the relative amounts of Zn, Sn, and P.

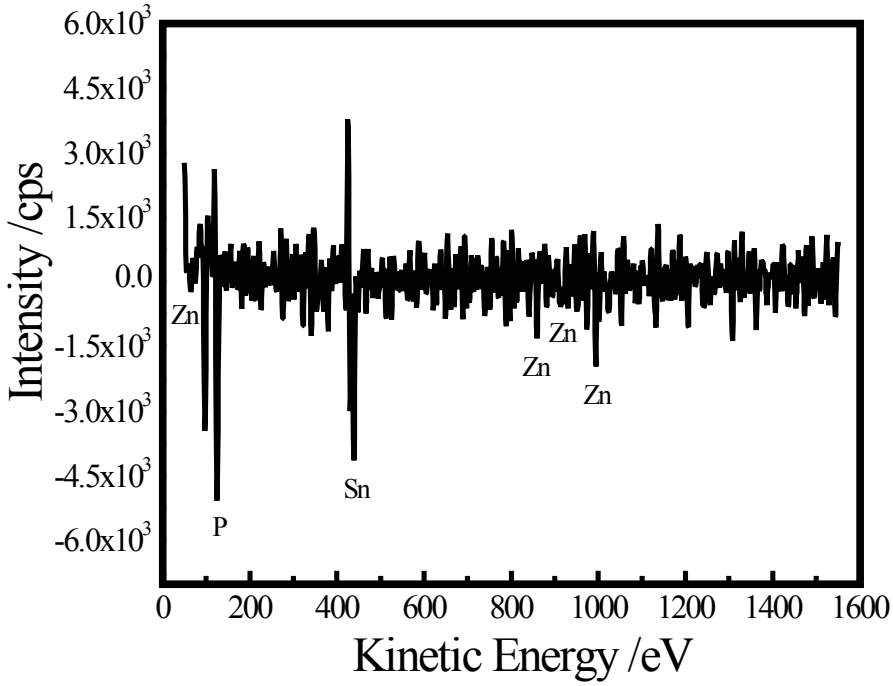

Figure IV.8. Differentiated Auger spectrum collected from representative $ZnSnP_2$ nanowires sample prepared from 20 nm Sn islands for 30 min.

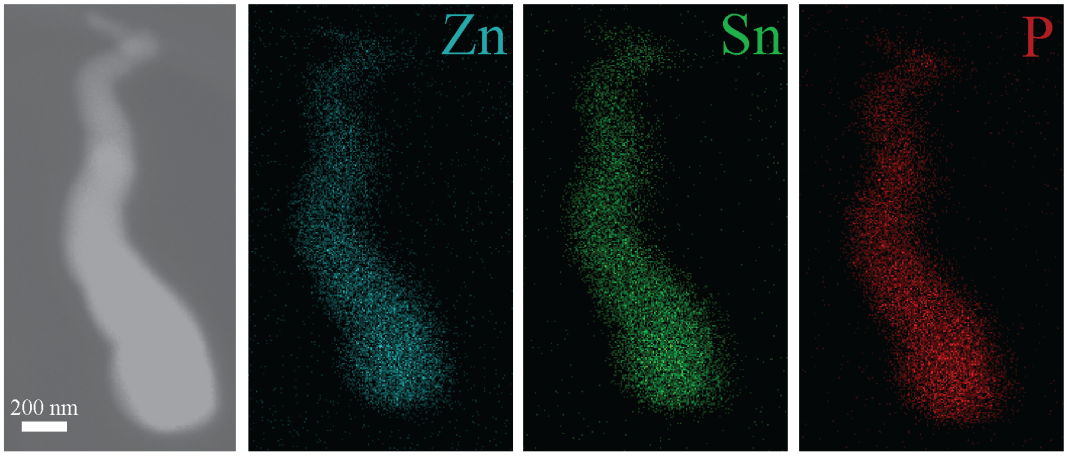

Figure IV.9. The distribution of Zn, Sn and P in these $ZnSnP_2$ nanowires (different nanowire within the sample) is homogenous throughout the length of the nanowire as shown in EDS mapping.

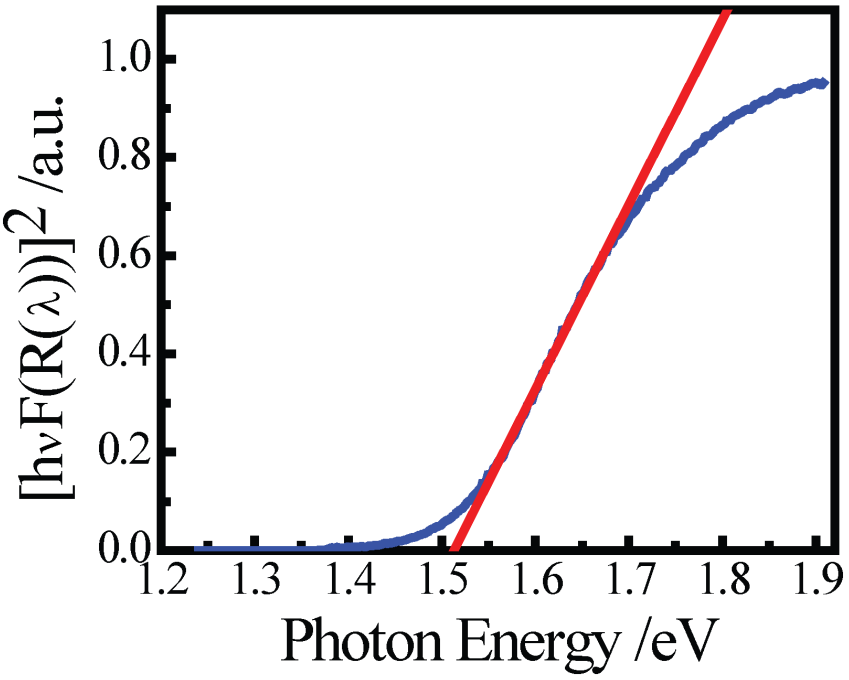

Figure IV.10. Optical properties of $ZnSnP_2$ nanowires films plotted using Tauc equation. The direct bandgap energy was determined to be 1.51 eV.

Preliminary photoelectrochemical experiments were performed to gauge the conductivity type of the as-prepared nanowire films. Figure IV.11 presents the photoelectrochemical response for the as-prepared $ZnSnP_2$ nanowire films measured in 20 mM methyl violgen (MV) and 1 M KCl electrolyte. This electrolyte was chosen for simplicity (since current should pass irrespective to the electrocatalytic activity of the native surface of $ZnSnP_2$ in water) and to facilitate the observation of any photo effect. Specifically, the standard potential of the $MV^{2+/+}$ couple is sufficiently negative (-0.65 V vs Ag/AgCl at T = 25 °C) that it will induce a strong photocathodic response from a p-type phosphide.[33] Conversely, if the materials are natively n-type, this same couple will induce no discernible photo effect and the light/dark responses should match each point for point. Figure IV.11a shows the voltammetric response of the nanowire films both in the absence and presence of illumination from an ELH lamp at 100 mW cm^{-2}. The nanowire films exhibited cathodic behavior when illuminated, i.e. a shift in the open-circuit rest potential to more positive values and an increased cathodic current density at very negative applied potentials, i.e. < -0.4 V vs. Ag/AgCl. This p-type behavior is consistent with the intrinsic p-type behavior previously ascribed to bulk Zn-IV-P_2 crystals.[12, 19, 34] The profile for the photocurrent density-potential relation indicated an extremely low overall photoelectrode energy conversion efficiency. Still, the chopped photocurrent response of the $ZnSnP_2$ nanowire film in Figure IV.11b collected at applied bias of -0.4 V vs. Ag/AgCl highlights the stability of the cathodic photoresponse.

D. Discussion

The data show the preparation of crystalline, phase-pure $ZnSnP_2$ nanowires using Sn nanoparticles as VLS catalysts is possible. The salient features of the presented method is that the growth of $ZnSnP_2$ nanowires did not require any organometallic precursors, $PH_3(g)$, or transition metal particles. Rather, solid powder sources of Zn, P, and Sn were used, enabling VLS governed by two chemical reactions. The chemical equation for the in-situ generation of P_2 and the generation of $ZnSnP_2$ can be written as Eqs IV.3 and IV.4.

$$2SnP_3(s) \xrightarrow{\Delta} 2Sn(l) + 3P_2(g) \qquad \text{(IV.3)}$$

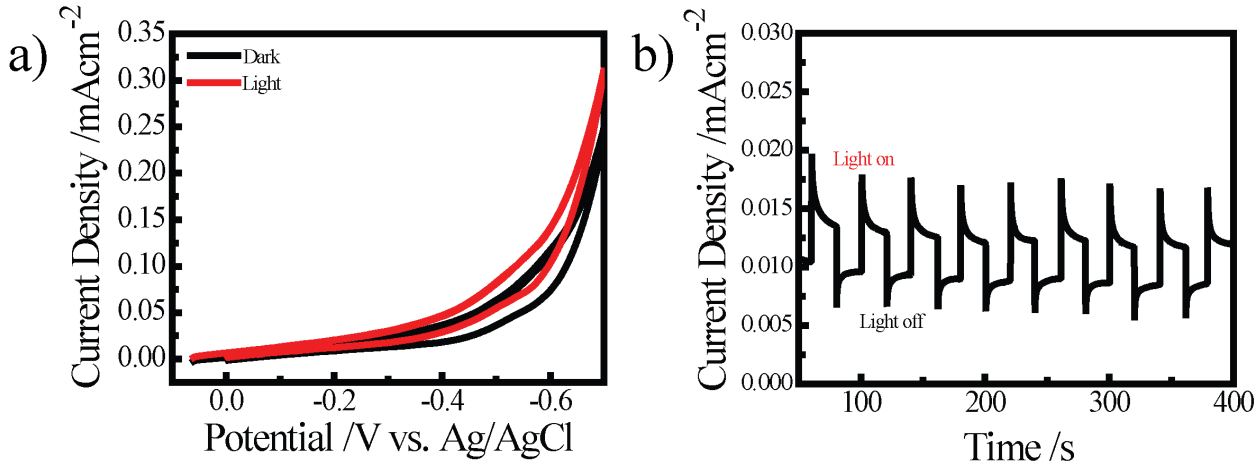

Figure IV.11. a) Current density vs. potential response of as-prepared $ZnSnP_2$ nanowire films in the dark (black) as well as under white light illumination (red). b) Chopped photoresponse of nanowire films when a bias of -0.4 V vs. Ag/AgCl was applied. The nanowires showed cathodic behavior when tested in 20 mM methylviologen and 1 M KCl.

$$Zn(g) + P_2(g) + Sn(l) \rightarrow ZnSnP_2 \qquad \text{(IV.4)}$$

The as-prepared nanowires $ZnSnP_2$ were fully crystalline. The available Raman spectroscopy, X-ray, and electron diffraction studies clearly support this point. However, the crystalline type was not chalcopyrite. Rather, the cumulative data indicated the materials prepared here possessed randomized intermixing of the Zn and Sn atoms at the cation sites, i.e. the sphalerite phase. The smaller bandgap measured here supports this fact. The growth rate of the nanowires was ~1.5-2 μm h^{-1}. This 'fast' crystal growth rate, relative to the growth of bulk crystals over the course of several days, likely promotes disorder in the position of metal cations.[13, 16] The latter aspect is in line with our previous report where Sn catalysts were also used to grow $ZnGeP_2$ nanowires.[7] In that work, although Sn from the growth catalyst was excluded from the as-prepared $ZnGeP_2$ nanowires, the available data similarly suggested that the material had a high degree of cation disorder. Accordingly, we tentatively assign the comparatively low temperatures (relative to those used to grow bulk chalcopyrite $ZnSnP_2$ crystals) and fast crystal growth rate as the most likely factors that favor the formation of the sphalerite phase.

A significant challenge in the deposition of $ZnSnP_2$ nanowires is the unintentional formation of Zn_3P_2 crystals. Zn_3P_2 has high tendency to nucleate on a Zn-rich surface in the presence of active P-containing ambients.[35-37] For this system, Zn_3P_2 was the predominant material deposited if the substrate was not heated at or above 400 ºC. Above 400 ºC, Zn and P apparently adsorb and dissolve into molten Sn nanoparticles to form $ZnSnP_2$. Since the Sn growth catalysts are consumed at the end of the $ZnSnP_2$ nanowire formation, the tip could become sufficiently Zn-rich to nucleate Zn_3P_2 from persistent P_2(g) as the reactor cooled. Although this possibility could be intentionally exploited to make particular heterojunction contacts, we found that to avoid it the reactor had to remain under strong vacuum while cooling. When this was done, the nanowires were consistently pure $ZnSnP_2$.

The observed photoelectrochemical behavior suggested a p-type doping [12, 19, 34] likely arising from Zn vacancies that gave rise to acceptor-type energy levels in $ZnSnP_2$. [15, 38] However, the level of photoactivity in the as-prepared $ZnSnP_2$ nanowires was poor. Specifically, the photovoltage and photocurrent densities observed for the films under these illumination conditions were far less than the values expected for a strongly depleted p-type semiconductor

with a bandgap of 1.68 eV immersed in such an electrolyte.[39] Still, such poor photoresponses for un-optimized materials are neither uncommon nor unexpected. For high aspect ratio semiconductor photoelectrodes, the morphological and electrical properties must be carefully tuned in concert. No attempts were made here to induce a specific level of doping. Rather, the results from these studies is that 'pure' undoped $ZnSnP_2$ is likely not attainable by this preparation method. Likely, a vanishingly small number of sub-stoichiometric defects (which can act as electrically active dopants) [34, 38] are unavoidable. Still, to make these nanowire films operate with high external quantum yields for solar energy conversion, rigorous control over the inclusion of additional dopants is necessary since the dopant level directly controls the Debye length in a non-degenerately doped semiconductor. If these nanowires are not doped enough, then the radii of these nanowires will be too small to support the full potential drop necessary for strong depletion. As we have determined previously,[40] deficiencies in the doping condition of semiconductor nanowires negates any other favorable optoelectronic property and renders them useless for solar energy conversion. Still, the studies here do indicate an important aspect relevant to solar water splitting applications. The p-type $ZnSnP_2$ nanowire materials naturally exhibit sufficient chemical and cathodic stability under illumination to permit continued study of their properties for aqueous photoelectrochemistry. Using lattice matching semiconductors such as GaAs and Ge for the growth substrates should be helpful in this regard.

E. Conclusion

We demonstrated a simple two-zone sublimation approach amenable for the growth and deposition of single-phase crystalline $ZnSnP_2$ nanowires using Zn, SnP_3, and molten Sn, with SnP_3 as the source of gaseous phosphorous and Sn nanoparticles/nanodroplets as the source of Sn in the crystalline lattice. The utility of two separate heating zones in the reactor is to separately heat the substrate and source materials to temperatures that promote the formation of $ZnSnP_2$ over Zn_3P_2 or any other impurity material. The cumulative Raman, X-ray, and microscopic structural characterizations showed crystalline $ZnSnP_2$ nanowires with the sphalerite lattice type. This preparation route yielded photoactive $ZnSnP_2$ nanowire films with native p-type character. These studies add to the available types of phosphides that can be explored as nanostructured light harvesting elements in photoelectrochemical or photovoltaic applications.

F. References

1. Hu, S.; Chi, C.-Y.; Fountaine, K. T.; Yao, M.; Atwater, H. A.; Dapkus, P. D.; Lewis, N. S.; Zhou, C., Optical, Electrical, and Solar Energy-Conversion Properties of Gallium Arsenide Nanowire-Array Photoanodes. *Energy Environ. Sci.* **2013,** *6* (6), 1879.
2. Sun, J.; Liu, C.; Yang, P., Surfactant-Free, Large-Scale, Solution-Liquid-Solid Growth of Gallium Phosphide Nanowires and Their Use for Visible-Light-Driven Hydrogen Production from Water Reduction. *J. Am. Chem. Soc.* **2011,** *133*, 19306-19309.
3. Price, M. J.; Maldonado, S., Macroporous n-GaP in Nonaqueous Regenerative Photoelectrochemical Cells. *J. Phys. Chem. C.* **2009,** *113* (28), 11988-11994.
4. Wallentin, J.; Anttu, N.; Asoli, D.; Huffman, M.; Aberg, I.; Magnusson, M. H.; Siefer, G.; Fuss-Kailuweit, P.; Dimroth, F.; Witzigmann, B.; Xu, H. Q.; Samuelson, L.; Deppert, K.; Borgstrom, M. T., InP Nanowire Array Solar Cells Achieving 13.8% Efficiency by Exceeding the Ray Optics Limit. *Science.* **2013,** *339* (6123), 1057-1060.
5. Woodhouse, M.; Goodrich, A.; Margolis, R.; James, T. L.; Lokanc, M.; Eggert, R., Supply-Chain Dynamics of Tellurium, Indium, and Gallium within the Context of PV Manufacturing Costs. *IEEE J. Photovolt.* **2013,** *3* (2), 833-837.
6. Lewis, N. S.; Nocera, D. G., Powering the Planet: Chemical Challenges in Solar Energy Utilization. *Proc. Natl. Acad. Sci. U.S.A.* **2006,** *103* (43), 15729-15735.
7. Collins, S. M.; Hankett, J. M.; Carim, A. I.; Maldonado, S., Preparation of Photoactive $ZnGeP_2$ Nanowire Films. *J. Mater. Chem.* **2012,** *22* (14), 6613-6622.
8. van Schilfgaarde, M.; Coutts, T. J.; Newman, N.; Peshek, T., Thin Film Tandem Photovoltaic Cell from II-IV-V Chalcopyrites. *Appl. Phys. Lett.* **2010,** *96* (14), 143503.
9. Yokoyama, T.; Oba, F.; Seko, A.; Hayashi, H.; Nose, Y.; Tanaka, I., Theoretical Photovoltaic Conversion Efficiencies of $ZnSnP_2$, $CdSnP_2$, and $Zn_{1-X}Cd_xSnP_2$ Alloys. *Appl. Phys. Express.* **2013,** *6* (6), 061201-061204.
10. Gashimzade, F. M., Band Structure of AII-BIV-C_2V-Type Semiconductor Compounds Having the Chalcopyrite Structure. *Sov. Phys. Sol. State.* **1963,** *5* (4), 875-876.
11. Shay, J. L.; Wernick, J. H., *Ternary Chalcopyrite Semiconductors: Growth, Electronic Properties, and Applications*. Pergamon Press: Oxford, 1975.
12. Davis, G. A.; Wolfe, C. M., Liquid Phase Epitaxial Growth of $ZnSnP_2$ on GaAs. *J. Electrochem. Soc.* **1983,** *130* (6), 1408-1412.
13. Ryan, M. A.; Peterson, M. W.; Williamson, D. L.; Frey, J. S.; Maciel, G. E.; Parkinson, B. A., Metal Site Disorder in Zinc Tin Phosphide. *J. Mater. Res.* **1987,** *2* (4), 528-537.
14. St-Jean, P.; Seryogin, G. A.; Francoeur, S., Band Gap of Sphalerite and Chalcopyrite Phases of Epitaxial $ZnSnP_2$. *Appl. Phys. Lett.* **2010,** *96* (23), 231913.
15. Scanlon, D. O.; Walsh, A., Bandgap Engineering of $ZnSnP_2$ for High-Efficiency Solar Cells. *Appl. Phys. Lett.* **2012,** *100* (25), 251911.
16. Borshchevskii, A. S.; Vysotina, M. G., Certain Characteristics of the Phase Diagram of Zn-Sn-P. *Izv. Akad. Nauk.* **1976,** *12* (4), 615-618.
17. Mughal, S. A.; Payne, A. J.; Ray, B., Preparation and Phase Studies of the Ternary Semiconducting Compounds $ZnSnP_2$, $ZnGeP_2$, $ZnSiP_2$, $CdGeP_2$, and $CdSiP_2$. *J. Mater. Sci.* **1969,** *4*, 895-901.
18. Rubenstein, M.; Ure, J. R. W., Preparation and Characteristics of $ZnSnP_2$. *J. Phys. Chem. Solids.* **1968,** *29*, 551-555.
19. Ajmera, P. K.; Shin, H. Y.; Zamanian, B., Vacuum Growth of Thin Films of $ZnSnP_2$. *Solar Cells.* **1987,** *21*, 291-299.

20. Sansregret, J., The Growth of Thin Films of Zinc Tin Phosphide. *Mater. Res. Bull.* **1981,** *16*, 607-611.
21. Francoeur, S.; Seryogin, G. A.; Nikishin, S. A.; Temkin, H., X-Ray Diffraction Study of Chalcopyrite Ordering in Epitaxial $ZnSnP_2$ Grown on GaAs. *Appl. Phys. Lett.* **1999,** *74* (24), 3678-3680.
22. Goel, S. C.; Buhro, W. E.; Adolphi, N. L.; Conradi, M. S., Low-Temperature Organometallic Synthesis of Crystalline and Galssy Ternary Semiconductors $M^{ii}m^{iv}p_2$ Where M^{ii} = Zn and Cd, and M^{iv} = Ge and Sn. *J. Organomet. Chem.* **1993,** *449*, 9-18.
23. Vaipolin, A.; Osmanov, E.; Prochukhan, V., Modifications of a(II)-B(IV)-C_2(V) Compounds with the Sphalerite Structure. *Izv. Akad. Nauk.* **1972,** *8*, 947-949.
24. Mintairov, A. M.; Sadchikov, N. A.; Sauncy, T.; Holtz, M.; Seryogin, G. A.; Nikishin, S. A.; Temkin, H., Vibrational Raman and Infrared Studies of Ordering in Epitaxial $ZnSnP_2$. *Phys. Rev. B.* **1999,** *59* (23), 15197-15207.
25. Bettini, M., Zone-Centered Phonons in Ternary Compounds of Chalcopyrite Structure. *Phys. Status Solidi B.* **1975,** *69*, 201-212.
26. Zlatkin, L. B.; Markov, J. F.; Stekhanov, A. I.; Shur, M. S., Lattice Reflection and Optical Constants of $ZnSnP_2$ Crystals with Chlcopyrite and Sphalerite Structure. *Phys. Status Solidi.* **1969,** *32*, 473-479.
27. Lazewski, J.; Parlinski, K., Dynamical Properties of Pnictide $ZnSnP_2$ from Ab Initio Calculations. *J. Alloy. Compd.* **2001,** *328*, 162-165.
28. Misiewicz, J., Optical Vibrations in the Zn_3P_2 Lattice. *J. Phys.: Condens. Matter.* **1989,** *1*, 9283-9299.
29. Pangilinan, G.; Sooryakumar, R.; Misiewicz, J., Raman Activity of Zn_3P_2. *Phys. Rev. B.* **1991,** *44* (6), 2582-2588.
30. Binions, R.; Blackman, C. S.; Carmalt, C. J.; O'Neill, S. A.; Parkin, I. P.; Molloy, K.; Apostilco, L., Tin Phosphide Coatings from the Atmospheric Pressure Chemical Vapour Deposition of SnX_4 (X=Cl or Br) and Pr_xh_{3-X} (R=Cyc^{hex} or Phenyl). *Polyhedron.* **2002,** *21*, 1943-1947.
31. Vaipolin, A. A.; Goryunova, N. A.; Kleshchinskii, L. I.; Loshakova, G. V.; Osmanov, E. O., The Structure and Properties of the Semiconducting Compound $ZnSnP_2$. *Phys. Status Solidi.* **1968,** *29*, 435-442.
32. Jeong, S.; McDowell, M. T.; Cui, Y., Low-Temperature Self-Catalytic Growth of Tin Oxide Nanocones over Large Areas. *ACS Nano.* **2011,** *5* (7), 5800-5807.
33. Schoenmakers, G. H.; Waagenaar, R.; Kelly, J. J., Methylviologen Redox Reactions at Semiconductor Single Crystal Electrodes. *Ber. Bunsenges. Phys. Chem.* **1996,** *100* (7), 1169-1175.
34. Goryunova, N. A.; Kesamanly, F. P.; Loshakova, G. V., Electrical Properties of $ZnSnP_2$ Crystals. *Sov. Phys. Semicond.* **1968,** *1* (7), 844-846.
35. Bae, I.-T.; Vasekar, P.; VanHart, D.; Dhakal, T., Low-Temperature Synthesis of Zn_3P_2 Nanowire. *J. Mater. Res.* **2011,** *26* (12), 1464-1467.
36. Brockway, L.; Van Laer, M.; Kang, Y.; Vaddiraju, S., Large-Scale Synthesis and in Situ Functionalization of Zn_3P_2 and Zn_4Sb_3 Nanowire Powders. *Phys. Chem. Chem. Phys.* **2013,** *15* (17), 6260-6267.
37. Kamimura, H.; Gouveia, R. C.; Dalmaschio, C. J.; Leite, E. R.; Chiquito, A. J., Synthesis and Electrical Characterization of Zn_3P_2 Nanowires. *Semicond. Sci. Tech.* **2014,** *29* (1), 015001.

38. Miyauchi, K.; Minemura, T.; Nakatani, K.; Nakanishi, H.; Sugiyama, M.; Shirakata, S., Photoluminescence Properties of $ZnSnP_2$ Single Crystals. *Phys. Status. Solidi C.* **2009,** *6* (5), 1116-1119.
39. Heben, M. J.; Kumar, A.; Zheng, C.; Lewis, N. S., Efficient Photovoltaic Devices for InP Semiconductor/Liquid Junctions. *Nature.* **1989,** *340*, 621-623.
40. Foley, J. M.; Price, M. J.; Feldblyum, J. I.; Maldonado, S., Analysis of the Operation of Thin Nanowire Photoelectrodes for Solar Energy Conversion. *Energy Environ. Sci.* **2012,** *5* (1), 5203-5220.

CHAPTER V

Preliminary Data for Realizing p-Type Nanowire Array for Photoelectrochemical Water Splitting and Dye-Sensitized Photocathodes

A. Introduction

This chapter contains details of *(1)* vapor-liquid-solid (VLS) growth of GaP nanowire array on patterned single crystalline substrates and *(2)* development of a non-surface specific dye attachment method on p-type GaP photocathode. The metal catalysts explored in this chapter were Sn and Au, and the substrates were Si(100) and GaP(111)B. "Bottom-up" p-type GaP nanowires have always been the key to realize high aspect ratio photoelectrode architecture for PEC water splitting cell as well as dye-sensitized cell. To date, the existing nanowire growth method in the group has been limited to solid sublimation and the resulting GaP nanowires are exclusively n-type. Hence, post-growth doping is necessary to convert the as-grown GaP nanowires to p-type under conditions that are not damaging to the nanowires. In Chapter II of this thesis, thermal Zn diffusion doping by atomic layer deposition showed promising, consistent results with potential highly tunable performance which would be suitable for nanowire system.[1] The developed doping scheme is used here to dope the as-prepared n-type GaP to p-type.

The second section of this chapter consists of preliminary data and progress in developing a non-surface specific dye attachment technique to persistently attach photosensitizers such as organic acid dyes (Rose Bengal or RB) onto p-type GaP(111)A, B, and GaP(100) phases. This is done by conformally coating thin layers of ZnO via atomic layer deposition (ALD) on the GaP surface, which serves as the metal/metal oxide sites for chelating with the carboxylate group on RB dyes.[2-3] A series of electrochemical characterizations and spectral response data are presented in the section to substantiate the fact for persistent dye attachment and subsequent sensitization or "hole injection" into the p-GaP photoelectrode.

B. GaP Nanowire Array

i. Experimental Section

(a) Photolithography

Si(100) (As-doped, 0.006 Ω cm, thickness = 0.5 mm, Wafer Works Corp.) and p-type GaP(111)B (Zn-doped, miscut ≤ 0.5º, 0.0536 Ω cm, thickness = 0.4 mm, ITME) were degreased in sequential H_2O (>18 ΩM cm, Barnstead Nanopure Purifier), methanol, acetone, methanol in an ultrasonic bath. Prior to use, all substrates were etched in 5 v/v% HF or concentrated H_2SO_4 (doubly distilled, Sigma-Aldrich) for 30 s and rinsed well with H_2O to remove native oxide layer. The photolithography steps are illustrated in Figure V.1. First, 700 nm SiO_x was deposited by PECVD followed by spin-coating AZ series photoresist on a degreased substrate. Then, the photoresist was exposed to a photomask to pattern an array of 0.7 μm wells with 1.5 μm pitch. < 200 nm Sn or Au thin films was evaporated onto the substrate, and the photoresist was removed with acetone to reveal the metal particle array.[4-5] The finished patterned wafer (Figure V.1f) was annealed at T = 650 – 900 ºC for 30 – 60 min in 1000 sccm Ar (g) to fuse the nanoparticles in the wells.

(b) Nanowire Preparation

Nanowire growths were conducted in a custom-built quartz tube reactor as depicted in Figure V.2. 15 mg of finely ground GaP powder (99.99%, metal basis, Sigma-Aldrich) was placed on a quartz platform and subsequently inserted into a quartz tube (2.2 cm diameter and 86 cm length) in Zone T_1. The metal-patterned growth substrate was diced into 0.5 cm x 0.5 cm and placed in Zone T_2. Once the patterned substrate and the source powders were loaded into the quartz tube, the assembly was evacuated with a roughing pump to below 0.06 torr before proceeding to the growth conditions outlined in Table V.1, 2 and 3. (*vide infra*). In general, the GaP source powder was sublimed at T = 830 ºC while the growth substrate was kept at a set temperature (T = 500-620 ºC, *vide infra*). The carrier gas flow rate and pressure were maintained at 12 sccm and 0.5 torr respectively throughout the growth duration. For both nanowire deposition types, the system was allowed to cool down to room temperature radiatively over the course of 4 h upon completion of the nanowire growth.

(c) Materials Characterization

Scanning electron micrographs were collected with a FEI NOVA Nanolab Dualbeam Workstation equipped with Schottky field emitter, a through-the-lens detector (TLD), and an EDS detector. High-resolution transmission electron microscopy images and the selected-area electron diffraction patterns (SAED) were acquired with a JEOL 3011 TEM equipped with a

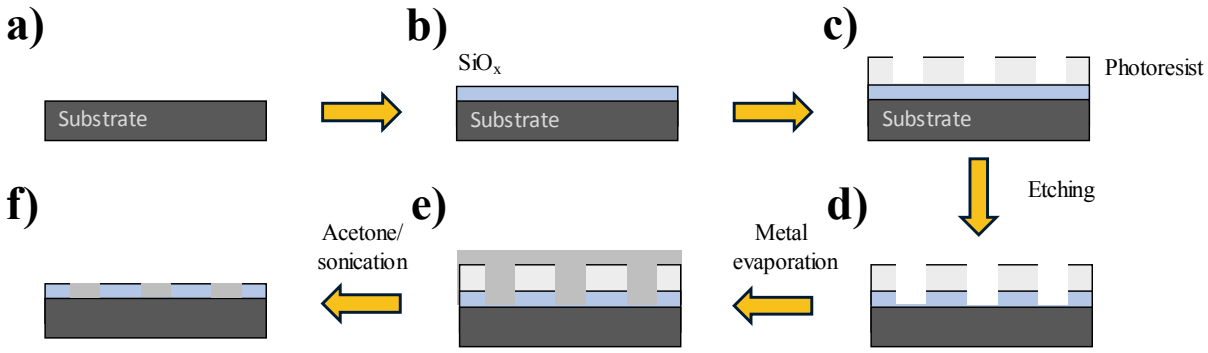

Figure V.1. Schematic depiction of the photolithography process employed to create metal particle array for "bottom-up" nanowire growth.

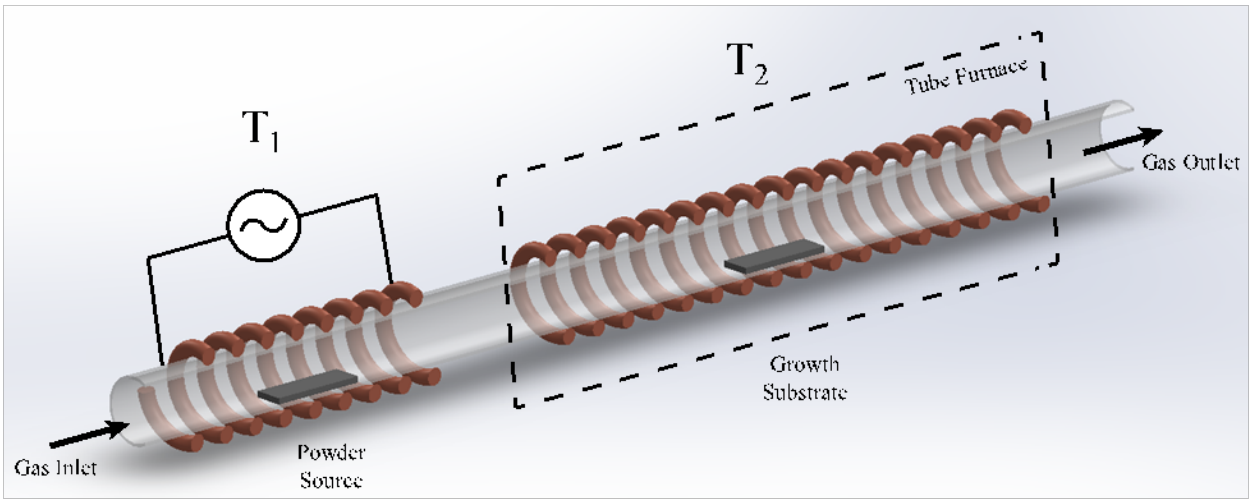

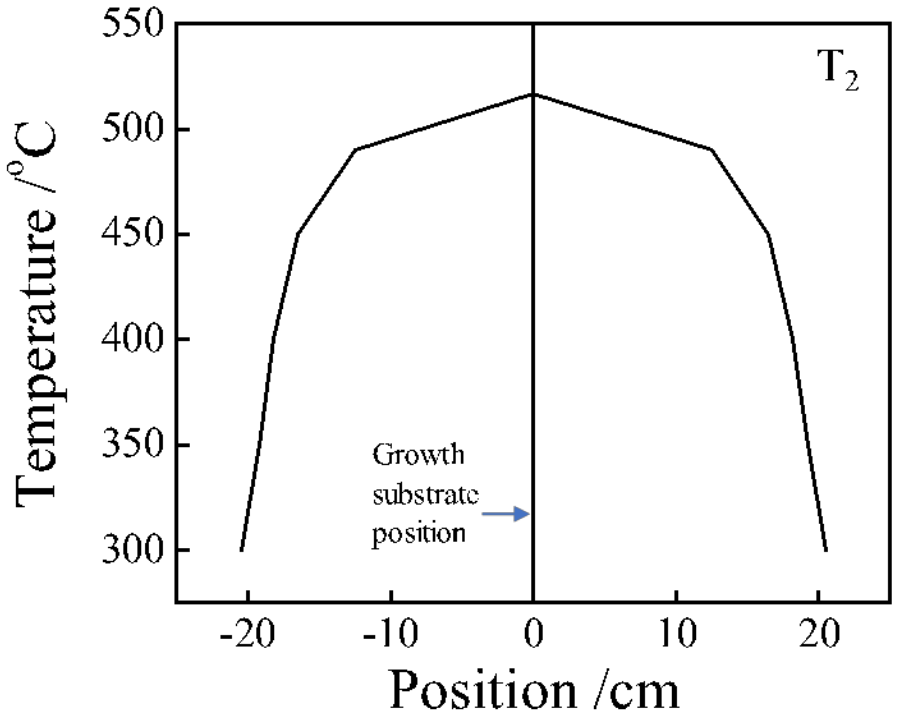

Figure V.2. Schematic illustration of the multi-zone tube furnace setup used for nanowire growth experiments. The temperature profile of Zone T_2 was measured with a thermocouple and T_2 was set to 500 ºC during the measurement.

LaB_6 source operated at 300 kV and an EDS detector. The samples for TEM were prepared by sonicating the as-prepared GaP nanowires in ethanol (190 proof, ACS spectrophotometric grade, Sigma-Aldrich) for 15 s to create a homogenous suspension. The suspension was then drop-casted onto copper TEM grids supported by an ultra-thin carbon film (Ted Pella).

(d) Atomic Layer Deposition of ZnO

Diethylzinc (≥ 52 wt. % Zn basis, Sigma-Aldrich) and deionized water were used as the precursors for ZnO deposition in a custom-built ALD tool.[6] No pretreatments were performed on the GaP samples prior to commencing ALD. During the deposition, the reaction chamber was kept at 150 ºC and a base pressure of 69.3 Pa. The diethylzinc precursor was pulsed for 0.05 s followed by 10 sccm Ar purge for 30 s. The cycle was repeated with 0.1 s pulse of DI water. The growth rate of ZnO films was 2.0 Å/cycle as measured by ellipsometry (Woollam M-2000DI Ellipsometer).

GaP nanowire films were first coated with 5 - 10 ALD cycles of ZnO and then annealed at T = 650 ºC in 100 sccm Ar flow at 101325 Pa in a 1-inch quartz tube with the presence of 5 mg red phosphorus.

(e) Photoelectrochemical Measurements

Ohmic contacts to GaP were prepared by first scratching the back of the substrate with a diamond scribe to mechanically remove oxide(s) and increase the surface roughness for better contact with the soldered metal, then etching with conc. H_2SO_4 for 30 s, followed by soldering a thin film of In-Zn (99:1 wt.), and then annealing in forming gas (5 % H_2 in N_2, Metro Welding) for 10 min at 400 ºC.

GaP electrodes were fabricated by attaching a tinned-copper wire to the back of substrate that already had an In-Zn ohmic contact with silver print (GC Electronics). The wire was then threaded through a glass tube, and the electrode was finally sealed with inert epoxy (Hysolc C, Loctite) to expose approximately 0.09 cm^2 active area. The epoxy was cured for at least 24 h at room temperature before the electrodes were used. A custom-built, 3-electrode quartz cell with an optically flat bottom was used for photoelectrochemical measurements. The reference and counter electrodes were a Ag wire coated with AgCl immersed in sat. KCl and a section of Pt mesh, respectively. An aqueous solution of 0.01 M europium(III) chloride hexahydrate (99 %, Acros) and 1 M KCl (Mallinckrodt, Analytical Reagent) was used as the active redox species. The solution was stirred during the measurement. Spectral response measurements were

collected with a lab-built system detailed previously.[7] The light was chopped at 15 Hz during measurements.

ii. Results

Figure V.3 presents the scanning electron micrographs (SEM) of Au-patterned Si substrate after removing the photoresist in acetone. The resulting lithography pattern had wells 0.7 μm in diameter and 1.4 μm apart. The thickness of the Au film was approximately 140 nm. The Au films not only coats the bottom of the well, but also the side well, as seen in Figure V.3. Annealing the Au films at T = 900 ºC in Ar for 1 h melted and fused the Au films in each well into a particle with the diameter of nominally 540 nm.[8-9] Figure V.4a-4c shows the SEM of the resulting nanowire array growth from annealed Au-patterned Si substrate. The growth condition used in Figure V.4a-4c is summarized in Table V.1. Nanowire was observed to grow perpendicularly to the substrate with very distinct Au metal tips on the nanowires. Almost exclusively one wire each well. The temperatures explored in Zone T_2 were 500-620 ºC, but only T between 560-580 ºC gave desirable results. Otherwise the nanowire grown are lateral/lying down on the SiO_x layer (data not shown). Without the Au annealing step, very thin nanowires (d <100 nm) formed all over the well and oxides layer. Figure V.4d shows the Raman spectrum collected from as-prepared nanowires in Figure V.4a. Two distinct Raman phonon modes were observed and assigned to the TO and LO modes of GaP at 364.2 cm^{-1} and 401.8 cm^{-1}, respectively. The TO and LO mode were asymmetric and broadened if compared to the bulk GaP (366.5 cm^{-1} (TO) and 403.8 cm^{-1} (LO)).[10] The downshifted and broadened phonon peaks were due to the nanowire's high aspect ratio geometry and submicron diameter.[11-12] Another weak peak was seen at 301 cm^{-1}, which corresponds to the LA phonon mode of c-Si.[13]

Au-catalyzed GaP nanowires prepared on GaP(111)B are epitaxial as shown in Chapter III in the thesis. In order to make epitaxy GaP nanowire array on GaP substrate, we applied the same lithography process in Figure V.1 to GaP(111)B wafer instead of Si wafer to obtain Au particles on the patterned substrate. However, the same process did not yield an ordered nanowire array. Firstly, when the as-prepared substrate with Au films was annealed at T = 650 ºC for 1 h (condition stable for GaP based on previous works in Chapter II), the temperature was not high enough to fuse the Au particles in each well (Figure V.5a and 5b). When the substrate with Au was annealed at T = 800 ºC for 30 min, patchy light gray matte films were observed after the annealing step. Under SEM, those were nanowires (Figure V.5d), most likely Ga_2O_3 and Si

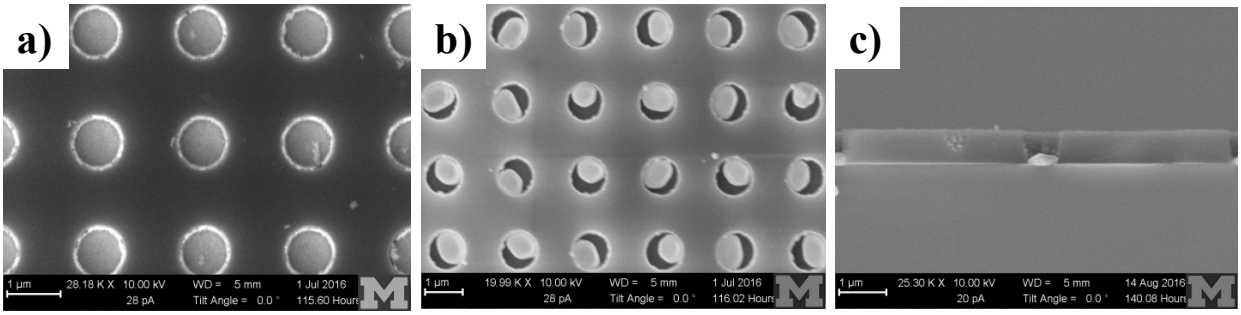

Figure V.3. Scanning electron micrographs of patterned SiO_x well array (a) with as-deposited ~140 nm Au film, (b) after annealing at 900 ºC in Ar (g) for 1 h. (c) Cross-sectional scanning electron micrograph of annealed Au film in patterned SiO_x well array.

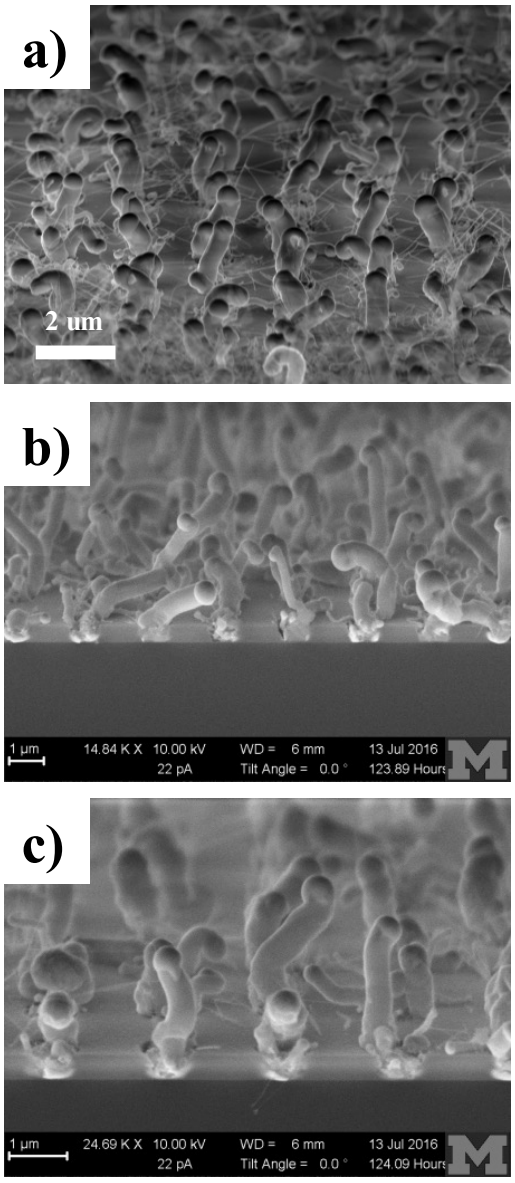

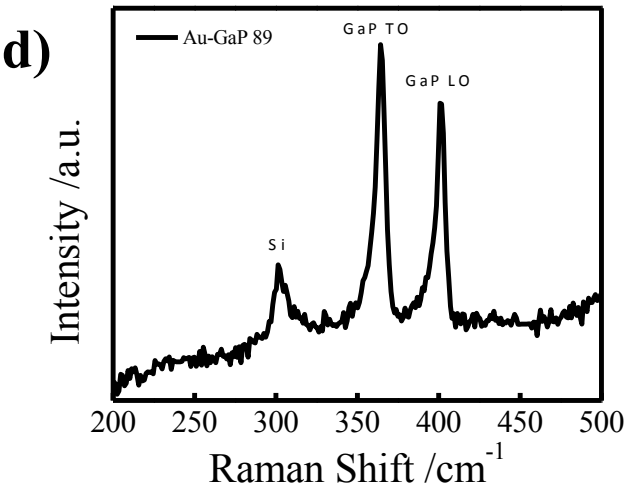

Table V.1. Summary of growth conditions used to prepare GaP NW on Au-patterned Si wafer

Sample #	VLS Growth Conditions
a	Substrate: Au patterned Si (annealed) Growth T = 580 ºC, Duration: 30 min 12 sccm Forming gas, P = 0.5 torr
b	Substrate: Au patterned Si (annealed) Growth T = 580 ºC, Duration: 30 min 12 sccm Forming gas, P = 0.5 torr
c	Substrate: Au patterned Si (annealed) Growth T = 560 ºC Duration: 30 min 12 sccm Forming gas, P = 0.5 torr

Figure V.4. (a-c) Cross-section scanning electron micrographs of nanowire array prepared from Au-patterned Si substrate using conditions in **Table VI.1**. (d) Unpolarized Raman spectrum collected from as-prepared nanowire array in (a).

nanowires since both nanowires were reported to be prepared by solid sublimation *via* VLS mechanism with the presence of Ga, Si and O from oxides layer.[14-15] The sites that were not light gray was not populated with nanowires, but there is an interesting observation – the wells were filled with materials and the morphology is very different than the Au particles in Figure V.3c.

The Au films annealing step did not fuse the Au particles in the well, but we still used the Au-patterned GaP substrate as deposited, i.e. without annealing step (Figure V.5a), with Au films still on the side wall of the patterned wells to grow nanowires. Figure V.6 shows the SEM images of Au-GaP nanowires prepared on patterned GaP substrate. As seen in Figure V.6a, the nanowires were very disordered and kinked. One notable observation is the partially etched GaP wafer at the bottom of the patterned well. The same observation was not found in Au/Si substrate. This etching is most likely a Ga-Au alloying effect as indicated in Ga-Au phase diagram.[16] The surface became Ga-rich during the nanowire growth as the low reactor pressure (P = 0.5 torr) and high temperature (T = 560-650 ºC) induced surface non-stoichiometric evaporation.[17] Several growth parameters were explored to minimize the etching, and the conditions were summarized in Table V.2. In general, it was necessary to maintain a high reactor pressure to minimize etching (Figure V.6c).

Sn metal particles were also explored in this chapter as an alternative VLS catalyst based on the findings in Chapter III of this thesis. Figure V.7 shows the SEM images of GaP nanowires grown from Sn-patterned GaP substrate. The as-prepared GaP nanowires were nominally 300 nm in diameter, and the parameters attempted were recorded in Table V.3. Note the large nanowires have an O-rich flower-shaped termination which indicated presence of oxidized metal catalyst.[18] Although the overall nanowire morphologies were not ideal, very minimal to no alloying between the Sn catalyst and GaP wafer was observed. The growth parameters need to be tuned to yield consistent nanowire morphology.

Figure V.8 presents the preliminary data for post-growth doping non-optimized nanowire films based on the findings of Chapter II of this thesis. The transmission electron micrograph (TEM) in Figure V.8a and 8c show an individual GaP nanowire coated with 10 cycles of ALD ZnO before and after annealing in the presence of P vapors. Qualitatively, the nanowire did not exhibit any Kirkendall effect after diffusion of Zn.[19] The energy X-ray dispersion spectroscopy (EDS) in Figure V.8b shows detection of Zn signals from the annealed nanowire. Figure V.8d presents the spectral response collected from Sn/GaP nanowire before and after thermal

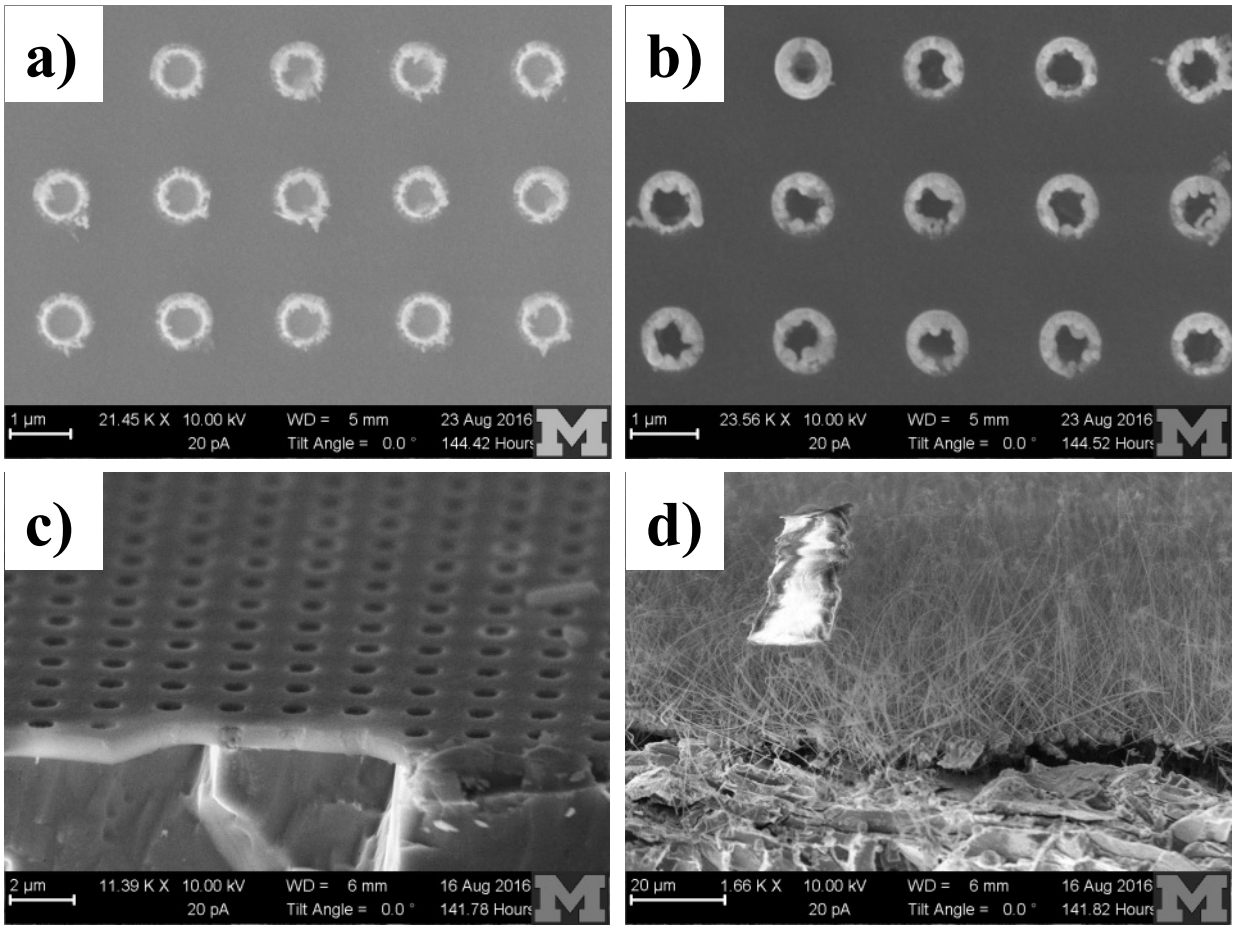

Figure V.5. (a) Top-down scanning electron micrograph of as-deposited Au films in patterned GaP wafer. (b) Au-patterned GaP wafer after annealing at T = 650 ºC for 1 h. (c, d) Cross-sectional scanning electron micrograph of Au-patterned GaP wafer after annealing at T = 800 ºC for 30 min imaged at two different locations within a substrate.

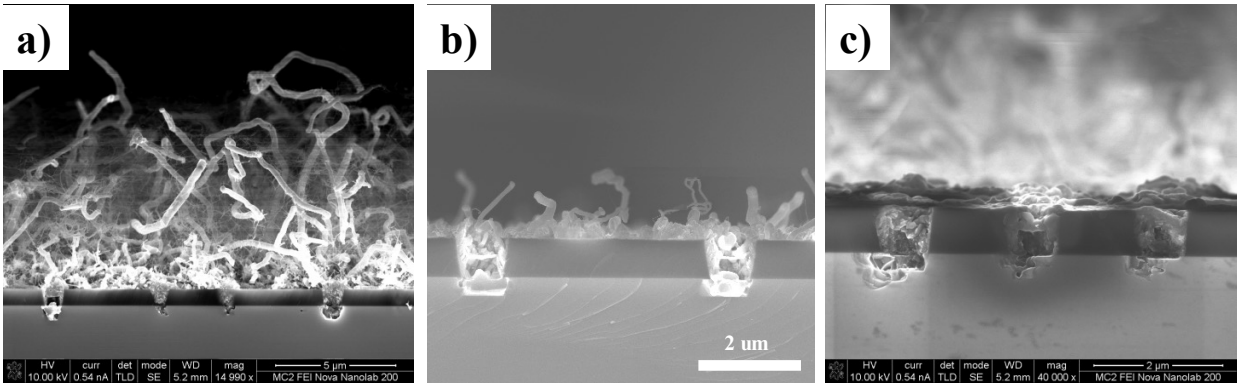

Figure V.6. Cross-sectional scanning electron micrographs of GaP nanowires grown from Au-patterned GaP (111)B substrates under conditions summarized in **Table VI.2**.

Table V.2. Summary of growth conditions used to prepare GaP nanowires on Au-patterned GaP(111)B wafer

Sample #	VLS Growth Conditions
a	Substrate: Au on patterned-GaP111B Pre-annealing step: T = 650 ºC, 20 min, 50 sccm forming gas, P = 2 torr Growth parameters: T = 580 ºC, 60 min, 12 sccm forming gas, P = 0.5 torr
b	Substrate: Au on patterned-GaP111B Pre-annealing step: None Growth parameters: T = 580 ºC, 60 min, 12 sccm forming gas, P = 0.5 torr
c	Substrate: Au on patterned-GaP111B Pre-annealing step: T = 620 ºC, 10 min, 70 sccm forming gas, P = 3 torr Growth parameters: T = 560 ºC, 45 min, 12 sccm forming gas, P = 0.5 torr

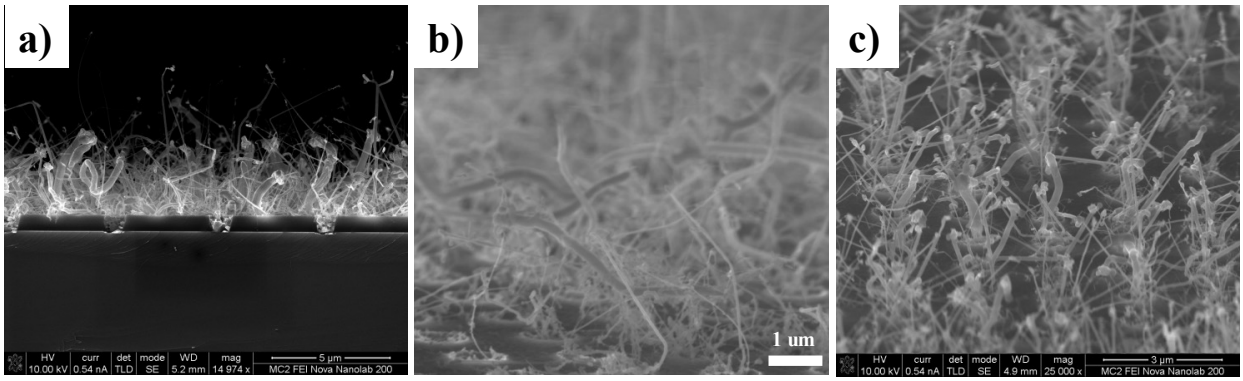

Figure V.7. Cross-sectional scanning electron micrographs of GaP nanowires grown from Sn-patterned GaP (111)B substrates under conditions summarized in **Table VI.3**.

Table V.3. Summary of growth conditions used to prepare GaP nanowires on Sn-patterned GaP(111)B wafer

Sample #	VLS Growth Conditions
a	Substrate: Sn on patterned-GaP111B Pre-annealing step: T = 300 ºC, 20 min, 70 sccm forming gas, P = 3 torr Growth parameters: T = 500 ºC, 45 min, 12 sccm forming gas, P = 0.5 torr
b	Substrate: Sn on patterned-GaP111B Pre-annealing step: T = 600 ºC, 20 min, 70 sccm forming gas, P = 3 torr Growth parameters: T = 500 ºC, 45 min, 12 sccm forming gas, P = 0.5 torr
c	Substrate: Sn on patterned-GaP111B Pre-annealing step: T = 600 ºC, 2 min, 70 sccm forming gas, P = 3 torr Growth parameters: T = 500 ºC, 45 min, 12 sccm forming gas, P = 0.5 torr

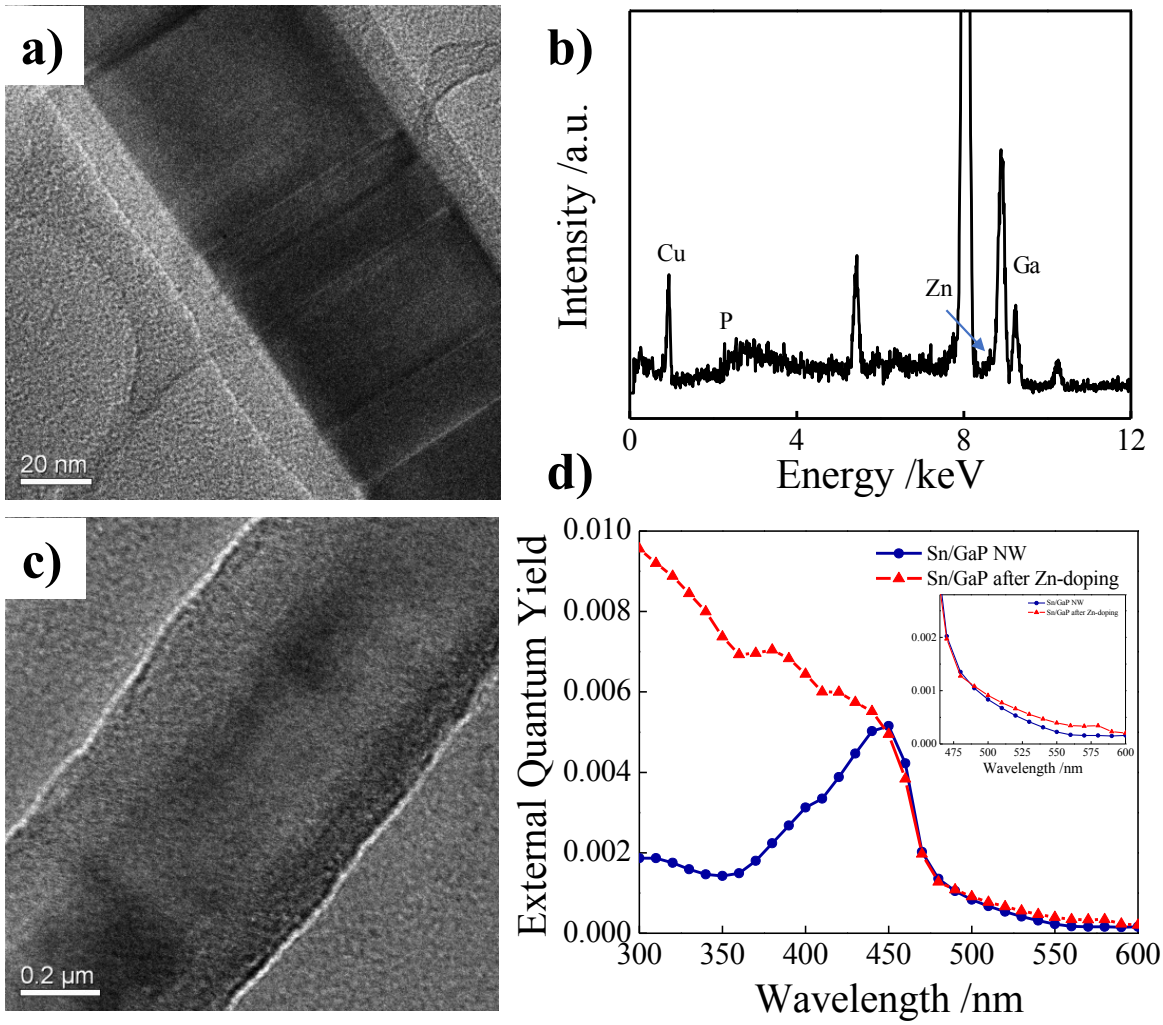

Figure V.8. Transmission electron micrographs of an individual nanowire coated with 10 cycles ALD ZnO (a) before and (c) after annealing at T = 650 ºC in the presence of P vapors. (b) EDS spectrum collected from (c). (d) Spectral responses of Sn-seeded GaP nanowire films measured at -0.5 V vs. Ag/AgCl in 1 M KCl with 2 mM $EuCl_3$ as-prepared (blue) and after annealing (red).

annealing at -0.5 V vs. Ag/AgCl in the presence of 2 mM $EuCl_3$ as the redox species. Before annealing, the external quantum yield (EQY) of the nanowire films was low in the short wavelength range up to GaP's direct band gap (300-450 nm). This indicated the nanowires on the surface of the substrate were not photoactive to sustain photocathodic current in the presence of Eu^{3+} species. After Zn-doping, the short wavelength EQY increased, indicating photoactivity at the nanowire films. However, the long wavelength EQY (470-548 nm) did not show significant enhancement, meaning the annealed nanowire films still not able to effectively separate charge carriers generated deep in the materials.[1, 20]

iii. Discussion

The collective data demonstrate the difference of Au-seeded GaP nanowires on patterned-Si and GaP substrate as well as Sn-seeded GaP nanowires on patterned-GaP wafer. So far, Au-patterned Si substrate was able to grow GaP nanowire array, but Au-patterned GaP has some substrate-metal alloying/etching problems as shown in Figure V.5 and V.6. Rather than using this system to grow "bottom-up" GaP nanowires, one could possibly utilize this alloying/etching issue to own advantage. In other words, one could anneal the Au-patterned GaP wafer in the conditions listed in Table V.2 to create p-type "negative nanowire" array.[21] Otherwise, it is difficult to avoid the wafer etching because the VLS growth precursors are supplied from sublimed GaP powder which requires low reactor pressure to generate. Fortunately, Sn-patterned GaP substrate did not have wafer etching problems, but a more reducing condition (e.g. high H_2:Ar ratio) is needed to reduce the oxide formation during the nanowire growth process to ensure no oxidation.

The spectral response data is still premature, although the external quantum yield of the short wavelength (300-450 nm) has increased after annealing, the enhancement from 470-548 nm is too little to be of any significance. Firstly, the nanowire films were thin, (<10 μm in length), not enough to capture the light from 500 to 548 nm ($\mathbf{E}_g$ of GaP).[7] According to the findings in Chapter III, Sn-seeded GaP resulted degenerately-doped n-type nanowires, more Zn acceptors are needed to compensate the Sn donors in GaP nanowire to render it cathodic character under illumination.

iv. Summary

Attempts to grow GaP nanowire arrays on GaP(111)B and Si(100) substrates using Au and Sn particles as the VLS catalysts were made. The nanowire array was successful with Au/Si

substrate, but not when Au/GaP(111)B was used. The bottom of the wells were etched due to surface evaporation of GaP(111)B surface and alloying with Au to form Au_xGa_y metal alloy. The alloying/etching did not happen with Sn-patterned GaP substrate, but highly reducing reactor will be necessary to decrease the "flower-shaped" tip formation during nanowire growth. The spectral response results were too preliminary, but look promising. It is necessary to increase the length or thickness of the nanowire films before attempting more Zn-doping in the future.

C. Dye-Sensitized GaP Photocathode

i. Experimental Section

(a) Materials

Three types of GaP wafers were used as the dye-sensitized photocathodes: p-type GaP(100) (Zn-doped, 0.086 Ω cm, thickness = 0.35 mm, ITME), p-type GaP(111)B (Zn-doped, miscut ≤ 0.5º, 0.0536 Ω cm, thickness = 0.4 mm, ITME), and p-type GaP(111)A (Zn-doped, miscut ≤ 0.1º, 0.046 Ω cm, thickness = 0.35 mm, ITME) The wafers were diced into 0.5 x 0.5 cm squares, degreased with sequential immersion/sonication in distilled water (> 18 MΩ cm, Barnstead Nanopure III purifier), methanol (> 99.8 % ACS Reagent, Sigma-Aldrich), acetone (Fisher Scientific), methanol, distilled water, and finally dried with N_2.

(b) Photoelectrode Preparation

Ohmic contacts to GaP were prepared by first scratching the back of the substrate with a diamond scribe to mechanically remove oxide(s) and increase the surface roughness for better contact with the soldered metal, then etching with 18 M H_2SO_4 for 30 s, followed by soldering a thin film of In-Zn (99:1 wt.), and then annealing in forming gas (5 % H_2 in N_2, Metro Welding) for 10 min at 400 ºC.

(c) Atomic Layer Deposition of ZnO

The GaP samples with ohmic contact were coated with 25 cycles of ALD ZnO. Diethylzinc (≥ 52 wt. % Zn basis, Sigma-Aldrich) and deionized water were used as the precursors for ZnO deposition in a custom-built ALD tool.[6] Prior to performing ALD, the GaP wafers were etched in 18 M H_2SO_4 for 30 s. During the deposition, the reaction chamber was kept at 150 ºC and a base pressure of 69.3 Pa. The cycle was begun with five 0.1 s pulses of DI water to populate the wafer surface with hydroxyl groups. Then, the diethylzinc precursor was pulsed for 0.05 s followed by 10 sccm Ar purge for 30 s. The cycle was repeated with 0.1 s pulse

of DI water. The growth rate of ZnO films was 2.0 Å/cycle as measured by ellipsometry (Woollam M-2000DI Ellipsometer).

(d) Dye Adsorption and Photoelectrochemical Measurements

Bare GaP and ZnO-coated GaP electrodes were fabricated by attaching a tinned-copper wire to the back of substrate that already had an In-Zn ohmic contact with silver print (GC Electronics). The wire was then threaded through a glass tube, and the electrode was finally sealed with inert epoxy (Hysolc C, Loctite) to expose approximately 0.1-0.15 cm^2 active area. The epoxy was cured for at least 24 h at room temperature before the electrodes were used.

To adsorb dyes on the surface of the ZnO-coated GaP electrode, the cured electrode was immersed in 6 mM dye solution (pH 5.8) and allowed it to react for 30 min to reach equilibrium with constant agitation or stirring. 30 min was sufficient for the adsorption to reach equilibrium. The electrode was then immersed in nanopure water (>18 ΩM cm, Barnstead Nanopure Purifier) to remove any excess or weakly adsorbed dyes before any photoelectrochemical measurements. The dye on the epoxy was removed by wiping the affected area with Kimwipe and acetone. In between measurements, the dye-adsorbed electrode was cleaned by soaking in acetone for 5 min and followed by rinsing in acidic solution (pH 2.2) to decompose all the adsorbed dye molecules. Dyes used in the studies were Rose Bengal (95 %, Sigma-Aldrich), Crystal Violet (≥90 %, Sigma-Aldrich), and Rhodamine-B (95 %, Sigma-Aldrich).

A custom-built, 3-electrode quartz cell with an optically flat bottom was used for photoelectrochemical measurements. The reference and counter electrodes were an Ag wire coated with AgCl immersed in sat. KCl and a section of Pt mesh, respectively. An aqueous solution of methyl viologen (98 %, Sigma-Aldrich), europium(III) chloride hexahydrate (Acros) and 1 M KCl (Mallinckrodt, Analytical Reagent) was used as the active redox species. The pH of the electrolyte was adjusted by KOH to 7.8. Spectral response measurements were collected with a lab-built system detailed previously.[7] The light source was an Oriel 150 W Xe arc lamp (Newport) and it was chopped at 15 Hz during measurements. The steady-state *J-E* photoresponses were collected with a digital PAR 273 potentiostat illuminated with a monochromatic light source from the Xe arc lamp.

(e) Material Characterization

Transmission electron microscopy (TEM) images, selected-area electron diffraction patterns (SAED), and elemental analyses were acquired with a JEOL 3011 equipped with a LaB_6

source operated at 300 kV. The samples for TEM were prepared in an FEI Helios Nanolab 650 Dualbeam Focused ion beam (FIB) workstation via conventional in-situ lift-out methods. All X-ray photoelectron spectroscopy (XPS) data were acquired using a PHI 5400 analyzer equipped with an Al Ka source without a monochromator. Spectra were collected without charge neutralization at a base pressure of $<2.5 \times 10^{-9}$ Torr. A 6 mA emission and a 12 kV anode high tension were used for spectral acquisition with a pass energy of 23.5 eV for high-resolution XP spectra. The XP spectra were calibrated to the C 1s at 284.6 eV. X-ray reflectivity curve of the thin films was collected with a Rigaku X-ray diffractometer equipped with a Cu-α X-ray source.

ii. Results

Figure V.9 shows the X-ray reflectivity measured at a GaP wafer that had been coated with 25 cycles of ALD ZnO films. The Fast-Fourier transform of the periods revealed the ZnO films to be approximately 3.4 nm thick. When viewing the cross-section of the ZnO/GaP interface under high-resolution TEM, the boundary between the single-crystalline GaP wafer and the ZnO films was clear as shown in Figure V.10. ZnO films deposited by ALD at low temperatures were polycrystalline.[6] As seen in Figure V.10, the lattice d-spacing of the polycrystalline grains at the interface were measured to be 0.26 nm and 0.24 nm, which correspond to the d-spacings of (002) and (011) planes, respectively. The measured d-spacing of the single-crystalline wafer was 0.32 nm, which corresponds to the (111) plane of GaP. A layer of amorphous oxide with unknown composition was observed in between the GaP wafer and ZnO layer.

The idea of chelating the RB molecules to the ALD ZnO films was tested (schematic shown in Figure V.11a), and the system's stability in aqueous electrolyte was presented in Figure V.11b and 11c. Figure V.11b shows the high-resolution Zn 2p XP spectra of p-GaP/ZnO immersed in 6 mM RB for 30 min before and after experiment, that is, soaking in aqueous electrolyte at pH 7.8 for 30 min. Zn signals were detected in both samples, but the spectrum of the "before" sample was shifted, mostly due to the conductivity of the samples. The high-resolution I 3d XP spectra in Figure V.11c shows the stability of the dye attachment scheme. I signals, an indication of the presence of RB molecules, were detected from the sample before and after experiment, indicating high stability of the chelated RB dyes on p-GaP/ZnO surface in aqueous electrolyte at pH 7.8. The data confirmed the stability and suitability of p-GaP/ZnO-RB photoelectrode for dye-sensitization.

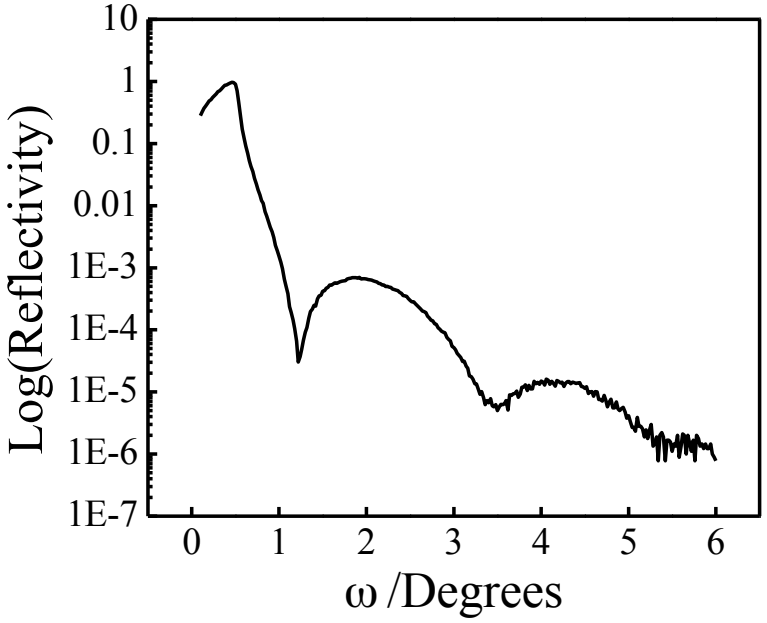

Figure V.9. The measured reflectivity of a GaP(111)B substrate coated with 25 cycles of ALD ZnO vs. incident X-ray angles. Fast-Fourier transform (FFT) of the periods indicated the ZnO film thickness was 3.4 nm.

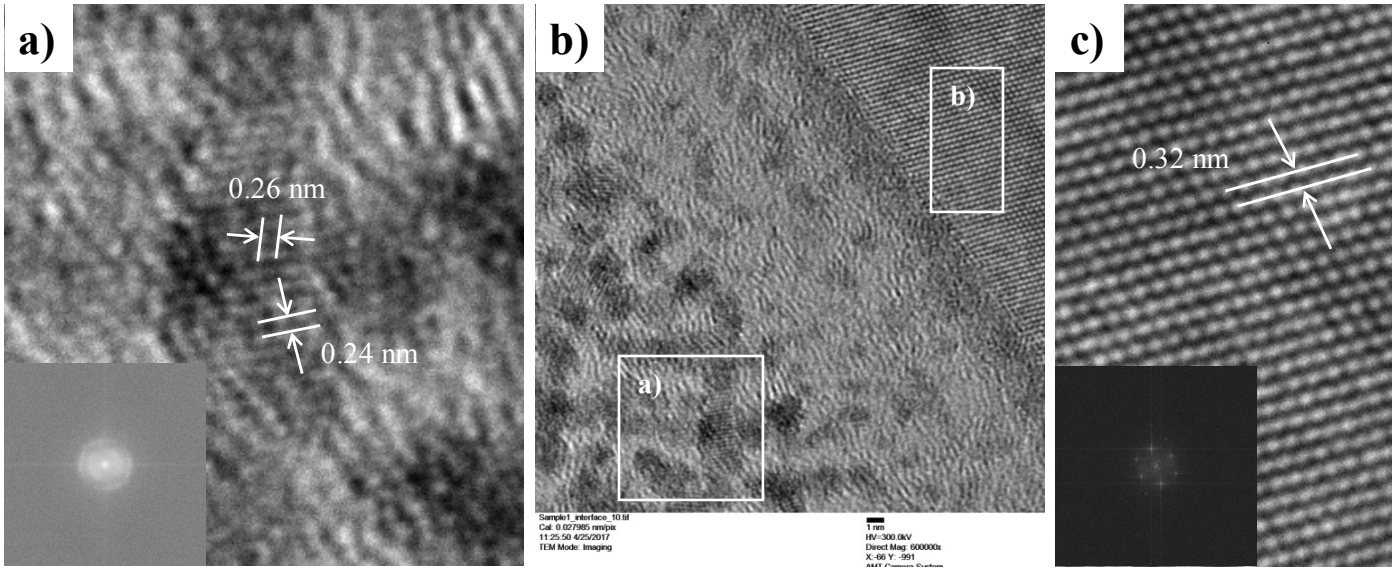

Figure V.10. High-resolution transmission electron micrographs of the ZnO/GaP wafer interface. (a) High-magnification image taken from the region indicated in (b) showing nanoparticles with lattice d-spacing that matched the d(002) and d(011) planes of wurzite ZnO [Inset: FFT of the polycrystalline ZnO nanoparticles] (c) High-resolution image taken from the region indicated in (b) showing atomic columns of GaP single-crystalline wafer. The lattice d-spacing was measured to be 0.32 nm, consistent with d(111) of zinc blende GaP. [Inset: FFT of the wafer confirms the plane orthogonal to the incident electron beam was [110]]

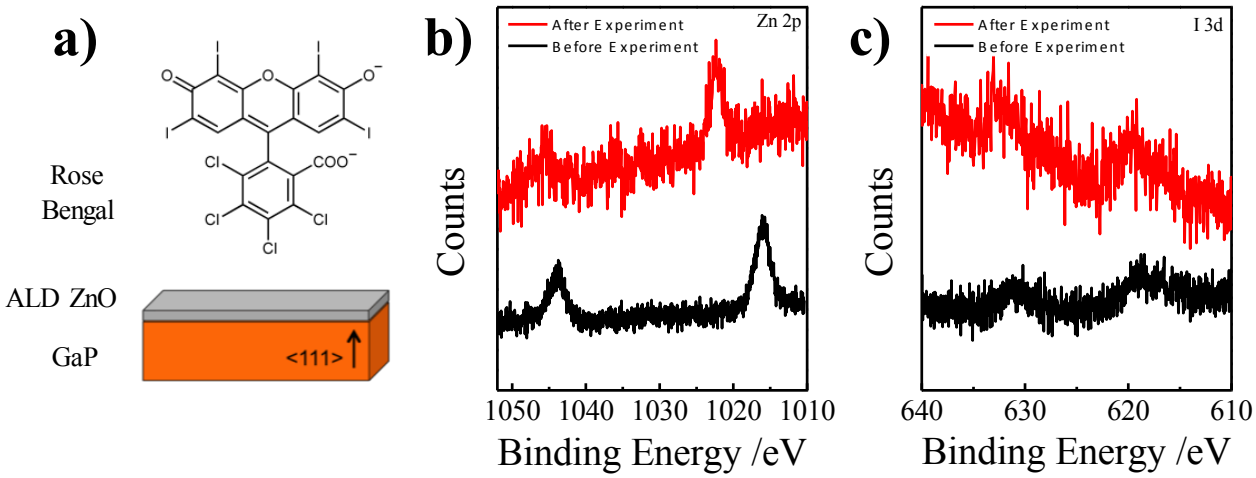

Figure V.11. (a) Schematic of an ALD ZnO-coated GaP wafer and the molecular structure of Rose Bengal without the cations. (b, c) High-resolution Zn 2p and I 3d XP spectra of a p-GaP(111)B/ZnO substrate adsorbed with Rose Bengal dyes before (black) and after (red) being in aqueous electrolyte for 30 min.

Previous tests with 25, 50, and 100 cycles ALD ZnO on p-GaP(111)B photocathodes showed sensitization photocurrent when the electrodes were first soaked in RB dye solution an then transferred to *clear* 1 M KCl electrolyte (data not shown). In order to systematically test the extent of dye adsorption and sensitization, a p-GaP(100)/ZnO electrode was first reacted with RB solution at various concentration, rinsed and then transferred to clear 1 M KCl electrolyte (pH 7.8) for wavelength-dependent photoresponse measurements. The external quantum yield (EQY) data were collected at -0.6 V vs. Ag/AgCl. The pH and potential were selected according to the Pourbaix diagram of Zn/ZnO.[22] Figure V.12a shows the measured wavelength-dependent EQY of p-GaP(100)/ZnO electrode in 1 M KCl that was previously soaked in RB solution ranging from 0.05 mM to 8 mM. The sub-band gap EQY at 580 nm strongly followed the concentration of the RB during the soaking/adsorption step. Figure V.12b plots out the EQY at 580 nm with respect to the RB dye concentrations. The trend roughly follows the model for monolayer adsorption,[23] but more data points and repetitions are needed in between 2 mM and 8 mM, as well as the surface dye concentration (can be obtained from XPS and/or UV-vis spectroscopy) to extract parameters from the Langmuir relation and modified Langmuir relation to gain more insights into the system (equations can be found in Reference 24).[24] Regardless of the adsorption model, electrode soaked in 6 mM RB solution exhibited the highest EQY, so in the subsequent tests on p-GaP(100), (111)A and (111)B electrodes, the electrodes were soaked in 6 mM RB solution before transferring to a clear 1 M KCl electrolyte with the presence of $Eu^{3+/2+}$ redox couple for photoresponse measurements.

Figure V.13 compiles the measured wavelength-dependent EQY from p-GaP(100), (111)A and (111)B electrodes that were previously immersed in 6 mM RB solution. The EQY were collected at -0.6 V vs. Ag/AgCl, and the electrolyte was 1 M KCl containing 5 mM $Eu^{3+/2+}$ redox couple. Sensitizations were observed on all phases. The current-potential photoresponses in Figure V.13b, 13d, and 13f showed consistent photocathodic currents under monochromatic sub-band gap illumination at 580 nm, indicating a "hole-injection" mechanism occurred at the electrode/electrolyte interface. In Figure V.13f, six consecutive EQY measurements were done on a RB-adsorbed p-GaP(111)B/ZnO electrode. The electrolyte was 1 M KCl containing 5 mM $Eu^{3+/2+}$ redox couple. The six EQY profiles were superimposed nicely, showing long-term sustainable net photocurrent from the adsorbed RB dyes (under 580 nm light).

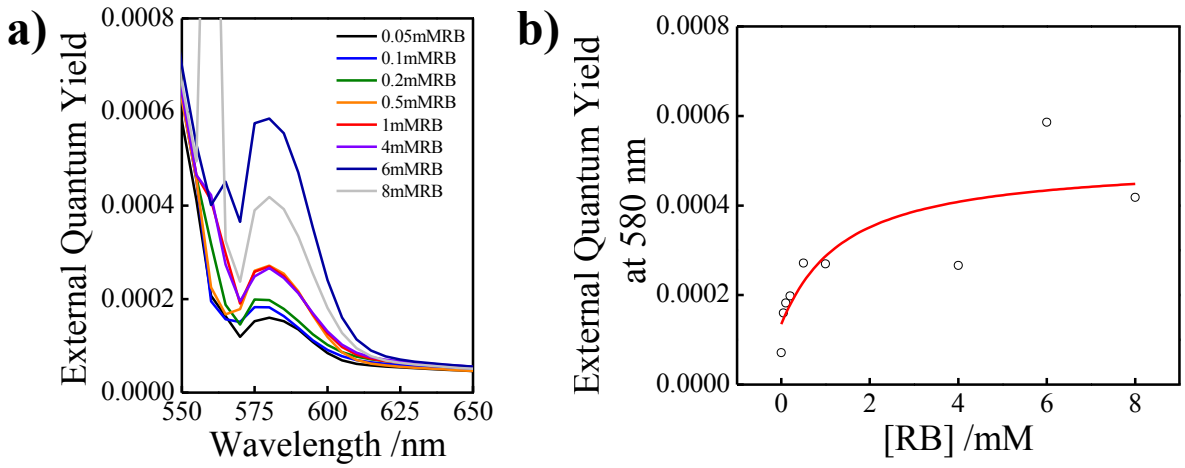

Figure V.12 (a) Measured external quantum yield at sub-band gap wavelengths for a p-GaP(100)/ZnO photoelectrode in clear 1 M KCl at pH 7.8. The electrode had been soaked in aqueous solutions containing concentrations of dissolved rose bengal ranging from 0.05 mM to 8 mM for 30 min prior to measurements. (b) Plot of measured external quantum yield at 580 nm as a function of the concentration of rose Bengal in the adsorption step. The data were collected at -0.6 V vs. Ag/AgCl.

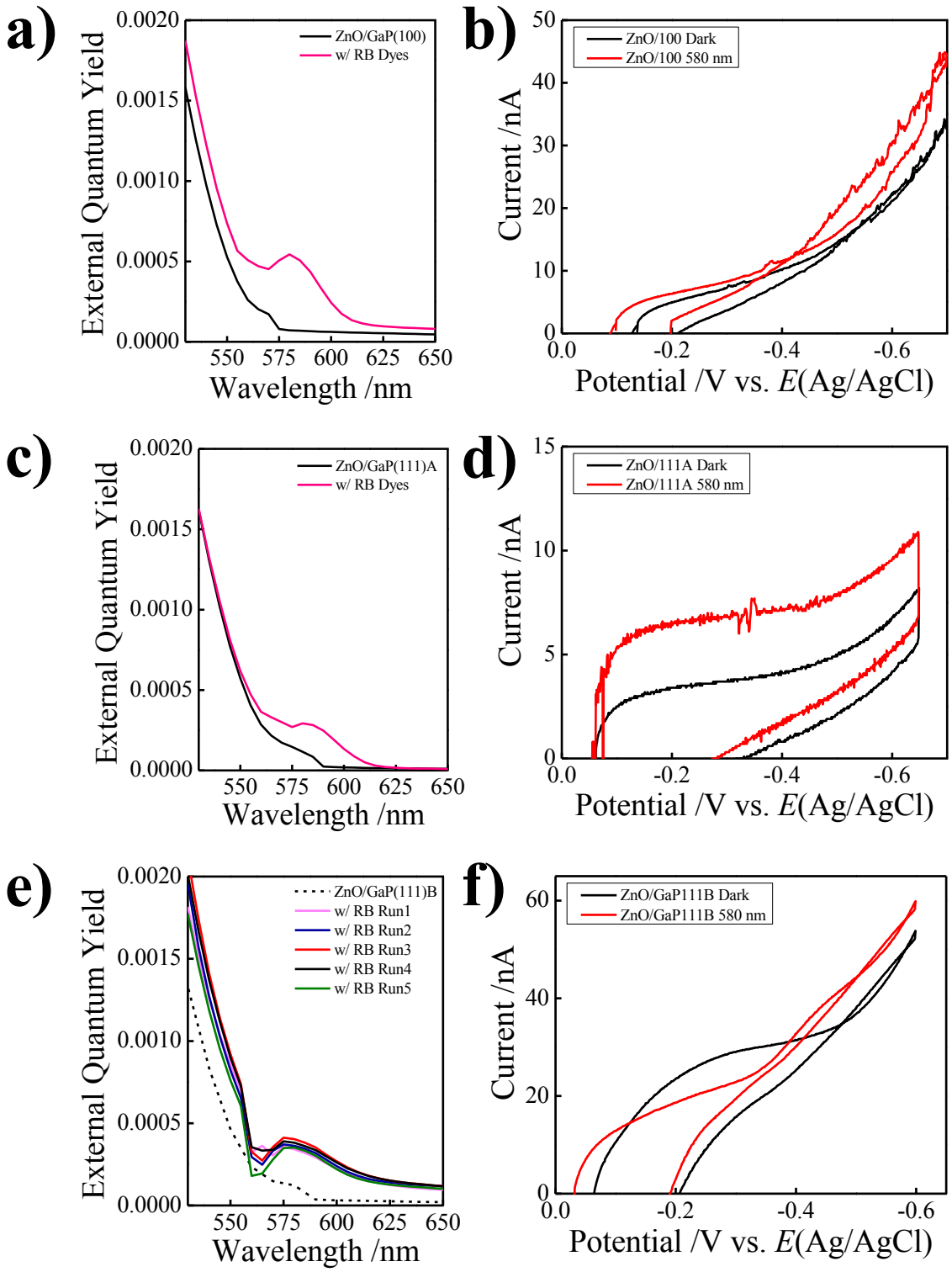

Figure V.13. Measured external quantum yield at sub-band gap wavelengths for (a) ZnO-coated p-GaP(100), (b) (111)A, and (c) (111)B photoelectrode in clear 1 M KCl at pH 7.8. Black line: Without RB; Colored line(s): With adsorbed RB. (b, d, f) Current-potential photoresponses of said electrodes in dark and under 580 nm light illumination. The EQY data collected at -0.6 vs. Ag/AgCl.

iii. Discussion

The cumulative data of RB-treated p-GaP/ZnO electrodes showed persistent dye adsorption and hole injection from the dyes to the p-GaP electrodes. The ZnO films on GaP substrate prepared by ALD were indeed polycrystalline. There was an amorphous interfacial layer between ZnO and GaP, and analytical TEM (with STEM capability) is necessary to determine the composition of the amorphous layer. Comparing to the TiO_2 film prepared by ALD at comparable temperatures and thickness, which is amorphous and flat, it is no surprise that the slightly rougher ZnO films facilitate more RB chelation than the TiO_2 film. Separate studies with TiO_2 did not show appreciable hole injection from dyes to the electrode (data not shown).[25] No I signals from RB molecules were detected in XPS on the p-GaP/TiO_2 samples after leaving in water for 20-30 min. Preliminary data showed that the adsorption of RB on p-GaP/ZnO is persistent and roughly follows monolayer coverage, although more data points and repetitions are necessary to fit the plot. Besides that, a model for surface coverage of the dyes on p-GaP/ZnO is necessary to quantify the concentration of RB molecules adsorbed on the electrode. This can be done with XPS and rigorous UV-vis spectroscopy measurements on an atomically flat and transparent substrate coated with ALD ZnO films.[24]

The stability of ZnO in aqueous electrolyte has always been a concern to the photoelectrochemistry field. So far, the ZnO layer is still intact after the EQY measurements, as confirmed by XPS. The X-ray reflectivity and TEM data of the GaP/ZnO interface *after* photoresponse measurements are pending. p-GaP/ZnO could potentially form a Type II buried junction when illuminated with photon energy/wavelengths greater than or equal to the band gap of GaP ($\geq$ 2.26 eV or $\leq$ 548 nm; $\mathbf{E}_g$ ZnO = 3.4 eV or 365 nm). The fact that photocathodic current was generated from the junction *with the presence of chromophores* when illuminated with sub-band gap wavelength was evidence of e^- transfer from p-GaP through the ZnO thin films. Despite the band energetic difference between the valence band edges of GaP and ZnO, at this point, the hole injection mechanism was believed to occur *via* mid-gap or defect states within the polycrystalline ALD ZnO layer. Electrochemical (e.g. current-potential measurements) and solid-state electrochemical impedance data would be useful for measuring the barrier heights and energy band positions of the p-GaP/ZnO heterojunctions.[26]

iv. Summary

This study shows persistent dye adsorption on a p-GaP/ZnO electrode prepared by ALD, that is, the dye molecules remained on the electrode surface after multiple photoresponse measurements in aqueous electrolyte. The adsorption was believed to be done by the chelation between the thin polycrystalline ZnO films on the GaP(100), GaP(111)A and (111)B surface and the carboxylate group on RB dye molecules. The magnitude of the EQY of the GaP electrode tracked with the concentration of the RB molecules during the adsorption step, although more repetitions are necessary to draw conclusion about the adsorption model. Net photocathodic current, an evidence for hole-injection from the dye molecules to the electrodes was consistently observed on ZnO-coated GaP(100), (111)A as well as (111)B phases. Electrochemical and solid-state electrochemical impedance data would be useful to provide insights to the p-GaP/ZnO heterojunction.

D. References

1. Lee, S.; Bielinski, A. R.; Fahrenkrug, E.; Dasgupta, N. P.; Maldonado, S., Macroporous p-GaP Photocathodes Prepared by Anodic Etching and Atomic Layer Deposition Doping. *ACS Appl Mater Interfaces.* **2016,** *8* (25), 16178-85.
2. Anselmi, C.; Mosconi, E.; Pastore, M.; Ronca, E.; De Angelis, F., Adsorption of Organic Dyes on TiO_2 Surfaces in Dye-Sensitized Solar Cells: Interplay of Theory and Experiment. *Phys. Chem. Chem. Phys.* **2012,** *14* (46), 15963-74.
3. Matsumura, M.; Matsudaira, S.; Taubomura, H., Dye Sensitization and Surface Structures of Semiconductor Electrodes. *Ind. Eng. Chem. Prod. Res. Dev.* **1980,** *19* (3), 415-421.
4. Wu, Y.; Yan, H.; Yang, P., Semiconductor Nanowire Array: Potential Substrates for Photocatalysis and Photovoltaics. *Top. Catal.* **2002,** *19* (2), 197-202.
5. Kayes, B. M.; Filler, M. A.; Putnam, M. C.; Kelzenberg, M. D.; Lewis, N. S., Growth of Vertically Aligned Si Wire Arrays over Large Areas (>1cm^2) with Au and Cu Catalysts. *Appl. Phys. Lett.* **2007,** *91* (10), 103110.
6. Bielinski, A. R.; Kazyak, E.; Schlepütz, C. M.; Jung, H. J.; Wood, K. N.; Dasgupta, N. P., Hierarchical Zno Nanowire Growth with Tunable Orientations on Versatile Substrates Using Atomic Layer Deposition Seeding. *Chem. Mater.* **2015,** *27* (13), 4799-4807.
7. Price, M. J.; Maldonado, S., Macroporous n-GaP in Nonaqueous Regenerative Photoelectrochemical Cells. *J. Phys. Chem. C.* **2009,** *113* (28), 11988-11994.
8. Rath, A.; Dash, J. K.; Juluri, R. R.; Rosenauer, A.; Satyam, P. V., Temperature-Dependent Electron Microscopy Study of Au Thin Films on Si(100) with and without a Native Oxide Layer as Barrier at the Interface. *J. Phys. D: Appl. Phys.* **2011,** *44*, 115301.
9. Bechelany, M.; Maeder, X.; Riesterer, J.; Hankache, J.; Lerose, D.; Christiansen, S.; Michler, J.; Philippe, L., Synthesis Mechanisms of Organized Gold Nanoparticles: Influence of Annealing Temperature and Atmosphere. *Cryst. Growth Des.* **2010,** *10* (2), 587-596.
10. Hobden, M. V.; Russell, J. P., The Raman Spectrum of Gallium Phosphide. *Phys. Lett. A.* **1964,** *13* (1), 39-41.
11. Gupta, R.; Xiong, Q.; Mahan, G. D.; Eklund, P. C., Surface Optical Phonons in Gallium Phosphide Nanowires. *Nano Lett.* **2003,** *3* (12), 1745-1750.
12. Xiong, Q.; Gupta, R.; Adu, K. W.; Dickey, E. C.; Lian, G. D.; Tham, D.; Fischer, J. E.; Eklund, P. C., Raman Spectroscopy and Structure of Crystalline Gallium Phosphide Nanowires. *J. Nanosci. Nanotechnol.* **2003,** *3* (4), 335-339.
13. Https://Www.Bruker.Com/Fileadmin/User_Upload/8-Pdf-Docs/Opticalspectrospcopy/Raman/Senterra/an/An520_Amorphous-Microcrystal-Silicon_En.Pdf.
14. Wang, N.; Tang, Y. H.; Zhang, Y. F.; Lee, C. S.; Lee, S. T., Nucleation and Growth of Si Nanowires from Silicon Oxide. *Phys. Rev. B.* **1998,** *58* (24), 58.
15. Dai, Z. R.; Pan, Z. W.; Wang, Z. L., Gallium Oxide Nanoribbons and Nanosheets. *J. Phys. Chem. B.* **2001,** *106*, 902-904.
16. Http://Resource.Npl.Co.Uk/Mtdata/Phdiagrams/Auga.Htm.
17. Borisenko, V. E.; Hesketh, P. J., Component Evaporation, Defect Annealing, and Impurity Diffusion in the III–V Semiconductors. In *Rapid Thermal Processing of Semiconductors*, Borisenko, V. E.; Hesketh, P. J., Eds. Springer US: Boston, MA, 1997; pp 113-148.
18. Wu, Y.; Fan, R.; Yang, P., Block-by-Block Growth of Single-Crystalline Si/SiGe Superlattice Nanowires. *Nano Lett.* **2002,** *2* (2), 83-86.

19. Yin, Y.; Rioux, R. M.; Erdonmez, C. K.; Hughes, S.; Somorjai, G. A.; Alivisatos, A. P., Formation of Hollow Nanocrystals through the Nanoscale Kirkendall Effect. *Science.* **2004,** *304* (5671), 711-714.
20. Hagedorn, K.; Collins, S. M.; Maldonado, S., Preparation and Photoelectrochemical Activity of Macroporous p-GaP(100). *J. Electrochem. Soc.* **2010,** *157* (11), D588-D592.
21. Yu, L.; Riddle, A. J.; Wang, S.; Sundararajan, A.; Thompson, J.; Chang, Y.-J.; Park, M. E.; Seo, S. S. A.; Guiton, B. S., Solid–Liquid–Vapor Synthesis of Negative Metal Oxide Nanowire Arrays. *Chem. Mater.* **2016,** *28* (24), 8924-8929.
22. Wippermann, K.; Schultze, J. W.; Kessel, R.; Penninger, J., The Inhibition of Zinc Corrosion by Bisaminotriazole and Other Triazole Derivatives. *Corros. Sci.* **1991,** *32* (2), 205-230.
23. Chitambar, M.; Wang, Z.; Liu, Y.; Rockett, A.; Maldonado, S., Dye-Sensitized Photocathodes: Efficient Light-Stimulated Hole Injection into p-GaP under Depletion Conditions. *J. Am. Chem. Soc.* **2012,** *134*, 10670-10681.
24. Spitler, M. T.; Calvin, M., Electron Transfer at Sensitized TiO_2 Electrodes. *J. Chem. Phys.* **1977,** *66* (10), 4294-4305.
25. Sriprang, P.; Wongnawa, S.; Sirichote, O., Amorphous Titanium Dioxide as an Adsorbent for Dye Polluted Water and Its Recyclability. *J. Sol-Gel Sci. Technol.* **2014,** *71*, 86-95.
26. Hu, S.; Richter, M. H.; Lichterman, M. F.; Beardslee, J.; Mayer, T.; Brunschwig, B. S.; Lewis, N. S., Electrical, Photoelectrochemical, and Photoelectron Spectroscopic Investigation of the Interfacial Transport and Energetics of Amorphous TiO_2/Si Heterojunctions. *J. Phys. Chem. C.* **2016,** *120* (6), 3117-3129.

CHAPTER VI

Education Research Contributions in Entry Level Chemistry Laboratory Courses

A. Overview

This chapter details my contributions to the designs and improvements of two introductory chemistry laboratory courses in the Department of Chemistry at the University of Michigan, namely *CHEM 242: Introduction to Chemical Analysis and Laboratory* and *CHEM 125 (Research-based): Organic-Inorganic Hybrid Perovskite Photovoltaic Cells*. The first section of the chapter describes a specific microfluidic laboratory experiment we developed for the CHEM 242 students. The experiment spans 2 weeks (8 hours total) and the students are introduced to the concepts of soft lithography as they design and characterize their own agar-based microfluidic chips. The goal of the experiment is to teach the students about the fundamentals of fluid dynamics through designing a chip that promotes optimum mixing within the channel. In the second week of the experiment, students are able to use the optimized chip to quantify the concentration of salicylic acid in iron(III)-salicylate complex by colorimetric analysis. The second section of the chapter describes a series of techniques and tools we developed for a freshmen-oriented research experience laboratory course with the intention to introduce multidisciplinary research to freshman students. This course spans 14 weeks (a 3-hour laboratory session and a 50-min lecture per week), and we chose the current hot topic in photovoltaic research field, i.e. the organic-inorganic hybrid perovskite solar cell, as the basis of the course due to its simplicity of construction and relevancy to the scope of general chemistry. Concepts of (photo)electrochemistry, solid state physics and light matter interactions are introduced in the course. We adopt a published protocol to fabricate these photovoltaic cells *via* electrodeposition, and the performance of the complete cells are characterized in a custom-made testing device under 1-sun illumination simulated using an ELH lamp. The students are encouraged to come up with a research question and conduct experiments to prove or disprove their hypotheses towards the final 4 weeks of the course. This chapter also accounts for my thoughts about the concept of multidisciplinary research laboratory course after being a Graduate

Student Instructor for this course for two semesters. The course's feasibility as well as suggestions for improvements is laid out at the end of this chapter.

B. On-Chip Mixing for Colorimetric Quantitation of Salicylic Acid in Agar Microfluidic Channels: An Undergraduate Laboratory Experiment

i. Introduction

"Lab on a chip" technology or microfluidics has gained much popularity over the past decade because high sensitivity can be achieved with very small sample size (down to nL) The field of microfluidics has potential to revolutionize chemical analysis as shown in clinical diagnostics, separations, DNA amplification, protein engineering, single cell analysis, to name a few.[1] Microfluidic devices are typically on the micrometer scale and can manipulate extremely small amount of fluids. In the on-going attempt to modernize undergraduate analytical chemistry curricula, many institutions have incorporated microfluidics as a tool to teach fundamental principles of chemistry such as crystallization and acid-base reactions.[2-5]

Photolithography is a common approach to device fabrication and polydimethylsiloxane (PDMS) is among the most common material used. Yang et al. introduced a soft lithography workflow which utilizes cost effective everyday materials such as coffee stirrers, paper plates, and Jell-O to mimic conventional photolithographic workflows.[6] In this experiment, we use agar as the base for our "polymer". Agar provides several advantages over Jell-O. It is translucent, allowing fluids to be easily visualized as they flow through microfluidic channels. It is also sturdy enough to peel off from the mold. Furthermore, agar cures relatively quickly (~15 minutes), significantly reducing the experimental time.

Fluid mixing in microfluidic channels can be challenging, thus making it difficult to probe chemical reactions. The chip geometries are modified in order to circumvent the issue of mixing, such as introducing bumps and turns to the microfluidics channels. Herein we describe a novel experiment, which uses image analysis (employing ImageJ, a Java-based image processing program available from the National Institutes of Health for free) to quantify the concentration of salicylic acid flowing through a microfluidic channel. This experiment will achieve several pedagogical goals; the goals of this experiment are (1) to introduce the fundamentals of microfluidics and (2) to teach the basics of lithography in the context of chip fabrication. Students will also use the chips they design to study fluid dynamics and to observe the difference

between laminar and turbulent flow. We choose the reaction of iron (III) and sodium salicylate because the iron (III) – salicylate complex is highly colored and easily visualized in the microfluidic device. Digital microscopes equipped with camera are used for data collection. Finally, students use RGB analysis to construct a calibration curve as a function of salicylate concentration. This calibration curve will be compared to a calibration curve constructed via a visible spectrometry (an experiment performed in the second week of the course).

ii. Experimental Overview

This experiment is intended for two 4-hour lab periods in a 200 level analytical laboratory course (Instrumental Chemical Analysis Lab). Chip fabrication and characterization can be accomplished in the first lab period. Students are encouraged to prepare multiple chips (at least 6) in the first lab period, to ensure success of the experiment. Figure VI.1 shows various chip geometries available for the experiment: a straight "Y-channel", a "Zig-Zag", and a "90°" right-angle design. Once the chips are made, students are responsible to characterize the chips by determining whether the chips promote laminar or turbulent flow regimes (see below for detailed description). The final part of the experiment is the on-chip detection of iron salicylate. Here, the students will use digital microscopes with camera and ImageJ to determine the concentration of various iron salicylate solutions by performing a RGB analysis.

(a) Fabrication of Microfluidic Chips

The main materials used to create the molds are aluminum weighing pans, wooden coffee stirrers, and super glue. The coffee stirrers are cut into different shapes and sizes depending on the design of the mold and then glued onto the aluminum pan, creating a specific pattern. Students produce three types of molds as shown in Figure VI.1: "Y-channel" molds, "Zig-Zag" molds, and "90°" molds. The Graduate Student Instructor will provide sample molds to ease the cutting process. Students get to construct their desired shape molds on the aluminum weighing pans by cutting and super gluing the coffee stirrers to their desired geometries. It is important that the entire length of each segment of the mold is glued securely, as any loose pieces can be displaced when the agar is added, thus ruining the chip. The channel(s) are arranged so that the inlets and outlets are at the edges of the plate. Once the coffee stirrers are glued to the pan, a light coat of nail polish is applied over the wooden stirrers and let dry. To make one mold, 4.5 g of agar powder is added to 150 mL of boiling DI water and stirred constantly with a stir bar. To streamline the process, the students are encouraged to use 600 mL of boiling water (1L glass

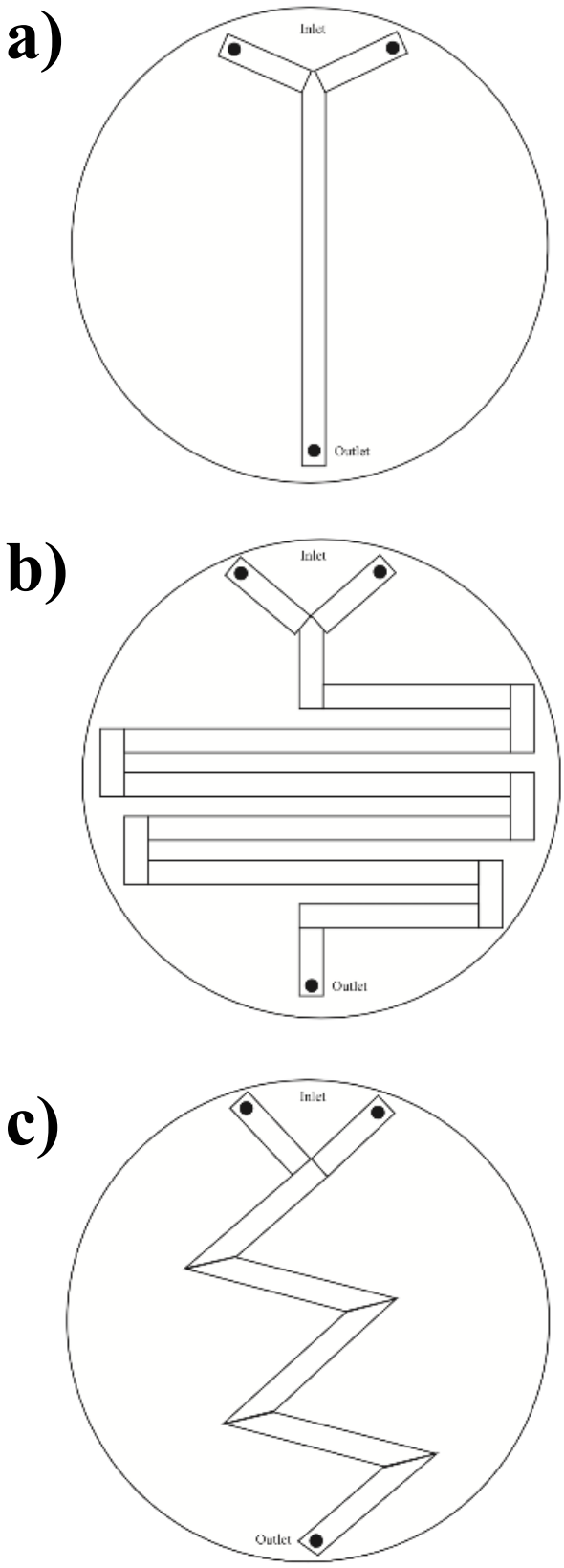

Figure VI.1: The outline of the channel geometries students will construct in the experiment. (a) A "Y" channel, (b) "90°" channel, and (c) "Zigzag" channel. Figures are not drawn to scale.

beakers are provided for this purpose) and add 18 g of agar slowly to avoid clumps (this amount should be enough for four molds so repeat twice). NOTE: As soon as the agar has been added and the solution is cooling, it will begin to set immediately, making transfer of the solution difficult if the chips are not ready for immediate pouring. The agar mixture is slowly poured into the molds, that were previously prepared, ensuring that the coffee stirrers are covered completely. The filled molds are allowed to cool to room temperature on the lab bench until they begin to set. After the chips have cured, carefully peel from the molds and place on acrylic surfaces.

(b) Characterization of Flow Regimes

Liquid flow is delivered at the "top" of the Y inlet by calibrated peristaltic pumps. The peristaltic pumps are set at flow rates in the range of 0.8-1.2 mL/min. To improve the robustness of the setup, the tubing are run through and held by the "helping hands" (Figure VI.2). Blue and red colored water are slowly, but evenly, injected into the separate channels. The flow profile is documented with digital microscope with cameras. The experiments are repeated with methanol-based solutions. Viscometers are used to measure the viscosity of the fluids; triplicate measurements are taken for statistics. All chip geometries are characterized in the same way.

(c) On-chip Detection of Salicylate

Five standard solutions of sodium salicylate are prepared in deionized water; 10 mM, 25 mM, 40 mM, 60 mM and 75mM. The chip design that promoted most mixing is the most ideal chip to use for this part of the experiment. Salicylate solutions are injected into one channel whereas acidic 10 mM ferric nitrate solution is injected into the other. In the case in which mixing is not achieved on any of the chips, students can mix 100 μL of each salicylate solution with 10 mL ferric nitrate solution and then inject this mixture into the single "Y" channel design. For either scenario, it is very important to start with the lowest concentration as there is some the purple solution tend to stain the channel in the chip. For RGB color analysis of the resulting images, the freeware ImageJ from the NIH is used.

(d) Hazards

Students should be in proper personal protective equipment at all times when working in the laboratory. Heat gloves or "hot hands" are strongly recommended when working with the boiling agar solutions. Laboratory gloves are also recommended when handling iron salicylate and acidic ferric nitrate solutions.

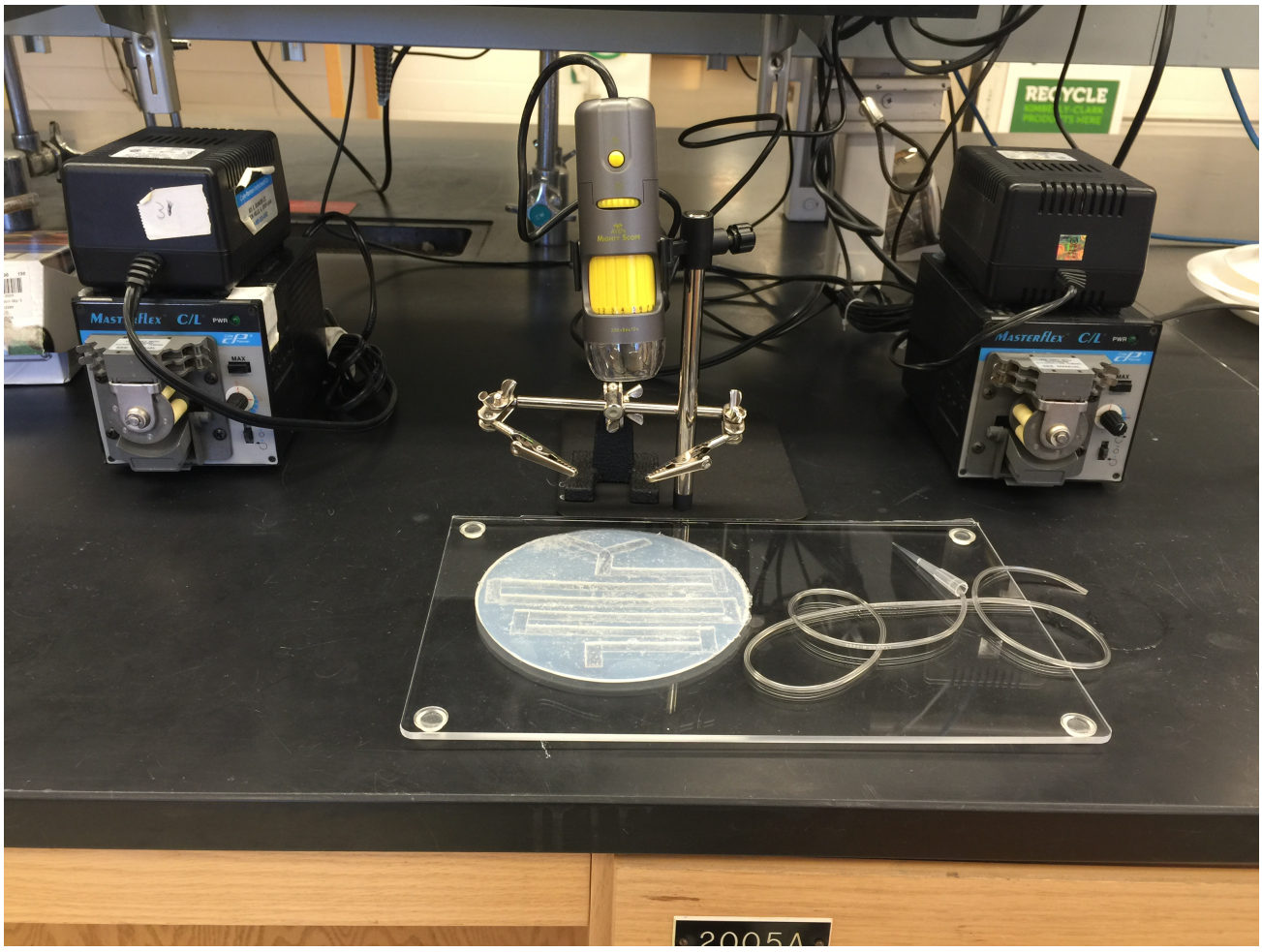

Figure VI.2: Experimental setup.

iii. Results and Discussion

(a) Chip Fabrication

The soft lithography technique used to fabricate the chip was adapted from the method in Yang et al. The changes made to their method provided many newly added benefits. Agar made much more sturdy and stable chip than Jell-O. The agar being translucent allowed for a clear visualization of on-chip mixing, in contrast to a Jell-O based mold that is highly colored, which was difficult for the Image J software to distinguish between colors during the analysis. The agar cured in less than 10 minutes compared to Jell-O, which took up to several hours to cure, and thus students were able to prepare many more chips in the event that some of their chips broke. Another change made here was the usage of superglue. Along with a light coat of nail polish, the coffee stirrer patterns that were glued using superglue, created a secure and smooth surface to enable very fine, uniform channels. Lastly, the cured chips were placed on an acrylic surface for analysis as oppose to a porous Styrofoam plate. The acrylic surface created a very good seal with the agar mold preventing any fluid from escaping the channels. With the aforementioned improvements, the students are able to prepare at least six chips in the first two hours of the first day of the two-part experiment. The ease of the protocol introduced students to lithography techniques in the context of fabricating microfluidic devices. The students were also given the opportunity to be creative in designing a chip in which they believed would provide optimal mixing.

(b) Characterization of chip: The Reynolds's Number

The microfluidic chips were characterized based on their ability to promote either laminar or turbulent flow. One consequence of laminar flow is that turbulent mixing of fluids does not occur, which is a major problem when attempting to perform reactions on chip, in our case attempting to mix iron (III) and salicylate on a chip. A number of dimensionless parameters exist which govern the behavior of fluids in microfluidic channels. The Reynolds number (R_e) relates inertial to viscous forces, the Peclet number which relates convection to diffusion, and the capillary number which relates viscous forces to interfacial forces, are all examples of such parameters. In this experiment, students were exposed to the R_e, as its variables are easily manipulated to alter the R_e value:

$$R_e = \frac{LV\rho}{\mu} \qquad \text{(VI.1)}$$

in which L is the channel length, V is the average fluid velocity, ρ is the fluid density, and μ is the dynamic viscosity. The R_e is used in this experiment to distinguish between laminar and turbulent flows. As the R_e increases, inertial forces dominate, destabilizing the flow, which result in irregular turbulent flow. Alternately, inertia becomes much less relevant at lower R_e numbers. The transition from laminar to turbulent flow regimes in a straight circular pipe occurs at R_e between 2000 and 3000, and this is the metric in which students used to differentiate the flow regimes (Table VI.1)[7]. The effect of R_e was demonstrated by having the students to manipulate the channel geometry and solvent viscosity in order to achieve on-chip mixing. Students used blue and red food coloring dye to visualize the fluid dynamics.

Figure VI.3 shows red and blue color dye as they flow through the "90°" geometry. The flow remains laminar through the channel when pure water was used (Figure VI.3a). As the methanol to water ratio increases, students observed more mixing in the channels (Figure VI.3b and 3c). Similar mixing behavior was observed with the other two channel geometries in another example. Mixing of the red and blue color dyes was not observed with 100% water despite the chip geometries (Figure VI.4a-4c). It was found that increasing the methanol content to 50% in water promoted mixing in the "Zig-Zag" and "90°" channels (Figure VI.4f and 4g, respectively). Very little to no mixing, however, was observed in the "Y" channel regardless to the methanol composition (Figure VI.4e) because of the lack of turns and angles to promote turbulent mixing.

The "90°" channel geometry exhibited the highest probability of fluid mixing, likely due to the long channel length and the amount of right angle turns in the chip. The R_e for the "90°" geometry was highest among the other chip geometries, as shown in Table VI.1, consistent with the observation we had earlier. The "Y" channel had the lowest R_e when compared to the other geometries, which explained the lack of mixing since the flows in the "Y" were almost exclusively laminar. One interesting finding in Table VI.1 is that the R_e value was much lower in the 50/50 water/methanol mixtures across all geometries because viscosity does not vary linearly with increasing methanol (Figure VI.5). As methanol and water were both presence in the mixture, it moves away from ideality.[8] Intermolecular forces (i.e. hydrogen bonds) increase as methanol content increase, resulting in a more viscous fluid. The viscosity peaked around 55% methanol in solution and then dropped when the solution is pure (either 100% water or 100% methanol) again.

Table VI.1. R_e as a function of methanol composition and channel geometry

Channel Geometry	Percent Methanol	Reynolds Number (R_e)
"Y"	0	256
	50	125
	100	296
"Zig-Zag"	0	430
	50	210
	100	496
"90°"	0	1530
	50	748
	100	1770

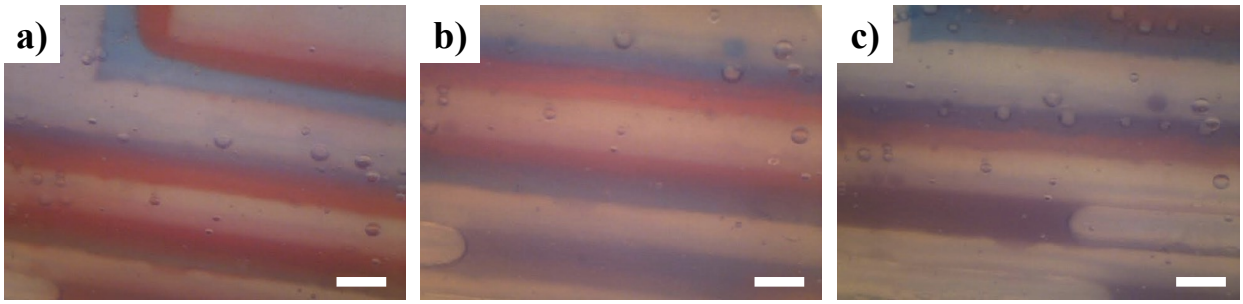

Figure VI.3: Representative digital photographs taken from student-built "90°" channel: (a) 100% DI water; the flow remains laminar. (b) 50/50 water/methanol; some degrees of mixing is observed. (c) 100% methanol; mixing is observed. The photos were taken from the same region of the channel. Scale bars: 5 mm.

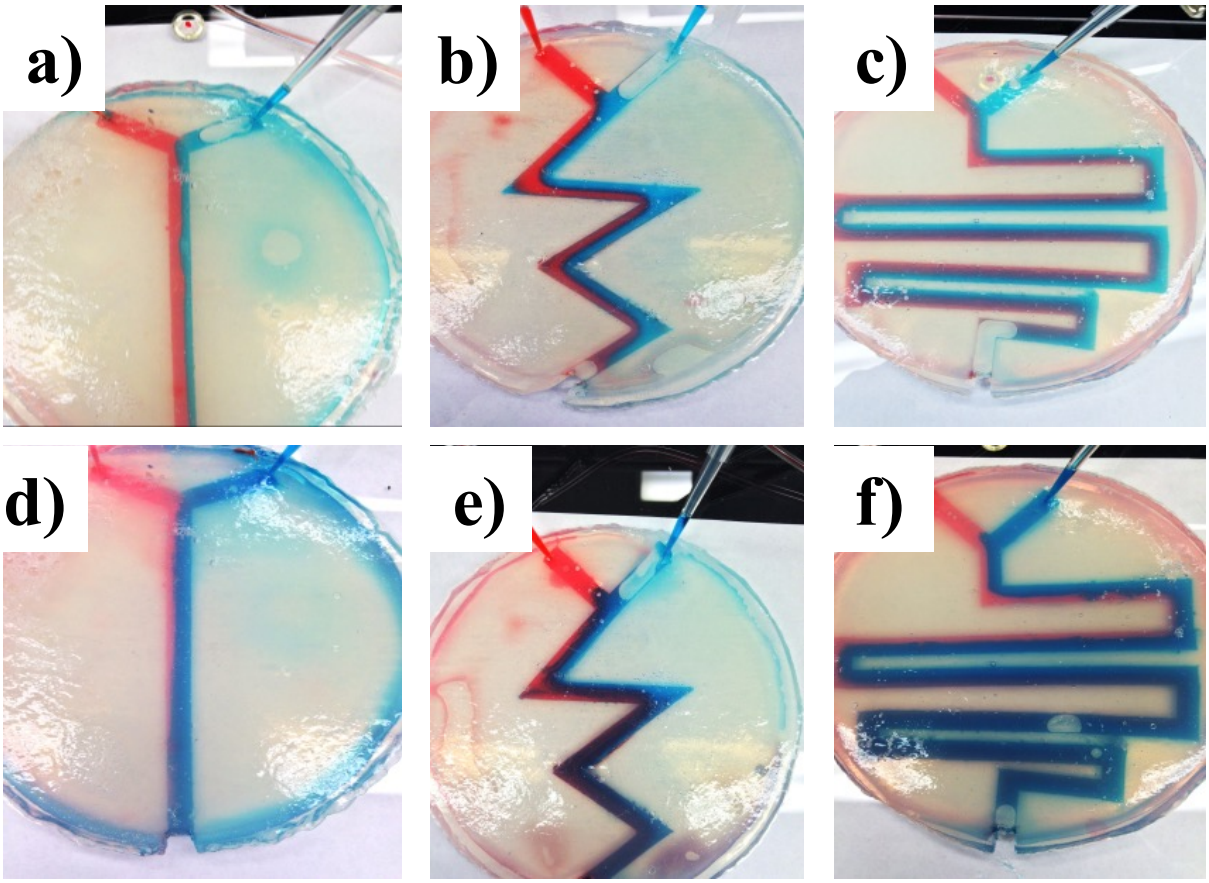

Figure VI.4: Digital photographs of student-built microfluidic devices. Channels shown in (a-c) has 100% water flowing through the channels. Despite the channel geometry, the flow remains laminar. Channels shown in (d-f) has 50% methanol added in the solvent. In this case, mixing is observed with the "Zigzag" and "90°" channels. Despite the fluid composition, very little to no mixing was observed in the "Y" channels.

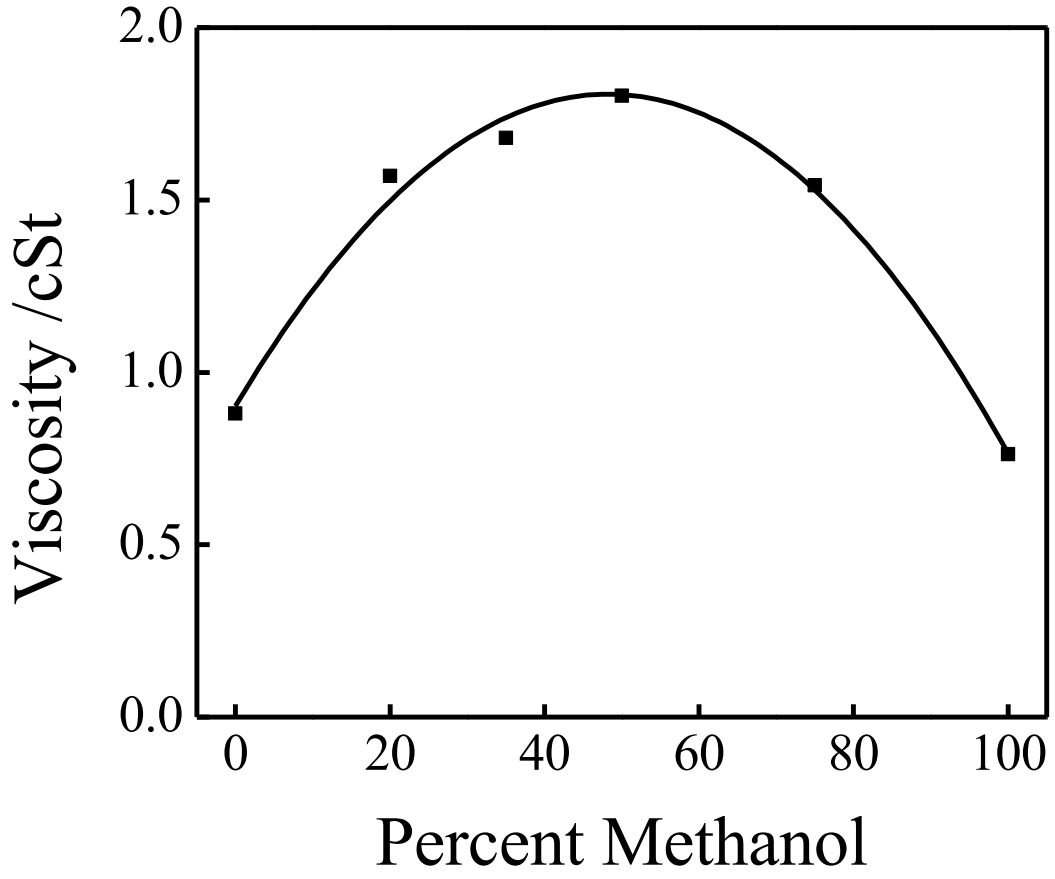

Figure VI.5: Kinematic viscosity as a function of methanol composition at room temperature.

(c) On-chip detection

During the second week of the experiment, students used RGB analysis to quantify known iron salicylate concentration to generate a calibration curve. The students compared the new calibration curve to the one generated using a UV-vis spectrometer (a previous experiment done at the beginning of the laboratory course). Since the iron(III)-salicylate complex is highly colored (purple), as the concentration of salicylate in solution increases, the darker the solution becomes (Figure VI.6), enabling the students to capture an image of the solution at the end of the microfluidic channel with a digital microscope/camera. Students then transferred the image to ImageJ where they calculated the RGB of the purple solution. Because the iron (III)-salicylate complex is purple, the average of red and blue color intensities were identified to be the most representative value for this type of analysis (red(mean) + blue(mean))/2). The students plotted the average RB values vs. concentration to generate a calibration curve. Note that in a RGB scale, the number decreases as the color gets darker. So in order to plot the calibration curve with a positive slope, the students subtracted the average RB values from 255 and plotted it against the known concentrations.

Figure VI.7 shows that a very good correlation between RGB and salicylate concentration can be achieved with the RGB analysis in ImageJ. It is important to note that in order to obtain reproducible data, students must carefully adjust the ambient lighting and be consistent in capturing images from the same region of the channel. In some cases, students preferred to use their smartphones to capture images as the smartphone cameras handled lighting better and produced higher resolution images. Nevertheless, the data shown is promising as it suggests that an agar-based microfluidic device can be used to quantify unknown concentrations of analytes.

We surveyed two laboratory sections before and after completion of the experiment. A total of 25 students completed the survey. The goal of the pre-survey was to gauge the level of knowledge the students had for microfluidics, fluid dynamics, and chip fabrication prior to performing the experiment. Whereas the post-survey gauged the level of confidence the students had on the aforementioned topics after the experiment. Figure VI.8 summarizes the results of the survey. Students responded to a series of statements with values ranging from 1 to 5, with strong disagreement as 1 and strong agreement as 5 respectively. Overall knowledge and understanding of microfluidics of the students increased after this experiment. Students, as a whole, felt much

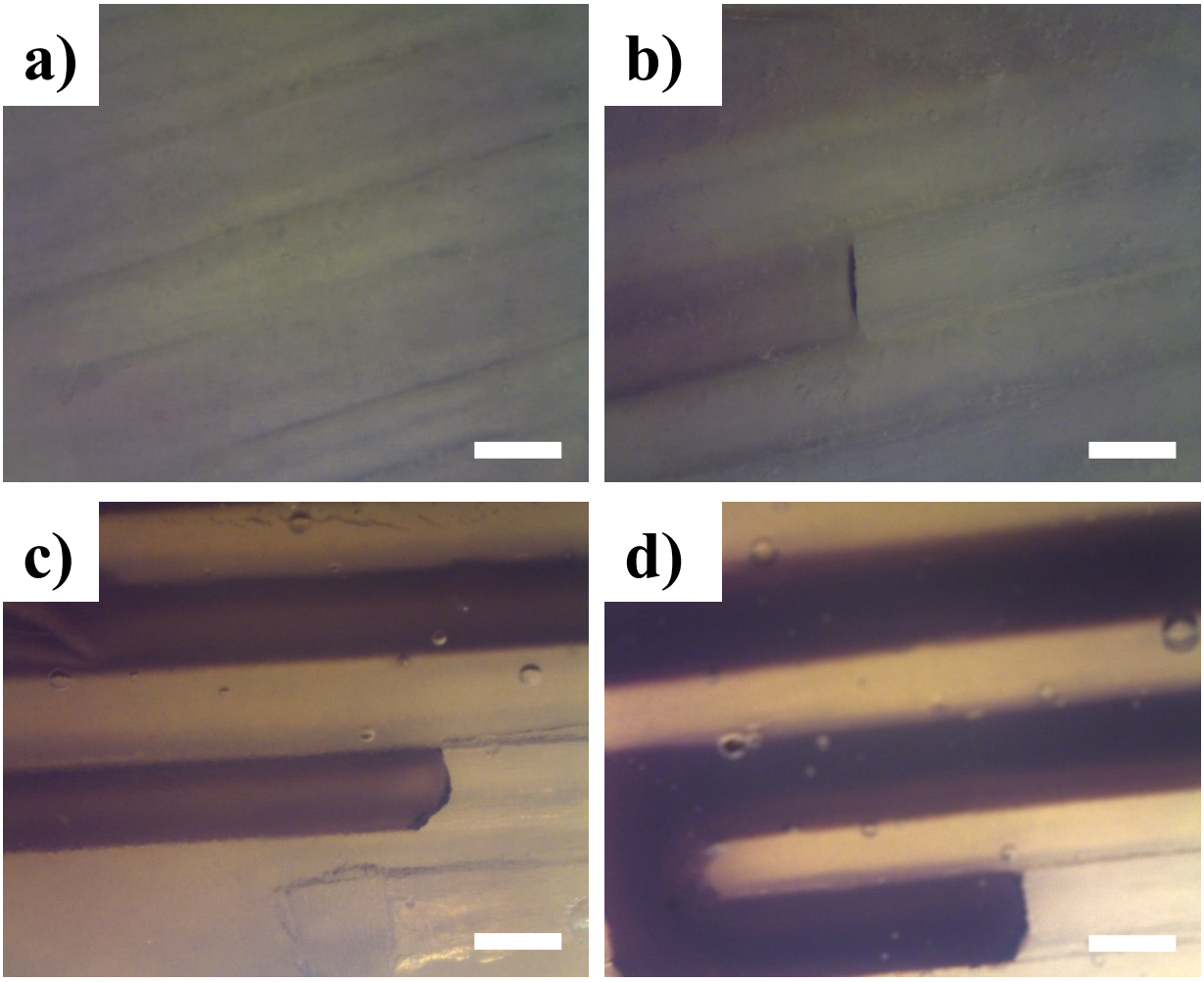

Figure VI.6: Close-up digital photographs of colored iron (III) – salicylate complex at increasing concentrations of salicylate ions. Scale bars: 5 mm.

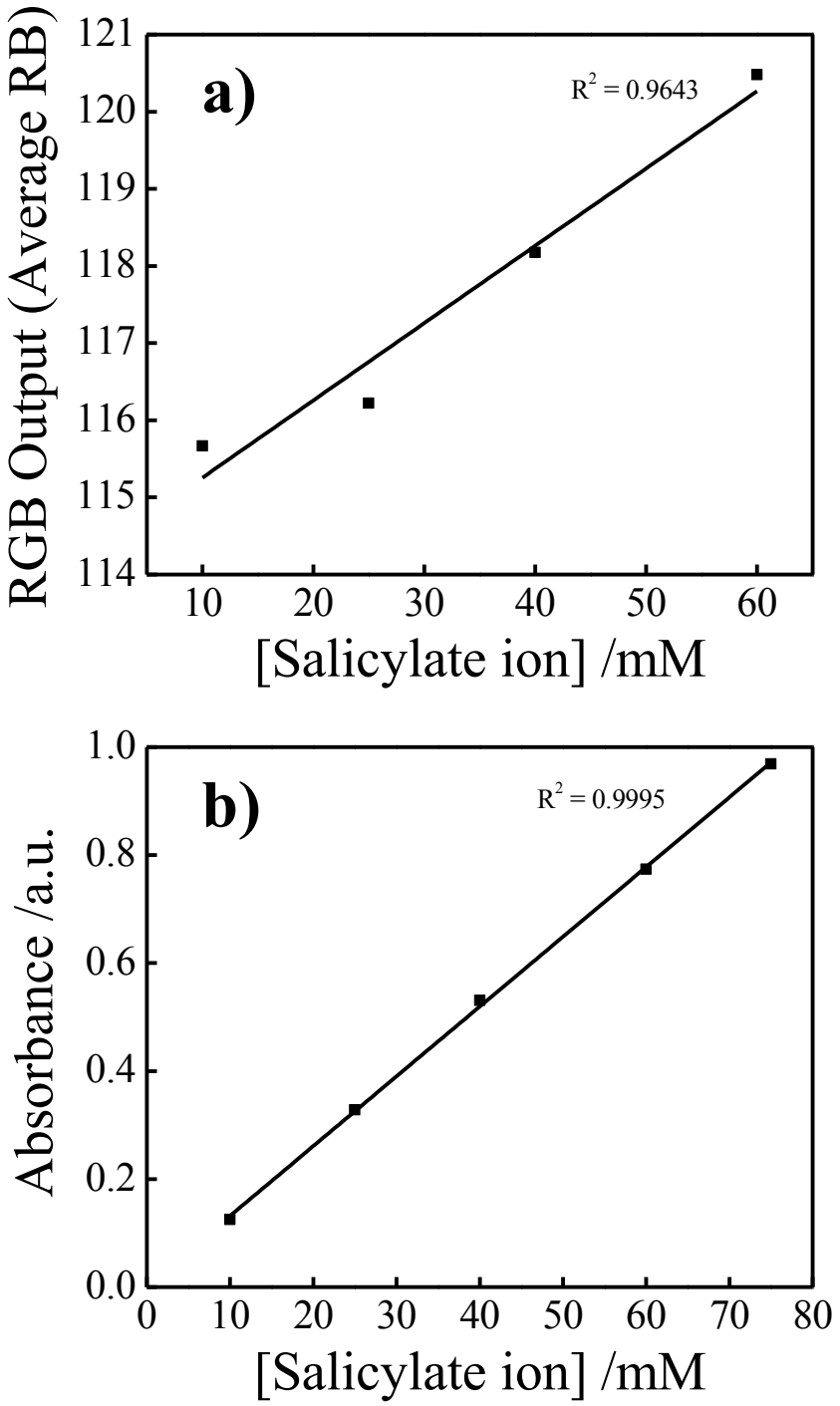

Figure VI.7: Representative calibration curve from student-built microfluidic device (a) and calibration curve generated via UV-vis spectroscopy (b). Very good correlation is observed between the RGB analysis and salicylate concentration as per the R^2 value of 0.96, comparable with the correlation observed in the absorbance vs. salicylate curve.

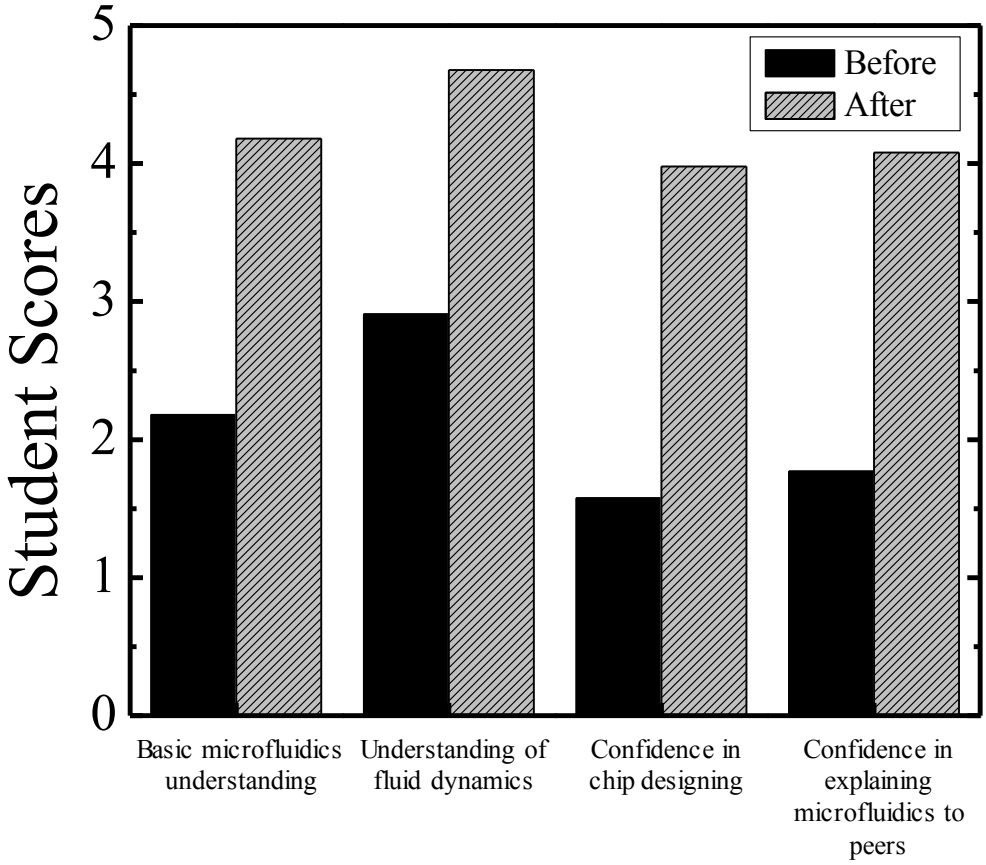

Figure VI.8: Results of student surveys: We surveys students across two sections (N = 25) before and after they completed the microfluidics experiment. Students replied to a series of statements with values that ranged from 1 (strongly disagree) to 5 (strongly agree).

more confident in explaining basic fundamentals of microfluidics to their peers after completing the experiment.

iv. Conclusion

The agar-based microfluidic experiment described in this report provided students with an inexpensive introduction to the field of microfluidics. Pedagogically, this experiment introduced students to the fundamentals of soft lithography, in the context of chip fabrications. Students also learned about fluid dynamics in a microfluidic channel. In addition to that, students were given the opportunity to be creative with everyday materials as they designed and optimized their own microfluidics devices for mixing. We are currently working on expanding this experiment to introduce an unknown sample component in which students will use their calibration curve generated from RGB analysis to determine the amount of salicylate present in the unknown sample. The experiment described here can be performed in high school and undergraduate laboratory courses everywhere.

C. Organic-Inorganic Hybrid Perovskite Materials Photovoltaic Cells

i. Introduction

Solar energy has been identified as a promising renewable resource alternative to fossil fuels. In order to harvest the energy from the sun effectively, the light absorber, usually a semiconductor, used in a photovoltaic cell must possess suitable band gap energy to capture a wide range of photons available in the atmosphere. Current thin film photovoltaic technology that employs GaAs (E_g = 1.45 eV) though has high solar-to-electricity conversion efficiency, its production cost is extremely high, which limited the accessibility of solar energy to developing countries, especially those that have poor grid system, near the equator. In order to implement this technology, it is essential to overcome the cost issue before we could harvest the immense amount available from the sun. In the last five years, organic-inorganic hybrid perovskite materials such as $CH_3NH_3PbI_3$ or $MAPbI_3$ (E_g = 1.5-1.7 eV) emerged as an attractive material for thin film photovoltaic due to its solution processability, high crystallinity, direct and tunable band-gaps, and high hole/electron transport ability,[9] which potentially lower the cost of production. Spin-coating is by far the preferred method to prepare the perovskite-based photovoltaic cell, but this method only deposits an even layer of material over a small substrate area and therefore unsuitable for large scale production. Recently, there are several reports

demonstrated electrodepositon as a potentially low-cost and highly scalable way to fabricate $MAPbI_3$ photovoltaic cells. Those reports suggested using an electrodeposition route to electrodeposit PbO_2 or PbI_2 and subsequently convert the as-deposited materials to $MAPbI_3$ *via* intercalation of CH_3NH_3I.[9-10]

The simplicity of this solution-processed $MAPbI_3$ provided us an opportunity to integrate photovoltaic research studies into college level chemistry syllabus since the photovoltaic device can be fabricated completely on bench-top. In this education report, we introduced and implemented a research-based entry-level chemistry laboratory course to college freshmen revolving around the fabrication of $MAPbI_3$ perovskite photovoltaic cell. This course spans 14-week with a 3-hour hands-on laboratory experience per week as well as a 50-min lecture that meets every week. The aims of this laboratory course are (1) to introduce multidisciplinary research experience to freshmen students and (2) to expose them to the scientific methods of making and testing their hypotheses, experimental designs and data collection. The structure of this *research-based* course still follows the standard syllabus of a general chemistry laboratory course for college freshmen, which covers topics related to acid-base chemistry, chemical reactions involving changes to the state of matter, periodic table chemistry and so on. However, topics such as light properties, electrochemistry and photoelectrochemistry are introduced and discussed during the course to help the students to understand the data they collected from their photovoltaic devices.

This report intended to cover the procedures for all the component of the photovoltaic cell fabrication process. Some of the data collected in the studies, mainly by myself from the trial experiments leading to the premier of the course, were presented to help the readers to visualize the type of results they anticipated from this course. Some survey data were collected from the students who took the course, although no presented in this report, showed a strong likeness to this multidisciplinary research experience in general. The suggestions for course improvements, both procedural (photovoltaic cell efficiency) and course structure, are outlined at the end of this report.

ii. Experimental Overview

This course structure is intended for 14 3-hour laboratory sessions conducted in one semester. The students spend 2/3 of the semester learning the protocols to make each component of the $MAPbI_3$ photovoltaic cell and use the remaining 1/3 of the sessions in the semester to

construct a hypothesis related to the $MAPbI_3$ photovoltaic research and test it. Students in this course follow the general experimental procedures outlined below, but are free to adapt and change the steps accordingly when making the photovoltaic cell.

(a) Preparation of TiO_2 Compact and Mesoporous Layers

The TiO_2 compact layer serves as an electron-transporting layer to regulate the direction of the electron flow in the photovoltaic cell. 0.15 M titanium diisopropoxide bis-acetylacetonate is prepared in1-butanol and spin-coated on a FTO glass using a 3-step setting: 500 RPM for 10 s → 600 RPM for 10 s → 1400 RPM for 20 s. The appropriate volume is 100 µL per 0.0625 cm^2. The TiO_2-coated FTO glass is then heated the to 125 ºC for 10 min to evaporate the solvent. To make the mesoporous layer, which serves as the scaffold for the $MAPbI_3$ crystals, 0.14 g 18NRT (obtained from Dye-Sol) is dissolved into 1 mL ethanol. The mixture is then spin-coated on the cured TiO_2/FTO glass at 2000 RPM for 20 s, with the ramp rate 400 RPM/s. The assembly is annealed in air for 30 min at 500 ºC.

(b) Electrodeposition of PbO_2 and Subsequent Conversion into $MAPbI_3$

The synthesis of $MAPbI_3$ on TiO_2/FTO glass is adapted from Chen at el. [10] which begins by electrodepositing PbO_2, then converting it to PbI_2 and finally into $MAPbI_3$. Electrodeposition is done in a custom-built electrochemical cell with a WheeStat potentiostat (Smokey Mountain Scientific, http://www.smokymtsci.com/project) as depicted in Figure VI.9. 0.1 M $Pb(CH_3COO)_2$, 0.2 M $NaNO_3$, and 0.1 M HNO_3 are used as the electrolyte for the electrodeposition in a standard two-electrode system, and the counter electrode is a platinized Cu strip which essentially is a 99.99% Cu strip that has been reacted electrodelessly in 0.042 M H_2PtCl_6 dissolved 2 M HCl for 45 min. The platinized Cu strip behaves like a pure Pt metal for hydrogen evolution reaction in 1 M H_2SO_4 (Figure VI.10). After electrodeposition, the brown PbO_2 samples are rinsed in DI water and dried under N_2 (g) thoroughly.

The conversion of PbO_2 to PbI_2 is done in 0.5-1.0 M HI in ethanol at room temperature. After the conversion, the substrate is washed in ethanol to remove excess HI and dried under a stream of N_2 (g). Conversion of the yellow PbI_2 to the dark brown $MAPbI_3$ is conducted by immersing the yellow substrate into CH_3NH_3I solution (6-10 mg/mL CH_3NH_3I in isopropanol). The as-prepared $MAPbI_3$ substrate is rinsed thoroughly in isopropanol and heated to 100 ºC for 15 min to evaporate the excess solvent.

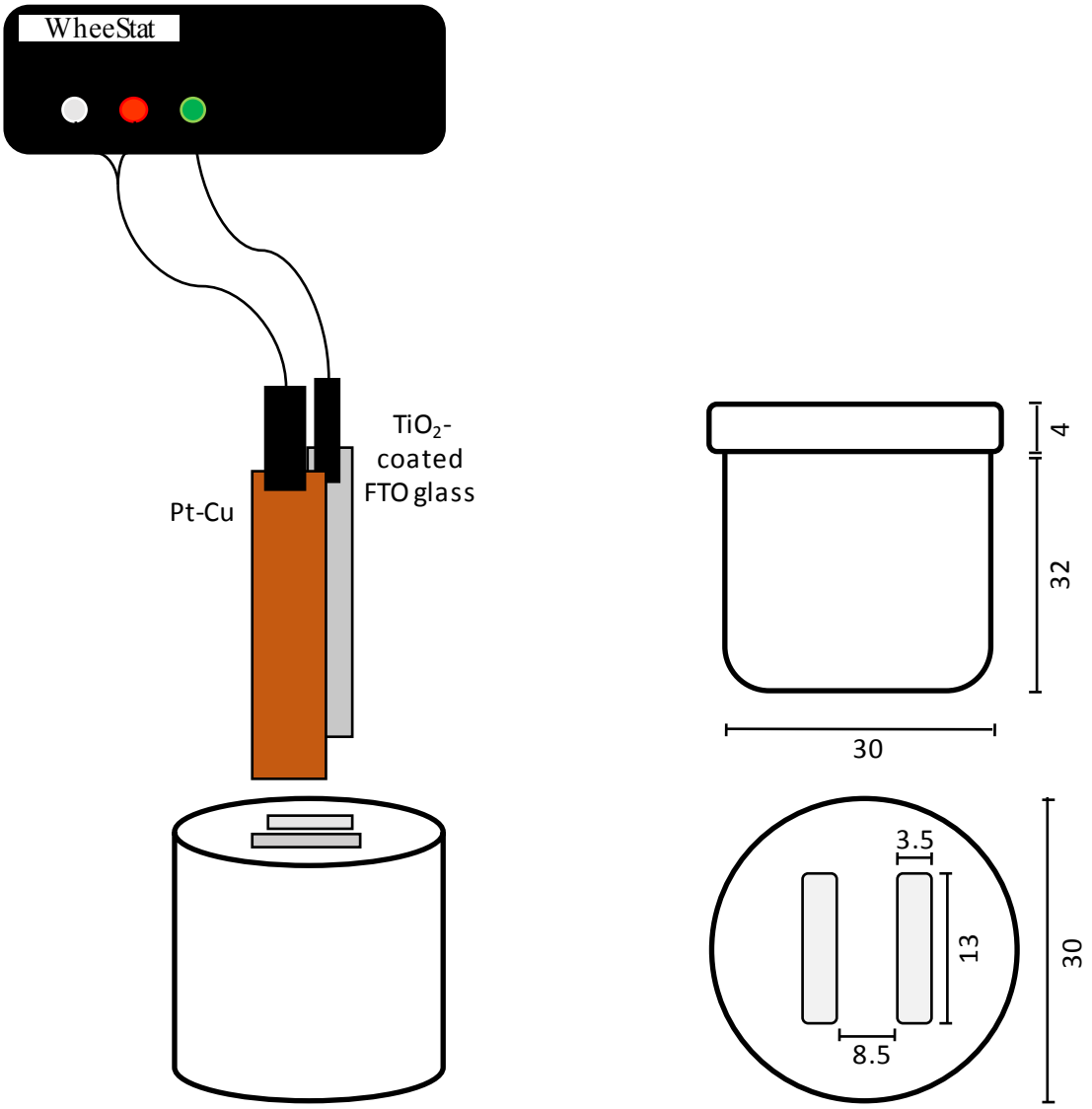

Figure VI.9. Schematic depiction of the electrodeposition experiment. The working electrode is the TiO_2-coated FTO glass, and the counter electrode is a platinized Cu strip. The dimensions and measurements of the electrochemical cell are listed in mm.

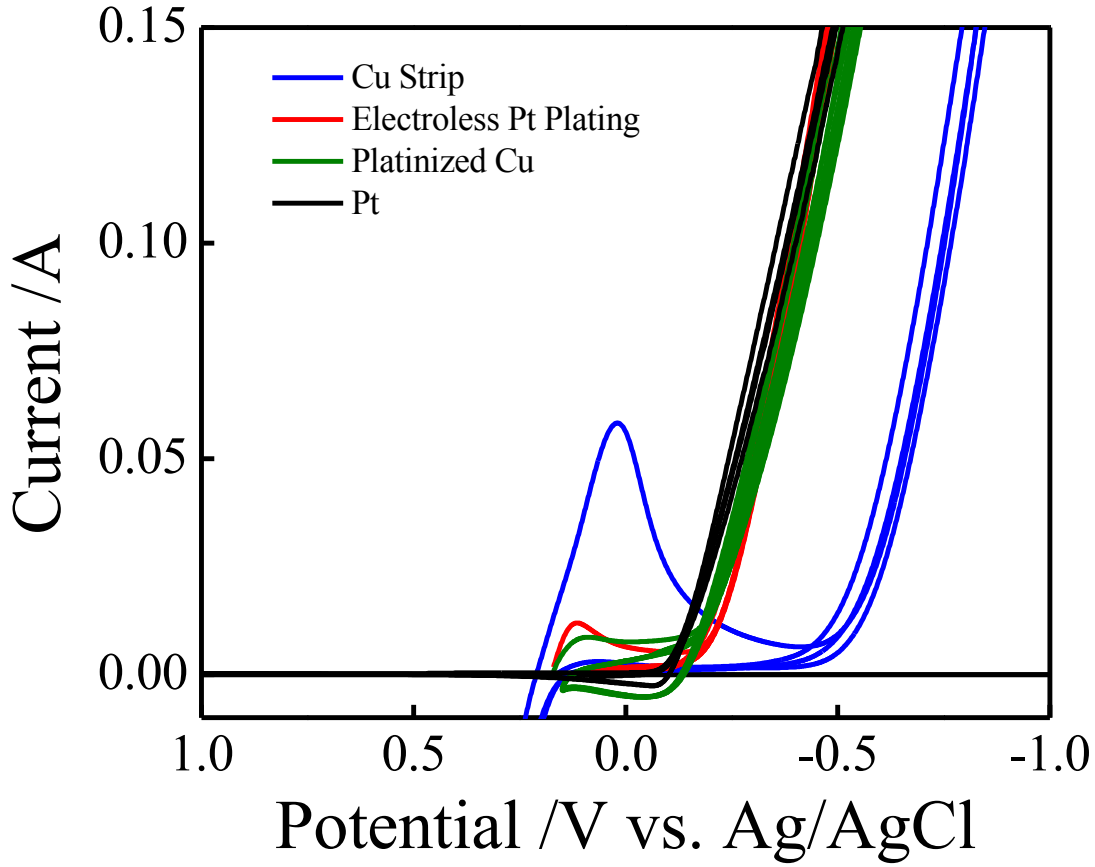

Figure VI.10. Current-potential curves of several counter electrode materials.

(c) Fabrication of Photovoltaic Cell

CuSCN is used as the hole-transporting layer for the $MAPbI_3$ photovoltaic cell. CuSCN is prepared by reacting molar equivalence ratio of $CuSO_4$ and KSCN using DI water as the solvent. The dried solid product is dissolved in dipropyl sulfide and deposited onto the cured $MAPbI_3$ layer by doctor-blading technique. The substrate is heated at 65 ºC on a hot plate for 5-10 min to evaporate the solvent. When the substrate is cooled to room temperature, a mask made of Kapton tape with an opening of 0.0707 cm^2 is placed onto the assembly to expose a small photoactive area for carbon ink deposition. The carbon ink suspension is prepared by mixing Super P with chlorobenzene. The finished photovoltaic cell is annealed at 100 ºC for 30 min.

(d) Light Absorption Properties of Photoactive Materials

The transparent yellow PbI_2 films is prepared by depositing approximately 60 μL of hot (T = 75 ºC) 0.8 M PbI_2 in N,N-dimethylformimide on a clean microscope glass slide using a spin coater. The coated glass slide is then dried on a hot plate set at 100 ºC to remove excess solvent. The orange intercalated Et-NH_2-PbI_2 films are prepared by reacting the dried PbI_2 films with ethanolamine vapor. Approximately 0.5 mL of ethanolamine is placed in a development chamber for 5-10 min to saturate the chamber with ethanolamine vapors. Then, the PbI_2 film is placed adjacent to the ethanolamine vapor source for 25 min or until a bright orange film is formed. To obtain the UV-vis spectra of the yellow and orange films, a custom-made acrylate holder designed to hold up to two glass slides (Figure VI.12) is used to collect the said data in an Ocean Optics spectrometer.

(e) Hazards

Students should be in proper personal protective equipment at all times when working in the laboratory. All experimental procedures described here must be performed in a fume hood as the chemicals used in the experiments are highly toxic and volatile if not handled properly. The students are highly recommended to familiarize themselves with the SDS of each chemical.

iii. Results and Discussion

Figure VI.11a-11d shows the schematic depictions of the general procedure the students were taught in the course to fabricate the $MAPbI_3$ photovoltaic cell, but they had the freedom to vary the details accordingly. The procedure used to prepare the TiO_2 compact as well as the mesoporous layers yielded thickness that were optimized for electron transfer from the $MAPbI_3$ crystals,[11] which were approximately 40 nm and 400 nm, respectively. Students were

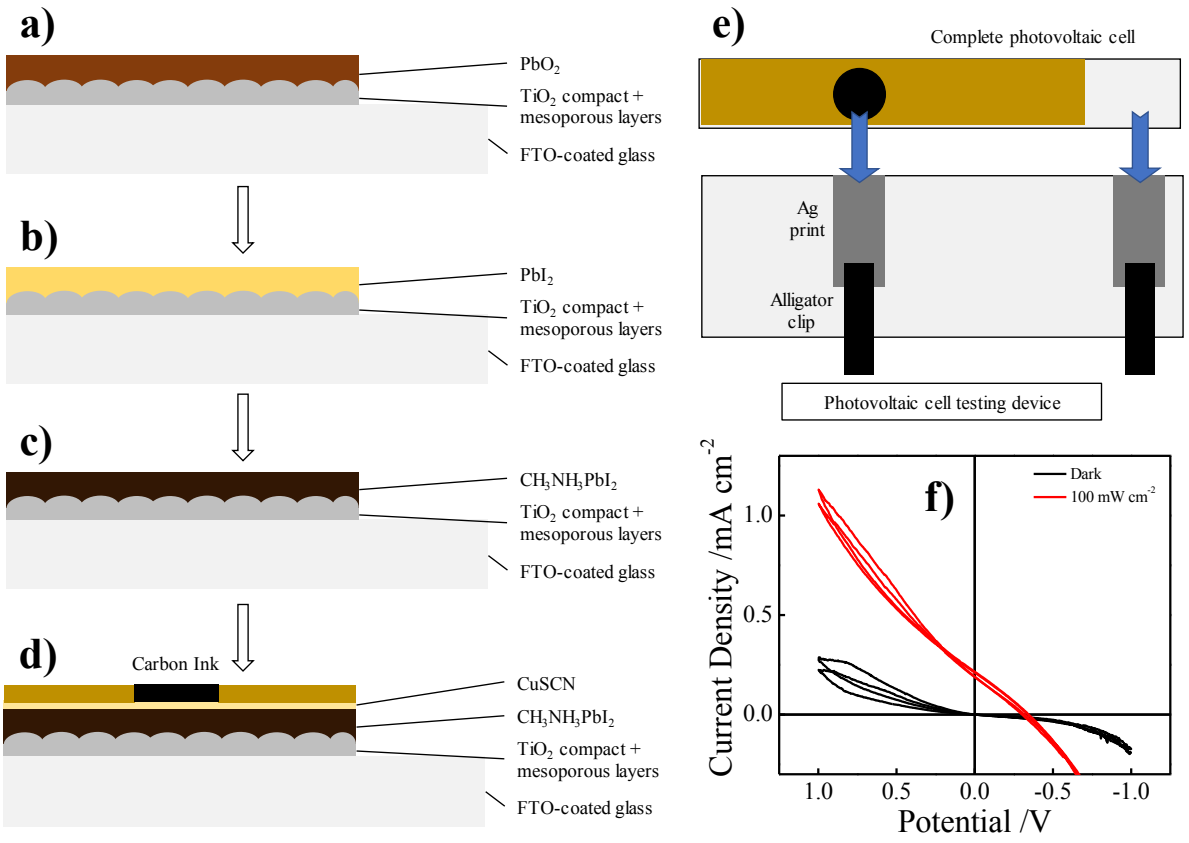

Figure VI.11. Schematic depiction at cross-section of the $MAPbI_3$ photovoltaic cell: (a) electrodeposition of PbO_2 on TiO_2-coated FTO glass, (b) conversion of PbO_2 to PbI_2, (c) conversion of PbI_2 to $MAPbI_3$, and (d) final assembly of photovoltaic cell completed with CuSCN layer, Kapton tape mask, and carbon ink as the ohmic contact. (e) Top-down view of the complete cell making electrical contact to a custom-built photovoltaic cell testing device for J-E measurement. (f) The J-E plot of a representative $MAPbI_3$ photovoltaic cell prepared as described in the text. Under 100 mW cm^{-2} illumination, $\eta = 0.02$ %.

familiarized with the band energy, functions and relationship of the TiO_2 and $MAPbI_3$ and how electrons diffused through the layers. Using the TiO_2/FTO glass substrate, the students electrodeposited PbO_2 by applying a potentiostatic bias calculated based on the following half reactions:

$$Pb^{2+} + 2H_2O \rightarrow PbO_2 + 4H^+ + 2e^- \qquad E^0 = +1.468 \text{ V vs. NHE} \qquad \text{(VI.2)}$$

$$2H^+ + 2e^- \rightarrow H_2 \qquad E^0 = 0.00 \text{ V vs. NHE} \qquad \text{(VI.3)}$$

Using the electrodeposition as example, the students were introduced to the concept of nonspontaneous chemical reactions (+ΔG), where an external energy was supplied to drive the chemical reaction. In the subsequent experiment the students were introduced to spontaneous chemical reaction (-ΔG) when they converted the PbO_2 films into the yellow PbI_2 and then the dark brown $MAPbI_3$ via reactions (4) and (5). This further shows the versatility of this course and how each experiment could be integrating into general chemistry topics/syllabus.

$$PbO_2 + 4HI \rightarrow PbI_2 + I_2 + 2H_2O \qquad \text{(VI.4)}$$

$$PbI_2 + CH_3NH_3I \rightarrow CH_3NH_3PbI_3 \qquad \text{(VI.5)}$$

Figure VI.11d shows the cross-section of the complete $MAPbI_3$ photovoltaic cell with a thin layer of CuSCN as the hole-transporting layer, Kapton tape as mask, and carbon ink as the ohmic back contact. The exposed FTO glass and the carbon ink were used to make contact to a testing device for power conversion efficiency measurements and characterizations, as depicted in the diagram in Figure VI.11e. There are three quantities that characterize the performance of a photovoltaic cell, namely short-circuit current (I_{sc}), open-circuit voltage (V_{OC}), and the fill-factor (FF). I_{sc} is the current that would flow between the two electrodes (FTO glass and carbon back contact) in the cell if connected directly to create a short circuit. The V_{OC} is a measure of the maximum Gibbs free energy that is available in the cell at open circuit, and FF is the rate at which the cell approaching its limiting short circuit current value. The complete photovoltaic cell were tested in the dark and under 1-sun illumination (P_{in} = 100 mW cm^{-2}) simulated by an ELH lamp by varying the magnitude of the resistive load in the external circuit. This can be done using a potentiostat/WheeStat or a variable resistor. A current density vs. potential (J-E) plot similar to the graph shown in Figure VI.11f was generated, and the V_{OC} and J_{SC} (short-circuit current *density*) were recorded to calculate the energy conversion efficiency of the photovoltaic cell using the following equations:

$$\eta = \frac{J_{sc} \times V_{oc} \times FF}{P_{in}} \quad \text{(VI.6)}$$

$$\text{where } FF = \frac{J_{mp} \times V_{mp}}{J_{ph} \times V_{oc}} \quad \text{(VI.7)}$$

in which J_{sc} is the current density value obtained at E = 0 V, V_{oc} is the photovoltage obtained at J = 0, and J_{mp} and V_{mp} is the maximum power point on the J-E plot indicated by the point where the product of its (x, y) is at its greatest value ($P = I\ x\ V$).

The power conversion efficiency of the cell in Figure VI.11f was η = 0.02% with V_{OC} = 350 mV, J_{SC} = 0.216 mA cm^{-2}, and FF of 0.25. Poor figure of merits were mainly due to the carbon ink layer cracking and/or flaking after the last annealing step. The unstable carbon layer failed to create a good ohmic contact between the $MAPbI_3$ and the pins on the photovoltaic cell testing device and exposed the underlying materials to the pins directly. Both which could increase the overall resistance and decrease the FF. Another cause for the low η value was the thickness of the electrodeposited PbO_2 films. The PbO_2 film was the foundation for $MAPbI_3$, but since the film was coated on a very rough mesoporous TiO_2 layer, there might be gaps and void spaces during the electrodeposition that carried through the end product. Such imperfections could cause short circuits in the photovoltaic cell and thus lowering the conversion efficiency. This problem could be overcome by encouraging the students to conduct electrodeposition with various durations and measure the PbO_2 thickness under ellipsometry, atomic force microscopy or scanning electron microscopy. And for the carbon ink, in the future, one could replace the chlorobenzene with another solvent more compatible with Super P and add a binder (polyvinylydene fluoride, PVDF) to the Super P suspension to create a more sticky ink layer. Other carbon ink deposition methods could be explored as well. For example, carbon deposited by pyrolyzer, soot from candle wax, reduced graphene oxide, and Chinese calligraphy carbon paste. The conductivity of the carbon should be measured beforehand to determine its suitability.

The light absorption properties of the photovoltaic materials were explored using a yellow PbI_2 film and an ethanolamine intercalated orange Et-NH_2-PbI_2 film in the UV-vis spectroscopy. Figure VI.12a and VI.12b shows the transmittance spectra of the PbI_2 and Et-NH_2-PbI_2 films obtained before and after reaction, respectively. The onset or point of inflection in these two spectra helped the students to learn the relationship between visible light absorption

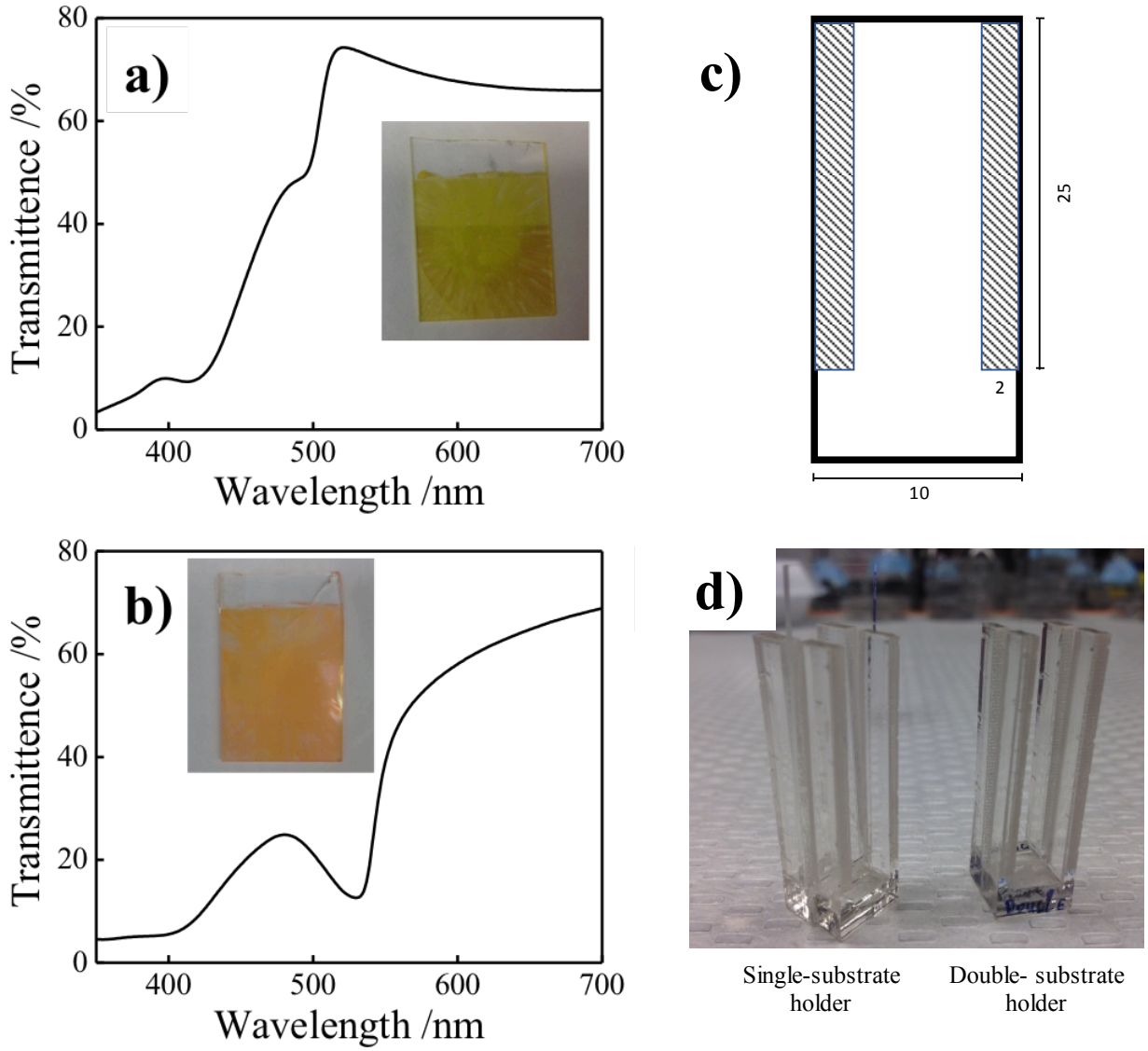

Figure VI.12. Transmittance spectra collected from the (a) yellow PbI_2 film and (b) the same film after converted to an orange Et-NH_2-PbI_2. (c) The measurements of the thin film UV-vis holder made from a 6 mm thick acrylic sheet in a CO_2 laser cutter; shaded area denotes "rastering mode" instead of cutting. (d) The digital photograph of the finished holders. The single-substrate holder is done by rastering the shaded area in (c) at 50% laser power while 80% is used to make the double-substrate holder.

and reflection in photoactive materials, and correlate it to the band gap energy of the materials. The details about the acrylic holder and designs were shown in Figure VI.12c and VI.12d.

The purpose of this laboratory course is to introduce college freshmen to interdisciplinary research that mimics the research experience of a researcher in a scientific field setting. Each component of the $MAPbI_3$ photovoltaic cell was thoroughly discussed in lectures with the fundamental concepts to help the students to understand the function of each layer. In the final 1/3 of the semester, the students were asked to provide a hypothesis related to an aspect of the perovskite photovoltaic field and propose an experimental plan to investigate the hypothesis. The students discussed their proposals with the professor and Graduate Student Instructors before embarking on their quest. Although the course received good feedback from the students, it was too ambitious in my opinion to try to teach them both chemistry fundamentals and research methods at the same time. The course was modeled after a regular general chemistry laboratory module, in which a theme/topic/experiment-of-the-week was introduced to the students and they handed in the in-lab reports and quizzes pertain to that week's topic for points. This module while is fine for a regular class it may not be suitable for a class that emphasized on multidisciplinary research experience, because students only would think about the subject when they were in that class, in other words, the students would not be creative and proactive with their research topic outside of the weekly 3-hour laboratory period. Several suggestions to consider when relaunching this course including (1) teaching the fundamentals of the experiments during the 50-min lectures and (2) introducing checkpoint or experimental suggestions for that particular laboratory period to sharpen the students' scientific/research skills early on. For example during the PbO_2 electrodeposition week, the GSIs could instruct the students to collect data that relate the thickness and deposition time and arrive at a conclusion (mandatory) as to which parameters is best suited for their purpose. The same idea could be applied to other weeks as well. And (3) grading the students' in-lab report based on their ability to plan for an experiment (before coming in) and to arrive at a strong, clear and unbiased conclusion at the end of the lab period. These suggestions, when implemented well, could keep the students on track in learning the research methods along with the fundamentals.

The idea of bringing multidisciplinary research experience to college students is great, but as mentioned before, it may be more rewarding to focus on teaching the students the scientific research methods than doing both research method and fundamentals. Hence, this

course model would better suit for the upperclassmen major in Chemistry and Physics. Instead of introducing the fundamentals week-by week, one could provide the students with journal articles relevant to the topics, and quizzes and exams on the fundamentals when appropriate throughout the duration of the course. The students could also be given chances to present their findings as teams of 2-4 persons in the form of research group meeting during the weekly 50-min lecture.

iv. Conclusion

The $MAPbI_3$ perovskite-based photovoltaic research was successfully implemented as an entry-level chemistry laboratory course with the vision to bring multidisciplinary research experience to college freshmen. The students were taught the usual general chemistry topics as well as solid state physics and (photo)electrochemistry during the course to help them to understand and interpret the data they collected.

D. References

1. Wheeler, A. R.; Throndset, W. R.; Whelan, R. J.; Leach, A. M.; Zare, R. N.; Liao, Y. H.; Farrell, K.; Manger, I. D.; Daridon, A., Microfluidic Device for Single-Cell Analysis. *Anal. Chem.* **2003,** *75*, 3581-3586.
2. Chia, M. C.; Sweeney, C.; Odom, T. W., Chemistry in Microfluidic Channels. *J. Chem. Ed.* **2011,** *88*, 461-464.
3. Piunno, P. A. E.; Zetina, A.; Chu, N.; Tavares, A. J.; Noor, M. O.; Petryayeva, E.; Uddayasankar, U.; Veglio, A., A Comprehensive Microfluidics Device Construction and Characterization Module for the Advanced Undergraduate Analytical Chemistry Laboratory. *J. Chem. Ed.* **2014,** *91* (6), 902-907.
4. Feng, Z. V.; Edelman, K. R.; Swanson, B. P., Student-Fabricated Microfluidic Devices as Flow Reactors for Organic and Inorganic Synthesis. *J. Chem. Ed.* **2015,** *92* (4), 723-727.
5. Hemling, M.; Crooks, J. A.; Oliver, P. M.; Brenner, K.; Gilbertson, J.; Lisensky, G. C.; Weibel, D. B., Microfluidics for High School Chemistry Students. *J. Chem. Educ.* **2014,** *91* (1), 112-115.
6. Yang, C.; Ouellet, E.; Lagally, E. T., Using Inexpensive Jell-O Chips for Hands-on Microfluidics Education. *Anal. Chem.* **2010,** *82*, 5408-5414.
7. Squires, T. M., Microfluidics: Fluid Physics at the Nanoliter Scale. *Rev. Mod. Phys.* **2005,** *77*, 977-1026.
8. Colin, H.; Diez-Masa, J. C.; Guiochon, G.; Czajkowska, T.; Miedziak, I., The Role of the Temperature in Reversed-Phase High-Performance Liquid Chromatography Using Pyrocarbon-Containing Adsorbents. *J. Chromatogr.* **1978,** *167*, 41-65.
9. Huang, J. H.; Jiang, K. J.; Cui, X. P.; Zhang, Q. Q.; Gao, M.; Su, M. J.; Yang, L. M.; Song, Y., Direct Conversion of Ch3nh3pbi3 from Electrodeposited Pbo for Highly Efficient Planar Perovskite Solar Cells. *Sci. Rep.* **2015,** *5*, 15889.
10. Chen, H.; Wei, Z.; Zheng, X.; Yang, S., A Scalable Electrodeposition Route to the Low-Cost, Versatile and Controllable Fabrication of Perovskite Solar Cells. *Nano Energy.* **2015,** *15*, 216-226.
11. Choi, J.; Song, S.; Horantner, M. T.; Snaith, H. J.; Park, T., Well-Defined Nanostructured, Single-Crystalline Tio2 Electron Transport Layer for Efficient Planar Perovskite Solar Cells. *ACS Nano.* **2016,** *10* (6), 6029-36.

APPENDIX

Effects of Redox Couple Concentration in Dye-Sensitized Photocathode Assembly

A. Background

Ever since O Regan and Grätzel introduced nanostructured n-TiO_2 dye-sensitized solar cell (DSSC) module with Ru-based dyes and a redox shuttle that boosted the overall photon conversion efficiency to 7% in 1991,[1] many modifications have been made to the cell, but little to no attention have been made to the concentration of the redox shuttle. In the Grätzel DSSC, iodide/triiodide in nonaqueous electrolyte is almost always used as the redox shuttle for n-TiO_2 or the dye-adsorbed photoanode. As explained in Chapter I, GaP has several advantages as a photocathode material for DSSC. So far, our group have demonstrated hole injection from dyes into the p-GaP photocathode in aqueous electrolyte containing methyl viologen ($MV^{2+/+}$)[2] and europium(III) chloride ($Eu^{3+/2+}$)[3-4] as they are good candidates to form a depleted junction in p-GaP with acceptable photovoltage. This section of the thesis reports data pertaining to the extent of photocurrent (arises from hole injection) measured from dye-sensitized p-GaP(100) photoelectrodes in various redox couple concentrations.

B. Experimental Section

i. Photoelectrode Fabrication

The fabrication steps were identical to the procedure described in Chapter V. GaP(100) (Zn-doped, 0.086 Ω cm, thickness = 0.35 mm, ITME) were used as the primary electrode materials.

ii. Dye Adsorption on GaP Photoelectrode

The cured p-GaP(100) electrode was etched in 35 wt.% HCl for 30 s to remove the native oxide, rinsed with nanopure water and then dried with N_2. The etched electrode was then immersed in 10 v/v% $(NH_4)_2S$ for 6-12 h to populate the surface with S^{2-} and NH^{4+} moieties. After 6-12 h, the electrode was rinsed in nanopure water and immediately transferred to the dye solution. To adsorb dyes on the surface of the GaP electrode, the cured electrode was immersed

in stirred 6 mM dye solution (pH 6) to react for 30 min to reach equilibrium. The electrode was then transferred to nanopure water to remove any weakly physisorbed dye before performing photoelectrochemical measurements. In between measurements, the dye-adsorbed electrode was cleaned in acetone and followed by acidic solution (pH 2) to decompose the adsorbed dye molecules. Dyes used in the studies were Rose Bengal (95 %, Sigma-Aldrich), Rhodamine-B (95 %, Sigma-Aldrich) and Rhodamine-6G (95 %, Sigma-Aldrich).

iii. (Photo-)Electrochemical Acquisition

A custom-built, 3-electrode quartz cell with an optically flat bottom was used for photoelectrochemical measurements. The reference and counter electrodes were an Ag wire coated with AgCl immersed in sat. KCl and Pt mesh, respectively. An aqueous solution of methyl viologen (98 %, Sigma-Aldrich), europium(III) chloride hexahydrate (Acros) and 1 M KCl (Mallinckrodt, Analytical Reagent) was used as the active redox species. Spectral response measurements were collected with a lab-built system detailed previously.[5] The light source was an Oriel 150 W Xe arc lamp (Newport) and it was chopped at 15 Hz during measurements. The steady-state *J-E* photoresponses were collected with a digital PAR 273 potentiostat.

iv. X-ray Photoelectron Spectroscopy

All X-ray photoelectron spectroscopy (XPS) data were acquired using a PHI 5400 analyzer equipped with an Al Ka source without a monochromator. Spectra were collected without charge neutralization at a base pressure of $<2.5 \times 10^{-9}$ Torr. A 6 mA emission and a 12 kV anode high tension were used for spectral acquisition with a pass energy of 23.5 eV for high-resolution XP spectra. The XP spectra were calibrated to the C 1s peak at 284.6 eV.

C. Findings and Summary

The effects of redox couple concentration was first tested with planar p-GaP(100) electrode in deaerated 1 M KCl containing 5 μM rhodamine-B. Figure A.1 shows the external quantum yield (EQY) measured at 580 nm monochromatic light vs. potential of the said electrode immersed in 5 μM rhodamine-B with 2, 5 or 10 mM Eu^{3+} or MV^{2+} redox species. The EQY of the GaP electrode increased as the concentration of the redox couple for both species increased.

The same experiment was done with dye adsorbed on the p-GaP(100) electrode. A monolayer of Rose Bengal (RB) dye molecules were physisorbed on the (100) phase of GaP

wafer using a method/treatment reported by Chitambar et al.[2] The S 2p and N 1s XP spectra of an etched GaP(100) substrate, a sulfide-treated substrate and a sulfide-treated substrate adsorbed with RB molecules were presented in Figure A.2a and 2b. The treatments were summarized in Table A.1. The sulfide-treated substrates showed signals corresponded to S^{2-} ions and N, indicating formation of NH^{4+} moieties on the treated surface besides the expected S^{2-} moieties as seen in GaAs(100).[6-8] Figure A.2c shows I 3d XP spectra collected from the aforementioned samples. I signals which came from RB dye molecules were only detected from surface that had been treated with 10 v/v% $(NH_4)_2S$ after immersing in 6 mM RB for 30 min, strong indication of the presence of dyes on the sulfide-treated GaP surface. The charge of the treated GaP surface was further probed using a cationic dye molecule like rhodamine-6G (Rh-6G). Figure A.3 presents the sub-band gap wavelength-dependent EQY of a sulfide-treated GaP(100) electrode in *clear* 1 M KCl after immersing in 6 mM RB or Rh-6G solution for 30 min. Maximum EQY at 580 nm for a monolayer of RB is ~0.001 and ~0.0015 for Rh-6G.[2] Based on Figure A.3, this sulfide treatment effectively adsorbed anionic or acid dyes like RB.

Anhydrous $EuCl_3$ is soluble in acidic salt solution. Therefore, it is crucial to know the pH effects on the net photocurrent measured from adsorbed RB molecules on p-GaP. Figure A.4 presents the sub-band gap wavelength-dependent EQY of a sulfide-treated GaP(100) electrode that was previously physisorbed with RB molecules in clear electrolyte at pH ranging from 2 to 4. The pH was adjusted with HCl and measured with a digital pH meter. The EQY is the largest at pH 4, but decreases as the pH decreases. This is mainly due to RB being decomposed at low pH although the shift of valence band edge in GaP might play a role.[9-10] One thing to note is that the sub-band gap EQY increases (at 640 nm) as the pH decreases. This is due to oxide formation at low pH solution.[10-11] The optimum pH for this study was 4 (4.2 in the subsequent measurements), and the maximum achievable concentration was 2 mM $EuCl_3$.

Sulfide treatment did not produce a stable surface, that is, the surface could degrade over time and the amount of RB molecules adsorbed could vary depending on the surface roughness, experiment length, and surface defects.[7] It was found that reliable comparisons could be made if the data were collected from the same electrode, and the handling between experiments became significant. Figure A.5 compiles the EQY measurements obtained from the technique mentioned in the Section B to show the reproducibility and reliability of this methodology.

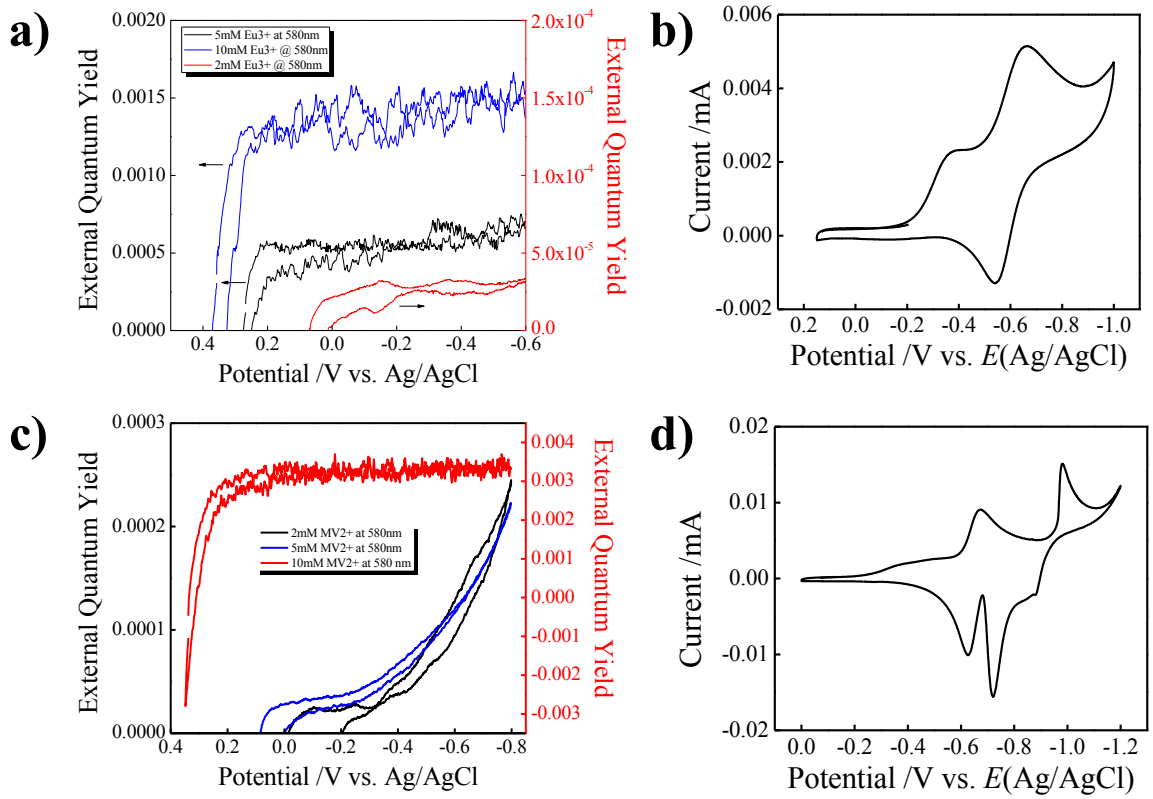

Figure A.1. Measured potential dependence of p-GaP(100) sensitized with 5 μM Rh-B in deaerated 1 M KCl electrolyte containing 2, 5 or 10 mM $1e^-$ reductive redox couples. (a) $EuCl_3$ and (c) methyl viologen dichloride ($MVCl_2$), and the electrodes were illuminated with 580 nm light at 0.27 mW cm^{-2}; pH = 4.2. (b, d) Current-potential responses collected from Au electrode in 1 M KCl with 2 mM (b) $EuCl_3$ and (d) $MVCl_2$; pH = 4.2.

Table A.1. Summary of sample names and the corresponding treatments

Sample Name	Treatments
GaP(100)	Etched in conc. HCl for 30 s
$(NH_4)_2S$-treated	Etched; Immersed in 10 v/v% $(NH_4)_2S$ 6 h
$(NH_4)_2S$-treated + RB	Etched; Treated in 10 v/v% $(NH_4)_2S$ 6 h and immersed in 6 mM rose Bengal dye for 30 min

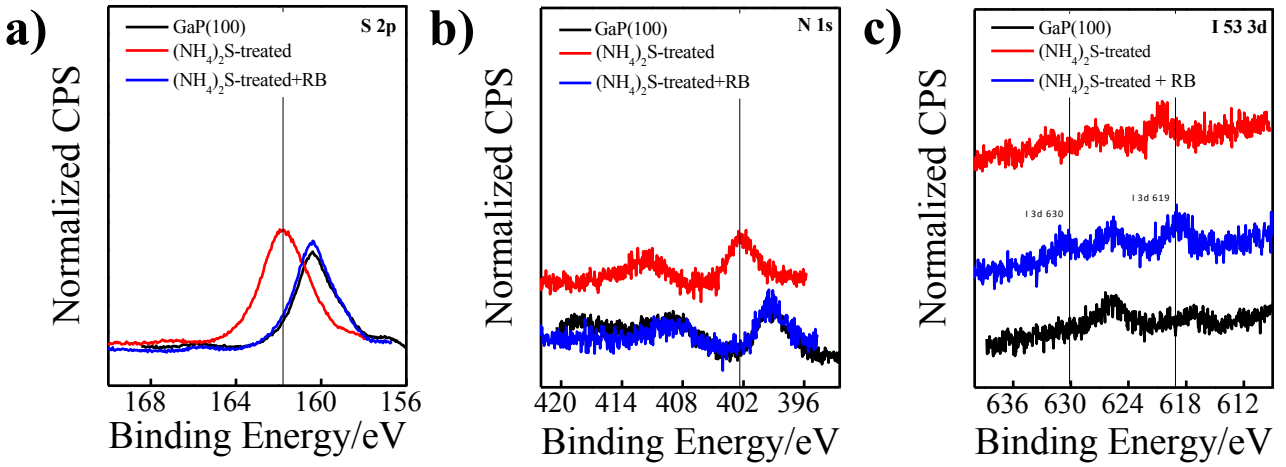

Figure A.2. High-resolution (a) S 2p, (b) N 1s, and (c) I 3d XP spectra of planar GaP(100) samples as-etched (black), after treating in 10 v/v% $(NH_4)_2S$ for 6 h (red), and after immersing in 6 mM rose Bengal solution for 30 min (blue). The black vertical lines indicate the expected binding energies for each element.

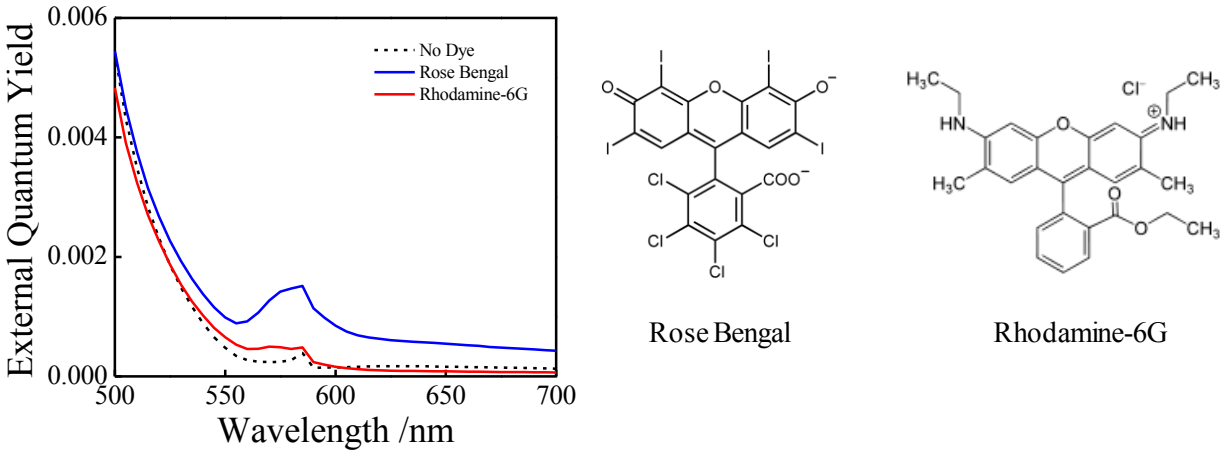

Figure A.3. Measured wavelength dependence net photocurrent generation from p-GaP(100) electrode in clear 1 M KCl. The electrode had been soaked in 10 v/v% $(NH_4)_2S$ (black dotted-line) and followed by 6 mM rose Bengal (anionic dye; blue line) or 6 mM rhodamine-6G (cationic dye; red line). The structure of each dye is shown. The electrode was poised at -0.65 V vs. Ag/AgCl.

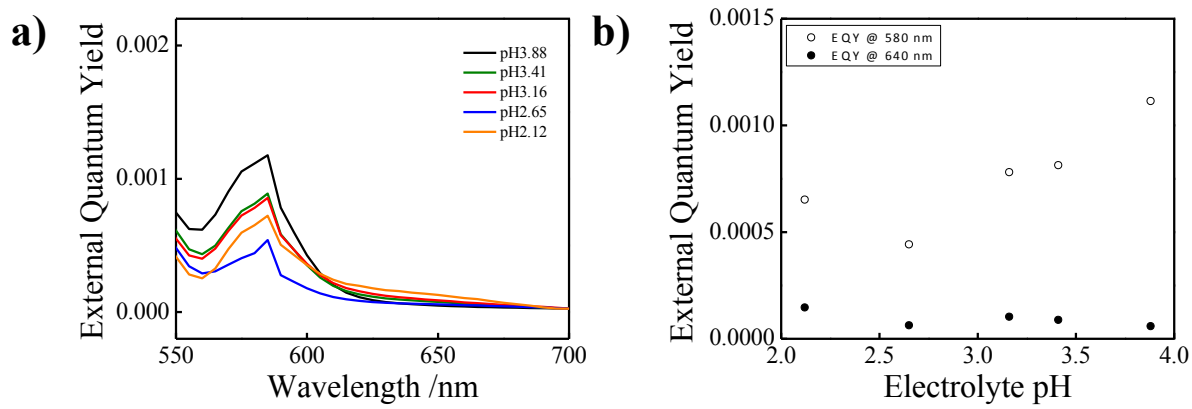

Figure A.4. (a) Measured external quantum yield at sub-band gap wavelengths of p-GaP(100) electrode that was previously treated with 10 v/v% $(NH_4)_2S$ and adsorbed with rose Bengal dyes in deaerated clear 1 M KCl at various pH. (b) External quantum yield measured at 580 nm and 640 nm light as a function of the pH of the electrolyte. The EQY were collected at -0.65 V vs. Ag/AgCl.

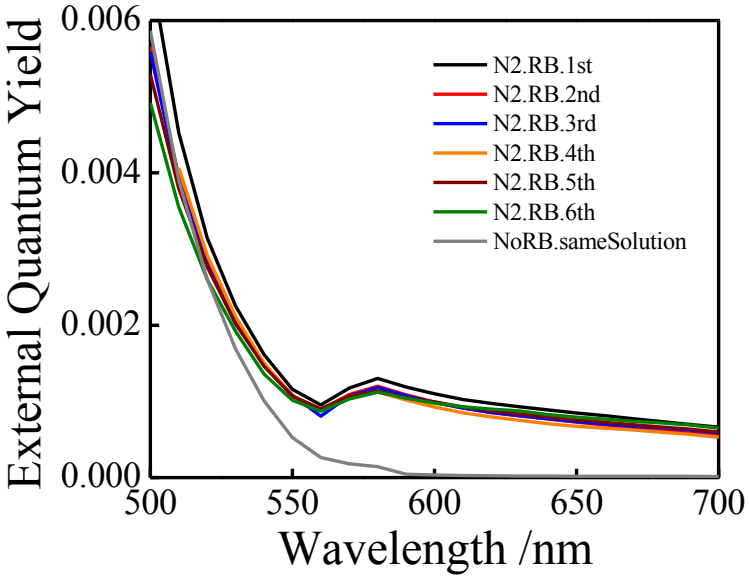

Figure A.5. Technique reproducibility: Measured external quantum yield in deaerated 1 M KCl (pH 4.2) at sub-band gap wavelengths of the same p-GaP(100) electrode that was previously treated with 10 v/v% $(NH_4)_2S$. The electrode was immersed in 6 mM RB for 30 min before each measurement, and subsequently cleaned in acetone and acid to remove adsorbed dye before the next data collection. The same electrode was soaked in RB solution to re-adsorb the dye molecule before next experiment. The EQY were collected at -0.65 V vs. Ag/AgCl.

Figure A.6 shows the trend of the wavelength-dependent EQY collected from RB-adsorbed p-GaP(100) in electrolyte containing 0 – 2 mM Eu^{3+}. Each trend was collected with one electrode (cleaned and re-adsorb dyes as mentioned in text) for reasons mentioned. The net photocurrent increased significantly when redox species were added to the electrolyte. The trend appears to level off at concentrations greater than 0.2 mM Eu^{3+}. Figure A.7a-d compiles the EQY collected from RB-adsorbed p-GaP(100) at 580 nm with MV^{2+} in the electrolyte. $MVCl_2$ is soluble in aqueous electrolyte, so concentrations of 0 – 20 mM were used in all MV^{2+} experiments, but the electrolyte pH was kept at 4.2. At low concentrations, the trend was similar to the case with Eu^{3+}. However, at 5, 10, and 20 mM MV^{2+}, the EQY at 580 nm became larger than the EQY of monolayer in just 1 M KCl. No significant difference in EQY among the high concentrations. Figure A.7e and 7f presents the EQY data collected while stirring the solution rigorously during the course of measurements to minimize any mass transport limitations. The trend still preserved. Figure A.7g and 7h shows EQY data collected with stirring, but the data were collected in decreasing order with the intention to randomize the collection sequence to obtain more insights of the system. Figure A.8 contains more data collected in decreasing order of concentration on several RB-adsorbed p-GaP(100) electrodes. Other than Electrode N7, Electrodes N6 and N8 both showed a rather constant (flat) EQY trend ranging from 0.1 to 2.0 mM MV^{2+} redox couple.

At this point, we have found that it is necessary to use the same GaP electrode in each set of study to produce comparable trends. Therefore, it is crucial to handle the electrodes with great care during as well as in between measurements. The handling/cleaning procedure has to be followed closely to minimize trend inconsistency and maximize result reproducibility. More repetitions are needed to obtain a statistics. Last but not the least, more electrochemical impedance data (EIS) are necessary to model the GaP band structures (before and after sulfide-treatment) with respect to the redox couples and RB dyes' HOMO/LUMO energy levels.

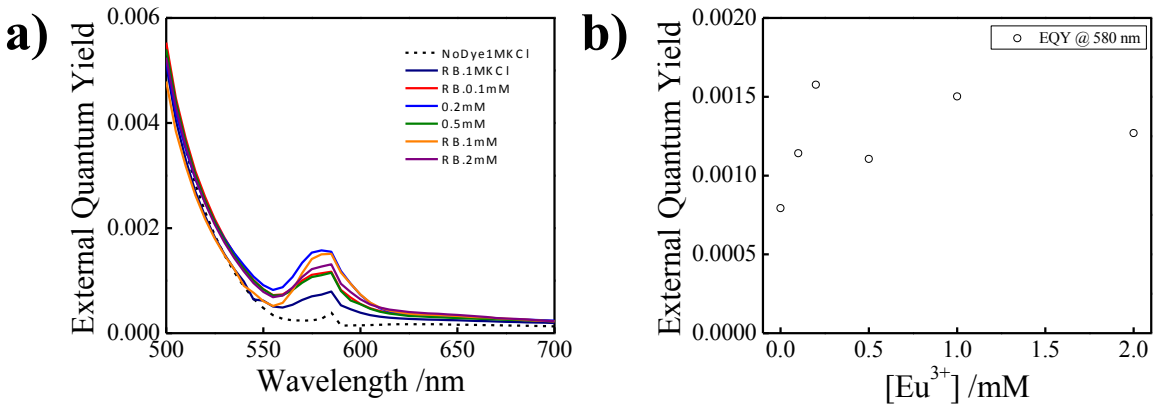

Figure A.6. (a) Measured external quantum yield at sub-band gap wavelengths of p-GaP(100) electrode that was previously treated with 10 v/v% $(NH_4)_2S$ and adsorbed with rose Bengal dyes in deaerated 1 M KCl containing 0 – 2 mM $EuCl_3$ at pH 4.2. The data were collected at -0.65 V vs. Ag/AgCl. (b) External quantum yield measured at 580 nm as a function of the concentration of Eu^{3+} species in the electrolyte.

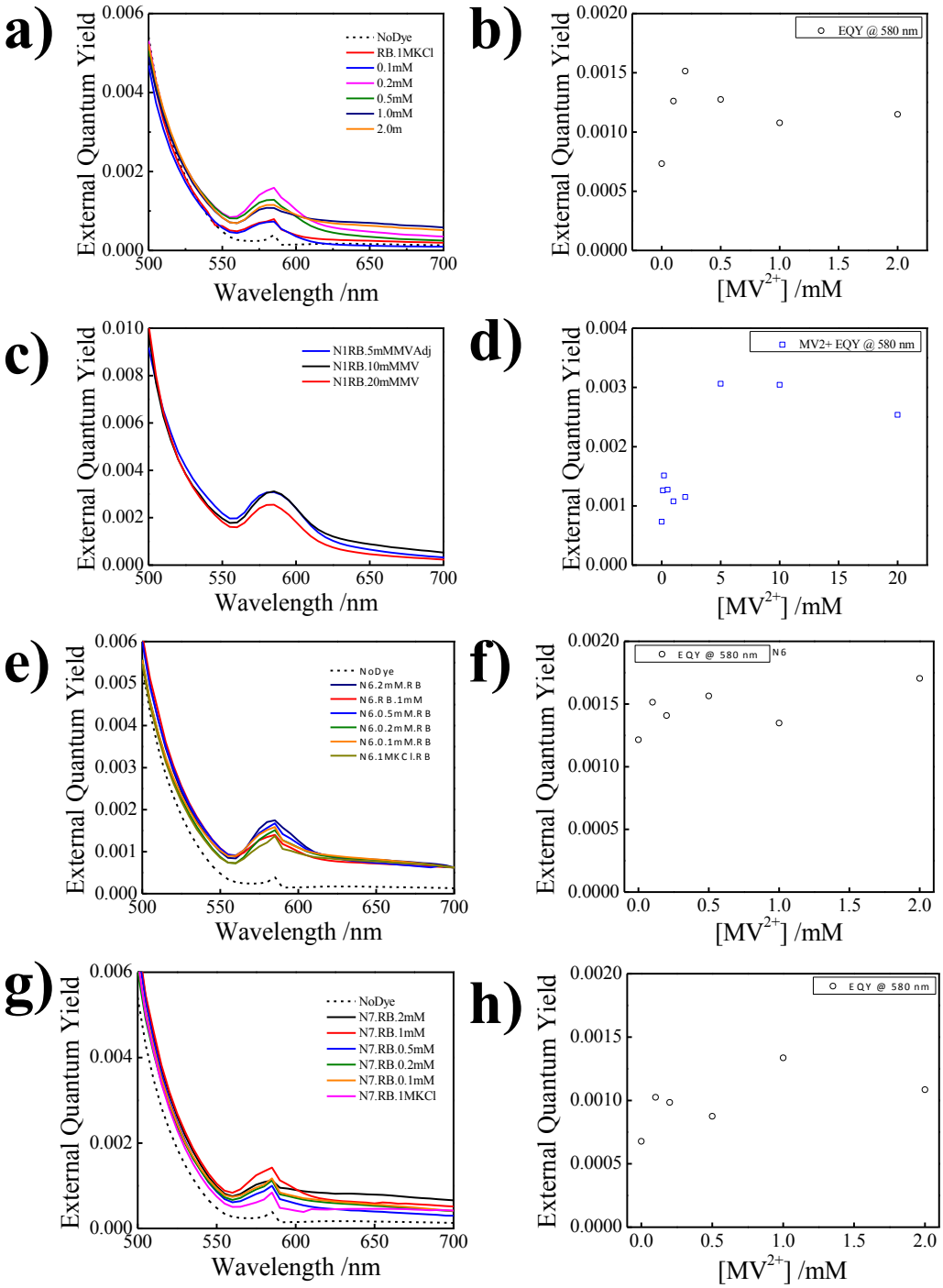

Figure A.7. (a, c) Measured external quantum yield at sub-band gap wavelengths of RB-adsorbed p-GaP(100) electrode in deaerated 1 M KCl containing 0 – 20 mM MV^{2+}. (b, d) External quantum yield measured at 580 nm as a function of the concentration of MV^{2+} species in the electrolyte. (e, g) External quantum yield collected from two separate RB-adsorbed GaP(100) electrodes in 1 M KCl with 0 – 2 mM MV^{2+}. The electrolyte was stirred rigorously throughout the data acquisition. (f, h) The corresponding plots of quantum yield measured at 580 nm against the concentration of MV^{2+} species. Note that (g) and (h) were collected in decreasing order, i.e. from electrolyte containing 2 mM MV^{2+} to 0 mM MV^{2+}. ($E_{applied}$: 0.65 V vs. Ag/AgCl)

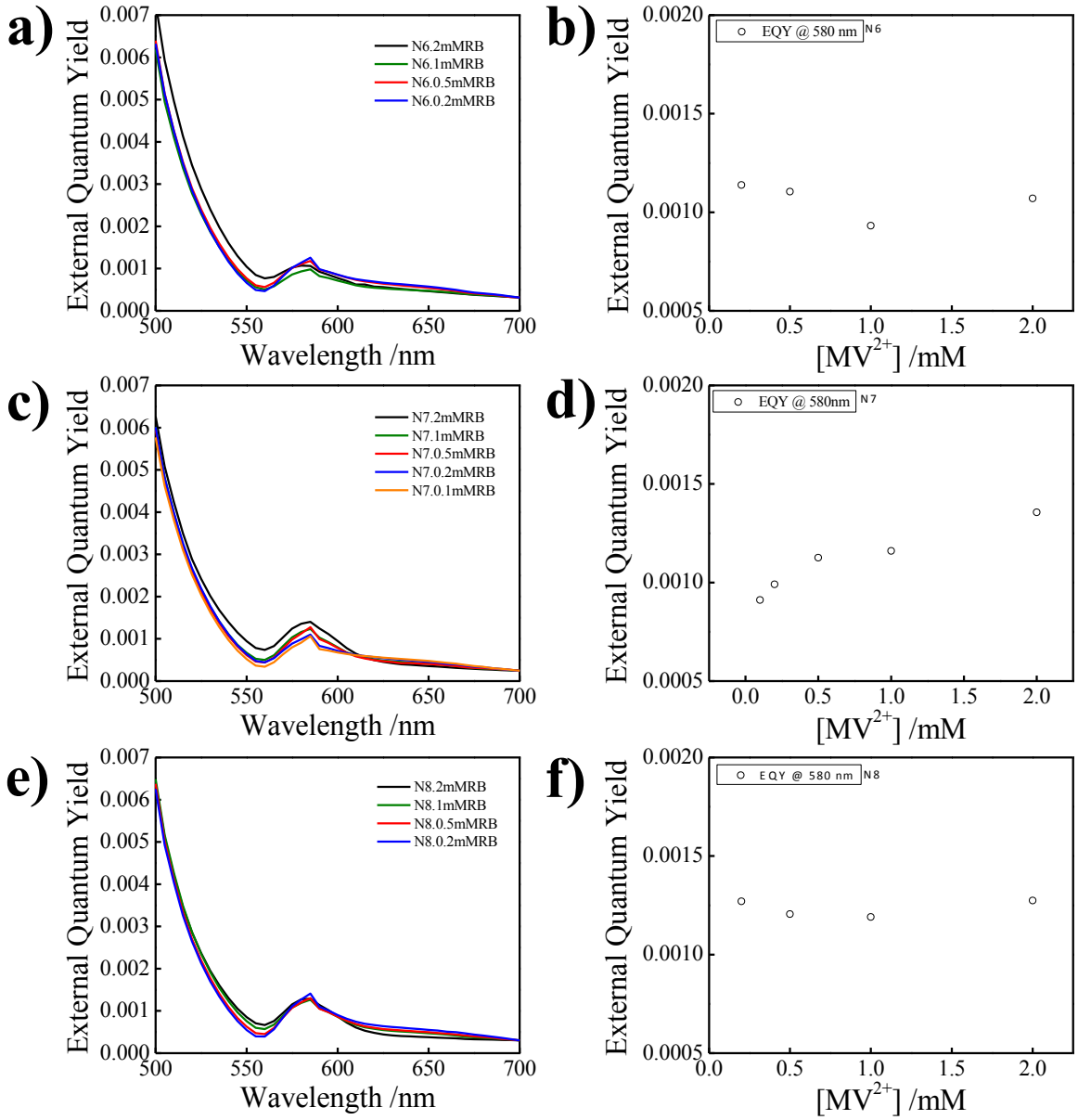

Figure A.8. (a, c, e) Measured external quantum yield at sub-band gap wavelengths of three separate RB-adsorbed p-GaP(100) electrodes in deaerated 1 M KCl containing 0 – 2 mM MV^{2+}. The data were collected in decreasing order, i.e. from electrolyte containing 2 mM MV^{2+} to 0 mM MV^{2+}. (b, d, f) Plots of external quantum yield measured at 580 nm from three separate electrodes as a function of the concentration of MV^{2+} species in the electrolyte. The data were collected at -0.65 V vs. Ag/AgCl.

D. References

1. O'Regan, B.; Grätzel, M., A Low-Cost, High-Efficiency Solar Cell Based on Dye-Sensitized Colloidal TiO_2 Films. *Nature.* **1991,** *353* (6346), 737-740.
2. Chitambar, M.; Wang, Z.; Liu, Y.; Rockett, A.; Maldonado, S., Dye-Sensitized Photocathodes: Efficient Light-Stimulated Hole Injection into p-GaP under Depletion Conditions. *J. Am. Chem. Soc.* **2012,** *134*, 10670-10681.
3. Wang, Z.; Shakya, A.; Gu, J.; Lian, S.; Maldonado, S., Sensitization of p-GaP with CdSe Quantum Dots: Light-Stimulated Hole Injection. *J. Am. Chem. Soc.* **2013,** *135* (25), 9275-8.
4. Ilic, S.; Brown, E. S.; Xie, Y.; Maldonado, S.; Glusac, K. D., Sensitization of p-GaP with Monocationic Dyes: The Effect of Dye Excited-State Lifetime on Hole Injection Efficiencies. *J. Phys. Chem. C.* **2016,** *120* (6), 3145-3155.
5. Price, M. J.; Maldonado, S., Macroporous n-GaP in Nonaqueous Regenerative Photoelectrochemical Cells. *J. Phys. Chem. C.* **2009,** *113* (28), 11988-11994.
6. Bessolov, V. N., Solvent Effect on the Properties of Sulfur Passivated GaAs. *J. Vac. Sci. Technol., B.* **1996,** *14* (4), 2761.
7. Cowans, B. A.; Dardas, Z.; Delgass, W. N.; Carpenter, M. S.; Melloch, M. R., X-Ray Photoelectron Spectroscopy of Ammonium Sulfide Treated GaAs (100) Surfaces. *Appl. Phys. Lett.* **1989,** *54* (4), 365.
8. Shin, J., The Chemistry of Sulfur Passivation of Gaas Surfaces. *J. Vac. Sci. Technol., A.* **1990,** *8* (3), 1894.
9. Nakato, Y.; Tsumura, A.; Tsubomura, H., Surface Intermediates of an N-Type Gallium Phosphide Electrode as Related with the Shifts of the Surface Band Energy Induced by Oxidants in Solution. *J. Electrochem. Soc.* **1981,** *128* (6), 1300-1304.
10. Brown, E. S.; Peczonczyk, S. L.; Wang, Z.; Maldonado, S., Photoelectrochemical Properties of CH_3-Terminated p-Type GaP(111)A. *J. Phys. Chem. C.* **2014,** *118*, 11593-11600.
11. Beckmann, K. H.; Memming, R., Photoexcitation and Luminescence in Redox Processes on Gallium Phosphide Electrodes. *J. Electrochem. Soc.* **1969,** *116* (3), 368-373.